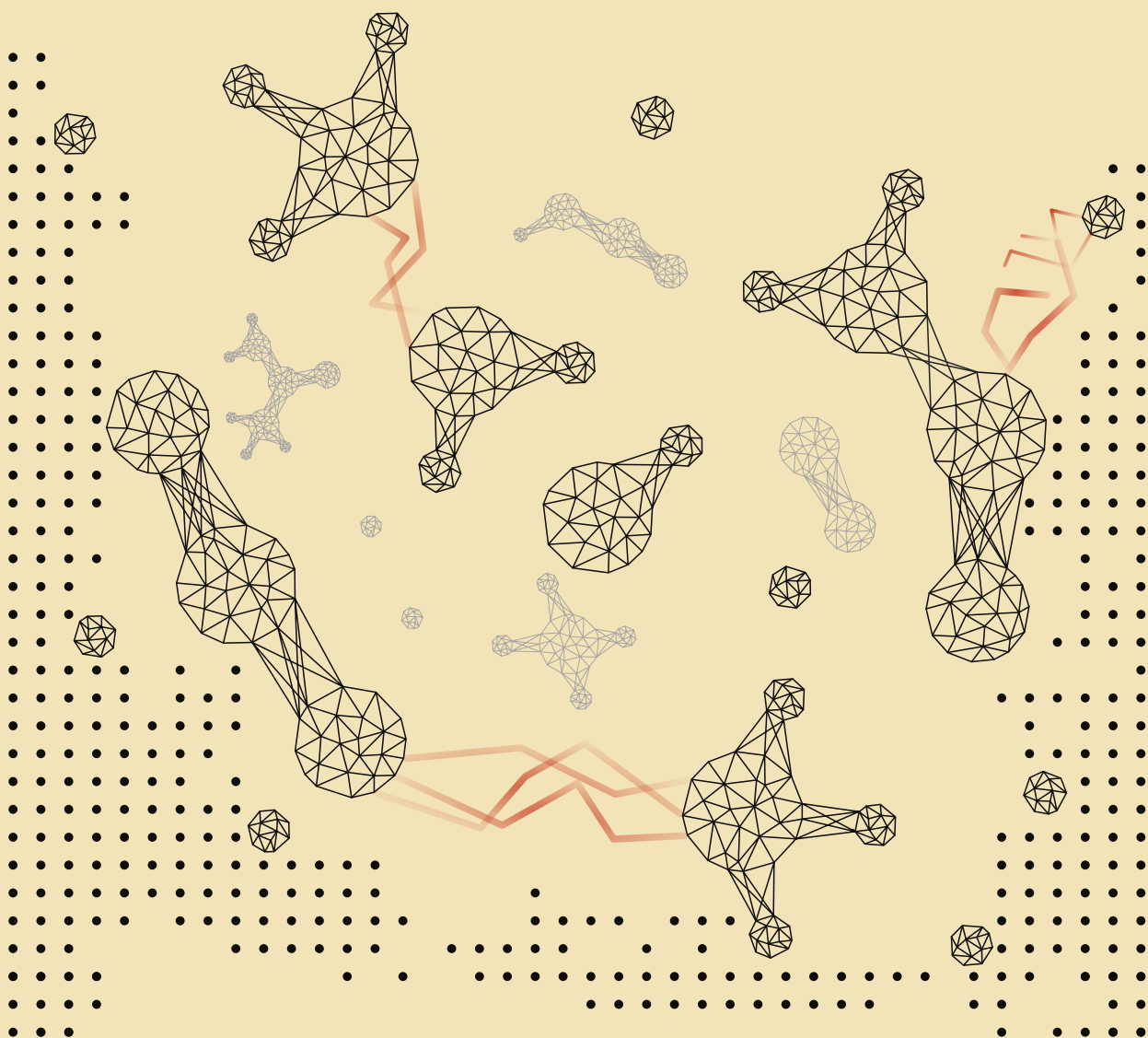

THE ASTROCHEMICAL FACTORY

a solid base for interstellar reactions



Niels Frank Willem Ligterink

The astrochemical factory

A solide base for interstellar reactions

1. It remains difficult to explain the observed abundances of cold, gaseous methanol in the interstellar medium.
-Chapter 4
2. With the availability of accurate laboratory spectra, JWST offers the possibility to securely identify a number of complex organic molecules in the solid-state.
-Chapter 5
3. Interstellar ice chemistry offers realistic pathways that result in the formation of amide-like and amide-bearing molecules.
-Chapter 6 and 7
4. The interstellar non-detections of CH_3NH_2 and NH_2OH reduces the relevance of mechanisms involving these molecules that lead to the formation of amino acids.
-Chapter 8 and 9
5. Upper limits on interstellar molecular reservoirs give key constraints to underlying chemical processes.
6. The interstellar presence of amide-bearing molecules should be seen as an indication that larger peptide-like fragments are present as well.
7. Multidisciplinary research and publications have to be encouraged to improve communication and understanding between laboratory, observational and modelling studies.
8. Research funding should also be acquired from private investors and industry in order to be less dependent on fluctuations in government spending.
9. Applicants to scientific positions should purely be judged on capabilities and suitability for the job.
10. If you are Dutch, doing a PhD in Leiden is a good way to learn about foreign cultures without leaving the comfort of your home country.
11. With Earths current population size, a sustainable future is near impossible.
12. Many people underestimate their ability to make choices for themselves.

Niels F.W. Ligterink
Leiden, December 18, 2017

The astrochemical factory
A solid base for interstellar reactions

N.F.W. Ligterink

The astrochemical factory

A solid base for interstellar reactions

Proefschrift

ter verkrijging van
de graad van Doctor aan de Universiteit Leiden,
op gezag van Rector Magnificus prof. mr. G.R. de Snoo,
volgens besluit van het College voor Promoties
te verdedigen op maandag 18 december 2017
klokke 11.15 uur

door

Niels Frank Willem Ligterink

geboren te Woerden, Nederland
in 1989

Promotiecommissie

Promotores: Prof. dr. E.F. van Dishoeck
Prof. dr. H. Linnartz

Overige leden: Prof. dr. J. Cernicharo (*Instituto de Ciencia de Materiales de Madrid*)
Prof. dr. P. Caselli (*Max Planck Institute for Extraterrestrial Physics*)
Dr. P.A Gerakines (*NASA Goddard Space Flight Center*)
Prof. dr. Paul van der Werf (*University of Leiden*)
Prof. dr. Huub Röttgering (*University of Leiden*)

Table of contents

1. Introduction	1
1.1. Forming an icy dust grain	3
1.2. Energetic processing of ices	6
1.2.1. Types of energetic processes	6
1.2.2. Laboratory investigations	7
1.2.3. Chemical modelling	9
1.3. Observing ice chemistry in the gas phase	10
1.3.1. Hot cores and corinos	10
1.3.2. Observations	11
1.4. Snowlines and non-thermal ice desorption	13
1.5. Icy rocks	14
1.6. This thesis	15
2. CryoPAD2 experimental set-up	19
2.1. Introduction	20
2.2. Description of CryoPAD2	21
2.3. Calibrations	24
2.3.1. QMS work function	24
2.3.2. QMS filament output correction	25
2.3.3. Column density and RAIRS correction	26
2.3.4. VUV photon flux	28
2.4. An experimental example	29
2.4.1. Introduction	29
2.4.2. Experimental	29
2.4.3. Results	29
2.4.4. Discussion	33
2.4.5. Conclusion	34
3. Controlling the emission of a Vacuum-UV lamp	35
3.1. Introduction	36
3.2. Experimental	37
3.2.1. Microwave discharge hydrogen-flow lamp	37
3.2.2. Greifswald UV/VUV spectrometer	38
3.2.3. Photon flux measurements	40
3.2.4. CryoPAD2	41
3.3. Results	42
3.3.1. Photon flux	42
3.3.2. H ₂ pressure dependence	42
3.3.3. Mixtures and different gasses	43
3.3.4. MDHL power dependence	44
3.3.5. Pumping efficiency in F- and T-type MDHLs	46
3.3.6. Distance dependence	47
3.3.7. Practical issues	48

3.3.8. CO photodepletion measurements	51
3.4. Conclusions	53
4. Methanol ice co-desorption to explain cold gas-phase methanol	55
4.1. Introduction	56
4.2. Experimental setup and results	58
4.2.1. Laboratory set-up and protocols	58
4.2.2. Experimental results	60
4.3. Modelling	64
4.3.1. Astrochemical model description	64
4.3.2. Astrochemical model results	66
4.4. Conclusions	70
5. IR spectra of frozen complex organic molecules	73
5.1. Introduction	74
5.2. Experimental	77
5.2.1. Set-up	77
5.2.2. Measurement protocol	77
5.2.3. Analysis protocol	78
5.3. Results and Discussion	78
5.3.1. Acetaldehyde	81
5.3.2. Ethanol	84
5.3.3. Dimethyl ether	84
5.4. COM ice features in W33A	85
5.5. Conclusions	88
6. An observational and laboratory study of CH₃NCO	89
6.1. Introduction	90
6.2. Observations	92
6.2.1. The ALMA PILS survey	92
6.2.2. Results	93
6.3. Laboratory experiments	98
6.3.1. Set-up and method	98
6.3.2. Results – IR Spectra	100
6.3.3. Results – temperature programmed desorption	101
6.4. Linking observations and laboratory data	104
6.5. Conclusions	104
6.6. Appendix	105
6.6.1. Line list	105
6.6.2. CH ₃ NCO $\nu_b=1$	107
6.6.3. $m/z = 56, 57$ and 58 upon VUV irradiation of pure CH ₄ and H ₂ NCO samples	107
7. Formation of amides in interstellar relevant ices	109
7.1. Introduction	110
7.2. Experimental	112
7.2.1. Setup and protocol	112
7.2.2. Data analysis	113
7.2.3. Fragmentation patterns and desorption temperatures	115

7.3. Results	117
7.3.1. Identification of the main products	117
7.3.2. Comparison between experimental conditions	125
7.4. Discussion	126
7.4.1. Key reactions and reaction network	126
7.4.2. Comparison with interstellar abundance ratios	128
7.5. Conclusions	130
8. Search for methylamine in high mass hot cores	131
8.1. Introduction	132
8.2. Observations	133
8.3. Data analysis	135
8.4. Results	137
8.4.1. CH ₃ NH ₂ limits	137
8.4.2. Abundance ratio comparison	138
8.5. Discussion	140
8.5.1. CH ₃ NH ₂	142
8.5.2. NH ₂ CHO	143
8.5.3. CH ₃ CN	143
8.5.4. Prospects for ALMA	144
8.6. Conclusions	144
8.7. Appendix	146
8.7.1. Transitions of methylamine and other molecules	146
8.7.2. ALMA	149
9. Small -NH₂ and NO molecules towards IRAS 16293-2422B	151
9.1. Introduction	152
9.2. Observations and data analysis	153
9.3. Results	154
9.4. Astronomical implications	158
9.5. Appendix	159
9.5.1. Spectroscopic data	159
9.5.2. Additional fit spectra of CH ₂ NH and NO	160
9.5.3. Upper limit column densities of NH ₂ OH and CH ₃ NH ₂	161
10. Interstellar bromine depletion matches cometary ices from <i>Rosetta</i>	163
10.1. Introduction	164
10.2. Data	164
10.2.1. Spectroscopy of HBr and HBr ⁺	164
10.2.2. Archival <i>Herschel</i> observations and selected sources	165
10.2.3. Analysis method	165
10.3. Search for HBr and HBr ⁺ in the <i>Herschel</i> spectra	167
10.4. Protostellar <i>vs</i> cometary abundance	167
10.5. Interstellar chemistry of Br	168
10.5.1. Chemical modelling results	170
10.6. Conclusions	171
10.7. Appendix	172
10.7.1. Linelist of HBr transitions in range of HIFI	172
10.7.2. Sgr B2(N) and NGC6334I at 500 GHz	173

10.7.3. Upper limit column densities of $\text{H}^{79+81}\text{Br}$ and column densities of reference molecules	174
Bibliography	177
Nederlandse samenvatting	189
Publications	195
Curriculum Vitae	197
Afterword	199



V-UV



Introduction

N.F.W. Ligterink

Astrochemistry is the study of chemical processes under the extreme conditions in the interstellar medium in which new stars and planets are born. This thesis deals with its three main research areas: laboratory experiments, astronomical observations and astronomical modelling. The common denominator between the chapters is the *interstellar icy dust grain*, a surface covered with frozen-out molecules on which much of the interstellar chemistry takes place. The introduction to this thesis follows the voyage that an icy grain takes through the cycle of star formation. Various interstellar phenomena interact with the ice layers of the grain and trigger physical and chemical processes. Laboratory, observational and modelling concepts and results will be introduced in this story along the way. The focus will be on the parts of the star formation cycle that are of particular interest to this thesis.

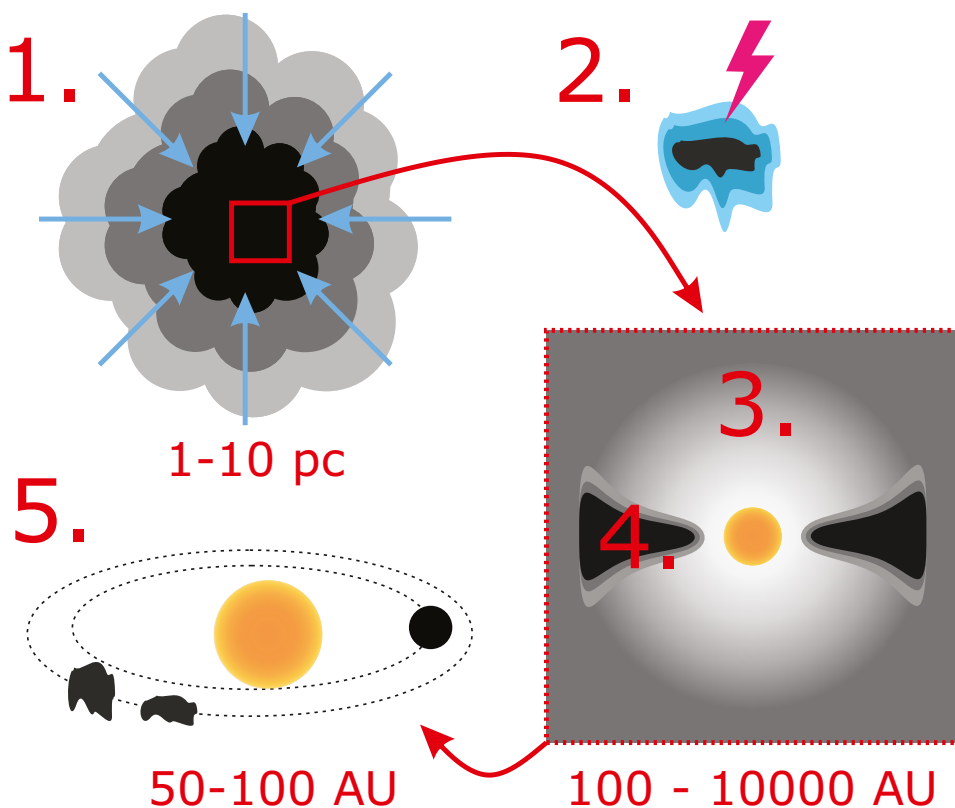


Figure 1.1: (1) Ice mantle formation on dust grains; (2) Energetic processing of ice mantles; (3) Gas-phase chemical complexity in the hot core after ice has thermally desorbed; (4) Non-thermal desorption processes in protoplanetary disks; (5) Formation of rocky bodies in the protoplanetary disk and the inheritance of ice from dust grains.

Schematically the journey of an interstellar dust grain from *diffuse cloud* to *protoplanetary disk* is depicted in Fig. 1.1. The numbering corresponds to the following sections and specific environments and processes they describe. Section 1.1 follows the collapse of clouds of gas and dust to dense *dark clouds*,

while dust grains simultaneously build up an ice mantle. Section 1.2 discusses energetic processes in the interstellar medium, especially *far – UV* irradiation, and how this enhances the chemical complexity on dust grains. In section 1.3 the transition from dark cloud to *protostar* is described and the effect this has on its surroundings. Specifically the *hot core* is important, which is an environment where the ice mantles are thermally desorbed and give a snap shot of the chemical complexity that was attained on the icy dust grain. Section 1.4 discusses the protoplanetary disk, mainly in the context non-thermal desorption mechanisms that cause the release of molecules to the gas-phase. In section 1.5 the final stage of star formation is discussed, when large rocky bodies, comets and *protoplanets* form in the protoplanetary disk. The comets retain the remnants of the earliest stage of star formation, the dust grains and their ice mantles, and are therefore link the beginning and the end of star formation.

1.1. Forming an icy dust grain

Dust grains consist of iron and magnesium containing silicates and carbonaceous material. Their size is small, ranging from nanometres to millimetres. Dust grains are the remnants of dying stars, but also may be formed through condensation and growth in the interstellar medium.

Grains reside in large low density diffuse clouds together with gas phase atoms and molecules. Typical densities are $n \sim 100 \text{ cm}^{-3}$ and extinctions of $A_v \approx 1$ magnitude (mag, 1 mag = 2.5 times reduction in intensity), caused by absorption and scatter of incoming radiation by dust. The gas is dominated by H, H₂ and He, followed by traces of carbon, nitrogen and oxygen. Even smaller fractions of small molecules can be present, such as CO, CN and HCO⁺. Diffuse clouds are relatively warm at around 100 K and subject to the intense radiation of the interstellar radiation field (ISRF, Mathis et al. 1983), the combined radiation field of all the stars at a typical location in the galaxy. Under these conditions molecules are readily destroyed and therefore mainly atomic gases with small abundances of molecules are present, mixed with dust grains.

Perturbations to the diffuse cloud, for example caused by shocks from supernovae, can locally increase the density of gas and dust. This local over-density gravitationally attracts more material and at some point the cloud becomes dense enough to shield its inner regions from the ISRF. This is accompanied by a decrease in temperature, which results in a gradual freeze out of atomic and molecular gas phase species. The cloud passes through a *translucent cloud* phase (10^3 cm^{-3} , $A_v \approx 1\text{-}5$ mag) and eventually becomes a so-called *dense or dark cloud* ($n \sim 10^4\text{-}10^6 \text{ cm}^{-3}$, $A_v \gg 5$ mag). External visible and ultraviolet light does not penetrate this type of cloud. The temperature keeps decreasing to as low as 10 K and most atoms and molecules freeze out onto the dust grains. Only substantial amounts of H₂, H and He stay in the gas phase (Herbst & van Dishoeck 2009).

The frozen out species do not remain idle on the surface of the dust grains. Diffusion is possible and various reactions can occur. One of the most prominent and well-studied reactions are those involving H-atom additions, so called hydrogenation reactions. Hydrogen atoms stick on the grain, diffuse over the surface and find a species with which they can react. Due to this so-called

Langmuir – Hinshelwood mechanism a large part of the atomic carbon, nitrogen and oxygen reservoir is converted to methane (CH_4), ammonia (NH_3 , Hidaka et al. 2011; Fedoseev et al. 2015b) and, fractionally the most abundant, water (H_2O , Oba et al. 2009; Ioppolo et al. 2008; Dulieu et al. 2010; Cuppen et al. 2010; Lamberts et al. 2014) in a non-energetic way. Via similar diffusion reactions carbon dioxide (CO_2) is formed from radical-molecule reactions between CO and OH, and to a lesser extent from CO + O reactions (Ioppolo et al. 2011, 2013).

Not only atoms, but also molecules can be hydrogenated, in particular carbon monoxide (CO). This molecule can be efficiently converted to formaldehyde (H_2CO) and eventually methanol (CH_3OH , Watanabe & Kouchi 2002; Fuchs et al. 2009). Contrary to the previously mentioned molecules, CO itself is mainly formed in the gas phase. Due to its very volatile nature carbon monoxide only freezes out at the coldest temperatures of the dark cloud stage, often after water, ammonia and methane have already formed. This results in a distinct water-rich and CO-rich layer and explains how a prototypical icy dust grain is build up: a silicate/carbonaceous core, covered by a water layer with methane, ammonia and some carbon dioxide, which is surrounded by a second mantle that consists of mainly CO, CO_2 , H_2CO and methanol (Boogert et al. 2015 and references therein, Fig. 1). Note that CO_2 is the only molecule that has substantial abundances in both layers.

These examples of water, ammonia and methanol formation show the importance of the dust grain as a catalytic surface, although not in the traditional chemistry sense. It is often found that gas-phase reactions are not efficient enough at low temperatures to account for the observed abundances of these molecules. The surface of a dust grain acts as a molecular reservoir that brings species together, promotes reactions to form these products and acts as a third body to take away excess energy of a reaction. Therefore an interstellar icy dust grain is of great importance not only to form these simple species, but, as we will see later, also much more complex molecules.

InfraRed (IR) observatories like the *Infrared Space Observatory* (ISO) and *Spitzer*, together with ground-based telescopes, have been fundamental in understanding the general structure and composition of interstellar ice (Gibb et al. 2004). Besides the main components also the spectral signatures of a number of other solid state species, such as OCN^- , OCS and possibly NH_4^+ , have been identified (Grim & Greenberg 1987; Palumbo et al. 1995). Even more species have been tentatively identified, for example ethanol ($\text{CH}_3\text{CH}_2\text{OH}$), the formate ion (HCOO^-), formamide (NH_2CHO) and acetaldehyde (CH_3CHO , Schutte et al. 1999; Raunier et al. 2004; Öberg et al. 2011). Although less abundant than the main ice species, these molecules are interesting because they can potentially tell us more about the chemical and physical processes that take place in the ice mantles that lead to their formation. Table 1.1 gives an overview of all ice species identified so far, also showing their relative abundances and a comparison with comets.

So-called Complex Organic Molecules (COMs) are only observed in the gas-phase, but their formation must have taken place in the solid state. The James Webb Space Telescope (JWST) with its higher spectral resolution and detection sensitivity will enhance our view of the Icy Universe, by identifying for the first time also their solid state signatures. Combining the gas phase and

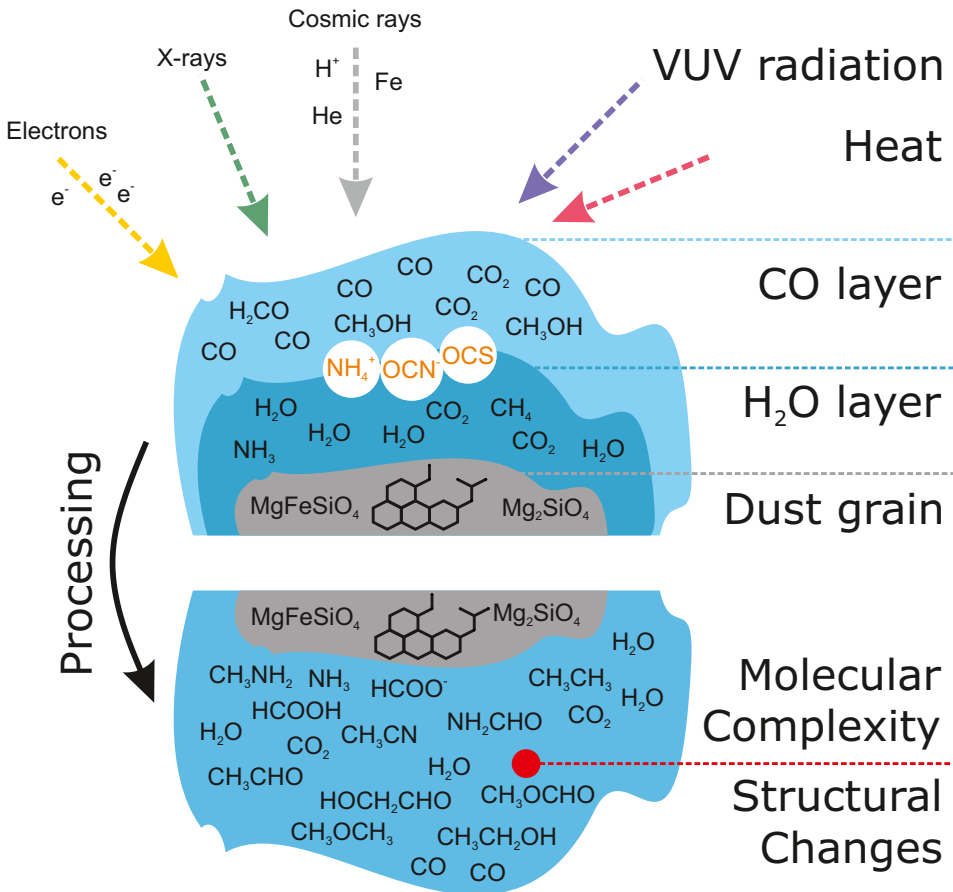


Figure 1.2: Schematic representation of an interstellar dust grain. The top half shows the dust grain surrounded by the water-rich and CO-rich layer. The species NH₄⁺, OCN⁻ and OCS are separately depicted, because they are not clearly attributed to either layer. Various energetic processes are shown which can lead to greater molecular complexity and structural changes in the ice, as is shown in the bottom part of the image.

Table 1.1: Interstellar ice species

Molecule	MYSO ^a	LYSO ^b %[H ₂ O] ^c	Comets
Securely identified			
H ₂ O	100	100	100
CO	3-26	(<3)-85	0.4-30
CO ₂	11-27	12-50	4-30
CH ₃ OH	(<3)-31	(<1)-25	0.2-7
NH ₃	~7	3-10	0.2-1.4
CH ₄	1-3	1-11	0.4-1.6
Likely identified			
OCN ⁻	0.1-1.9	(<0.1)-1.1	-
OCS	0.03-0.16	≤1.6	0.1-0.4
H ₂ CO	~2-7	~6	0.11-1.0
Possibly identified			
HCOOH	(<0.5)-6	(<0.5)-4	0.06-0.14
CH ₃ CH ₂ OH	~HCOOH	-	-
HCOO ⁻	0.3-1.0	~0.4	-
CH ₃ CHO	HCOO ⁻ × 11	-	-
NH ₄ ⁺	9-34	4-25	-
SO ₂	(<0.9)-1.4	~0.2	0.2
PAH	~8	-	-
HNCO	<0.3-0.7	-	0.02-0.1
NH ₂ CHO	<1.5	-	0.002

Notes. ^aMassive Young Stellar Objects and ^bLow-mass Young Stellar Objects. ^cValues represent the full range of abundances w.r.t. water (100). Table reproduced from Table 2 & 3 of Boogert et al. (2015).

solid state data may answer the question how the two phases are physically connected. Chapter 5 shows the spectroscopic data of the interstellar relevant COMs acetaldehyde, ethanol and dimethyl ether, that can be used to guide future JWST observations.

1.2. Energetic processing of ices

1.2.1. Types of energetic processes

The chemistry taking place on a dust grain in a dark cloud is not limited to non-energetic hydrogenation reactions. Energetic processes, taking place simultaneous with hydrogenation, play a part as well and can explain the formation of the larger, more complex species on the grains. These larger species will become "visible" in the gas-phase following ice sublimation.

There are a number of processes that can release energy in the ice mantle of the dust grain. Cosmic rays are highly energetic particles such as protons, H^+ , helium and various heavy metal nuclei that are found throughout the interstellar medium. They are able to transfer large amounts of energy into an icy dust grain upon collision and in this way cause chemical reactions. Electrons, either moving through space freely or as secondary particles from a hydrogen-cosmic ray collision, can do the same. X-rays can penetrate dark clouds and cause chemical reactions as well. Also, far-UV (often denoted by experimentalists as Vacuum-UV or VUV) radiation causes chemical reactions, although this may seem unexpected, since UV radiation does not penetrate deep into a dark cloud. However, a dark cloud has an internal source of VUV radiation that stems from cosmic ray ionization of gas-phase H/H_2 to form energetic electrons, that in turn excite H_2 , which then decays to its ground state by emitting a far UV photon (Prasad & Tarafdar 1983; Heays et al. 2017). For atomic hydrogen this is a photon of 121.6 nm, the so-called Lyman- α wavelength. Excited H_2 can emit photons in a large number of discrete lines as well as a broad emission spectrum between 140 and 165 nm. In dark clouds this results in a VUV flux of $\sim 10^4$ photons $cm^{-2} s^{-1}$ (Shen et al. 2004). Hydrogen plasma VUV lamps are known to mimic this radiation field closely and considerable laboratory effort has been put into characterizing laboratory VUV sources (Chen et al. 2014; Es-Sebbar et al. 2015; Ligterink et al. 2015, see Chapter 3 of this thesis). The laboratory work conducted in this thesis focuses on chemistry induced by VUV radiation.

Finally, thermal processing is the last form of energetic processing mentioned here. Its relevance to dark clouds is limited, due to the low temperature of this stage. However, it becomes more relevant as the system starts evolving towards a protostar and temperatures start increasing. Certain acid-base reactions proceed more efficiently at elevated temperatures and in some cases neutral molecules react as well (van Broekhuizen et al. 2004; Bossa et al. 2009; Danger et al. 2011). Radicals become more mobile at higher temperatures, which increases the reaction rate. Photodissociation or other processes can produce energetic products which have enhanced reaction rates.

An icy dust grain experiences all these energies over its life time, but their importance relative to each other remains under debate. The energy input can cause the breaking of molecular bonds, diffusion of species on the grain surface and to overcome reaction barriers. Also structural changes may occur, such as phase changes from amorphous to crystalline ice and ice segregation (Fig. 1.2 bottom).

1.2.2. Laboratory investigations

Laboratory Equipment

Many laboratory experiments have been conducted to simulate ice mantles and processes in various ways (e.g., Muñoz Caro et al. 2010; Allodi et al. 2013; Ioppolo et al. 2013; Paardekooper et al. 2014). The experimental set ups are at their basis often similar. They consist of (ultra-)high vacuum chambers with a cryogenically cooled surface. This surface can either be a transmission window or a reflecting metal, carbon or silicate surface and is meant to act as dust grain analogue. A gas inlet mechanism ensures that gases or gas mixtures

can be deposited on this surface. A source to process the ice, for example a VUV lamp, particle accelerator or synchrotron, is attached to the set-up. Chemical and physical changes in the ice sample are monitored in-situ with IR or UV/Vis spectroscopy, mass spectrometry and laser interferometric techniques. In some cases ex-situ Nuclear Magnetic Resonance (NMR) spectroscopy and gas chromatography techniques are used as well, although these usually have the drawback that a sample needs to be extracted from the set-up and exposed to atmosphere before analysis. A more detailed description of the inner workings of a representative laboratory set-up and the VUV lamp as irradiation source for energetic processing as used in this thesis can be found in Chapters 2 and 3, respectively.

Experiments

Experiments often start from the known, most abundant, interstellar ice components: H_2O , CO_2 , CO , CH_3OH , NH_3 , CH_4 and/or HNCO/OCN^- . Some of the earliest laboratory astrochemistry experiments investigated the VUV processing of complex mixtures, such as $\text{CO}:\text{NH}_3:\text{H}_2\text{O}:\text{CO}_2$, $\text{H}_2\text{O}:\text{CO}:\text{NH}_3:\text{CH}_4$ and $\text{H}_2\text{O}:\text{CH}_3\text{OH}:\text{NH}_3:\text{CO}$ showing the formation of radicals like HCO , NH_2 and HOCO and more complex molecules such as HNCO , NH_2CHO , HCOOH and H_2CO (Hagen et al. 1979; D'Hendecourt et al. 1986; Allamandola et al. 1988). More recent papers show the formation of even more complex species in similar ice mixtures. The VUV irradiation of a $\text{H}_2\text{O}:\text{CH}_3\text{OH}:\text{CO}:\text{NH}_3$ mixture by Bernstein et al. (1995) demonstrates not only the formation of species like ethanol, formamide, acetamide and nitriles, but also very complex molecules like hexamethylenetetramine, polyoxymethylene and a host of more complex alcohols, ethers, aldehydes and amides. Experiments conducted by Muñoz Caro et al. (2002) show that the residue of an irradiated $\text{H}_2\text{O}:\text{CH}_3\text{OH}:\text{NH}_3:\text{CO}:\text{CO}_2$ mixture contains amino acids and a host of other complex molecules.

Although these experiments show the direction interstellar ice chemistry might take, they give little quantitative information in terms of reaction networks, kinetics and reaction rates. To get this information a bottom-up approach must be taken. First the behavior and chemistry of interstellar relevant molecules in pure form must be studied (Gerakines et al. 1996; Collings et al. 2004; Raunier et al. 2004; Bennett et al. 2007; Öberg et al. 2009a; Paardekooper et al. 2016). Methanol is particularly noteworthy in this respect, because on its own it can lead to a vast oxygen-bearing chemical complexity. VUV processing of methanol leads to species like acetaldehyde, formic acid, dimethyl ether, ethanol and methylformate. For the nitrogen-bearing species, HNCO/OCN^- is of great interest, since VUV processing of this species leads to the formation of, among others, formamide, one of the most abundantly observed complex nitrogen-bearing species in the gas-phase and smallest amide or peptide-bonded molecule. The other abundant nitrogen-bearing species in interstellar ice, NH_3 , does not form complex species on its own, but small species like N_2H_4 and N_2 . It does however also produce the NH_2 radical, which can react with other species.

Processing of binary mixtures adds an extra degree of complexity to the system. Parent species, intermediate radicals and products of the pure species can all react with each other to form new, more complex species. In this way it is shown that for example methanol can be formed in processed $\text{H}_2\text{O}:\text{CO}$

mixtures or complex species like OCN^- , NH_2CHO , CH_3NCO and CH_3CONH_2 from $\text{NH}_3:\text{CH}_3\text{OH}$ mixtures (Hudson & Moore 1999; Muñoz Caro et al. 2014; Henderson & Gudipati 2015). It must be noted however that observations indicate that the species in both these mixtures are found in distinct layers and therefore these mixtures likely do not explain the formation of these species. In this respect the formation of methylamine (CH_3NH_2) from electron irradiated $\text{C}_x\text{H}_y:\text{NH}_3$ mixtures is more likely to occur (Kim & Kaiser 2011). Methylamine is of particular interest because of its implied involvement in the formation of the smallest amino acid glycine. Several laboratory experiments hint that energetic processing of $\text{CH}_3\text{NH}_2:\text{CO}_2$ mixtures leads to glycine formation (Holtom et al. 2005; Bossa et al. 2009). This example shows that biologically relevant molecules, such as amino acids seen in the experiments of Muñoz Caro et al. (2002), can be explained in interstellar ices by a sequence of chemical reactions. However, for many other biologically relevant, or prebiotic, species such a pathway is not yet investigated. This is for example the case for amide molecules, species with a $\text{R}_1\text{-(C=O)-NH-R}_2$ bond, such as HNCO , NH_2CHO , CH_3NCO , CH_3NHCHO and CH_3CONH_2 . Despite their potential importance to peptide chemistry, the formation mechanism(s) of, and links between these species have not yet been unravelled. Even for the simplest unit in this chain, HNCO , no consensus yet exists on its formation (Marcelino et al. 2010; Quan et al. 2010; Jiménez-Escobar et al. 2014). This thesis investigates several potential and plausible pathways for amide formation (Chapters 6 and 7).

1.2.3. Chemical modelling

Laboratory experiments thus give a wealth of information on the formation of molecular species and besides qualitative information also provide quantitative constraints to study the kinetics and infer reaction rates. These reaction rates are essential for theoreticians as input in chemical models. This allows to expand the conclusions drawn from experiments on a laboratory time scale to astronomical values (Cuppen et al. 2017). Simulation programs like GRAINOBLE, UMIST and the OSU/KIDA gas-grain network can study dark cloud chemistry based on dozens of molecules, many thousands of reactions and a variety of processes (Garrod et al. 2008; Wakelam et al. 2012; McElroy et al. 2013; Taquet et al. 2015). The systems that can be studied in this way are thus also much larger than what can be handled in a laboratory set-up.

Both laboratory and modelling are used for a better understanding on what kind of chemical complexity can be attained from relatively simple ices observed on icy dust grains. This makes it possible to connect astronomical observations of different objects, linking chemical snapshots in time. They explain some of the more complex components found in interstellar ices and help to understand molecular complexity observed in the gas-phase, subject of the following section.

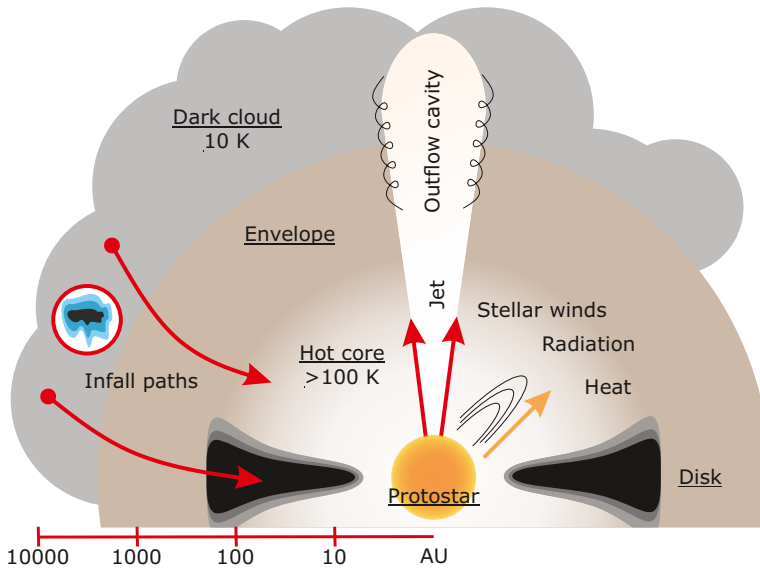


Figure 1.3: Schematic representation of the protostellar environment. The protostar attracts material from the cloud that moves into the protoplanetary disk and onto the star. Some of the material flowing into the young star is spewed out again via an outflow. Radiation and heat from the young star heats its surrounding and creates a hot core region.

1.3. Observing ice chemistry in the gas phase

1.3.1. Hot cores and corinos

While chemical and physical processes are ongoing on dust grains, the dark cloud as a whole also undergoes changes. Dense regions within the cloud start to gravitationally attract gas and matter, a process that will speed up as the density increases. Once a protostar has formed - a ball of hot gas in which nuclear fusion does not yet take place - it will heat and irradiate its surroundings. This protostar will eventually evolve into a (pre-) main sequence star.

Grains and gas move towards the protostar and leave the dark cloud environment into the envelope around the protostar. Through an accretion disk this material spins inward to the protostar and falls upon it. Depending on the evolutionary stage of the young stellar object, the disk has a high density and shields its midplane from the radiation and heat of the protostar. However, in the directions perpendicular to the disk, densities are lower and thus radiation and heat easily traverse this region and impinge on the envelope edge. Also, along the axis of the protostar it releases a jet and winds of hot gas at high velocities that sweep up material in the envelope in a so-called outflow. At the envelope-protostar interaction the dust grains are heated up and start to thermally release their ice mantles. What results is a bubble of warm gas, typically 100 K or warmer, where most of the molecular species from the grains have instantaneously desorbed together with water, the most abundant ice mantle component (see Fig. 1.3). This is called a hot core in case of high mass

sources like Orion KL, Sgr B2, W33A or NGC6334I or a hot corino for its low mass counter part, such as IRAS 16293–2422 or NGC 1333-IRAS 2A. Because the complete ice mantle is rapidly desorbed to the gas phase, hot cores are thought to give a relatively good representation of the compositions of icy grains.

In many aspects high and low mass sources, and thus hot cores and corinos, are similar, however there are also fundamental differences. From an observational perspective it is easier to detect molecules toward high mass sources, due to their greater brightness. However, multiple high mass protostars are often found to contribute to the emission of this type of source. This makes it hard to understand the processing history of gas and grains. Also the fact that these sources are located at large distances, more than 1000 parsec (pc, 1 pc = 3.26 light year) is common, makes it hard to resolve their structure.

Low mass sources are quite the opposite. Their envelopes are less massive, making it harder to detect molecules. On the other hand low mass sources are often not as clustered as high mass sources are. Interferometers can for example easily resolve the two protostars, A and B, in the low mass binary source IRAS 16293–2422. The fact that this source (and many other low mass sources) is relatively nearby at ~ 160 pc helps and mitigates its lower envelope mass. From these objects it is thus easier to get a clean snap shot of the chemistry that is going on. This leads to easier to interpret chemical pathways and physical structures.

Besides observational differences there are physical differences between high and low mass sources as well. High mass protostars are warmer, send out more UV radiation and evolve much more quickly than their low mass counterparts. This reflects in the chemistry. Different time scales for the hydrogenation processes in ice apply, varying levels of radiation or energetic processing are a possibility and the ice could be relatively warm, even in the pre-collapse stages.

1.3.2. Observations

The gases in hot cores and corinos are mainly studied with millimeter-wave telescopes such as *James Clerk Maxwell Telescope* (JCMT), *Atacama Pathfinder Experiment* (APEX), *Submillimeter Array* (SMA), IRAM 30m and *Atacama Large Millimeter/submillimeter Array* (ALMA). Because the sensitivity of these techniques is higher than IR spectroscopy, often by a factor of 10^{2-3} , molecules at lower abundances can be detected. Whereas in the ice about 10 species have been detected, close to 200 molecules are now known in interstellar gas, the majority discovered by millimeter-wave telescopes.

By far most molecules have been detected towards Orion KL and the galactic centre source Sagittarius B2. The brightness and large chemical complexity of these star forming regions have made them favourite targets for observations since the early days of millimeter-wave astronomy. Some of the abundant, commonly observed molecules such as acetonitrile (CH_3CN), formamide (NH_2CHO), dimethyl ether (CH_3OCH_3) and ethanol ($\text{CH}_3\text{CH}_2\text{OH}$) have been detected first in these sources (Solomon et al. 1971; Rubin et al. 1971; Snyder et al. 1974; Zuckerman et al. 1975). Other molecules, like the elusive methylamine (CH_3NH_2) have exclusively been observed towards these sources (Kaifu et al. 1974). More exotic molecules like the halogens HF and HCl, tracers of the hydrogen reservoir, have been found here as well (Zmuidzinas et al. 1995;

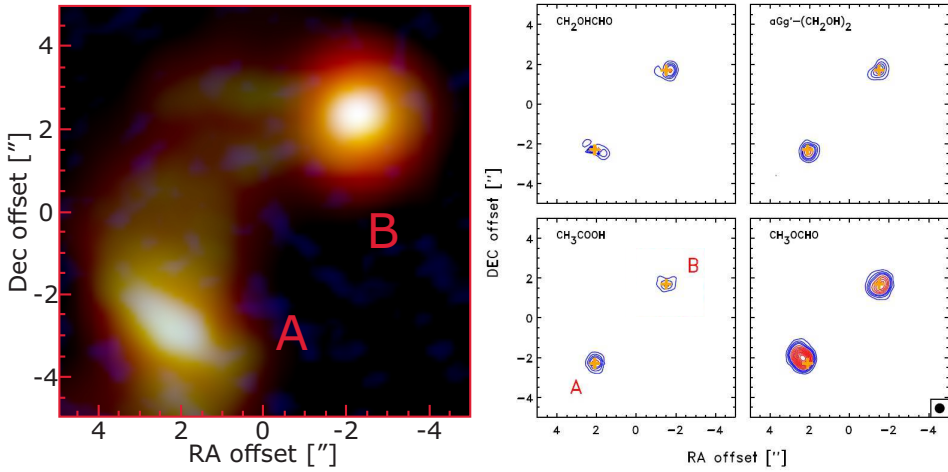


Figure 1.4: Left: the continuum emission map due to cold dust from 0.87 to 3.0 mm of IRAS 16293–2422 with the location of source B and A indicated. 1'' corresponds to 160 AU. Right: the contour maps of the species glycolaldehyde (362.406 GHz; upper left), ethylene glycol (348.550 GHz; upper right), acetic acid (352.872 GHz; lower left), and methyl formate (360.467 GHz; lower right). Images taken from Jørgensen et al. (2016).

Neufeld et al. 1997). On a yearly basis molecules keep being found in these sources, with some of the more recent finds being the amides acetamide and N-methyl formamide (CH_3CONH_2 & CH_3NHCHO), ethanimine (CH_3CHNH), methyl isocyanate (CH_3NCO) and the chiral molecule propylene oxide ($\text{C}_3\text{H}_6\text{O}$, Halfen et al. 2011; Loomis et al. 2013; Cernicharo et al. 2016; McGuire et al. 2016; Belloche et al. 2017). These latest results show that a large part of the interstellar chemistry is not yet explored, particularly of the nitrogen bearing species.

Many of the more abundant interstellar molecules have been observed toward other high mass and low mass sources as well. Methanimine (CH_2NH), an implied precursor of methylamine and glycine, has been found in several high mass sources (Dickens et al. 1997; Suzuki et al. 2016). Various observational results show that HNCO and NH_2CHO are related and hint that at least formamide is formed on dust grains and that hot corinos can be just as chemically complex as their high mass counterparts (van Dishoeck & Blake 1998; Bisschop et al. 2007a; López-Sepulcre et al. 2015; Taquet et al. 2015; Coutens et al. 2016). This is certainly the case for the sun-like protostars of IRAS 16293–2422 (see Fig. 1.4). Due to its relatively high brightness it has become one of the best studied low mass sources and gained a reputation as a low mass counterpart of Orion KL. Many studies have been dedicated to this source (e.g., van Dishoeck et al. 1995), including the including the *Protostellar Interferometric Line Survey* (PILS) with ALMA. An overview of the PILS survey and earlier studies on this young stellar object can be found in Jørgensen et al. (2016). Chapters 6 and 9 make use of the PILS data. Chapters 8 and 9 present the observational investigation of methylamine.

1.4. Snowlines and non-thermal ice desorption

The dust grains can also follow an infall path taking them into the protoplanetary disk. The densities in this disk can be high ($n \sim 10^{6-15} \text{ cm}^{-3}$), but vary greatly from the lower density outer edge and upper layers to the dense midplane region. In the midplane, temperatures are similar to that of a dark cloud, whereas the top layer of the disk is heavily irradiated and heated by the protostar. It is possible that molecular complexity survives in the midplane, but chemical processes also continue into the protoplanetary disk and add to further complexity (Bergin et al. 2007; Walsh et al. 2014; Drozdovskaya et al. 2014, 2016).

In the upper warmer regions of the disk the grain mantles desorb, enriching the gas phase with molecules. Because of the temperature gradient throughout the disk toward the protostar, these species release at distinct locations which are dependent on their specific binding energy. For example water has a high binding energy and thus will desorb closer to the star than CO, which has a low binding energy. The resulting ring-like structures around the protostar are called snowlines and indicate the border between freeze-out and sublimation. In the age of ALMA it has become possible to image these snowlines in protoplanetary disk, for example, the snowline of CO has been imaged via DCO^+ and N_2H^+ in various sources (Qi et al. 2013; Mathews et al. 2013; Qi et al. 2015; Öberg et al. 2015). It is important to note that the concept of snowlines is not unique to protoplanetary disks, but they can also be present in protostellar envelopes (Jørgensen 2004; Anderl et al. 2016).

Interestingly, snowlines have been observed that are spatially located in disk regions where the dust temperature is too low for thermal desorption to occur. For example, around the young star IM Lup a double CO ring is imaged (Öberg et al. 2015, Fig. 1.5 left). The inner ring belongs to thermally desorbing CO, but the outer ring cannot be explained by this mechanism. Similar is the case for water, ammonia and methanol observed in the TW Hya disk, where they are located in regions that are too cold for thermal desorption to occur (Hogerheijde et al. 2011; Walsh et al. 2016; Salinas et al. 2016). Both these examples hint to non-thermal desorption mechanisms being at play.

One such mechanism is photodesorption, the VUV induced release of a molecule from the solid state to the gas phase. Many laboratory studies have investigated this effect, mainly for CO (Öberg et al. 2007; Muñoz Caro et al. 2010; Fayolle et al. 2011; Chen et al. 2014; Muñoz Caro et al. 2016; Paardekooper et al. 2016, Chapter 3), but also for water, methane and CO_2 (Öberg et al. 2009c,b; Fayolle et al. 2013; Fillion et al. 2014; Dupuy et al. 2017). In many cases photodesorption rates are found to be high ($10^{-2}-10^{-3} \text{ molecules photon}^{-1}$) and are for the case of CO sufficient to explain the observation of a second ring in IM Lup. However, the opposite is true for methanol for which recent laboratory experiments show that it does not photodesorb intact (Bertin et al. 2016). Its upper limit ($\leq 3 \times 10^{-6} \text{ molecules photon}^{-1}$) is deep enough to show that it can not explain the methanol observation in the TW Hya disk. Clearly other non-thermal desorption mechanisms need to be invoked.

A number of alternative options do exist; reactive desorption, cosmic ray spot heating and co-desorption. With reactive desorption two species, for example radicals, react to form a product and the residual energy of the reaction is

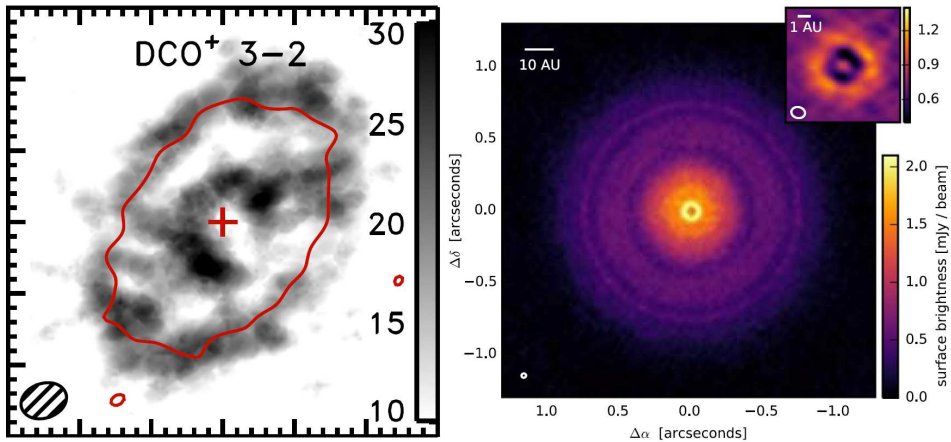


Figure 1.5: Left: the double ring structure of DCO⁺ found in IM Lup attributed to the thermal CO snowline and an outward CO photodesorption ring. Image reproduced from Öberg et al. (2015). Right: the dust ring structure found in TW Hydrae, which in the inner 1 AU (inset) is potentially caused by a planetary object cleaning out its orbit. Image reproduced from Andrews et al. (2016)

used to break the physisorbed bond to the surface and release the product to the gas phase (Garrod et al. 2007; Minissale et al. 2016). Cosmic ray spot heating is the localized heating of the ice mantle and thermal desorption of its contents after it is hit by a cosmic ray (Shen et al. 2004; Ivlev et al. 2015). Co-desorption is a mechanism whereby a thermally desorbing species drags another molecular species with it to the gas phase. In this way it is possible that volatile species with a low desorption temperature carry species with a high desorption temperature, such as methanol, with them to the gas phase. For the case of methanol, these non-thermal desorption mechanisms are not well studied and more laboratory investigations are needed to study the relevance of these effects. The co-desorption case is studied in **Chapter 4**.

1.5. Icy rocks

ALMA also opened up the possibility to investigate the mechanisms that lead to planet formation in protoplanetary disks. Dust traps, i.e. regions where mm-sized dust grains can pile up and coagulate together, have been found (van der Marel et al. 2013). Also gaps in disks, cleared of a substantial part of their grains, have been imaged and attributed to a young planet emptying its orbit (Bruderer et al. 2014; Pérez et al. 2014; van der Marel et al. 2016; Andrews et al. 2016, Fig. 1.5 right). These observations hint to a general mechanism where submicron-size dust grains enter the protoplanetary disk and at some point efficiently coagulate together and grow to large rocky bodies up to comet size. The kilometer-size large rocks gravitationally attract each other and form a larger body that cleans out its orbit of all material and eventually forms a planet. Not all rocks are incorporated into planets, however. These rocks, or comets, are the

left overs of planet formation. Since they are formed from icy dust grains there is the possibility that the chemical complexity reached in a dark cloud is transferred all the way to comets.

This idea was the basis for the *ROSETTA* mission to the comet 67P/Churyumov-Gerasimenko (67P/C-G). Since comets spend most of their lifetime in the cold outer part of the solar system, they should be the “cleanest” remnants of star and planet formation, they are well suited to study the chemistry in the earliest times of our solar system. Mass spectrometers on the orbiter and the Philae lander were used to study the coma and icy surface of the comet. On the surface a large number of complex molecules were found, although identification is limited due to low mass resolution of the mass spectrometer and limitations of IR spectroscopic techniques (Goesmann et al. 2015; Capaccioni et al. 2015). Data from the orbiter confirmed the presence of many complex molecules, especially the ROSINA mass spectrometer instrument with its high mass resolution, including the amino acid glycine (Le Roy et al. 2015; Altwegg et al. 2016). Also many sulphur bearing molecules, such as OCS, SO₂ are found to be present in 67P/C-G’s coma (Calmonte et al. 2016). More exotic species such as HF, HCl, HBr, organo-halogens and phosphorus are detected as well (Dhooghe et al. 2016; Altwegg et al. 2016). These results not only show that the known chemical complexity observed towards protostars is preserved in comets, but also that the ingredients are available in the ice to make other life-bearing molecules. In Chapter 10 the ROSINA data on halogens is used to compare archive *Herschell* observations on HBr.

1.6. This thesis

The journey that icy dust grains follow takes them through many different environments. Formation of ice layers start in the dark cloud when gas phase atoms and molecules stick long enough on grain to be hydrogenated to a number of simple species. The chemical complexity is enhanced by energetic processes, for example VUV irradiation. As the grains move toward the protostar they can enter the hot core around the young star, where the ice mantles thermally desorb and it becomes possible to study the chemical complexity of the dust grain in the gas phase. Another fraction of the dust grains will end up in the disk midplane. Here ice grain chemistry can continue, but also non-thermal desorption processes are evident. Finally, the grains in the midplane start to coagulate and form large rocky bodies, ranging from comets to planets. The ice coating of grains is locked up in comets and allows us to study the earliest stages of star formation. The chapters in this thesis touch upon all of these aspects of the icy dust grain. A number of key questions are addressed:

- What is the mechanism that drives low-temperature, non-thermal desorption of COMs, specifically methanol?
- Can COMs be directly observed in interstellar ice with *JWST*?
- What are the formation pathways to form nitrogen-bearing species with amine or amide functional groups?

- Which nitrogen-bearing COMs are observed in the interstellar medium, under which specific conditions, and what can we learn about their formation from these observations?
- Can we link the abundances of nitrogen-bearing COMs to comets?

The results of the chapters of this thesis are summarized as follows:

- **Chapter 2** details the construction and functioning of the Cryogenic Photoproduct Analysis Device 2 (CryoPAD2), a newly constructed set-up based on the original CryoPAD. This set-up is capable of performing VUV irradiation experiments on interstellar ice analogues under ultra-high vacuum (UHV) conditions. Compared to the previous set-up, capabilities to accurately determine photon fluxes and VUV spectra have been added and the implementation of a high sensitivity Quadrupole Mass Spectrometer (QMS) gives the possibility to measure low abundance photo-products.
- **Chapter 3** presents a full characterization of the Microwave Discharge Hydrogen-flow Lamp (MDHL), the source of VUV radiation in laboratory experiments. Using a calibrated VUV spectrometer, the effects of hydrogen flow and pressure, input power, add-mixing of noble gasses, microwave cavity position, pumping efficiency and lamp types are investigated. VUV spectra and fluxes are shown to be dependent on all these parameters, with the add-mixing of helium being the most significant to obtain a Lyman- α dominated spectrum (up to 80% of the flux of the full spectrum). Finally, a comparison of the CO desorption rate of an ice irradiated with a MDHL running on H₂ and a H₂:He mixture shows that this rate differs by a factor of 2, which is significant, but cannot explain order of magnitude differences seen in CO photodesorption experiments reported in the literature.
- **Chapter 4** revolves around the unexplained ALMA observation of rotationally cold methanol in the protoplanetary disk TW Hya. Non-thermal desorption mechanisms like photodesorption and reactive desorption have been unable to explain this observation. A combined laboratory and modelling investigation into a third mechanism, low temperature co-desorption of methanol with thermally desorbing CO molecules, is conducted. The laboratory work does not show any methanol releasing at the thermal release peak of CO, resulting in a co-desorption upper limit of $\leq 7.3 \times 10^{-7}$ methanol molecules CO⁻¹. Using this stringent upper limit co-desorption ratio in a chemical model does show that significant abundances of methanol can still be released to the gas phase.
- **Chapter 5** presents medium resolution infrared spectra of acetaldehyde, ethanol and dimethyl ether in pure form or mixed in astronomically relevant water, CO, methanol and CO:methanol ice matrices, to be used to guide future *JWST* interstellar ice observations. A number of spectral peaks are identified to be the most likely to be observed and a full peak position and *FWHM* characterization of these lines is presented. These results are used to re-analyse the 7.41 μm feature in *ISO* spectra of W33A. In agreement with previous results this feature can be explained by

acetaldehyde mixed in water, but acetaldehyde mixed in CO:methanol at cold (15 K) temperatures can explain this feature as well. Higher sensitivity and resolution *JWST* measurements are needed to securely determine in which layer acetaldehyde resides in interstellar ice.

- **Chapter 6** presents the first detection of methyl isocyanate (CH_3NCO) toward a low-mass protostar, IRAS 16293–2422, and the first laboratory investigation into its formation. A total of 43 spectral lines of CH_3NCO are unambiguously identified, but its isomers, CH_3OCN and CH_3CNO , are not. Column density ratios of $\text{N}(\text{HNCO})/\text{N}(\text{CH}_3\text{NCO}) = 12$ and 4 are found toward source B and A, respectively. Abundance ratios compare well with those found in high-mass sources. The laboratory results show that CH_3NCO is likely formed in the VUV irradiation of interstellar ice analogue mixtures of $\text{CH}_4:\text{HNCO}$ at 20 K, where the VUV is used to produce CH_3 radicals. A proposed reaction mechanism is by CH_3 radical addition to $(\text{H})\text{NCO}$.
- **Chapter 7** aims to expand the work of Chapter 6 into a larger network of peptide bonded molecules in VUV irradiated $\text{CH}_4:\text{HNCO}$ mixed ices at 20 K. Specifically the H-atom addition reaction to CH_3NCO to form CH_3NHCHO is tested and the formation of other amides from reactions with intermediates and products resulting from HNCO . Processing of these ices shows the formation of acetamide (CH_3CONH_2), but not N-methylformamide (CH_3NHCHO). The non-detection of the latter species means the H-atom addition reaction has a barrier that can not be overcome or intermediates are efficiently destroyed in the ice. Formamide (NH_2CHO), urea (NH_2CONH_2) and methylamine (CH_3NH_2) are identified as well. Overall the work indicates that the NH_2CO radical is an important intermediate in the formation of amide bearing molecules. Indications of the formation of more complex molecules, likely amides as well, are found. Experimentally derived $\text{CH}_3\text{CONH}_2 / \text{NH}_2\text{CHO}$ ratios are compared with interstellar observed ratios of the same two molecules toward Sgr B2 and show good agreement. This gives a strong indication that formamide and acetamide have a common formational origin, which is found in interstellar ices.
- **Chapter 8** presents the results of a JMCT survey toward several high-mass sources in order to detect methylamine (CH_3NH_2). This molecule is important to astrochemistry due to its implied link to amino acid formation, specifically glycine. No spectral features of methylamine are detected. A comparison of (upper limit) abundance ratios with methylamine detections in the high-mass source Sgr B2, shows that the upper limits are not deep enough to claim a difference between Sgr B2 and other sources, but hint that methylamine is overproduced in hot core models. The upper limits of this chapter can be used to guide future deeper searches for methylamine with ALMA.
- **Chapter 9** investigates the relation between the molecules NO , N_2O and NH_2OH and between CH_2NH and CH_3NH_2 with ALMA observations toward IRAS 16293–2422B to elucidate the formation mechanisms of

NH_2OH and CH_3NH_2 , two species thought to be of importance to the formation of amino acids. We detected NO and, for the first time toward a low-mass source, CH_2NH , tentatively identify N_2O and do not detect NH_2OH and CH_3NH_2 . The presence of CH_2NH around IRAS 16293–2422B shows that this suggested parent molecule to the formation of the amino acid glycine could already have been present at the earliest formational stages of our own solar system. However, the non-detection of NH_2OH and CH_3NH_2 makes amino acid formation routes involving these two species less relevant. Furthermore, upper limit abundance ratios determined for CH_3NH_2 show that these are at least 1-2 orders of magnitude deeper compared to detections of this molecules toward Sgr B2, showing that significantly less methylamine is present in this low-mass source and different physical conditions in these two sources play a role in the formation of CH_3NH_2 .

- **Chapter 10** constrains the interstellar abundances of HBr with archive *Herschel* data on Orion KL, Sgr B2 and NGC6334, finding upper limits for this molecule in all three sources. Upper limit abundance ratios are compared with detections of HBr in the coma gas of the comet 67P/C-G and show that the upper limits are at a similar level as the comet detections. A chemical network for the formation of HBr is constructed, which suggests that HBr could be depleted from the gas phase, potentially locked up in interstellar ice.

The future is bright with ALMA, JWST and Rosetta data to follow the journey of icy grains from formation to incorporation in solar systems.



V-UV



2

CryoPAD2 experimental set-up

N.F.W. Ligterink, M. Witlox & H. Linnartz

2.1. Introduction

The majority of the measurements in this thesis are carried out on the Cryogenic Photoproduct Analysis Device 2 (CryoPAD2, Fig. 2.1), a newly constructed and upgraded version of the original CryoPAD. This machine has as purpose to study Vacuum-UV (VUV, 115-180 nm, 6.9-10.8 eV) induced chemical and physical processes on interstellar dust grain analogues. The original CryoPAD has shown its merits over the past decade in a number of publications (Öberg et al. 2007, 2009a,c,b). The goal of CryoPAD2 is to build on these successes and add new capabilities to the machine, such as full spectral and flux calibration of the VUV source, addition of a high sensitivity mass spectrometer that can detect low abundance complex molecules, and improved, oil-free Ultra-High Vacuum (UHV) conditions.

In the following sections the technical details and capabilities of CryoPAD2 will be discussed. The calibration methods for the mass and IR spectrometers, and for the VUV photon flux are shown as well. Finally, the functioning of CryoPAD2 is demonstrated by a trial experiment.

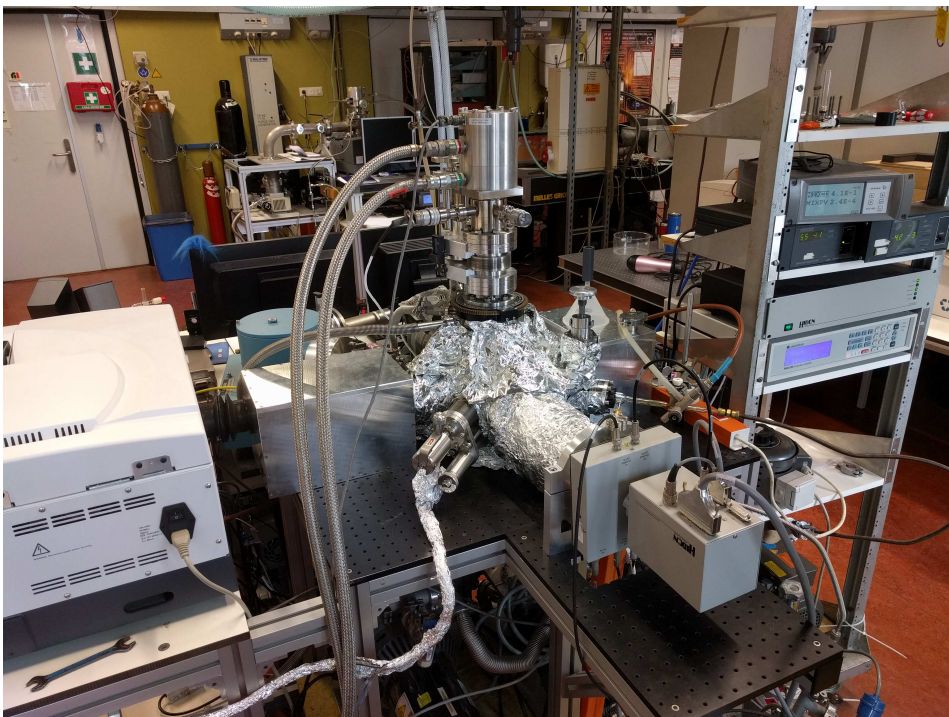


Figure 2.1: A picture of the CryoPAD2 set-up showing the UHV chamber at the center, on top the cryostate, in front the QMS and to the left the FTIR Spectrometer.

2.2. Description of CryoPAD2

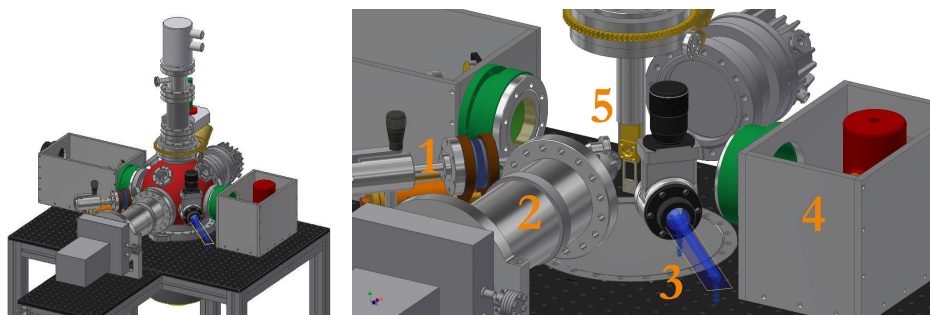


Figure 2.2: Mechanical drawing of the CryoPAD2 set up. 1) Deposition line, 2) QMS, 3) V-UV lamp, 4) IR detector in purge box, 5) Cryogenically cooled gold coated reflection surface.

CryoPAD2 consists of a main UHV chamber, typically $\sim 7 \times 10^{-11}$ mbar, to which all instruments are attached (see Fig. 2.2). Directly attached at the bottom of the chamber is an Agilent V1001 turbomolecular pump (900 L/s), which is backed by an oil free TS-300 dry-scroll pump (300 L/minute), also manufactured by Agilent. Horizontally attached to the chamber is a second Agilent TwisTorr 304 FS turbo pump, backed by the same scroll pump. The vacuum is monitored by a hot ion gauge, which is read out by a Granville-Phillips 350 ionization gauge controller and placed under a 45° angle with respect to the center line of the set-up. Three fused-silica view ports are located on other ports in the same plane.

At the top of the chamber an Advanced Research Systems (ARS) DE-202 cryostat is mounted via a translational and rotational UHV feed through. The feed through ensures that the cryostat can be rotated over 360° and vertically moved to allow the use of different instruments. Differential pumping of the rotational feed through occurs in two stages. The first stage is pumped by the TS-300 scroll pump and the second stage by a Varian V-301 turbomolecular pump, backed by an Agilent SH-110 dry-scroll pump. Attached to the tip of the cryostat, surrounded by a heat-shield, is a gold coated reflection substrate. This surface makes it possible to perform Reflection Absorption InfraRed Spectroscopy (RAIRS), which will be discussed shortly. Two thermocouples (Chromel-AuFe 0.07%) and a heating wire are attached to the substrate. The two thermocouples are located at the top and bottom of the reflection surface, while the heating wire is located a few centimetres above the top thermocouple. Read-out of the thermocouples and control of the heating wire is done by a Lakeshore Model 350 Cryogenic Temperature Controller. The lowest attainable temperature is around 12 K. Relative temperature read-out error of the thermocouples is ± 1 K and the absolute error is ± 2 K. The heating wire can heat the sample up to 300 K and higher.

Finally, at the bottom of the substrate a VUV grade AXUV-100 photodiode is mounted by thermally isolating PolyEther Ether Ketone, or PEEK, material, for photon flux measurements. The photodiode is calibrated by the

Physikalisch-Technische Bundesanstalt (PTB) for the range of 115 to 250 nm. Read out occurs through a Keithley 485 autorange picoammeter. Section 2.3.4 will go into further detail of the VUV photon flux determination.

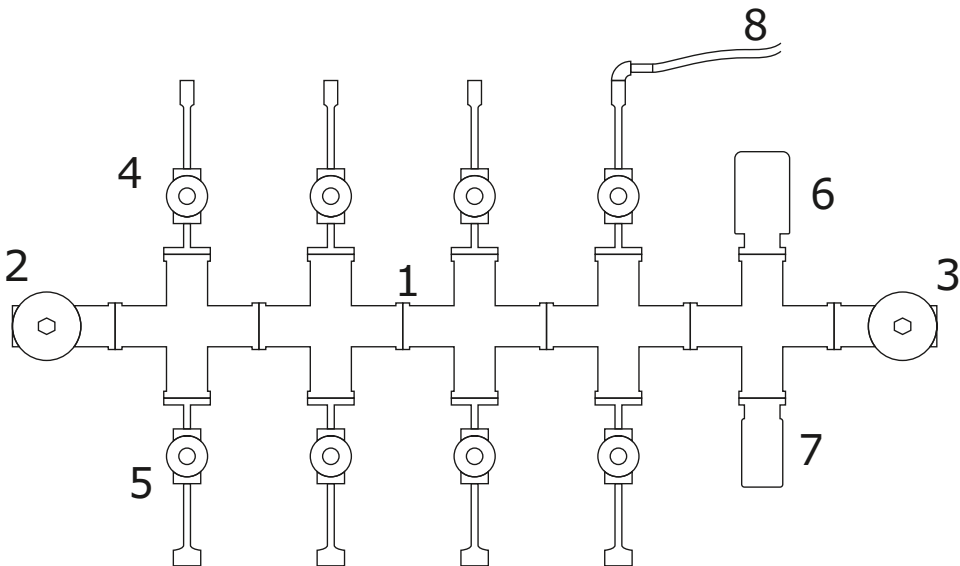


Figure 2.3: Schematic representation of the CryoPAD2 gas mixing line. The elements are: 1) Backbone consisting of CF38 cross pieces, 2) valve to prepump, 3) valve to turbo pump, 4) swagelok valve to three gas bottle connections, 5) swagelok valve to four tube connections for liquids and bulbs, 6) CDG-500 gas independent gauge, 7) PVG-500 pirani gauge, 8) swagelok valve and tube connection to the setup.

A deposition line connected to a high-precision gas-mixing system is used to grow ice layers on the cooled substrate. Pure and mixed gases are prepared in the gas-mixing system, see Fig. 2.3. The backbone of this system is a number of ConFlat cross-pieces (1). At both ends of the system are valves connecting to either a SH-110 dry-scroll pump for prepumping or a Varian V-301 turbomolecular pump, backed by a SH-110 scroll pump for High Vacuum (HV) pumping (2,3). Two connections house an Agilent PVG-502 pirani gauge (7), for monitoring the pressure, and a CDG-500 gas-independent diaphragm gauge (6) to create accurate gas mixtures. The remaining connections are used to attach gases (4) and liquids (5). Stainless steel Swagelok SS-4H-TH3 valves are in place here to regulate the gas-flow. gases are connected via a 6 mm Swagelok connection, while tubes with liquids are attached with a Cajon connection. From the gas-mixing system a tube (8) connects to an all-metal high precision leak valve, which extends into a deposition tube in the vacuum chamber. The leak valve is placed on a translation stage in order to move the deposition tube as close as possible to the substrate surface. At the end of the deposition tube a Micro Capillary Plate (MCP) is placed to create a linear flow of gases and uniform deposition. In general deposition of gases is done from a distance of 5 mm and under an angle of 45° with respect to the surface.

Samples that are deposited can be treated with VUV radiation coming from

a Microwave Discharge Hydrogen-flow Lamp (MDHL). The MDHL will be extensively discussed in Chapter 3, but a short description is given here. This lamp is operated by flowing H_2 from the gas bottle through the glass lamp into an oil pump. On the lamp a microwave cavity is placed, which excites the hydrogen flow into a plasma. From this plasma excited H atoms and H_2 molecules release VUV light around 121 nm (Lyman- α) and between 140 to 170 nm (molecular hydrogen emission). Via a Magnesium Fluoride (MgF_2) window, that also acts as a vacuum seal, the VUV light enters into the vacuum chamber. This window transmits light from visible wavelengths and down to 115 nm. Between the window and chamber a shutter is placed that acts as an “on/off” button for the MDHL.

Opposite from the MDHL a McPherson Model 234 0.2 meter VUV Monochromator is located to monitor the VUV spectrum of the lamp. The monochromator is connected via a tube and a MgF_2 window onto the vacuum chamber. This system is being pumped by a Leybold Turbovac 50 turbomolecular pump, which is backed by a SH-110 scroll pump. The monochromator covers a range of 30 to 550 nm. It makes use of a 1200 gr/mm grating and two adjustable slits, to obtain a spectral resolution of 0.1 nm at 313.1 nm center wavelength. At the end VUV light is collected by a Model 658 photomultiplier detector. Control and read out occurs with a Model 789A-4 Scan Controller and a Keithley 6485 picoammeter, which are connected to a LabView program. A typical VUV spectrum is shown in Fig. 2.4.

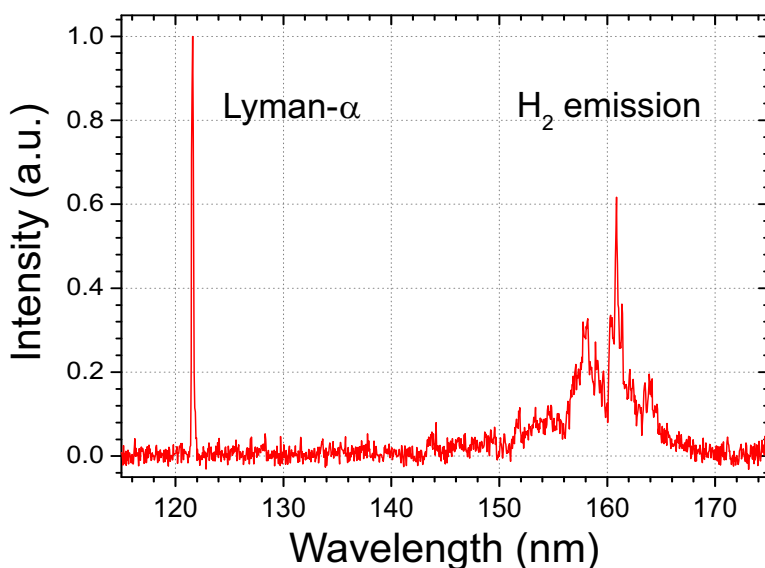


Figure 2.4: Typical spectrum of the MDHL measured with the McPherson Model 234 Monochromator. H-atom Lyman- α emission is seen around 121.6 nm, while molecular hydrogen emission lines and continuum are seen between 140–170 nm.

Two detection techniques are used in this set-up. At the front side a Hiden HAL/3F RC 1000 PIC Quadrupole Mass Spectrometer (QMS) is located. It is capable of measuring gas-phase particles with masses between 1 and 300 amu

at high sensitivity. Gas-phase species are detected from 1) the background atmosphere of the chamber, 2) deposition of gases, 3) photodesorption of ice samples, and 4) Temperature Programmed Desorption (TPD) of the ice on the substrate. The latter two options are most important trace the physical and chemical changes in the ice. The electron source of the QMS is located roughly 6 centimeter from the reflection surface at the center of the chamber. As default, the electron source emits electrons at 70 V and a flux of 20 μA , but both settings are tunable. Altering the electron voltage can change the fragmentation pattern of gas-phase molecules entering the QMS, while the current can be increased to enhance the sensitivity to gas particles. Calibrations of the QMS are covered in Sections 2.3.1 and 2.3.2.

The second instrument is an Agilent 660 FTIRS system, set up in RAIRS via the reflection surface on the substrate. With the RAIRS set-up chemical and physical changes are traced in-situ in the ice. Two ZnSe windows are used to couple the light from the FTIR spectrometer into the set-up and out again toward a liquid nitrogen cooled Mercury Cadmium Telluride (MCT) detector. A number of gold-coated mirrors and off-axis parabolic mirrors guide the IR light from the FTIR to set-up and focus it on the substrate and MCT. The entire beam path of the RAIRS set-up outside the main chamber, including the FTIR itself, is purged with dry air to remove gas-phase IR features of water and carbon dioxide. With the FTIR a range of 500 to 4000 cm^{-1} or 2.5 to 20 μm can be covered. A spectral resolution as high as 0.1 cm^{-1} can be attained, although in practice 1 to 2 cm^{-1} resolution is used.

2.3. Calibrations

2.3.1. QMS work function

Each mass spectrometer has its own specific work function, or sensitivity per mass. Over large mass ranges the work function can vary substantially. This in turn can substantially alter mass fragmentation patterns and therefore needs to be adjusted for.

Mixtures of noble gases are used to measure their sensitivity and extrapolate these data points to cover the full mass range. A mixture of He:Ar:Kr:Xe at 88:4:4:4 ratio is used to measure at masses of 4, 40, 84 and 131 amu. Noble gases do not have fragmentation pattern, so this does not have to be corrected for. However, electron absorption cross sections are atom specific and do need to be taken into account. These values are taken from literature at 70 V as $\sigma_{\text{He}} = 2.96$, $\sigma_{\text{Ar}} = 25.2$, $\sigma_{\text{Kr}} = 34.5$ and $\sigma_{\text{Xe}} = 46.7 \text{ \AA}^2$. When the gas mixture is leaked into the set-up and measured by the QMS, the resulting corrected signal $S_{\text{corrected}}$ is obtained by:

$$S_{\text{corrected}} = S_{\text{QMS}} \times \frac{C_{\text{mol}}}{\sigma_{\text{mol}}}, \quad (2.1)$$

where S_{QMS} is the original QMS input, C_{mol} is a correction for the concentration (4 for Helium, 88 for the other three noble gases) and σ_{mol} is the electron absorption cross section of each atom. From the corrected signal the normalized ratios between the four atoms can be found and exponentially fitted,

see Fig. 2.5. This fit is used to correct mass traces when accurate mass ratios are needed.

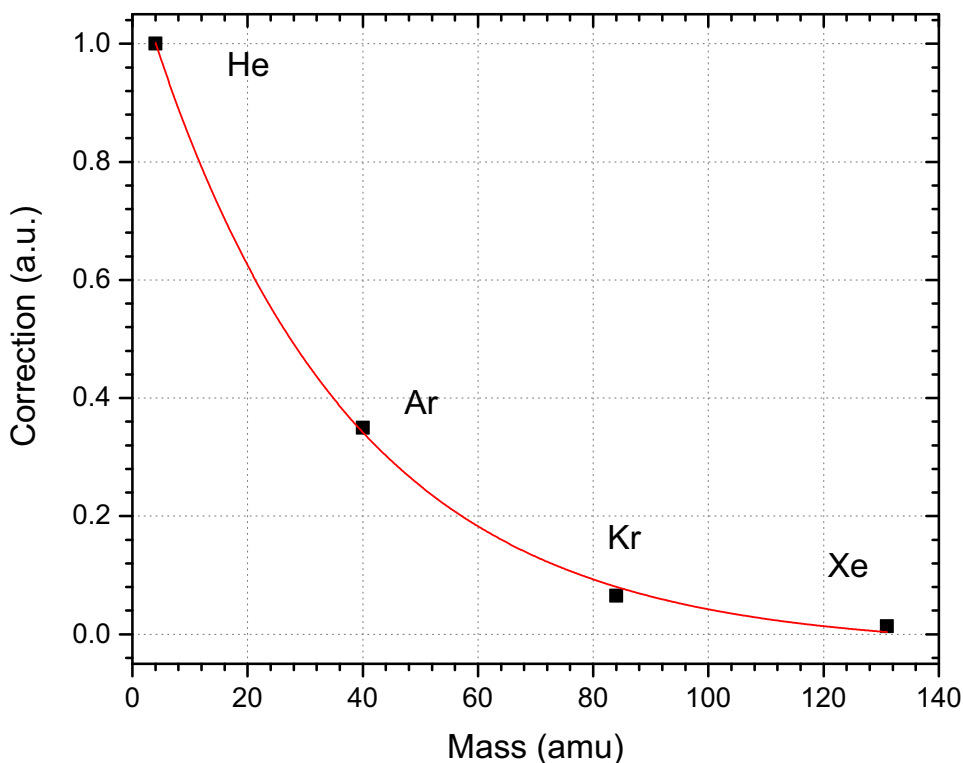


Figure 2.5: Workfunction of the Hiden QMS. Black squares indicate the normalized data points of the noble gases. An exponential curve is fitted through these points (red).

2.3.2. QMS filament output correction

The QMS system on CryoPAD2 has the ability to tune the electron output of the filament in its ionisation source. An increase of the electron current means that more gas-phase molecules can get ionised, thus effectively making the QMS more sensitive to a certain mass or masses. The opposite is possible as well, to decrease the current and become less sensitive to a certain mass. This is particularly useful to prevent the Secondary Electron Multiplier (SEM) detector from overranging, which occurs at measuring 1×10^7 counts s^{-1} (hits of fragments).

The effects of tuning the electron energy are investigated in order to determine 1) how the sensitivity changes with electron current, and 2) if fragmentation patterns change. $^{13}\text{CH}_3\text{OH}$ is leaked into the chamber while measuring its main masses at 30, 32 and 33 amu in sequence at filament currents of 5, 10, 20, 30, 40 and 50 μA . Data are used when the leak rate into the chamber has stabilised and a variety of leak rates are used in order to see if pressure effects play a role. All the masses are normalised to the standard electron current setting of 20 μA . Figure 2.6 shows the resulting sensitivity curve, which is slightly

exponential. Between each current setting the variation in the masses is minimal, so no change in fragmentation pattern is seen. Different leak rates showed negligible differences in sensitivity. Between measurements at 5 and 50 μA the sensitivity increases by a factor of 14.

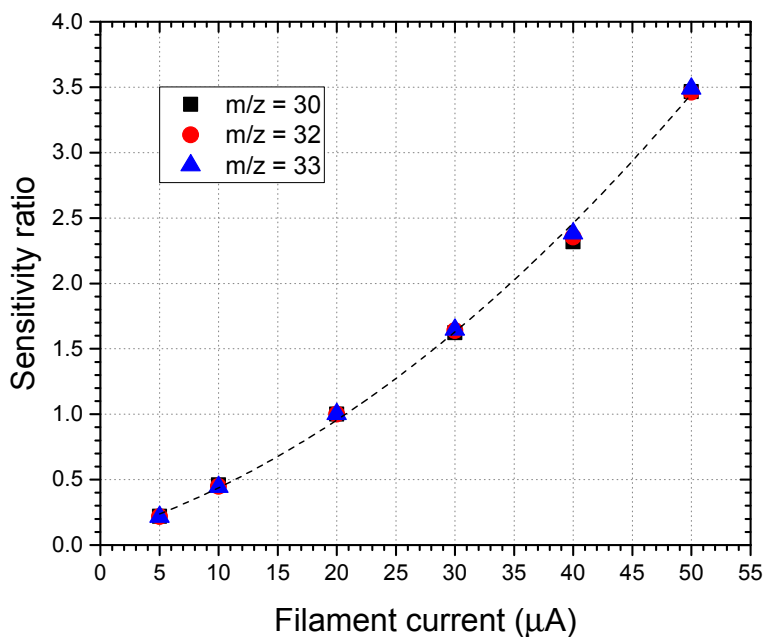


Figure 2.6: Sensitivity of the Hidden QMS at various filament currents, normalised to the value at 20 μA . The main fragments of $^{13}\text{CH}_3\text{OH}$ at $m/z = 30$, 32 and 33 are plotted versus filament current.

2.3.3. Column density and RAIRS correction

Column densities of parent species and products are in-situ determined by IR spectroscopy with the following equation:

$$N_{\text{species}} = 2.303 \frac{\int_{\text{band}} \tau d\nu}{A_{\text{band}}}, \quad (2.2)$$

where N_{species} is the column density of the investigated species in molecules cm^{-2} , $\int_{\text{band}} \tau d\nu$ the integrated absorbance of the band in cm^{-1} and A_{band} the band strength in cm molecule^{-1} . IR band strengths listed in literature are usually determined in transmission. However, RAIRS set-ups make use of a reflection through the ice sample, which results in a longer path length and thus higher band strength values. Effectively this means that measuring the exact same amount of material in a transmission and RAIRS set-up results in a *larger* integrated absorbance peak in the RAIRS set-up. How much larger depends on

the geometry and technical details of the RAIRS set-up and is therefore set-up specific.

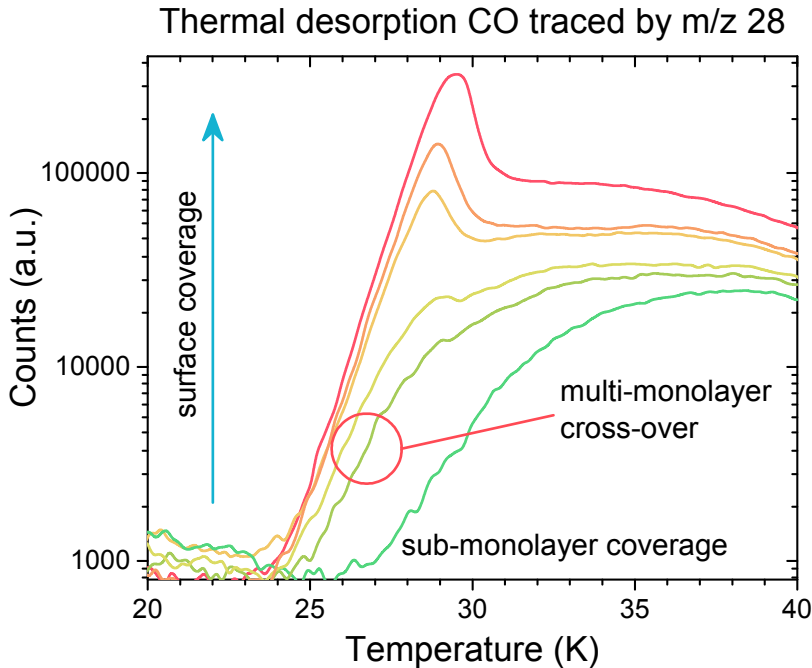


Figure 2.7: Desorption traces of CO for various surface coverages. The desorption temperature is seen to shift to higher values at lower coverage.

In CryoPAD2 the band strength of CO is determined by thermal desorption of thin CO films. Thick layers of a molecule are dominated by molecule-molecule binding energies, which are weaker than molecule-substrate bonds. Therefore a thin film, in the order of ~ 1 ML thick, is more tightly bound to the substrate and exhibits a clear shift in desorption temperature compared to bulk ice. This effect is used to find the monolayer regime for CO, see Fig. 2.7. The desorption traces for a number of depositions are shown. The high coverage experiments start desorbing around 24 K, but at lower coverage the curve is seen shifting to 25 K. This is taken as the monolayer regime. At even lower, submonolayer, coverage the curve is seen to shift even further to 26 K.

The IR data of the monolayer curve are used to find its integrated absorbance band as 0.01497. By making the assumption that the monolayer is covered by 1×10^{15} molecules cm^{-2} , Eq. 2.2 can be used to find the band strength as $A_{\text{RAIRS,CO}} = 3.4_{-0.5}^{+0.5} \times 10^{-17}$ cm molecule^{-1} . Literature transmission values put the band strength at 1.12×10^{-17} cm molecule^{-1} (Bouilloud et al. 2015). Based on the set-up specific and literature transmission band strengths of CO and under the assumption that band strengths in the set-up scale all with the same factor, a

modified equation for the column density can be made:

$$N_{\text{species}} = 2.303 \frac{1.1}{3.4} \frac{\int_{\text{band}} \tau d\nu}{A_{\text{band}}}, \quad (2.3)$$

which now includes a correction factor of $\frac{1.1}{3.4}$. It is important to realise that this correction value can change by changes made in the geometry of the RAIRS set-up. Therefore the value should be remeasured each time such changes have been made.

2.3.4. VUV photon flux

Measuring the VUV photon flux starts by measuring the VUV photocurrent between 115 and 180 nm with the SXUV-100 photodiode. Since this photodiode is not only sensitive to high energy radiation, but also emission upto and beyond 1000 nm, it picks up visible emission from the MDHL. Therefore the VUV photon current I_{VUV} is determined by measuring the total photo current generated by the regular MDHL (I_{total}) and subtracting the visible part, here loosely defined as any wavelength ≥ 230 nm. The visible part is measured by using a MDHL which is closed-off with a fused-silica window (I_{vis}). This window does not transmit radiation below 230 nm, but has a transmittance of 0.9 ± 0.03 of the visible light beyond 230 nm. Both open and closed-off lamps are operated under the same conditions, e.g. flow pressure, input power. This leads to the following equation to measure the VUV photocurrent:

$$I_{\text{VUV}} = I_{\text{total}} - \frac{I_{\text{vis}}}{0.9}, \quad (2.4)$$

The VUV photocurrent consists of contributions at different wavelengths in the VUV spectrum. Therefore the current needs to be assigned in a percentage wise fashion to each wavelength in the spectrum. To give an example, if the Lyman- α peak at 121 nm contributes 25% of the total spectrum between 115 and 230 nm, then $0.25 \times I_{\text{VUV}}$ will be assigned to it. The VUV spectrum that is used depends on the settings of the MDHL (see Chapter 3 for MDHL settings and VUV spectra). From the following equation the wavelength dependent flux, $\Phi(\lambda)$, is determined:

$$\Phi(\lambda) = \frac{I(\lambda)}{e\epsilon(\lambda)}, \quad (2.5)$$

where e is the electron charge and $\epsilon(\lambda)$ the wavelength dependent quantum efficiency. By integrating over the range between 115 and 230 nm the total VUV photon flux can be determined. As an example, for an VUV photocurrent of $I_{\text{VUV}} = 1.05 \mu\text{A}$ a VUV photon flux of $1.1 \pm 0.1 \times 10^{14}$ photons $\text{cm}^{-2} \text{s}^{-1}$ is derived. Besides being dependent on the MDHL settings, this flux number can change over time due to differences in orientation of the sample, the use of collimator tubes or simply contamination of the lamp. Therefore it needs to be measured at regular intervals.

2.4. An experimental example

To demonstrate the capabilities of CryoPAD2, results of an VUV processing experiment of a thin, pure isocyanic acid (HNCO) film are presented. Examples are given on how to handle RAIRS spectroscopy and TPD mass spectrometry data. This section will conclude by showing what can be learned from these kind of experiments.

2.4.1. Introduction

HNCO is abundantly found in the gas-phase in the ISM (Bisschop et al. 2007b; Bergner et al. 2017). In its ionic form, OCN^- has been detected in interstellar ices (Boogert et al. 2015). Several observational studies have linked HNCO to the formation of more complex prebiotic species such as formamide (NH_2CHO López-Sepulcre et al. 2015; Coutens et al. 2016) and state that formation occurs in the ice phase. Laboratory experiments have shown that HNCO can undergo efficient acid-base reaction with NH_3 to form $\text{OCN}^- \text{NH}_4^+$ salts (van Broekhuizen et al. 2004). VUV irradiation of HNCO shows that OCN^- is one of the main products, but also more complex species like NH_2CHO and NH_2CONH_2 form (Raunier et al. 2004). These reactions have so far only been studied in a qualitative way.

2.4.2. Experimental

A pure sample of HNCO is prepared by thermally cracking cyuramic acid, a trimer of HNCO. With freeze-pump-thaw cycles impurities, mainly CO and CO_2 , are removed from the gas. The gas is deposited on the substrate at 15 K, after which it is irradiated for 20 minutes in 1 minute intervals. After each interval an IR spectrum is taken between 700 and 4000 cm^{-1} at a resolution of 0.5 cm^{-1} in order to trace chemical changes in the sample. These spectra are baseline subtracted, for which an example is shown in Fig. 2.8. Column densities are determined according to Sect. 2.3.3 from the integrated band area. Expected molecular products and their band positions and strengths are listed in Table 2.1.

The VUV flux for this experiment is determined to be 2.86×10^{14} photons $\text{s}^{-1} \text{ cm}^{-2}$, according to Sect. 2.3.4. In 20 minutes of irradiation this amounts to a fluence of 3.4×10^{17} photons cm^{-2} . The VUV spectrum is dominated by H_2 transitions around 150-160 nm and no Lyman- α is present, see Fig. 2.9. The absence of Lyman- α could be reflected in the chemistry, because strongly bonded molecules may not be broken.

The QMS is set to measure known and expected products of HNCO processing. In Table 2.2 expected products are listed together with their main fragment masses and desorption temperatures for pure ices. At the end of the irradiation time a TPD is set at a rate of 10 Kmin^{-1} . The QMS data are corrected for the work function according to Sec. 2.3.1.

2.4.3. Results

Figure 2.10 presents the IR spectrum of HNCO after deposition and after 20 minutes of VUV irradiation for the region between 2100 and 2400 cm^{-1} . Some

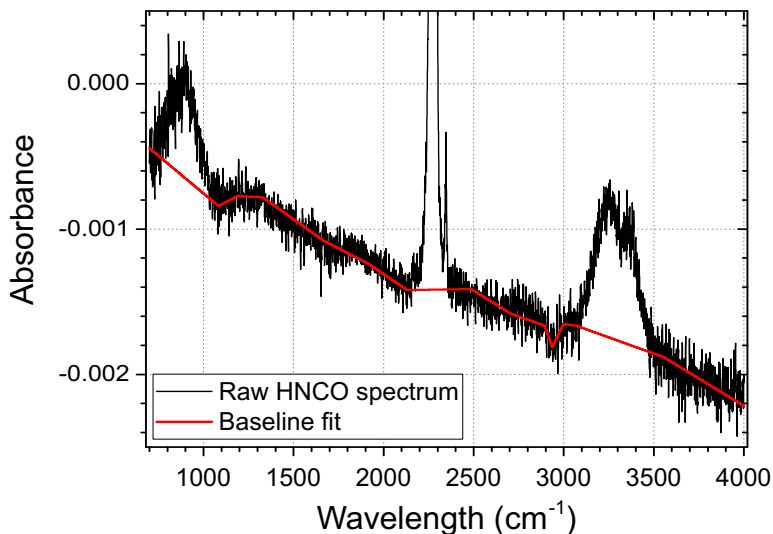


Figure 2.8: Baseline fit of the HNCO deposition

CO_2 contamination is visible in the deposition spectrum. No CO and OCN^- are visible. From the HNCO integrated peak area a column density of $2.6 \times 10^{15} \text{ cm}^{-2}$ is determined. After irradiation, the HNCO peak has decreased, while the formation of OCN^- and some additional CO_2 is seen. The OCN^- counter ion, NH_4^+ , is not seen at 1470 cm^{-1} and neither is CO is at 2142 cm^{-1} . The latter may be blended in the OCN^- peak, however. Two other potential products, HNC and its isomer HCN, are not seen either. Around 1700 cm^{-1} , where H_2CO , NH_2CHO and NH_2CONH_2 have prominent CO stretching modes, no feature shows up over the course of irradiation, indicating that little or none of these species are formed. Based on an upper limit integrated absorbance area of 0.01, the upper limit column densities for HCN/HNC and NH_2CHO are determined to be $\leq 1.5 \times 10^{15}$ and $\leq 1.1 \times 10^{14}$ molecules cm^{-2} at the end of irradiation. Due to possible blending with OCN^- , a more conservative upper limit integrated absorbance of 0.02 is used for CO , resulting in an upper limit column density of $\leq 1.3 \times 10^{15} \text{ cm}^{-2}$.

The normalized TPD trace of m/z 27, 28, 45 and 60 are shown in Fig. 2.11 and correspond to masses of the molecules HCN/HNC, CO , NH_2CHO and NH_2CONH_2 that were not seen in the IR spectra. The position where the bulk of HNCO desorbs (m/z 43) at 115 K is indicated by a red dotted line. HCN is not seen desorbing around 140 K, but a significant signal is seen at 115 K. However, since m/z 27 is also present in the HNCO fragmentation pattern, HCN/HNC can at most partially contribute to this feature. In the m/z 28 signal a peak is seen around 40 K that can be attributed to CO desorption, although N_2 can not be ruled out either. Formamide is seen in the m/z 45 trace where it releases at 210 K. The other two peaks at this mass correspond with $^{13}\text{CO}_2$ and co-desorption of formamide. NH_2CONH_2 can not clearly be claimed in the m/z 60 trace. A low intensity feature does show up around 270 K, but is not strong enough to claim a detection.

Table 2.1: IR band positions and band strengths of HNCO and photolysis products

Molecule	Mode	Position cm^{-1}	Band strength $\times 10^{-17} \text{ cm molecule}^{-1}$
NH_4^+	bend.	1470 ^d	-
NH_2CHO	CO str.	1708	6.54 ^e
HNC	NC str.	2029	-
HCN	CN str.	2099	0.51 ^b
CO	CO str.	2142	1.12 ^a
OCN^-	OCN str.	2162	13 ^c
HNCO	NCO str.	2282	7.8 ^c
CO_2	CO str.	2342	7.6 ^a

Notes. ^aBouilloud et al. (2015), ^bGerakines et al. (2004), assumed to be the same for HNC, ^cvan Broekhuizen et al. (2004), ^dRaunier et al. (2004), ^eBrucato et al. (2006)

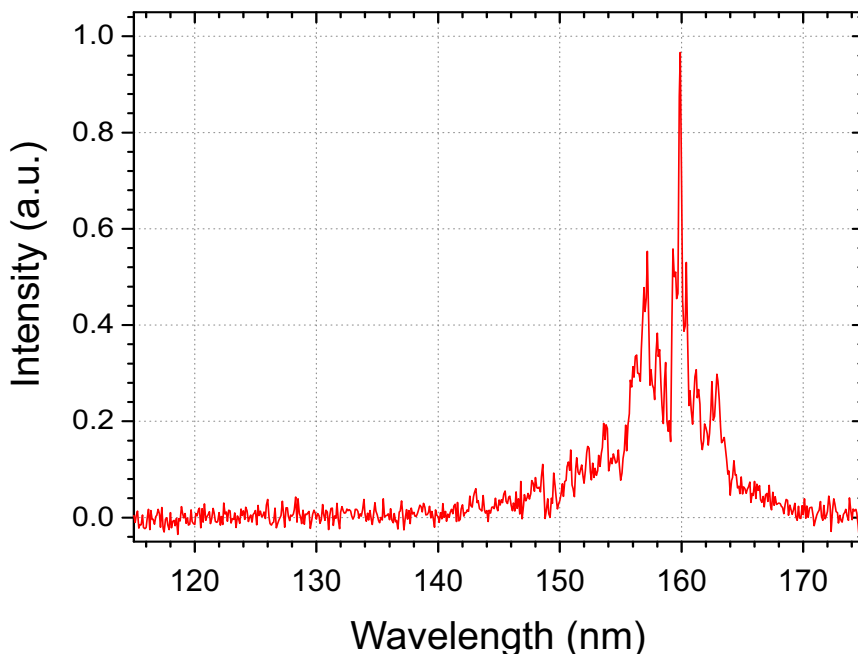


Figure 2.9: Spectrum of the VUV light used in the irradiation of HNCO.

Table 2.2: Molecular mass and desorption temperatures

Molecule	CO/N ₂	HCN	CO ₂	HNCO	NH ₂ CHO	NH ₂ CONH ₂
m/z	28	27	44,28	43,42	45	60
T _{des} (K)	30 ^a	140 ^b	75 ^c	115	210 ^d	>240

Notes. ^aÖberg et al. (2005), ^bTheule et al. (2011), ^cCollings et al. (2004), ^dlab verification experiments.

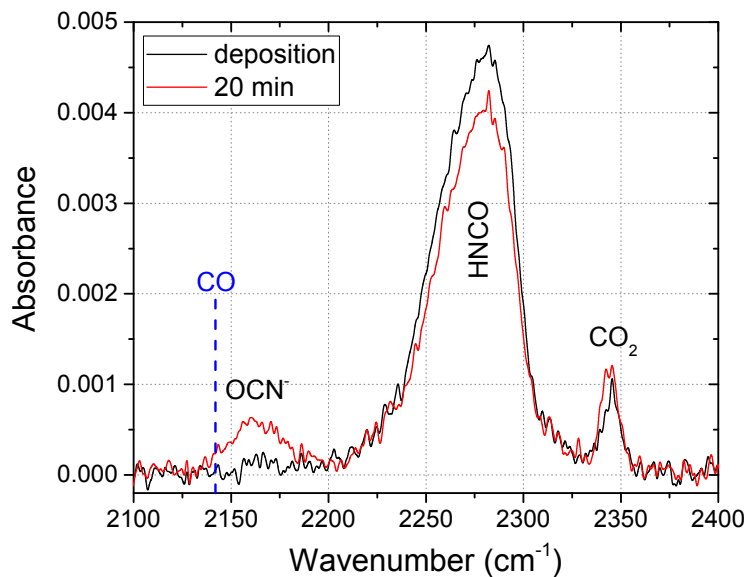
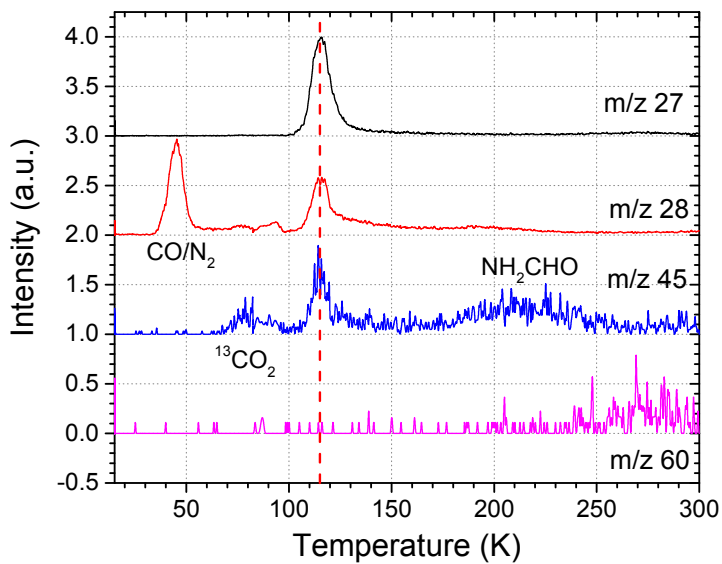


Figure 2.10: Spectra of HNCO after deposition and 20 min irradiation.

Figure 2.11: TPD traces of m/z 27, 28, 45 and 60. The dashed red line indicates the HNCO desorption peak.

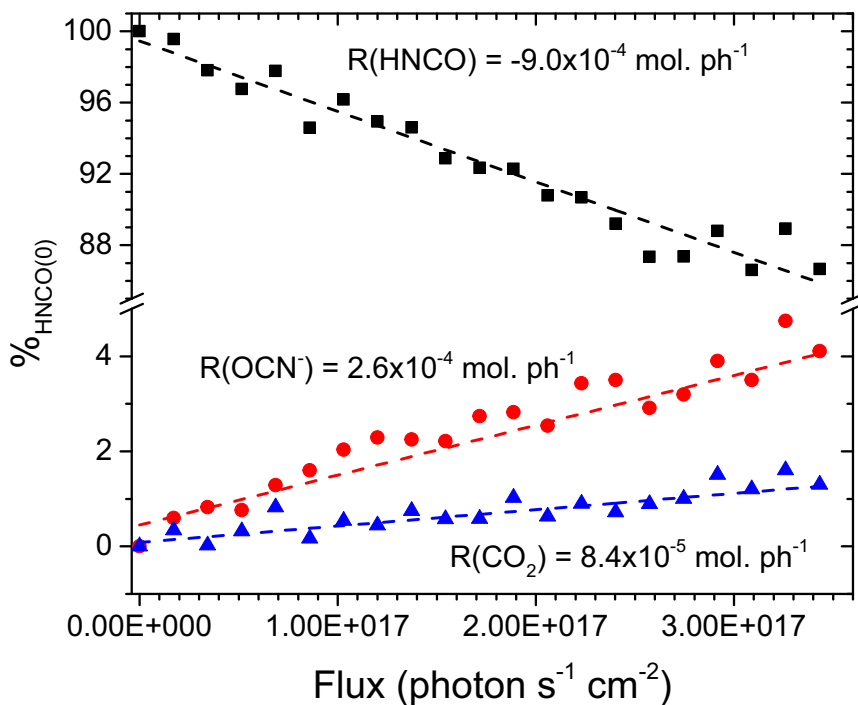


Figure 2.12: Photodestruction rate of HNCO and photoproduction rate of OCN^- and CO_2 . The uncertainty of each data point amounts to $\sim 20\%$.

2.4.4. Discussion

Figure 2.12 plots the column densities of HNCO, OCN^- and CO_2 as a percentage of the starting amount of HNCO. A photodestruction rate is determined for HNCO, while photoformation rates are obtained for OCN^- and CO_2 . They are -9.7×10^{-4} , 2.6×10^{-4} and 8.4×10^{-5} molecules photon $^{-1}$, respectively, with an estimated uncertainty of $\sim 20\%$. The (upper limit) formation rates of (non-)detected species are listed in Table 2.3.

Experimental results like these can help understand the reaction network of isocyanic acid. A number of possible HNCO reactions are listed in Table 2.4. The formation CO_2 (reaction [10]) can only be caused by the presence of oxygen atoms, as produced by reaction [3], although contributions of contaminants like water can not entirely be ruled out based on one experiment. OCN^- formation indicates that ammonia needs to be present to undergo the acid-base reaction, see reactions [8] and [9]. This in turn means that reaction [1] and/or [2] are occurring to produce N and N* that lead to NH_3 . In this case contamination does not play a role since the only nitrogen-bearing contaminant is N_2 , which can not be dissociated by VUV light of our lamp. Therefore the only source of nitrogen is HNCO. During processing of the ice much of the hydrogen reservoir gets locked up in ammonia and formamide. Both molecules need two additional hydrogen atoms to form from NH or HNCO, respectively. Assuming contaminations like water play a limited role, there must remain a large NCO reservoir, at least

Table 2.3: Column densities after 20 min irradiation and production/destruction rates

Molecule	N_{final} $\times 10^{15}$ mol. cm^{-2}	R_{molecule} $\times 10^{-4}$ mol. ph^{-1}
HNCO	1.92	-9.0
CO	≤ 1.3	≤ 38
HCN	≤ 1.5	≤ 44
HNC		
CO ₂	0.03	0.84
OCN ⁻	0.1	2.6
NH ₂ CHO	0.11	≤ 3.2

Table 2.4: Overview of possible HNCO reactions

Nr.	Reaction	Products	Note
1	HNCO + VUV	H + NCO → N + CO	
2		HN + CO	
3		HNC + O	<i>Needed for CO₂ formation</i>
4	HNCO + VUV + H	H ₂ NCO/HNCHO → NH₂CHO	<i>Net H loss channel</i>
8	HNCO + NH ₃	OCN⁻ NH ₄ ⁺	
9	(H)N + H	NH ₃	<i>Net H loss channel</i>
10	CO + O	CO₂	

Notes. Species that have been detected in the experiment are indicated in red.

1×10^{14} for ammonia (based on the OCN⁻ column density). This NCO reservoir must be locked up in double and triple bonded molecules, most likely N₂ and CO.

2.4.5. Conclusion

CryoPAD2 has been constructed and commissioned. This final section has shown a typical experiment as conducted on the set-up. From the data kinetics results, specific photodestruction and production rates can be inferred. With the QMS it is possible to detect low abundance products in the TPD. This shows the potential of this set-up to investigate reaction dynamics in interstellar ice analogues up to low abundance complex molecules.



V-UV



3

Controlling the emission of a Vacuum-UV lamp

N.F.W. Ligterink, D.M. Paardekooper, K.-J. Chuang, M.L. Both, G.
A. Cruz-Diaz, J.H. van Helden & H. Linnartz

Ligterink et al. 2015b, *Controlling the emission profile of a MW driven H₂ discharge lamp to simulate interstellar radiation fields*, *A&A*, 584, A56

3.1. Introduction

For the last 2 decades, microwave discharge hydrogen-flow lamps (MDHLs) (Warneck 1962; Davis & Braun 1968) have been widely used as vacuum-ultraviolet (VUV) light sources in laboratory experiments to simulate interstellar radiation fields in astrochemical studies (Westley et al. 1995; Gerakines et al. 1996; Baratta et al. 2002; Muñoz Caro et al. 2002; Cottin et al. 2003; Leto & Baratta 2003; Loeffler et al. 2005; Watanabe et al. 2007; Öberg et al. 2007; Muñoz Caro et al. 2010; Islam et al. 2014; Cook et al. 2014; Henderson & Gudipati 2015). These experiments aim to simulate and ultimately unravel the complex photoprocesses (photodesorption, photodissociation, and photochemistry) taking place in interstellar ice analogues. The spectral distribution of the interstellar radiation field (ISRF) is strongly dependent on the interstellar environment. As ice processing is particularly interesting in dark interstellar clouds which are largely shielded from external light sources, laboratory studies have been focusing on simulating the VUV photons emitted by H and H₂ after excitation by cosmic rays that do penetrate the cloud. In the laboratory, these photons are produced using a MDHL. Typically, it has been assumed that the lamp spectrum is dominated by Lyman- α photons around 121 nm, with a broad and weaker emission band situated around 160 nm. The estimated flux of the MDHL at sample position in a number of papers is based on previously reported values in the literature, which roughly span between 10^{13} - 10^{15} photons s⁻¹cm⁻² and generally lack information on the spectral energy distribution (SED). However, exact running conditions of the lamp, i.e. the dependence on the experimental settings, influence both the total photon flux and the SED of the impacting radiation at the ice sample. In other situations the flux of the lamp is either directly measured using a NIST (National Institute of Standards and Technology) calibrated photodiode or indirectly by actinometry using for example the conversion of O₂ to O₃ (Gerakines et al. 1996; Cottin et al. 2003; Islam et al. 2014; Fulvio et al. 2014). When using a NIST calibrated photodiode for photon flux measurements, the quantum yield is known at different wavelengths. Since the photodiode is also sensitive to visible light, the contribution of visible light emitted by the MDHL has to be taken explicitly into account as well. In the actinometry case, the O₂ to O₃ conversion efficiency typically used is taken from gas phase experiments performed by Groth (1937). Recent experiments indicate that the quantum efficiency in the solid state is significantly lower (Cottin et al. 2003; Fulvio et al. 2014) and hint toward a wavelength dependency, although detailed wavelength dependent studies are still lacking in the literature. It is clear that both calibration methods require knowledge of the emission spectrum of the lamp to accurately determine the flux at different photon energies, which strongly depends on the experimental settings.

The importance of controlling the emission spectrum of the MDHLs has been pointed out by various recent studies (Chen et al. 2014; Es-Sebbar et al. 2015). Photodesorption rates for several molecules using synchrotron radiation (Fayolle et al. 2011, 2013) as well as direct cross section measurements of the main constituents of interstellar ice show strong wavelength dependences in the VUV domain. (Cruz-Diaz et al. 2014a,b) Recently, Chen et al. (2014) showed that the differences in CO photodesorption rates reported by various groups

over the past decade may be partly explained by differences in MDHL emission spectra. Carbon monoxide is an excellent example, since it strongly absorbs 160 nm photons while Lyman- α photons are clearly off resonance, as has been shown in independent experiments (Fayolle et al. 2011; Cruz-Diaz et al. 2014a).

The main purpose of the present study is to systematically identify the importance of various parameters for operating the MDHL: pressure, gas compositions (H_2 , D_2 , addition of He), microwave power, lamp geometry, pumping efficiency, and cavity positioning. The systematic approach presented here allows the optimization of lamp settings for specific experiments, using the MDHL in a more wavelength selective way. The study complements the work of Chen et al. (2014) and more recently Es-Sebbar et al. (2015). The main difference between the present work and these two recent studies is that the spectral irradiance of the MDHLs is characterized absolutely, using a fully calibrated measurement procedure. This allows us to obtain the relative photon flux in full wavelength dependence.

We also list a number of very practical issues, such as the degradation of MgF_2 windows that are typically used and potentially affect the overall outcome of studies in which accurate flux numbers are needed. It should be noted though, that the chapter is not intended as a reference to skip calibration procedures. In the best case, the right order of magnitude can be derived from the information given here. The dependences that are described below will make it clear that flux measurements at the sample distance are necessary to guarantee that numbers depending on absolute photon fluxes are correct.

3.2. Experimental

Section 3.2.1 describes the microwave discharge hydrogen-flow lamp, while in section 3.2.2 the UV/VUV spectrometer used for characterization is described. To convert the different radiation units, from irradiance to photon flux at the sample distance, an additional calibration set-up had to be constructed, which is described in section 3.2.3. To test the implications that result from this work, in section 3.2.4 the main characteristics of one of our UHV ice set-ups are described. The astronomical relevance of the MDHL findings is illustrated here with VUV ice irradiation experiments for different lamp settings.

3.2.1. Microwave discharge hydrogen-flow lamp

The MDHL consists of a pyrex lamp-tube and an air-cooled Sairem Evenson microwave cavity which is powered by a Sairem GMP 03 K/SM microwave generator. The plasma is ignited using a BD-10A high frequency generator. The geometry of the lamp-tube can be either F- or T-type, as depicted in figure 3.1. This lamp-tube is connected to a set-up using an UHV MgF_2 window (Torr Scientific Ltd) and a custom-made connection piece. A rubber ring seals off the connection at the lamp side, the other two available ports are used for the inlet and outlet of the gas flowing through the tube. The port near the MgF_2 window is typically the inlet of the gas. The system is evacuated by either a TS300 dry scroll pump or a DS-302 rotary vane pump, both manufactured by Agilent. The typical base pressure of the system obtained with the scroll pump

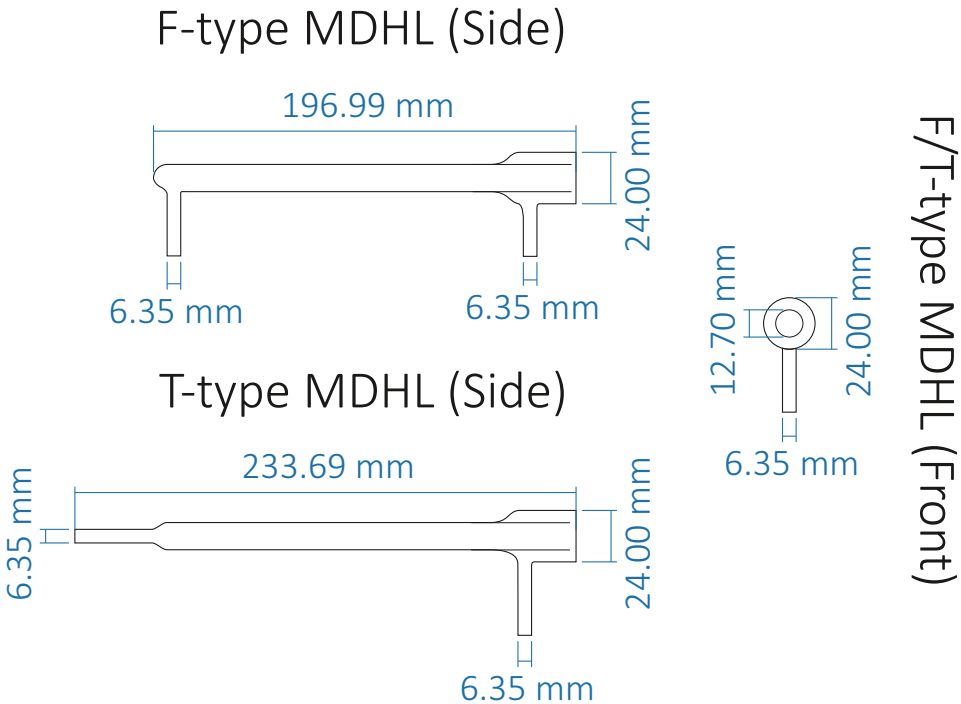


Figure 3.1: Schematic of the F- and T-type MDHL used in this study. Both lamps are based on commercially available Opthos Instruments MDHLs.

and oil pump are $\sim 10^{-2}$ mbar and $\sim 5 - 10 \times 10^{-3}$ mbar, respectively. Pressure monitoring is performed at various positions. Two gauges (Agilent PCG-750 and Granville-Phillips Convection gauge) are situated at the inlet of the gas flow and an additional Agilent PCG-750 is attached near the outlet. These gauges have been calibrated for H_2 with reference to both 0.00 – 10.00 mbar and 0 – 1000 mbar Edwards Barocell manometers with a 0.15% accuracy of reading. All the pressure values mentioned and presented are absolute values. The gas inlet of the lamp-tube can be directly connected to a needle valve, reducer, and gas bottle or to a flow controller gas mixing system. The latter can be used for pure gasses and binary gas mixtures. Flow rates in this system are given in standard cubic centimetres per minute (sccm). The gas outlet of the lamp tube is connected to a pump without further flow restrictions. Gasses used in our experiments are hydrogen (99.999% pure, Air Liquide / Alphagaz), helium (99.999% pure, Air Liquide / Alphagaz), and deuterium (99.8% pure, Air Liquide / Alphagaz).

3.2.2. Greifswald UV/VUV spectrometer

All spectra presented here were measured in November 2014 during a one-week measurement campaign at the UV/VUV spectroscopy set-up located at the Leibniz Institute for Plasma Science and Technology (INP Greifswald). This set-up, schematically depicted in figure 3.2, has been routinely used for the last two decades as a diagnostic tool for characterizing the UV/VUV emission of

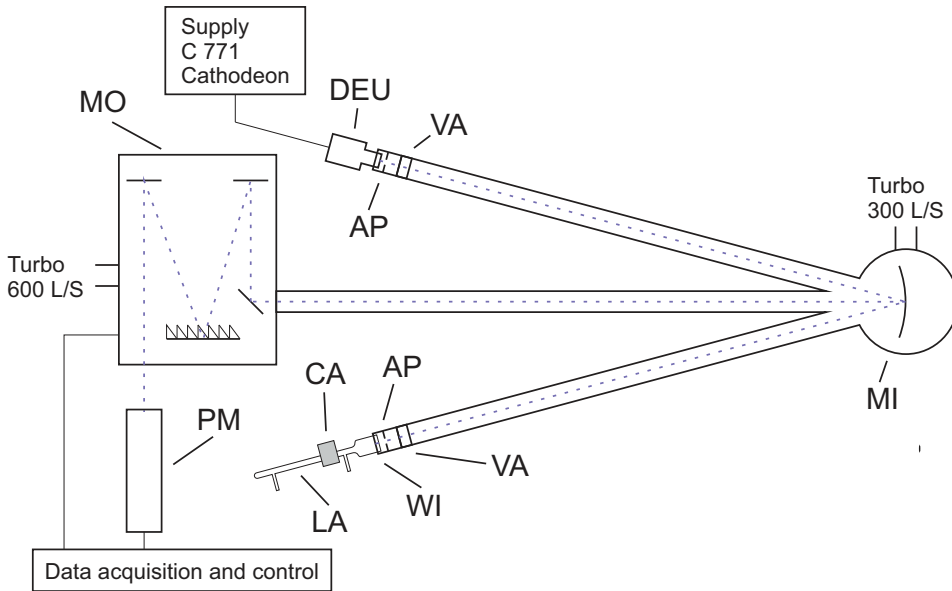


Figure 3.2: Experimental set-up at the INP Greifswald for VUV measurements, (DEU): Physikalisch Technische Bundesanstalt (PTB) calibrated D₂ lamp, (AP): Aperture, 0.6 mm (diameter), (VA): Valve, (MI): Mirror, $f= 1.5$ m, (WI): MgF₂ window, (PM): Photomultiplier, (MO): VUV-Monochromator (VM-505 Acton Research); 0.5m, 1200g/mm, (LA): Microwave Discharge Hydrogen-flow Lamp, (CA): Microwave Evenson cavity.

(atmospheric) plasma (Foest et al. 2007; Lange et al. 2009). The system consists of two independent optical beam lines which can be coupled into the VUV-monochromator by a shared rotatable parabolic mirror. The entire set-up is evacuated to high vacuum ($\sim 2 \cdot 10^{-6}$ mbar) conditions by turbo molecular pumps. The MDHL is mounted onto the inlet of the first beam line, while the rest of the system is kept at high vacuum conditions by a shutter valve. The light from the lamp passes through a MgF₂ window (Torr Scientific Ltd, 115 nm cut off) and a pinhole (0.6 mm diameter), and is directed towards the parabolic mirror. The second beam line houses a deuterium lamp (Cathodeon V03) of which the spectral radiance (E_{λ} : $\mu\text{W sr}^{-1} \text{mm}^{-2} \text{nm}^{-1}$) in the 116-220 nm range is known; this lamp was calibrated by the Physikalisch Technische Bundesanstalt (PTB). The orientation of the rotatable parabolic mirror (focus length 1.5 m) determines which of the two beam lines is optically connected to the spectrometer. The entrance slit of the spectrometer is set to 1.0 mm, giving a spectral bandwidth of 1.6 nm. In this way the absolute response of the complete system is thus determined for a spectral bandwidth of 1.6 nm.

The 0.5 m path-length spectrometer (VM-505 Acton Research) has a 1200 g/mm grating. Light exits through a 1 mm slit and is detected by a VUV-photon multiplier tube. The output of the calibrated spectra is given in absolute spectral radiance as $\mu\text{W sr}^{-1} \text{mm}^{-2} \text{nm}^{-1}$.

3.2.3. Photon flux measurements

The conversion of spectral radiance ($\mu\text{W Sr}^{-1} \text{mm}^{-2} \text{nm}^{-1}$) to photon flux at the sample location ($\text{photon cm}^{-2} \text{s}^{-1}$) is far from trivial. This is true even when all the dimensions of the set-up are known. In the Greifswald set-up only a small fraction of the plasma contributes to the light passing through the pinhole (diameter 0.6 mm); extrapolating to the full plasma introduces a large error and assumes that the plasma is homogeneous. Therefore, a set of complimentary VUV photon flux measurements of the MDHLs at various settings have been performed on a small set-up specifically constructed for this purpose in Leiden. It consists of a calibrated photodiode, shutter valve, and MgF_2 window with connection piece for the MDHL. The photodiode is a 1 cm^2 NIST calibrated AXUV-100, of which the photocurrent is measured using a Keithley 485 autorange picoammeter. The distance between the MgF_2 window and photodiode is 31 cm. The entire set-up is evacuated to a pressure of 10^{-2} mbar. The photodiode is used to measure the total flux emitted by the MDHL. This type of photodiode has a low band gap of 1.12 eV and is therefore also sensitive to visible light. The contribution of visible light to the photocurrent has to be subtracted. Flux measurements are thus performed with and without a KBr window in the optical path. This window blocks any radiation below 240 nm and has 90% transmission above this wavelength, up to 1000 nm. By subtracting the visible response from the total photocurrent of the diode, corrected for the absorption of KBr, the photocurrent in the range between 115 to 240 nm can be determined. This yields the total energy in this spectral range, and combined with the spectrum obtained at the calibrated set-up in Greifswald, the photocurrent per wavelength can be determined. It must be noted that the energy recorded in the range 115-240 nm is assumed to be equal to the energy in the range 116-220 nm, since no hydrogen emission is present from 220 to 240 nm. The transmission of the MgF_2 window between 115 and 116 is small. The calibrated spectrum is then converted to units of $\text{photons sr}^{-1} \text{mm}^{-2} \text{nm}^{-1}$ and normalized to an integrated value of one. Next, the measured total VUV photocurrent is assigned proportionally to each wavelength by the normalized spectrum. This results in a wavelength dependent photocurrent that can be converted to a wavelength dependent photon flux according to equation 3.1,

$$I(\lambda) = \frac{i(\lambda)}{e \cdot \eta(\lambda)}, \quad (3.1)$$

where $I(\lambda)$ is the wavelength dependent photon flux in $\text{photon cm}^{-2} \text{s}^{-1}$, $i(\lambda)$ the photocurrent, e the electron charge, and $\eta(\lambda)$ the detection efficiency. The resulting wavelength dependent photon flux can be integrated to obtain the total photon flux of the lamp. Absolute Lyman- α and molecular emission photon fluxes are determined by integrating the 120-124 and 155-165 nm regions, respectively. In our spectra more emission from molecular hydrogen transitions can be seen outside the 155-165 nm region, especially at shorter wavelengths between 130-155 nm. However, the molecular emission peaks at 158 and 161 nm account by far for most of the emission and are therefore considered to be most sensitive to changes in the lamp settings.

Lyman- α and molecular emission fluxes are normalized to 100% of the total flux of the spectrum in order to visualize trends in the contribution of certain

spectral regions. The remaining part of the spectrum is discussed as well. The 2σ error is determined from 15 individual measurements performed at identical settings throughout the measurement run. Errors are found to be $\pm 11\%$ in the total photon flux, $\pm 4\%$ in the Lyman- α contribution, $\pm 1\%$ in the molecular emission contribution and $\pm 3\%$ in the remaining emission contribution.

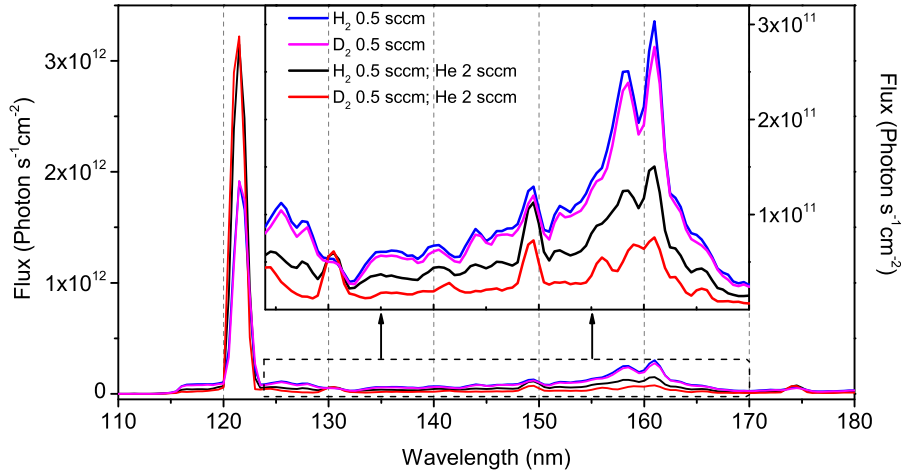


Figure 3.3: VUV spectra in the 110 – 180 nm range of a T-type geometry MDHL, the H_2/D_2 partial pressure is kept at 0.41 mbar. The effect of adding Helium with the H_2 or D_2 is clearly shown. Photon flux (y-axis) estimations are based on NIST photodiode measurements. Emission at ~ 130 , ~ 149 , and ~ 175 nm indicate traces of oxygen and nitrogen.

3.2.4. CryoPAD2

The Cryogenic Photoproduct Analysis Device 2 (CryoPAD2) is used to experimentally test the MDHL SED calibrations on interstellar ice analogues. The set-up is an upgraded version of the system described by Öberg et al. (2007). Ices are grown on a gold coated ‘cold finger’ that is mounted on top of a UHV chamber (5×10^{-11} mbar) through directed deposition. A closed-cycle helium cryostat realizes temperatures as low as 17 K and a temperature regulator (Lakeshore) allows accurate temperature settings. Ice thicknesses are determined using isothermal desorption techniques. Also mounted onto the chamber is the MDHL with a MgF_2 window to sample distances of 16 cm. The ice diagnostics upon VUV irradiation are realized both spectroscopically and mass spectrometrically. The light of an Agilent FTIR 660 spectrometer ($500\text{--}4000\text{ cm}^{-1}$, 2.0 cm^{-1} resolution) is guided in reflection modus onto a MCT detector to obtain RAIR (reflection absorption infrared) spectra. The entire IR beam path is purged with water-free dry air. Perpendicular to the IR beam, a Pfeiffer QMA200 Quadrupole Mass Spectrometer (QMS) is mounted to sample gas phase species that are emitted from the ice surface. This construction allows the photoprocessing of the ice upon VUV irradiation to be studied in situ and

in real time. Details of the methods used have been described in Ioppolo et al. (2014) and Linnartz et al. (2015).

3.3. Results

3.3.1. Photon flux

The most commonly used settings for either an F- or T-type MDHL are 0.41 mbar pure hydrogen pressure, at an input power of 100 W. We take the output generated by the T-type lamp as standard. Photon fluxes obtained from other experiments are normalized to this value for the majority of the data.

The spectrum of the lamp for these settings is shown in figure 3.3. Following the method described in Sect. 3.2.3 using a calibrated photodiode, a total VUV photocurrent of $1.6 \pm 0.2 \mu\text{A}$ is measured for the standard T-type lamp at a distance of 31 cm (MgF_2 window to photodiode). From this current, a photon flux of $(9 \pm 2) \cdot 10^{12} \text{ photons s}^{-1} \text{ cm}^{-2}$ is derived. Uncertainties in photo current and total flux determine the error in this value. The Lyman- α contribution to the total output is 36%, the molecular emission between 155 and 165 nm contributes 19% to the total output and the remaining emission of the lamp has a contribution of 45%. The remaining emission consists of all the output between 116 and 220 nm, excluding what is present in Lyman- α and the molecular part.

Based on the irradiance measurements performed in Greifswald, assuming a homogenous circular emitting source at the position of the aperture, we have calculated the photon flux. This leads to a total VUV photon flux at the photodiode position of $\sim 1.3 \cdot 10^{13} \text{ photons s}^{-1} \text{ cm}^{-2}$, within a factor of two agreement with the value acquired in the direct flux measurement in Leiden.

3.3.2. H_2 pressure dependence

In figure 3.4, the response of an F-type MDHL is plotted as a function of hydrogen pressure. The total flux is normalized with respect to the standard settings of the T-type MDHL. The relative contributions of Lyman- α (120-124 nm), molecular emission (155-165 nm), and remaining emission is presented as well. Clearly visible at 0.41 mbar H_2 is a maximum in the total flux. For this pressure, the contribution of the Lyman- α band reaches the maximum as well, while the contribution in molecular emission is still significantly high. The remaining emission clearly has a local minimum at this pressure. At higher H_2 pressure, above 1 mbar, the total flux gradually decreases. It starts increasing again above 4 mbar. Lyman- α gradually decreases to zero for pressures above 0.41 mbar. The molecular emission shows a similar trend up to 4 mbar. At this point the molecular contribution steeply increases again and is responsible for the overall increase in total flux.

In summary: higher H_2 pressures (with respect to the standard settings) favour emission in the 160 nm region, whereas pressures between 0.4-0.8 mbar are better for Lyman- α emission.

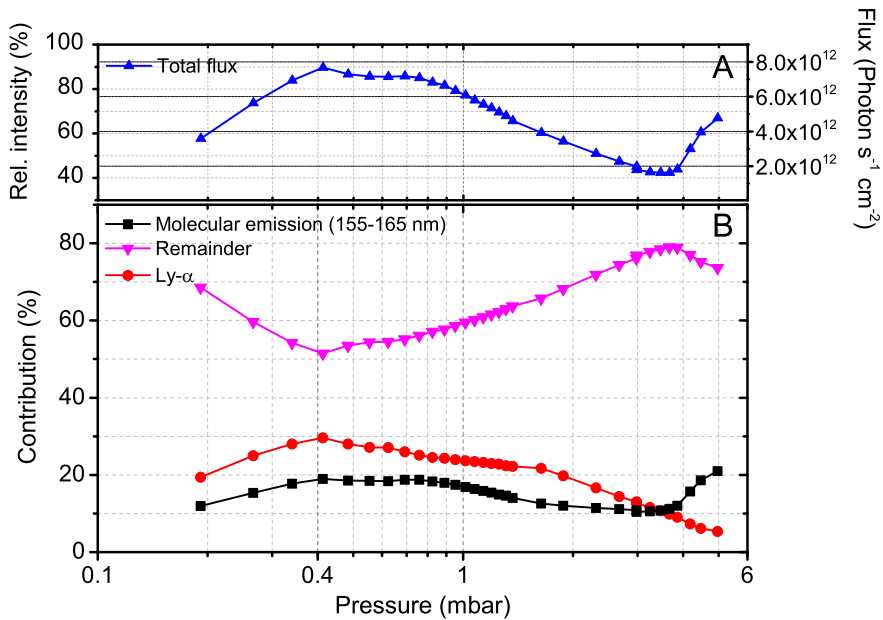


Figure 3.4: Total flux (A) and spectral contribution (B) as a function of H_2 pressure dependence of a F-type MDHL for standard settings. The relative intensity (left axis) is normalized to 100% of the standard T-type MDHL, photon flux (right axis) estimations are based on NIST photodiode measurements.

3.3.3. Mixtures and different gasses

Adding helium to hydrogen in a MDHL can have a significant influence on the SED and flux (Holländer & Wertheimer 1994; Benilan et al. 2011; Chen et al. 2014; Cook et al. 2014; Es-Sebbar et al. 2015). This is illustrated in figure 3.5A, which shows a decline in the total flux moving to higher concentration of helium admixtures. However, a dependence on the H_2 pressure used in the mixture is also seen. The general trend is comparable with the flux variation in pure H_2 where flux decreases towards higher pressure. In figure 3.5B, the spectral contribution is depicted for different H_2 pressures (0.41, 0.59, and 0.76 mbar). Within the error bars, the spectral contributions measured at different H_2 pressures overlap, confirming that in this pressure regime the amount of He is the dominant source of spectral change.

The addition of He to H_2 (and D_2 as will be discussed below) significantly alters the spectral emission pattern. By adding 2 sccm of He, the spectral purity of Lyman- α increases by a factor of ~ 1.65 from 35 – 40% to 60 – 65% while the total flux is nearly constant. The helium has a quenching effect on the molecular hydrogen, while increasing the effective Lyman- α flux.

As more He is added to H_2 , the Lyman- α and molecular emission contributions reach a maximum and minimum, respectively, and remain at a stable level. In contrast to the spectral contributions, the total photon flux peaks around an H_2 :He 1:2 mixing ratio and slowly decreases for higher amounts of

helium.

Further alteration of the MDHL output can be accomplished by changing from H₂ to D₂ mixed with helium. This results in the highest contribution (up to ~ 75%) of Lyman- α and lowest molecular emission and remaining contributions. The photon flux is reduced by roughly 15% compared to 0.41 mbar hydrogen mixed in helium, however. The corresponding VUV spectra are shown in figure 3.3.

Similar to the 1:15 H₂:He mixing ratio shown in Chen et al. (2014), we find a substantial effect of helium addition to hydrogen. A different mixing range has been evaluated in Es-Sebbar et al. (2015), but extrapolating our settings to theirs seems to yield a comparable trend in photon flux decrease. The changing H₂ concentration might be the explanation for the increase in Lyman- α contribution. From the extended measurements performed in this article more trends become apparent. At higher ad-mixing of helium, the total flux decreases while the spectral purity of Lyman- α does not increase further. We conclude that the highest observed contribution of Lyman- α emission, is realized for D₂ in He.

3.3.4. MDHL power dependence

The microwave (MW) cavity input power determines the strength of the microwave field used in the MDHL, and thus directly influences how intensely the plasma is excited. This may also effect the SED. So far, three studies have been reported that focus on the MW dependency. Cottin et al. (2003) presented flux measurements over a limited range, from 30 to 80 W. Cruz-Diaz (2014) presented data about the peak intensities at Lyman- α , 157.8 nm and 160.8 nm, for MW powers ranging from 55 to 90 W. Finally, Es-Sebbar et al. (2015) conducted a wavelength dependent study in combination with actinometry of the MW power on H₂:He mixtures. All three of the studies hint towards a linear behaviour between flux and MW input power. This is confirmed in our study. Figure 3.6 shows the relative output of an F-type MDHL at 0.41 mbar hydrogen versus microwave cavity input power, in the range of 50 to 130 W. Up to 110 W, the total photon flux increases linearly with input microwave power. Above 110 W the increase in flux is not as steep, but still significant. At 130 W, the trend suggests that the flux is reaching a plateau. At this microwave power the air cooling is no longer sufficient and the temperature of the cavity starts increasing. Therefore no higher microwave power measurements were performed. The relative contributions of Lyman- α , molecular, and remaining emission are also presented in figure 3.6. As can be seen, the lamp spectrum does not follow the photon flux trend linearly, but the deviations are not substantial. This finding is different from the conclusion derived in Es-Sebbar et al. (2015) for H₂:He mixtures. The molecular emission and the Lyman- α contribution have a respective minimum and maximum at 100 W input power. The relative difference is as big as 10%. In conclusion, tuning the input power between 60 and 120 W offers a way to tune the photon flux output by up to a factor of 2. With the change in power small changes in SED are also found.

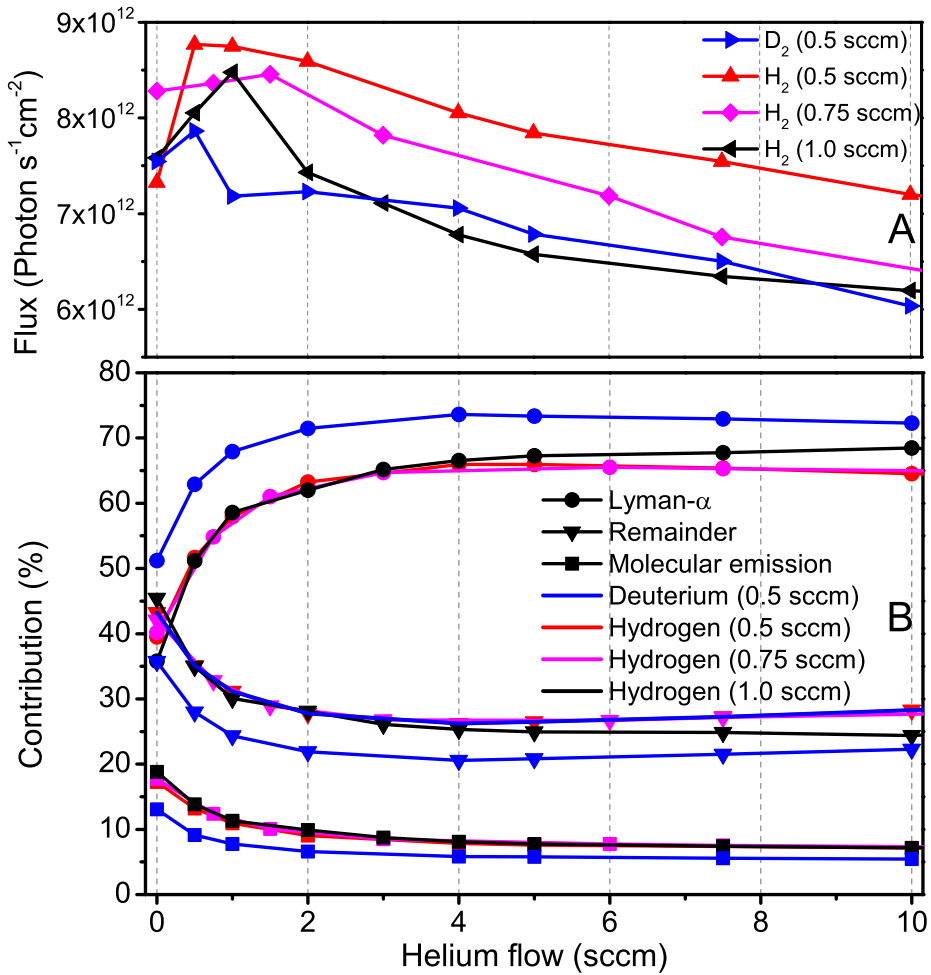


Figure 3.5: Flux dependence (A) and spectral contribution (B) of H_2 or D_2 as function of helium flow. Different fixed molecular hydrogen flows are shown (0.5, 0.75, and 1.0 sccm), resulting in 0.41, 0.59, and 0.76 mbar as a function of the helium flow rate. Additionally, D_2 in He is depicted (0.5 sccm / 0.41 mbar).

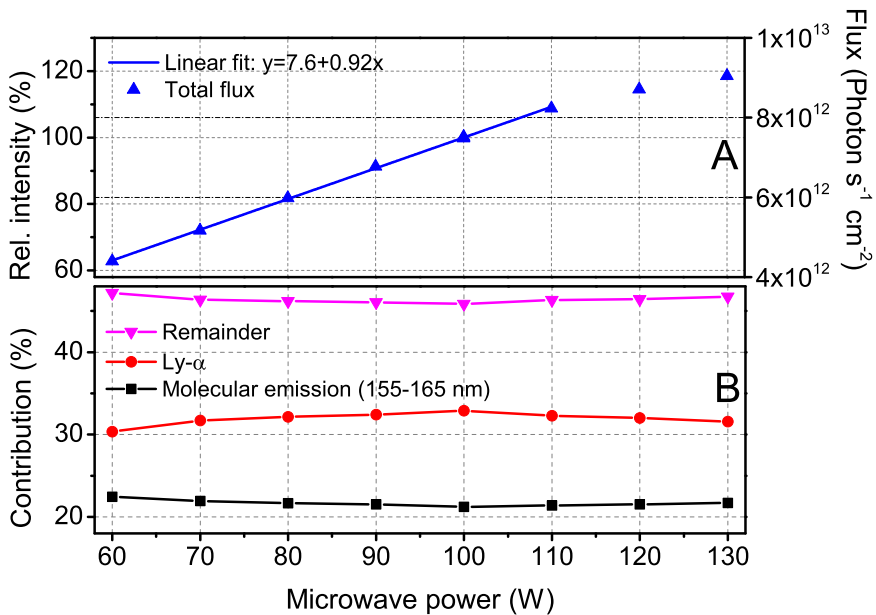


Figure 3.6: Relative flux dependence on microwave cavity input power. The total flux is normalized to the 100 W value. Lyman- α , molecular emission and remainder are given as percentages of the total flux. Corrected for time dependent behaviour.

3.3.5. Pumping efficiency in F- and T-type MDHLs

Comparative measurements between an F- and T-type MDHL have been performed. Under identical settings the output was measured for a number of hydrogen pressures ranging from 0.24 to 0.7 mbar. In figure 3.7 an example is presented for a hydrogen pressure of 0.41 mbar.

The T-type lamp is found to increase the Lyman- α emission by 30% on average, compared to the F-type MDHL. At the same time the molecular hydrogen emission remains identical for the F- and T-type MDHL. A total photon flux increase is also observed for the T-type lamp, which can be explained by the increase in Lyman- α emission. The increase of this particular atomic hydrogen line was also reported by Chen et al. (2014) for a pressure of 0.4 torr (0.53 mbar). They found an increase in Lyman- α when using a T-type MDHL of more than 100% compared to an F-type lamp as well as a decrease in molecular emission. These findings are not fully in line with the results in the present study.

Chen et al. (2014) suggested that different pumping efficiencies were responsible for the difference in spectral output of the F- and T-type MDHLs. The T-shape geometry ensures that gasses can be more easily evacuated from the MDHL. This in turn limits collisional de-excitation of excited atomic hydrogen and therefore an increase in Lyman- α output is seen. Building on this argument, using different pumping capacities on the same lamp should make it possible to reproduce this effect. This can be achieved by using different types of pumps, for example a scroll pump and rotary vane pump. Respectively, these pumps are

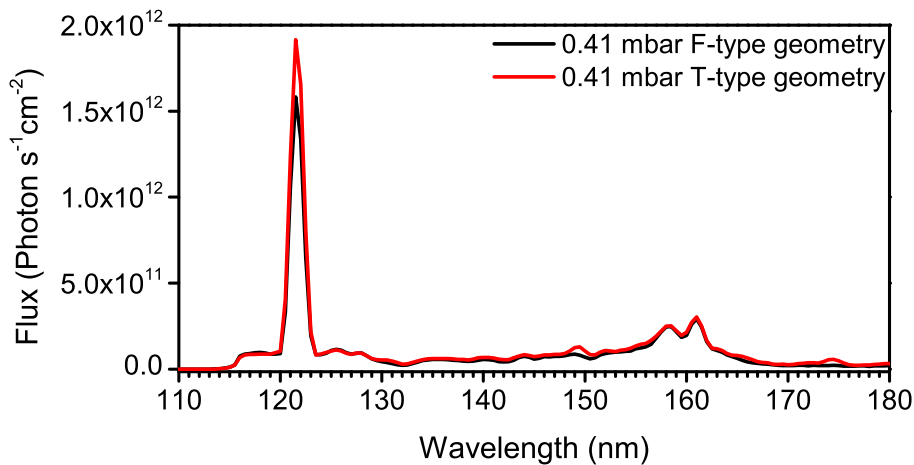


Figure 3.7: VUV spectra in the 110 – 180 nm range of different geometry MDHLs (F- and T-types) at a molecular hydrogen pressure of 0.41 mbar.

able to reach a base pressure in the low 10^{-3} and low 10^{-2} mbar region and have a pumping capacity of 285 l/min and 300 l/min for air. In addition, it is known that scroll pumps do not pump hydrogen as efficiently as oil-based rotary vane pumps.

Two sets of measurements were performed with an F-type lamp running at various H_2 pressures, while being pumped by either a scroll pump or a rotary vane pump. Although the input pressure is identical in both sets of experiments, a pressure difference between the two pumps was observed on the gauge at the pump side. Pressures are between 6 and 60% lower for the rotary vane pump, confirming that the rotary vane pump removes hydrogen more efficiently from the MDHL than the scroll pump.

The VUV spectra, shown in figure 3.8, show no significant change in the spectral distribution of the lamp output for the two different pumps. Only the total photon flux output is higher for the measurements with the scroll pump. Therefore the pumping efficiency cannot explain the differences in spectral distribution between an F- and T-type lamp. It is not fully clear what causes this difference in Chen et al. (2014), because for similar settings the effect is not found here. It could be caused by the slightly different geometries of the lamps.

In conclusion, choosing a T-type cavity can be beneficial when higher Lyman- α and total flux is required. Although the spectral distribution is not expected to change for different pumping efficiencies, the total photon flux can be slightly affected. Therefore, when running a series of experiments, the same pumping system should always be used.

3.3.6. Distance dependence

In this study measurements are performed to determine the influence of the microwave cavity positioning on the output spectrum. The measurements are

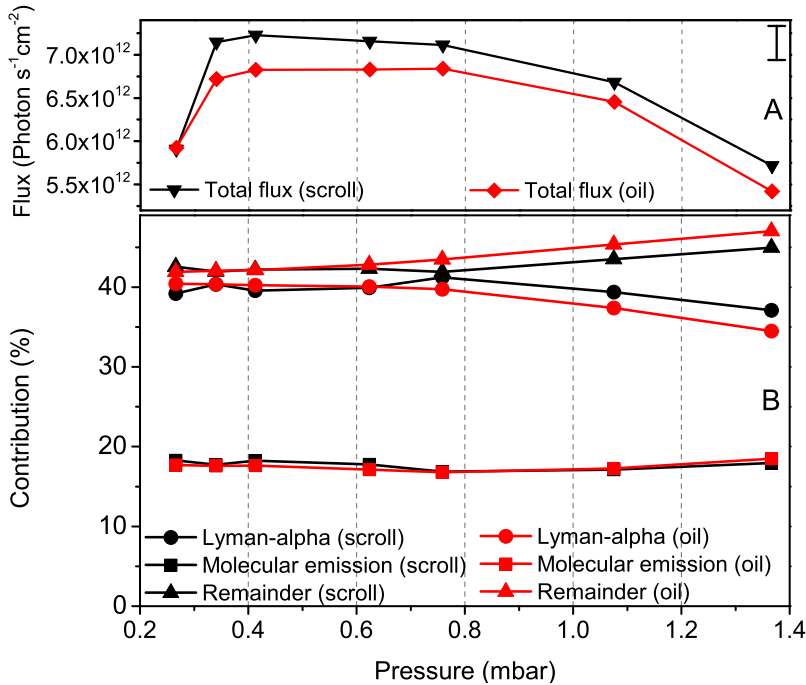


Figure 3.8: Lyman- α (circles), molecular emission (squares), remainder (triangles) contribution, and normalized total photon flux (top) for various pressures with different pumps. The oil pump (black) gives a lower photon flux than the scroll pump (red), but the contributions are virtually identical.

done at cavity positions of 9.0, 7.3, and 5.5 cm from the MgF₂ window for H₂ flow pressures of 0.41, 0.59, and 0.76 mbar (see figure 3.9). The overall trend is that the total photon flux decreases slightly while moving the cavity away from the MgF₂ window. Additionally, the spectral energy distribution does show minor changes as well. The percentage-wise contribution of Lyman- α increases and the molecular emission contribution decreases when the cavity is moved towards the MgF₂ window. Although this is small and within the error, this effect is observed for all pressures studied.

Although it is a small effect (for the distances studied here), the change in photon flux is interesting. The limited data set available scales with an isotropic r^{-2} decrease, suggesting that the MW cavity defines a point source. The change in spectral output may be related to a higher column density of rest gases in between the plasma and window when increasing the distance, affecting the SED in a wavelength dependent way. At this stage it is not possible to say more; the overall effects are small. Nevertheless, as the position does matter, keeping the cavity on a fixed position during a set of experiments is recommended.

3.3.7. Practical issues

In addition to the systematic dependences discussed before, there are also a number of very practical issues that should be taken into account when

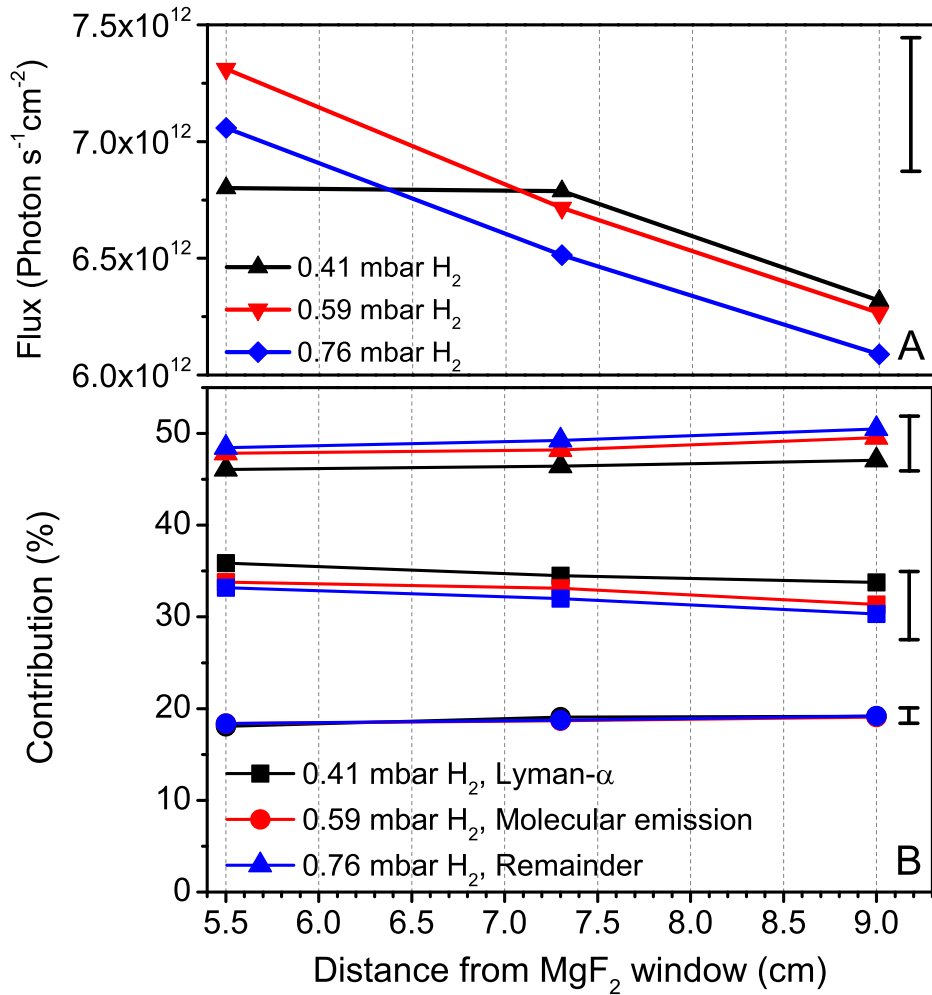


Figure 3.9: Variations in spectral output depending on cavity location, 0.41 mbar (black), 0.59 mbar (red), and 0.76 mbar (magenta) H₂ flow pressure. Lyman- α (squares), molecular emission (circles), and remainder of the VUV spectrum are shown (triangles).

operating the MDHL. The most prominent practical issues running MDHLs involve stability over time (section 3.3.7) and the effect of degradation of the MgF_2 window (section 3.3.7).

MDHL stability over time

In many of the previous studies using MDHLs it was found that these exhibit changes in the output photon flux over operating time. Two important contributors to this effect are thermal settling of the lamp and degradation and pollution of the transmission window (Warneck 1962; Chen et al. 2014). To determine the stability of our lamp spectrum over time, a T-type MDHL was run at 0.41 mbar H_2 for an hour while taking a spectrum every 5 minutes (see figure 3.10). The first spectrum was taken immediately after turning on the MDHL. In the first 5 minutes a drop in total photon flux is seen, after which the output linearly decreases. This decrease is mainly caused by a quick drop in molecular emission. The linear decrease in flux is similar to that reported by Chen et al. (2014); however, no stable region is reached, possibly owing to the shorter duration of the experiment (one hour in this work and two and a half hours in Chen et al. (2014)).

More interesting are the Lyman- α and molecular emission contributions to the total flux. These are found to remain at a stable level after the first 5 minutes of lamp operation, which guarantees that spectral properties of the lamp are directly proportional to its photon flux.

This result is surprising, since Warneck (1962) found that the contribution of the Lyman- α component decreases more rapidly than the molecular contribution. This is possibly due to differences in the way the SEDs are determined. Warneck (1962) made use of a nickel photocell to detect the 120 - 130 nm range and ozone actinometry for the 135 - 185 nm region. These broadband techniques are not suitable for distinguishing wavelength dependences and consequently only provide information on the overall flux. For general lamp operation starting the irradiation experiments after the lamp has settled for 10 to 15 minutes is recommended. In this way the photon flux and spectral fluctuations do not play a dominant role in the experiment. After this period the spectral contributions will remain stable and therefore it is sufficient to only trace variations in the photonflux.

Effects on the MgF_2 window

As already suggested in paragraph 3.3.7, pollution of the MgF_2 window can have a big influence on the output of the MDHL. Carbon products formed in the plasma can deposit on the MDHL side of the window. Especially if the VUV lamp is being pumped with an oil-based pump, there will be oil vapours in the system that can be processed by the plasma and deposited as a residue on the window. On the vacuum chamber side, gas molecules can be adsorbed on the window, and residual gas molecules will be present in the vacuum chamber. When the lamp is in operation these molecules can be processed by the VUV field to form a residual layer. Es-Sebbar et al. (2015) showed a decrease of 50% in transmission of the MgF_2 window after 8 hours of irradiation, which was ascribed to the deposition of trace species. We do not observe such a drastic

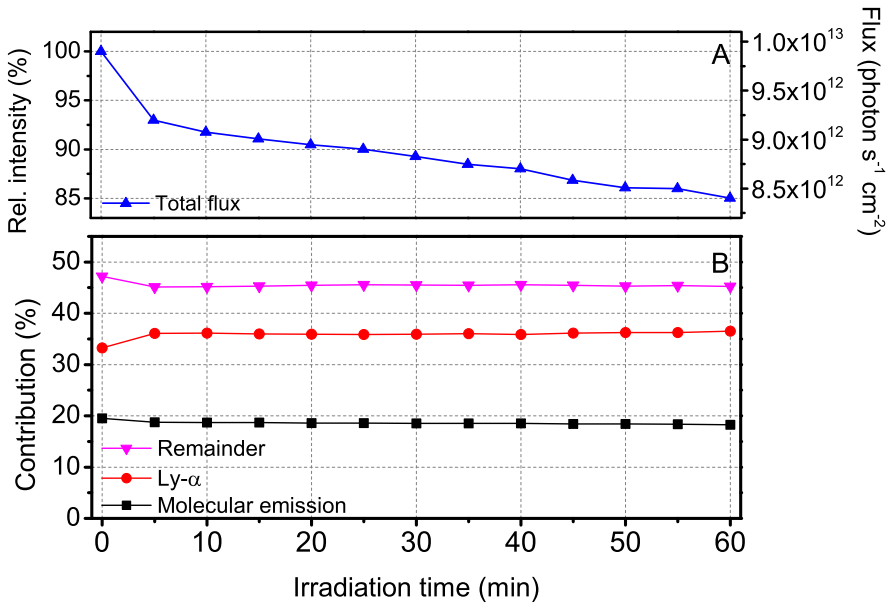


Figure 3.10: Relative flux decrease over time, combined with the relative contribution of Lyman- α , molecular, and remaining emission for standard MDHL settings, using a T-type lamp.

decrease in transmission. However, this discrepancy could be explained by a difference in measurement technique. A third effect is the processing of the window itself. The harsh VUV output of the lamp causes structural changes of the material over time. This was shown by Warneck (1962) for LiF, and it is also likely to happen for MgF_2 , although on a different time scale. These two effects, pollution and window processing, can be responsible for diminishing the flux and may cause spectral changes over longer periods of time.

It should be noted that in the Greifswald measurements, the window degradation has not been explicitly taken into account, as this would imply that the window had to be removed regularly. Instead, we expect that degradation effects along a series of measurements, focussing on one specific parameter, are negligible or much less relevant than the effect of the changing parameter under investigation.

3.3.8. CO photodepletion measurements

Laboratory experiments have shown that photodesorption offers an effective non-thermal mechanism that explains the detection of molecular gas phase species in low temperature regions in the ISM where these species are expected to be fully frozen out. However, the exact numbers vary between different groups, even when experimental procedures are largely identical. This has become clear, particularly for the photodesorption yield obtained for pure

Table 3.1: Parameter influences

Influence	Effect on SED (Lyman- α)	Effect on SED (Mol. Emission)	Effect on flux (photon $\text{cm}^{-2} \text{s}^{-1}$)
Pressure	L, $\sim 30\%$	L, $\sim 15\%$	L, $\sim 30\%$
Power	S, $\sim 3\%$	S, $\sim 3\%$	L, $\sim 50\%$
Helium	L, $\sim 100\%$, $\sim 50\%$	S, $\sim 5\%$
Deuterium	M, $\sim 10\%$	M, $\sim 10\%$	M, $\sim 15\%$
F- vs. T-type MDHL	M, $\sim 20\%$	S	M, $\sim 20\%$
Cavity	S, $\sim 3\%$	S, $\sim 3\%$	S
Time	N	N	S,M, $\sim 7\%$

Notes. L = Large effect, M = Moderate effect, S = Small effect, N = No effect

CO ice. Öberg et al. (2007), Muñoz Caro et al. (2010), and Chen et al. (2014) provide values of $(2.7 \pm 1.3) \cdot 10^{-3}$, $(35 \pm 5) \cdot 10^{-3}$, and $(212 \pm 3) \cdot 10^{-3}$ molecules per incident photon, respectively. These measurements have been performed with broadband MDHLs. In a monochromatic and wavelength dependent study Fayolle et al. (2011) showed that CO photodesorption occurs predominantly at longer wavelengths between 135 and 165 nm, following a desorption induced by electronic transition (DIET) mechanism. For wavelengths around Lyman- α the photodesorption is much less efficient. Therefore, different SED characteristics, specifically the Lyman- α to molecular emission band ratio, will definitely influence the overall photodesorption rate that follows from the MDHL experiments. This is illustrated in Figure 3.11 where the corresponding SEDs of two well-characterized lamp settings are used to derive photodesorption rates.

Using CryoPAD2, a T-type MDHL is operated at 100 W and either 0.41 mbar of pure H_2 or a 1:3 H_2 :He gas mixture, at a pressure of 2.13 mbar, is used. The SEDs for these settings comprise 36% and 67% of Lyman- α and 19% and 8% molecular emission, respectively, while the total flux for both settings is similar (less than $\sim 0.5 \cdot 10^{12}$ photons $\text{s}^{-1} \text{cm}^{-2}$ difference, or about 6%, in the calibrated measurements). The vacuum UV photons impinge on thin ice layers (13 or 16 MonoLayers (MLs), 1 ML = 10^{15} molecules) of pure CO deposited on top of a 17 K gold surface; the layers are thick enough to exclude surface effects. A typical experiment lasts 2 hours. The ongoing photodepletion (the combined effect of photodesorption and photochemistry) of the CO ice over time is subsequently tracked by the decrease in the 2142 cm^{-1} CO band.

Taking thicknesses of 5 ML or more as the regime where surface effects can be neglected, the linear fits allow a photodepletion rate to be derived. As expected from the work by Fayolle et al. (2011), an ice irradiated with light from the MDHL running on the H_2 :He mixture (suppressed 160 nm emission) photodepletes less rapidly than the ice irradiated with pure H_2 that exhibits a molecular emission that is roughly two times bigger. Obviously, this photodepletion value is different for the different lamp settings, fully in agreement with the main findings of the work presented in this chapter. It also may explain, at least to some extent,

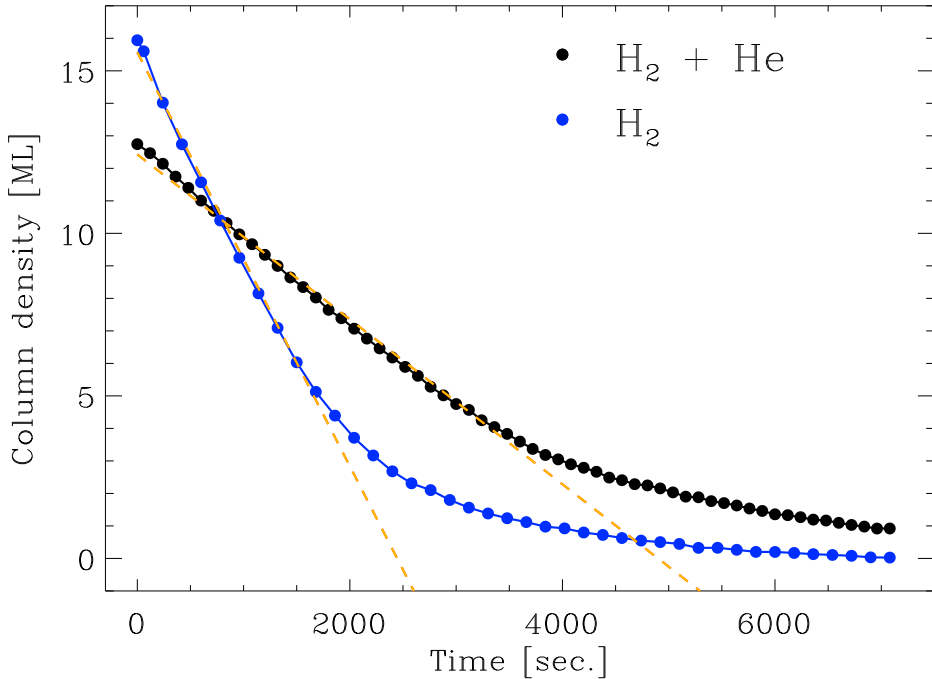


Figure 3.11: CO photodesorption of ices irradiated with either Pure H_2 at 0.41 mbar (blue) or H_2 :He 1:3 (black) at 2.13 mbar.

the deviations found in the different photodesorption studies in agreement with Chen et al. (2014). It is for this reason that we stress how important it is to record the SEDs in situ. Other artefacts might also be at play; it is likely that other photo induced effects affect the final values, (wavelength dependent) chemical processes forming CO_2 , for example, that in turn may photodesorb (wavelength dependent, see Fillion et al. (2014)). The two curves in the figure yield a photodepletion rate of $(6 \pm 3) \cdot 10^{-3}$ and $(3 \pm 1) \cdot 10^{-3} \text{ ML s}^{-1}$ for H_2 and the H_2 :He mixture, respectively. It will take a greater effort to bring all experimental numbers in line, but obviously an important uncertainty has now been characterized. Besides quantitative issues, a changing SED may also affect the outcome of many chemical studies performed over the past decades; different molecules may react resonantly with different emission bands, and particularly higher energetic photons may cause bonds to cleave more easily. With the information provided here such dependencies can now be studied relatively easily.

3.4. Conclusions

In this work the influence of various running conditions on both flux and SED of the microwave discharge hydrogen-flow lamp has been studied. The main findings are summarized in table 3.1. The conclusions of this work are:

1. The effects of hydrogen pressure, ad-mixing helium, exchanging hydrogen

for deuterium, microwave power, pumping efficiency, cavity position, and practical issues such as stability over time need to be taken into account.

2. The relative contribution of Lyman- α to the emission profile of the MDHL can be increased by up to 65% when helium is added to the hydrogen. Further spectral purity of Lyman- α of up to nearly 75% can be achieved by exchanging hydrogen for deuterium. Alternatively, high percentages of molecular emission can be generated by increasing the hydrogen pressure.
3. Recommendations are given on how to operate the MDHL at the highest efficiency and consistency. They include allowing sufficient time for the settling of the lamp, using a fixed cavity position, and accounting for pollution on the lamp window.
4. Variations in the SED can, to a certain extent, explain the differences in the literature among different laboratory experiments. However, it seems unlikely that it will explain order of magnitude differences.
5. It is important to characterize the SED and photon flux in situ, preferably with a combination of monochromator and calibrated photodiode.

Acknowledgement

Thanks go out to the INP Greifswald for making their UV/VUV set-up available to this research and Peter Holtz for his invaluable help in the laboratory. Many thanks to Jean-Hugues Fillion and Mathieu Bertin (UPMC Paris) and Alan Heays and Gleb Fedoseev (University Leiden for many helpful discussions. Finally I would like to thank the referee of the article, Joseph Nuth, whose open report and suggestions were very helpful.

The research leading to these results has received funding from the European Union Seventh Framework Programme (FP7/2007-2013) under grant agreement n°316216.



V-UV



Methanol ice co-desorption to explain cold gas-phase methanol

N.F.W. Ligterink, C. Walsh, R.G. Bhui,
S. Vissapragada, J. Terwisscha van Scheltinga & H. Linnartz

N.F.W. Ligterink et al. 2017, *Methanol ice co-desorption as a mechanism to explain cold methanol in the gas-phase*, subm. to A&A

4.1. Introduction

Methanol is one of the smallest complex organic molecules (COMs, Herbst & van Dishoeck 2009) observed in the interstellar medium (ISM). It has been identified in both the gas-phase and solid-state towards many types of sources, among which are dark clouds, hot cores, protostellar envelopes, protoplanetary disks and comets (Ball et al. 1970; Grim et al. 1991; Bockelée-Morvan et al. 1991; Bisschop et al. 2007b; Bottinelli et al. 2010; Taquet et al. 2015; Boogert et al. 2015; Walsh et al. 2016). Gas-phase reactions account only for a small fraction of methanol production (Geppert et al. 2005; Garrod et al. 2006). It has been demonstrated that methanol ice efficiently forms by sequential hydrogenation of CO on interstellar dust grain analogues (Watanabe & Kouchi 2002; Fuchs et al. 2009; Linnartz et al. 2015, and references therein). Evidence for this formation pathway in the ISM is supported by infrared (IR) observations of interstellar ices which show that CO and methanol are both abundant ice species that are intimately mixed (Pontoppidan et al. 2003; Cuppen et al. 2011; Penteadó et al. 2015).

The release of methanol from ice mantles on dust grains to the gas-phase is generally thought to occur either via thermal desorption or photodesorption, depending on the physical conditions governing the local environment. For example, young stellar objects (YSOs) enrich the gas-phase with warm methanol released by thermal desorption in their hot core/corino phase (e.g., Turner 1991; van Dishoeck et al. 1995; Bisschop et al. 2007b; Taquet et al. 2015). Photodesorption of methanol ice has been invoked to explain gas-phase abundances of rotationally cold methanol in cold ($\ll 100$ K) environments such as dark clouds (Friberg et al. 1988).

The photodesorption mechanism, whereby a VUV (vacuum-ultraviolet) photon impinges on solid-state molecules and induces a release to the gas-phase, is well established for CO ice. Quantification of this process has been realized mainly in the laboratory (Öberg et al. 2007; Muñoz Caro et al. 2010; Fayolle et al. 2011; Chen et al. 2014; Paardekooper et al. 2016) and is also theoretically supported (van Hemert et al. 2015). It has been used to interpret recent observations of a disk showing a double snowline (Öberg et al. 2015). Experimental and theoretical evidence of intact water photodesorption is also available (Westley et al. 1995; Andersson et al. 2005; Andersson & van Dishoeck 2008; Öberg et al. 2009b; Arasa et al. 2015). Methanol photodesorption has not been as rigorously studied. Öberg et al. (2009a) indirectly inferred a photodesorption rate for pure methanol ice of 2.1×10^{-3} molecules photon⁻¹ from fitting multiple components to the rate of methanol ice loss. Cruz-Diaz et al. (2016) recently revisited the broadband VUV irradiation of pure methanol ice including direct detection of the photodesorption products via mass spectrometry. Only products of VUV ice processing were directly detected (H₂, CO, and CH₄) leading to an upper limit of $< 3 \times 10^{-5}$ molecules photon⁻¹ photodesorption of intact methanol. At the same time Bertin et al. (2016) performed wavelength dependent experiments on methanol and methanol:CO mixed ice. In both the pure and mixed ice the role of dissociative photodesorption was studied and the photodesorption rate of intact methanol was found to be low (in agreement with Cruz-Diaz et al. 2016). For a pure methanol ice this

is in the order of $1\text{-}2 \times 10^{-5}$ molecules photon⁻¹, whereas for the mixed ice an upper limit of $\leq 3 \times 10^{-6}$ molecules photon⁻¹ was found. The resulting methanol photodesorption rates are several orders of magnitude lower than the typical yields of $10^{-2}\text{-}10^{-3}$ molecules photon⁻¹ for CO and H₂O photodesorption and are too low to explain gas-phase abundances of methanol in cold regions of the ISM. Also, the result of the mixed ice is interesting because it shows that indirect photodesorption, known to be efficient for the N₂:CO case (Bertin et al. 2013), is an inefficient process in the case of methanol:CO mixtures. Therefore to explain the presence of rotationally cold methanol other transfer mechanisms from the solid-state to the gas-phase need to be investigated.

One such option is chemical or reactive desorption. In this mechanism two fragments, usually radicals or ions, react with each other to form the product species and the excess energy from the reaction is available to release the product from the solid-state to the gas-phase. This mechanism was investigated by Martín-Doménech et al. (2016) for methanol. In VUV irradiated H₂O:CH₄ ices they concluded on the chemi-desorption of photo-produced formaldehyde at $\approx 4.4 \times 10^{-5}$ molecules photon⁻¹; chemi-desorption of methanol ice was not found, even though the experiments showed CH₃OH formation.

Another possible transfer mechanism is thermal co-desorption (Sandford et al. 1988; Öberg et al. 2005; Fuchs et al. 2006; Brown & Bolina 2007; Martín-Doménech et al. 2014; Burke & Brown 2015). This term is applied to any thermal release of a molecule to the gas-phase induced by a second matrix ice species. Most cases involve species that are trapped above their respective desorption temperature in a matrix with a higher desorption temperature than said species. These species release partially to the gas-phase at their regular desorption temperature and co-desorb when the matrix undergoes a phase change (for example the change of amorphous solid water to crystalline water) or when the matrix itself begins to thermally desorb (e.g. Bar-Nun et al. 1985). In both cases, co-desorption is driven by the fact that the molecule is initially hindered to thermally desorb because of its matrix environment. The opposite of the previous case is co-desorption of a molecule below its desorption temperature, i.e. when the matrix has a lower desorption temperature than the molecule, and the matrix carries the less volatile species with it when desorbing. This specific kind of co-desorption is the subject of the present study and further mention of the term co-desorption refers to desorption of a molecule below its desorption temperature induced by the thermal release of matrix species.

It is well established that methanol ice forms *in situ* on ice mantles on cold dust grains via the sequential hydrogenation of CO ice (Watanabe & Kouchi 2002; Fuchs et al. 2009). We therefore investigate the potential release of methanol to the gas-phase with a thermally desorbing CO matrix at low temperatures. As noted above, recent photodesorption and reactive desorption experiments suggest that methanol does not come off intact in either case (Bertin et al. 2016; Cruz-Diaz et al. 2016; Martín-Doménech et al. 2016). The aim here is to test if the proposed co-desorption mechanism can explain the presence of rotationally cold gas-phase methanol in the ISM. Laboratory experiments are discussed that study the thermal desorption dynamics of CO:CH₃OH ice mixtures and the results are tested in astrochemical models. The models adopted are representative of the physical conditions in the protoplanetary disk around TW Hya in which cold

gas-phase methanol was recently detected with ALMA (Walsh et al. 2016). This was the first detection of methanol in a protoplanetary disk and is a particularly interesting test case for thermal co-desorption given the range of temperatures in this or similar objects.

This chapter is organized in the following way. The experimental set-up and procedure are described in Sect. 4.2, that also summarizes the experimental results. In Sect. 4.3 the astrochemical model is described and used to interpret the experimental findings. The conclusions are presented in Sect. 4.4.

4.2. Experimental setup and results

4.2.1. Laboratory set-up and protocols

CryoPAD2

All laboratory measurements in this chapter are carried out on the Cryogenic Photoproduct Analysis Device 2 (CryoPAD2), a recently upgraded setup to study VUV induced processes in interstellar ice analogues. In short, this setup consists of a main chamber at oil-free, ultra high vacuum (UHV, 1×10^{-10} mbar). At its center a cryogenically cooled gold coated reflective surface is mounted, which can be cooled to a lowest temperature of 12 K. Gasses are prepared in a gas mixing line and deposited on the cryogenically cooled surface to form an ice layer, using a leak valve connected to a nozzle positioned in front of deposition zone. A Lakeshore Model 350 temperature controller controls the feedback loop between a thermocouple and heating wire to set the base temperature and temperature ramp on the substrate with a relative accuracy better than ± 1 K, and absolute accuracy not exceeding ± 2 K. The composition of the deposited ices are analysed *in situ* by Reflection Absorption InfraRed Spectroscopy (RAIRS) at a resolution of 2 cm^{-1} . Gas-phase species are analysed with a Hiden 3F RGA quadrupole mass spectrometer (QMS), which is connected to the temperature controller and records the temperature at the same time. This QMS faces the gold surface directly. Mass fragmentation patterns of desorbing species can be linked to characteristic temperatures in order to record temperature programmed desorption (TPD) mass signals.

Experimental protocol

Mixtures of carbon monoxide (Linde Gas, 99.997%) or methane (Linde Gas, 99.995%) and ^{13}C -methanol (Sigma-Aldrich, 99%) are prepared in the mixing line. $^{13}\text{CH}_3\text{OH}$ has a unique mass at m/z 33, which does not overlap with the masses of the $^{12/13}\text{C}$ and/or $^{16/18}\text{O}$ carbon monoxide isotopologues, nor with potential contaminants like molecular oxygen ($^{16}\text{O}_2$ at m/z 32, $^{16}\text{O}^{18}\text{O}$ at m/z 34). Methanol is purified in a number of freeze-pump-thaw cycles before use. The mixing ratio is determined with a gas independent gauge.

Deposition on the substrate occurs at 15 K, after which an IR spectrum is taken to verify and characterize the composition of the ice. The system is given time to pump any residual gases of the deposition until a pressure of 1×10^{-10} mbar or better is reached, in order to have good baseline conditions. Next, a temperature ramp, typically 10 K min^{-1} , is set to heat the deposited sample. The high heating

Table 4.1: IR positions and transmission band strengths of CO, methanol, methane and isotopologues

Molecule	Mode	Position cm ⁻¹	Transmission band strength ×10 ⁻¹⁷ cm molecule ⁻¹
CO	CO str.	2138	1.12 ^a
¹³ CO	CO str.	2092	1.32 ^a
¹³ CH ₃ OH	CO str.	1020	1.07 ^a
CH ₄	deform.	1302	0.97 ^b

Notes. ^aBouilloud et al. (2015), ^bGerakines & Hudson (2015)

ramp is chosen in order to give the ice less time to undergo structural changes and make it more likely that methanol will co-desorb with CO. IR spectra are continuously recorded in order to trace ice changes due to thermal processing. In parallel, the QMS records the (co-)desorption of molecules from the sample, focusing mainly on m/z 16 and 33.

Recorded mass spectra are corrected for the QMS response function. Since the QMS detector can saturate at high signal intensities, a good alternative approach is to trace desorption of a certain molecule at a minor fragmentation channel instead of its main channel. Particularly for CO, of which large amounts desorb in the experiments, it is better to trace this molecule at $m/z = 16$, because the O⁺ fragment signal is ~60 times less intense in the signal than that of the main CO⁺ fragment channel at $m/z = 28$.

Column densities (N_{species}) are determined from the IR spectra by the equation:

$$N_{\text{species}} = \frac{1.1}{3.4} \ln(10) \frac{\int_{\text{band}} \tau dv}{A_{\text{band}}}, \quad (4.1)$$

where $\int_{\text{band}} \tau dv$ is the integrated band area, A_{band} is the band strength and $\frac{1.1}{3.4}$ a scaling factor explained below. Band strengths can be different in a RAIRS set-up with respect to transmission spectroscopy, due to the difference in path length. Therefore, additional band strength determinations have been performed. In our experiments, for CO the equivalent of one monolayer (ML) was determined mass spectrometrically from TPD experiments and correlated to the CO stretch absorption signal in the IR. By assuming a column density of 10^{15} molecules cm⁻², the set-up specific RAIRS band strength for CO was found to be $3.4_{-0.5}^{+0.5} \times 10^{-17}$ cm molecule⁻¹. Under the assumption that other set-up specific band strengths scale in the same way as CO, a factor of $\frac{1.1}{3.4}$ is used to adapt transmission band strengths taken from literature (Bouilloud et al. 2015). The bands used for analysis and their band strengths in transmission are listed in Table 4.1. The total ¹²⁺¹³CO column density is determined by multiplying $N(^{13}\text{CO})$ by (90+1), where 90 is the ¹²CO/¹³CO isotope ratio. The ¹²CO band is deemed less reliable for column density determination because high intensity effects make a baseline fit more difficult and because it is susceptible to non-linear RAIRS effects (Teolis et al. 2007).

Table 4.2: Fragmentation patterns of CO and $^{13}\text{CH}_3\text{OH}$ upon 70 eV electron impact ionization.

Mass (amu)	CO	$^{13}\text{CH}_3\text{OH}$	CH_4
12	0.04268	-	0.01686
13	-	0.00081	0.0474
14	-	0.00245	0.09062
15	-	0.00690	0.39404
16	0.01580	0.05059	0.44375
28	0.92936	-	-
29	0.01115	0.01874	-
30	-	0.18205	-
31	-	0.02650	-
32	-	0.40824	-
33	-	0.30372	-

Notes. Fragmentation pattern and intensities based on NIST data. The most commonly used channels are highlighted in red.

Methanol co-desorption rate determination

The co-desorption yield of methanol released in tandem with the thermal release of CO (or CH_4), R_{methanol} , is calculated from the TPD spectrum using the following relation,

$$R_{\text{methanol}} = \frac{\phi_{\text{m/z,CO}}}{\phi_{\text{m/z,methanol}}} \frac{\sigma_{\text{CO}}}{\sigma_{\text{methanol}}} \frac{A_{\text{methanol}}}{A_{\text{CO}}}, \quad (4.2)$$

where ϕ is the fragmentation fraction of CO and methanol at a specific mass, σ the total electron impact ionization cross section of CO (or methane) and methanol at 70 eV and A the integrated QMS signal of CO or methanol. σ_{CO} is given as 2.44\AA^2 (Hudson et al. 2004) and σ_{methanol} is 4.44\AA^2 (Hudson et al. 2003). For methane it is 3.93\AA^2 (Nishimura & Tawara 1994). The mass fragmentation patterns of CO, CH_4 and $^{13}\text{CH}_3\text{OH}$ are given in Table 4.2.

4.2.2. Experimental results

Most co-desorption experiments conducted in this work have been performed with $^{13}\text{CH}_3\text{OH}:\text{CO}$ mixed ices, but layered ices ($^{13}\text{CH}_3\text{OH}$ deposited on top of a layer of CO) have been investigated as well. A variety of thicknesses and mixing ratios have been used. A full list of the performed experiments is given in Table 4.3.

A typical IR spectrum taken after deposition is shown in Fig. 4.1 for the 1:24 mixed $^{13}\text{CH}_3\text{OH}:\text{CO}$ experiment. At 1015 cm^{-1} the CO stretch mode of methanol is visible. Note that this mode has two components. The strong component is associated with monomeric methanol, methanol that is largely isolated in the CO matrix. The smaller, blue-shifted component is mainly caused by methanol clusters, but minor contributions of $^{12}\text{CH}_3\text{OH}$ impurities in the sample cannot

Table 4.3: Upper limit co-desorption rates (R) for a systematic set of different experiments.

Methanol (ML)	CO ^a (ML)	CH ₄ (ML)	Ratio	Type	Ramp (K min ⁻¹)	R _{methanol} (MeOH CO ⁻¹)
5.7	137.4	-	~1:24	mixed	1	≤ 3.3 × 10 ⁻⁶
2.9	52.2	-	~1:18	mixed	10	≤ 2.6 × 10 ⁻⁶
8.7	119.7	-	~1:14	mixed	10	≤ 1.1 × 10 ⁻⁶
11.4	123.3	-	~1:11	mixed	10	≤ 1.9 × 10 ⁻⁶
24.6	126.9	-	~1:5	mixed	10	≤ 7.3 × 10 ⁻⁷
31.2	30.5	-	~1:1	layered	10	≤ 3.2 × 10 ⁻⁵
13.1	21.0	-	~3:5	mixed on CO	10	≤ 6.8 × 10 ⁻⁶
3.9	-	31.9	~1:8	mixed	10	≤ 3.2 × 10 ⁻⁵

Notes. ^aDetermined by the ¹³CO band multiplied by 91 to retrieve the total ¹²⁺¹³C column density.

be excluded. Depending on the mixing ratio, ice thickness and temperature the profile of this band can change from fully monomeric to clustered methanol. At 2092 cm⁻¹ the ¹³CO peak is visible and next to it the intense CO stretching mode at 2143 cm⁻¹. Between the two CO isotope peaks an artefact is visible that is caused by the high intensity of the CO peak. The same figure also shows the IR spectrum at 100 K during the TPD. CO has desorbed at this point, but methanol is still present. Its peak shape has changed, however, due to the removal of the CO matrix. Table 4.3 lists the ice column densities of all experiments.

From the same experiment, a typical desorption pattern is shown in Fig. 4.2. CO is traced at *m/z* 16, while ¹³CH₃OH is traced by *m/z* 33. CO desorbs around 30 K (e.g., Acharyya et al. 2007), while bulk methanol desorption occurs around 130 K. The *m/z* 16 signal around 130 K is the ¹³CH₃ fragment of the methanol fragmentation pattern, but can partially also be caused by trace amounts of CO trapped in the methanol ice and releasing upon methanol desorption. No release of *m/z* 33 is seen around 30 K.

Figure 4.3 shows a close-up of the CO desorption peak, traced at *m/z* 16, for the 1:5 ¹³CH₃OH:CO mixed ice experiment. The C¹⁸O and ¹³C¹⁸O isotopes are shown as well at *m/z* 30 and 31, respectively. At the CO desorption peak no increase of *m/z* 33 is seen. An increase in signal of *m/z* 32 is seen, but at a ratio of *m/z* (32/33) ≈ 10, much larger than the same fragment ratio of ~1.3 in the ¹³CH₃OH fragmentation pattern (see Table 4.2). Therefore, it is unlikely that ¹³CH₃OH is co-desorbing. *m/z* 32 is likely tracing small quantities of O₂ contamination. Using the formalism described in Sect. 4.2.1, an upper limit co-desorption rate can be determined from the CO peak and ¹³CH₃OH *m/z* 33 baseline; the inferred limit in this specific experiment is R_{methanol} ≤ 7.3 × 10⁻⁷ CH₃OH CO⁻¹.

In none of the experiments, including the layered ones, we found *m/z* 33 desorbing simultaneously with CO. This leads to a series of upper limit co-desorption rates listed in Table 4.3. The above mentioned upper limit is the most constraining, but generally the upper limits are found to be of the order of a few × 10⁻⁶.

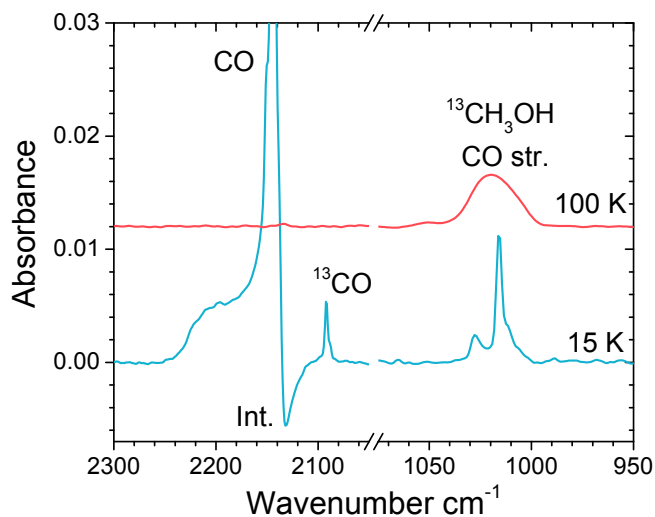


Figure 4.1: Representative IR spectrum taken after deposition at 15 K (blue) of the 1:24 $^{13}\text{CH}_3\text{OH}:\text{CO}$ mixture and during the TPD at 100 K (red), showing the main IR features of CO and $^{13}\text{CH}_3\text{OH}$. For the methanol CO stretch mode, the ^{13}CO and CO peak (cut-off due to its high peak intensity) are visible. Between the two CO peaks an artefact, labelled int., is visible caused by the high intensity of the CO peak.

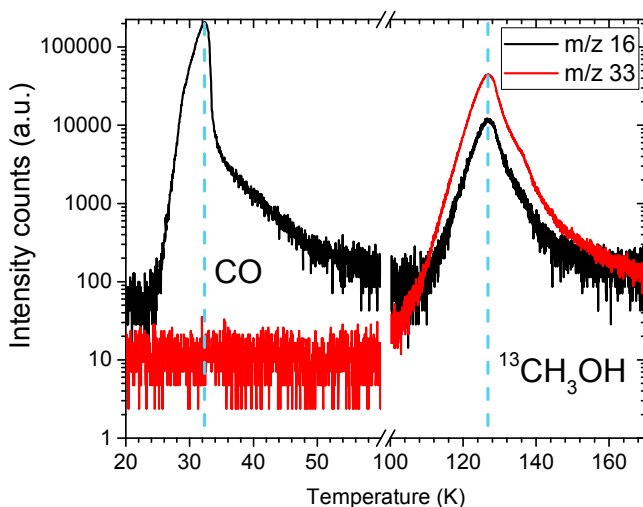


Figure 4.2: Desorption profile of the 1:24 $^{13}\text{CH}_3\text{OH}:\text{CO}$ mixture, heated at 1 K min^{-1} . CO is traced by m/z 16 (black) and desorbs just above 30 K, while ^{13}C -methanol is traced by m/z 33 (red) and desorbs around 130 K. The presence of m/z 16 at the methanol desorption peak is due to the $^{13}\text{CH}_3$ (= 16 amu) fragment.

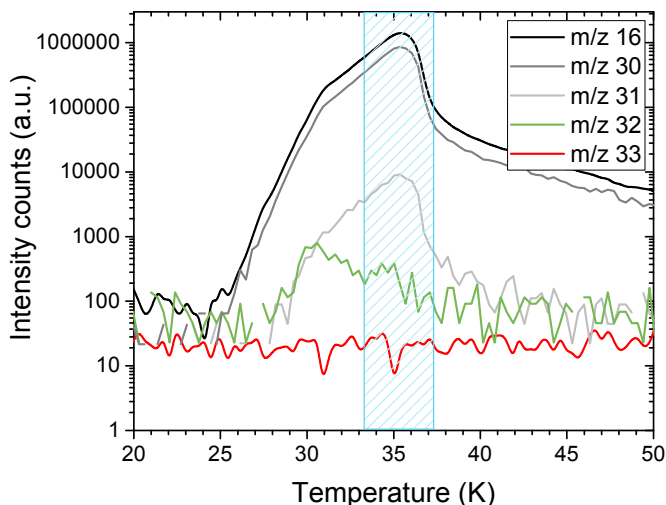


Figure 4.3: Close-up of the CO desorption peak (shaded blue) for the 1:5 $^{13}\text{CH}_3\text{OH}:\text{CO}$ mixed ice. m/z 16 (black) traces CO, while m/z 30 (dark grey) and 31 (light grey) trace C^{18}O and $^{13}\text{C}^{18}\text{O}$, respectively. The signal in m/z 32 (green) is caused by minor traces of $^{16}\text{O}_2$. m/z 33 (red) is associated with $^{13}\text{CH}_3\text{OH}$. Note the logarithmic scale.

To test whether other low volatility molecules can induce co-desorption of methanol, a TPD experiment was run with a $^{13}\text{CH}_3\text{OH}:\text{CH}_4$ mixture. Methane has a comparable desorption temperature to CO of roughly 40 K (Collings et al. 2004). Figure 4.4 shows a close-up of the methane desorption peak around 41 K, traced by m/z 13. The methanol, traced by m/z 33, is again not co-desorbing. In a similar way as described before, for this experiment an upper limit $R_{\text{methanol}} \leq 3.2 \times 10^{-5}$ is determined.

The fact that methanol does not co-desorb with either molecule sets an upper limit on low temperature methanol:CO or CH_4 co-desorption. Also, the fact that most of these experiments make use of a heating rate of 10 K min^{-1} should be considered as extra constraining. At lower heating ramps the volatile molecules have more time to diffuse out of the ice, whereas (monomeric) methanol is able to form clusters and remain on the surface. If there is any interaction between CO- CH_3OH when CO desorbs to the gas-phase, it must be weak, resulting in low quantities of desorbing methanol that are below our detection limit.

The weak interaction between CO and methanol is also seen in small quantities (a few ML) of CO trapped in methanol ice after CO desorption. Depending on the amount of methanol that was used in a specific experiment, CO signals are found in IR spectra of the ice to temperatures as high as 90 K. However, the outgassing of CO does not release methanol with it. Perhaps the hydrogen bonding network that methanol forms with itself is too strong to be broken by the desorption of low volatility molecules. For the case of monomeric methanol it is possible that time scales, even at a heating rate of 10 K min^{-1} , are sufficiently long for methanol to form hydrogen bonds and not to co-desorb.

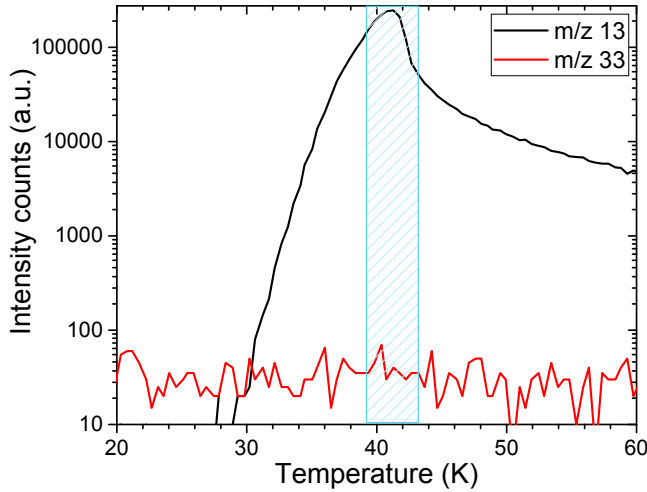


Figure 4.4: Close-up of the CH_4 desorption peak (shaded blue) for the 1:8 $^{13}\text{CH}_3\text{OH}:\text{CH}_4$ mixed ice. m/z 13 (black) traces methane, while m/z 33 (red) is associated with $^{13}\text{CH}_3\text{OH}$. Note the logarithmic scale.

4.3. Modelling

4.3.1. Astrochemical model description

The upper limits derived from the CO co-desorption experiments for $\text{CH}_3\text{OH}:\text{CO}$ ice mixtures are implemented in an astrochemical model. Our aims are to explore whether this process, although found to be inefficient in the laboratory, is able to release a small amount methanol into the gas-phase under astrophysical conditions.

At the low temperatures found in dark clouds (~ 10 K), gas-phase methanol is routinely detected with an abundance $\sim 10^{-10} - 10^{-8}$ relative to molecular hydrogen (e.g., Bacmann & Faure 2016). Cold methanol has also been detected towards so-called photon-dominated regions (PDRs) with an appreciable abundance ($\sim 10^{-10} - 10^{-9}$ with respect to H_2 (Guzmán et al. 2013; Cuadrado et al. 2017). The presence of gas-phase methanol in a PDR appeared to support the theory that intact methanol could be released via the process of photodesorption (Öberg et al. 2009a; Guzmán et al. 2014). As discussed here, this is now contradicted by recent laboratory work (Bertin et al. 2016; Cruz-Diaz et al. 2016).

The recent detection of cold gas-phase methanol in a protoplanetary disk provides new impetus to consider alternative desorption mechanisms (Walsh et al. 2016). Modelling of the CH_3OH gas-phase line profile suggests that the methanol resides in a ring with the emission peaking at ≈ 30 au. This radius is within 10 au of the position of the CO snow line in this source (Qi et al. 2013; Schwarz et al. 2016; Öberg et al. 2017; Zhang et al. 2017; van 't Hoff et al. 2017,

subm.). The derived abundance is low, ranging from $\sim 10^{-12} - 10^{-11}$ relative to H_2 , depending on the assumed vertical location of the molecule. The detected methanol transitions have upper energy levels ranging from 22 to 38 K consistent with the gas-phase methanol arising in a relatively cold region of the disk. At this radius (≈ 30 au) these temperatures are only reached in TW Hya below $z/r \approx 0.1$, i.e., the disk midplane. The spatial coincidence of H_2CO and CH_3OH emission in TW Hya (Walsh et al. 2016; Öberg et al. 2017) supports the hypothesis of a CO-ice-mediated chemistry in the vicinity of the CO snow line (and snow surface) in protoplanetary disks. Hence, protoplanetary disks offer a good test case for the proposed co-desorption route to gas-phase methanol.

Here, we explore the relative efficiencies of the various non-thermal desorption mechanisms proposed for non-volatile molecules like methanol at low temperatures: photodesorption, reactive desorption, and the process discussed here; thermally induced co-desorption. The chemical model used includes gas-phase chemistry and gas-grain interactions (i.e., adsorption and desorption), as well as grain-surface chemistry. The base network has been used in numerous studies of protoplanetary disk evolution and formation (Walsh et al. 2014, 2015; Drozdovskaya et al. 2016, and references therein for full details). The network used here has been updated to account for new grain-surface formation pathways to glycolaldehyde and ethylene glycol (Fedoseev et al. 2015a; Chuang et al. 2016). The photodesorption pathways for methanol fragmentation and desorption upon UV irradiation are included (Bertin et al. 2016). In addition, binding (desorption) energies of all ice species in the network have been reviewed and updated according to the literature compilation presented in Cuppen et al. (2017). However, in order to better explore the effects of the different non-thermal desorption mechanisms and simplify the grain-surface chemistry, we do not include ice photodissociation throughout the bulk ice mantle except for the case of fragmentation upon photodesorption which is restricted to the top two monolayers (see e.g., Walsh et al. 2014, for details). We allow quantum tunnelling for surface reactions involving atomic and molecular hydrogen (assuming a barrier width of 1Å), and allow efficient diffusion of surface species at low temperature ($E_{\text{diff}}/E_{\text{des}}=0.3$). However, we do not consider reaction-diffusion competition; hence, the surface reaction rates are dictated by the rates of thermal and quantum hopping and the barrier height for reaction. We also only allow surface chemistry to happen in the top two monolayers of the ice mantle.

We model the chemical evolution in time across vertical slices of a protoplanetary disk using a physical model representative of the disk around TW Hya (from Kama et al. 2016). The initial abundances of primary C-, O-, and N-containing volatiles are the same as the ‘molecular’ set used by Eistrup et al. (2016) which are representative of ice abundances in the ISM (Öberg et al. 2011; Boogert et al. 2015). However, we use a depleted value for sulphur ($\text{S}/\text{H} = 8.0 \times 10^{-8}$), initially in the form of H_2S ice, because Eistrup et al. (2016, 2017) find that a high abundance of elemental sulphur ($\text{S}/\text{H} \sim 10^{-5}$) can influence the oxygen chemistry in the ice mantle. We also include additional elements (with initial abundances from McElroy et al. 2013) which are important for the ionisation balance in the disk atmosphere: Si, Fe, Na, and Mg. The chemistry is then evolved at each grid point for $\approx 10^7$ yr to allow extraction of abundances as a function of time up to the estimated age of TW Hya (~ 10 Myr).

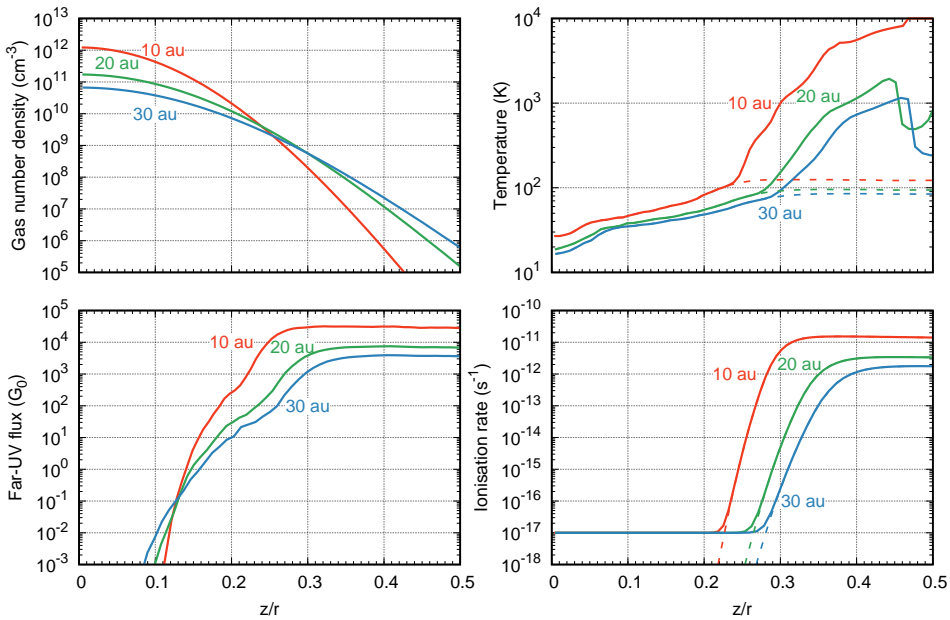


Figure 4.5: Physical structure of the TW Hya disk slices at 10 au (red lines), 20 au (green lines) and 30 au (blue lines) as a function of disk height, z , scaled by the radius, r . From the top-left panel and moving clockwise: gas number density (cm^{-3}), gas (solid lines) and dust (dashed lines) temperature (K), ionisation rate (s^{-1}) due to X-rays and cosmic rays (solid lines) and x-rays only (dashed lines), and far-UV flux (in units of G_0 , where $G_0 = 1.3 \times 10^{-3} \text{ erg cm}^{-2} \text{ s}^{-1}$ is the average interstellar radiation field).

4.3.2. Astrochemical model results

Figure 4.5 shows the physical structure of three vertical slices in the disk at 10, 20, and 30 au, chosen to probe the region in the vicinity of the CO snowline in TW Hya. The gas density ranges from $\sim 10^{11} - 10^{12} \text{ cm}^{-3}$ in the disk midplane ($z/r = 0$) to $\sim 10^6 - 10^7 \text{ cm}^{-3}$ in the disk atmosphere. The gas temperature also spans several orders of magnitude across the vertical extent of the disk, from $\approx 20 - 30 \text{ K}$ in the midplane to $\gtrsim 1000 \text{ K}$ in the upper surface layers of the disk. Because of the diffuse nature of the gas which decreases the efficiency of gas cooling via gas-grain collisions, the gas and dust temperatures decouple such that the dust temperature remains $\lesssim 100 \text{ K}$ at 10 and 20 au, but the gas temperature is very high (see e.g., Bruderer et al. 2012; Kama et al. 2016). As the primary source of heating, the far-UV flux closely follows the gas temperature: the disk midplane is significantly shielded from the stellar radiation. At all three radii considered here, the UV flux is less than the average interstellar radiation field ($G_0 = 1.0$) below $z/r \approx 0.15$. In the disk surface layers, due to the proximity to the central star, the far-UV flux reaches values \gtrsim a few times $10^3 \times G_0$.

Figure 4.6 shows the fractional abundance of CH_3OH gas, and Fig. 4.7 shows the ice as a function of z/r for the explored non-thermal desorption scenarios at 10 (left), 20 (middle), and 30 (right) au. In all plots, the progressively darker colours represent increasing time steps from 0.5, 1.0, 5.0, and 10.0 Myr. The top

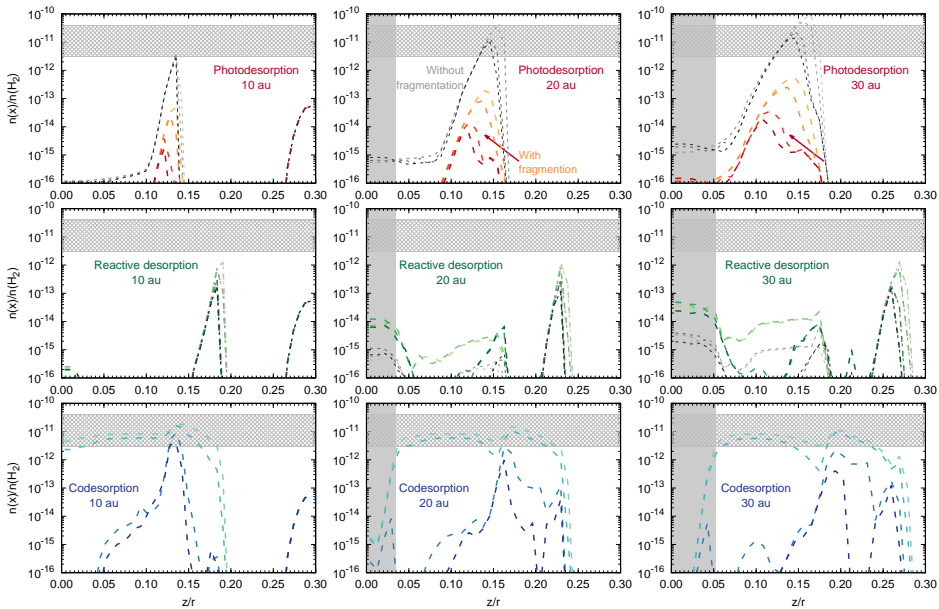


Figure 4.6: Fractional abundance of methanol gas as a function of z/r for radii of 10 (left), 20 (middle), and 30 (right) au. Results are shown for three different non-thermal desorption mechanism: photodesorption only (top), reactive desorption only (middle), and codesorption with CO only (bottom). The colour gradient from light to dark represents four different time steps: 0.5, 1.0, 5.0, and 10 Myr. The grey lines in the top and middle plots represent the “fiducial” model as described in the text (i.e., photodesorption of intact methanol with a yield of $\sim 10^{-3}$ and a reactive desorption probability of 1%). The vertical grey lines in the plots at 20 and 30 au mark the CO snow surface (see Figure 4.8).

panels show the results from a model with photodesorption only (PD model). The grey lines show the results assuming that CH_3OH does not fragment upon photodesorption (i.e., assuming the yield determined by Öberg et al. 2009a), whereas the orange/red lines show the results for a model with fragmentation upon photodesorption. The middle row shows results from a model with reactive desorption only (RD model) at an efficiency of 1% (grey lines) and at an efficiency of 10% (green lines). This range is chosen to explore that constrained by recent analyses of reactive desorption efficiencies for a range of reactions (e.g., Minissale et al. 2016). The bottom panels show the results when including only the proposed co-desorption mechanism (CD model) assuming the upper limit co-desorption yield of 10^{-6} CH_3OH molecules per CO molecule indicated by the experiments. That is, only one CH_3OH molecule co-desorbs intact for every 10^6 CO molecules which are *thermally* desorbed from the ice mantle.

There are several general observations. First, in the models with photodesorption only (PD model), the methanol snow surface lies deeper in the disk than for the model with reactive desorption only (RD model; $z/r < 0.2$ versus $z/r \gtrsim 0.2$). The position of the snow surface for the co-desorption only results (CD model) is intermediate between the PD and RD results. This illustrates the importance of photodesorption in setting the location of the snow

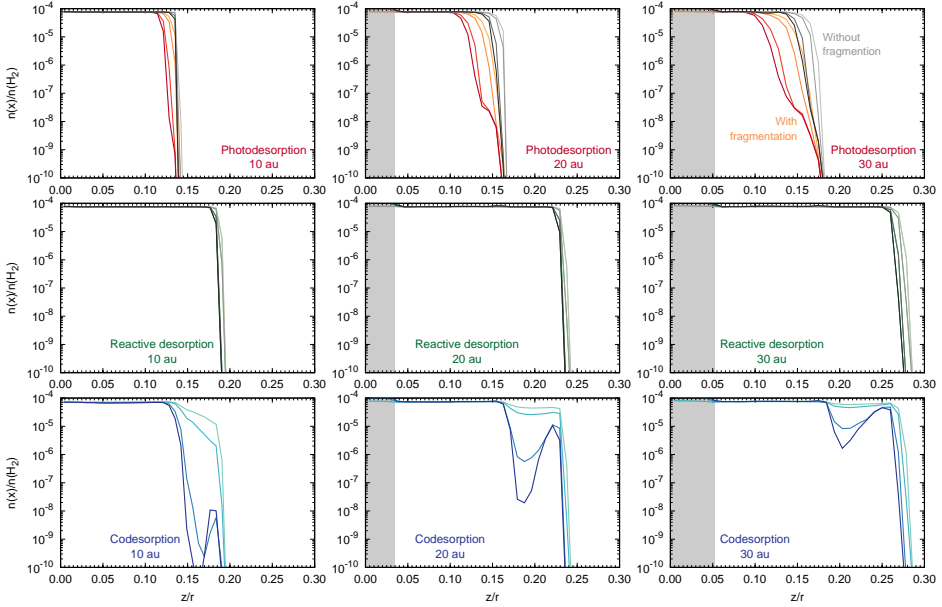


Figure 4.7: As Fig. 4.6, but for methanol ice.

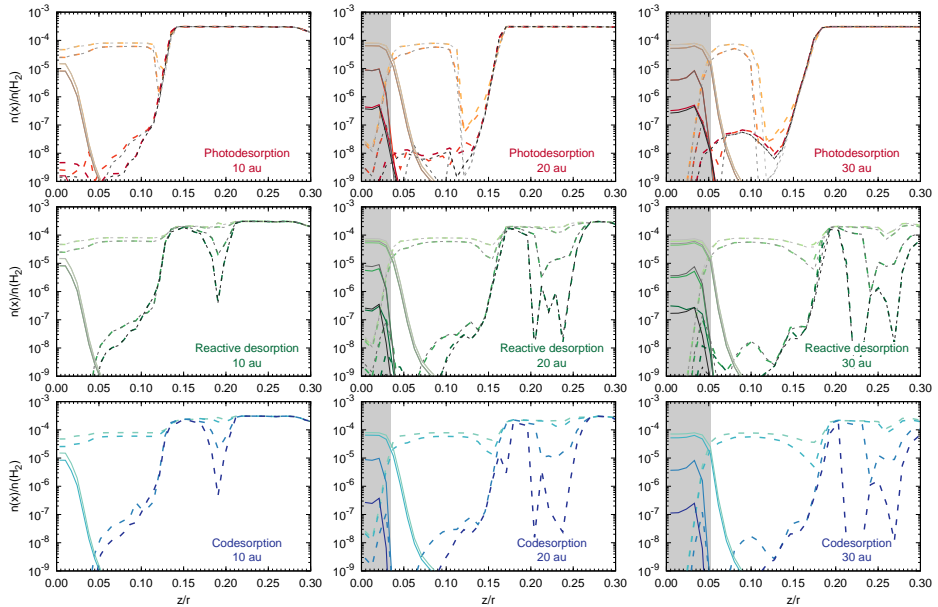


Figure 4.8: As Fig. 4.6, but for CO gas and ice.

surface in the disk atmosphere for non-volatile ice species such as CH_3OH and H_2O even at radii as close in as 10 – 30 au. For the PD model, the position of the snow surface also becomes deeper with time. Including the fragmentation of methanol upon photodesorption has two effects: (i) the peak abundance of gas-phase methanol has decreased by 2 – 3 orders of magnitude in line with the magnitude of the decrease in the CH_3OH photodesorption yield, and (ii) the shift in the location of methanol snow surface is larger ($\times 2$ or more). This latter effect is due to the necessity for methanol ice to reform from its fragments upon photodesorption. In the original treatment, photodesorption mainly competes with re-adsorption of intact methanol.

Turning now to the gas-phase methanol abundance and distribution, the peak in the absolute abundance coincides with the position of the methanol snow surface for both the PD and RD models. Further, in both of these models the peak abundance lies always below 10^{-12} with respect to molecular hydrogen. For the RD model, an optimistic reactive desorption probability of 10% is necessary to reach these values. The results for 1% lie an order of magnitude below this. In the model with the original (and incorrect) treatment for methanol photodesorption, the abundance does reach that derived from the ALMA observations. Hence, these results show that, with a realistic treatment of methanol ice photodesorption and an optimistic reactive desorption probability, neither of these processes alone can explain the observed abundance in TW Hya.

On the other hand, the co-desorption results using the laboratory upper limit reveal an interesting distribution and abundance for gas-phase methanol. As expected from the hypothesis of a CO-mediated ice chemistry, the gas-phase methanol peaks between the CO and CH_3OH snow surfaces covering a larger vertical extent than the other models. At early times (up to 1 Myr) the peak fractional abundance is $\approx 10^{-11}$ with respect to H_2 and remains fairly constant between the two snow surfaces. However, the distribution does change with time, leading to a distribution which again peaks at around the location of the CH_3OH snow surface. The reason for this change in gas-phase methanol distribution over time is related to the concurrent chemical processing and loss of CO ice (and gas). Figure 4.8 shows the results for CO gas and ice for the same models as shown in Figs. 4.6 and 4.7 for methanol. Despite this model not including the radiation processing of the bulk ice mantle except for fragmentation upon photodesorption, (i.e., only gas-phase processing is included), beyond 1 Myr, CO ice and gas are significantly depleted within and around the location of the methanol snow surface. This chemical processing is one explanation for the low disk masses derived from CO observations as the canonical gas-phase ratio $\text{CO}/\text{H}_2 \sim 10^{-4}$ no longer holds (e.g., Walsh et al. 2015; Reboussin et al. 2015; Yu et al. 2016; Eistrup et al. 2017). Hence, co-desorption appears to only work up to 1 Myr which is the timescale within which CO is not significantly depleted. This timescale conflicts with (i) the estimated age of TW Hya (up to 10 Myr), and (ii) observational evidence for CO depletion in TW Hya (e.g., Favre et al. 2015; Schwarz et al. 2016; Zhang et al. 2017)

These model runs were performed assuming the canonical cosmic-ray ionisation rate of 10^{-17} s^{-1} : this is the main source of processing in the disk midplane and is what drives the chemical conversion of CO, whether in the gas, or in the ice. Figure 4.5 shows how the X-ray ionisation level drops below

the canonical cosmic-ray ionisation rate below $z/r \lesssim 0.2 - 0.3$, depending on radius. There has been recent arguments that T Tauri stars have sufficiently strong stellar winds to deflect galactic cosmic rays (evidenced by modelling of the cation abundance and emission from TW Hya; Cleeves et al. 2015). Hence, if X-rays and short-lived radionuclides are the only sources of ionisation in the TW Hya disk midplane, this may (i) increase the longevity of the co-desorption effect, and (ii) delay the onset of CO depletion to better match the magnitude seen in TW Hya (around a factor of 100).

4.4. Conclusions

This work presents an experimental and modelling investigation of the low temperature methanol co-desorption mechanism. Laboratory experiments put upper limits on the thermal methanol co-desorption with CO. Modelling based on upper limits of these experiments shows however that low temperature methanol co-desorption can still be a significant mechanism, even at this low limit. The main conclusions of this work are summarized as follows:

1. Methanol is not seen co-desorbing with CO at a laboratory temperature of 30 K giving a general upper limit of $R_{\text{methanol}} < \text{a few } \times 10^{-6}$, with the lowest limit found at $R_{\text{methanol}} < 7.3 \times 10^{-7} \text{ CH}_3\text{OH CO}^{-1}$.
2. Co-desorption of methanol with methane is not seen down to a level of $R_{\text{methanol}} < 3.2 \times 10^{-5} \text{ CH}_3\text{OH CH}_4^{-1}$
3. Results presented in this chapter suggest that the interaction between desorbing CO/CH₄ and solid methanol is weak and can not (easily) overcome the hydrogen bonded network of methanol.
4. Astrochemical models employing a co-desorption upper limit of $10^{-6} \text{ CH}_3\text{OH CO}^{-1}$ are able to reproduce the observed abundance and distribution of gas-phase methanol between 10-30 au in the TW Hya protoplanetary disk. The models employing a more realistic treatment of methanol photodesorption only or an optimistic treatment of reactive desorption only, do not reproduce the observed abundance. It should be noted, though, that the actual thermal co-desorption may be less efficient, as the experiments discussed here only provide upper limits.
5. The gas-phase methanol peaks between the CO and CH₃OH snow surfaces; yet, a moderate abundance ($\sim 10^{-11}$) is retained only up to ~ 1 Myr, beyond which chemical processing of CO impedes the co-desorption effect.
6. The chemical processing of CO in the disk midplane is driven primarily by cosmic rays: it remains to be tested whether processing by X-rays and/or short-lived radionuclides can help the co-desorption effect persist to the estimated age of TW Hya (~ 10 Myr).
7. Although the models suggest that thermal co-desorption could contribute to the production of gas-phase methanol at and around the CO snowline in protoplanetary disks, the lack of a confirmed signal in the laboratory

experiments means that the impact of the actual thermal co-desorption may be less, as the experiment only provides an upper limit. As a consequence, other non-thermal desorption mechanisms cannot be ruled out at this time.

Acknowledgement

Thanks go out to Ewine van Dishoeck for useful input and discussions on this work.

Astrochemistry in Leiden is supported by the European Union A-ERC grant 291141 CHEMPLAN, by the Netherlands Research School for Astronomy (NOVA) and by a Royal Netherlands Academy of Arts and Sciences (KNAW) professor prize. CryoPAD2 was realized with NOVA and NWO (Netherlands Organisation for Scientific Research) grants. C. Walsh acknowledges financial support from the Netherlands Organisation for Scientific Research (NWO, programme 639.041.335) and start-up funds from the University of Leeds.



V-UV



5

IR spectra of frozen complex organic molecules

J. Terwisscha van Scheltinga, N.F.W. Ligterink,
A.C.A. Boogert, E.F. van Dishoeck & H. Linnartz

Terwisscha van Scheltinga et al. 2017, *Infrared spectra of complex organic molecules in astronomically relevant ice matrices I: Acetaldehyde, ethanol and dimethyl ether*, subm. to A&A

5.1. Introduction

Water was the first molecule to be detected in the solid state in the interstellar medium (Gillett & Forrest 1973). Since then more than ten other molecules have been identified in icy form (i.e., CO, CO₂, CH₄, NH₃ and CH₃OH) and it has become clear that icy dust grains play a key role in the formation of both these small molecules and more complex organic molecules (COMs), like glycolaldehyde (HOCH₂CHO) and ethylene glycol (HOCH₂CH₂OH). The combined outcome of astronomical observations, specifically space based missions such as the *Infrared Space Observatory* (ISO) and *Spitzer Space Telescope* (Kessler et al. 1996; Werner et al. 2004), laboratory and astrochemical modelling studies have resulted in a detailed picture of the composition and structure of ice mantles on interstellar dust grains and the chemical processes taking place (see reviews by Gibb et al. 2000a; Herbst & van Dishoeck 2009; Öberg et al. 2011; Caselli & Ceccarelli 2012; Tielens 2013; Boogert et al. 2015; Linnartz et al. 2015; berg 2016). It is generally accepted that interstellar ices form on the surface of dust grains in cold dark clouds through accretion in two distinct layers, a polar H₂O-rich and an apolar CO-rich layer. Water, together with NH₃, CO₂ and CH₄, forms through atom addition reactions in lower density environments (Hiraoka et al. 1995; Miyauchi et al. 2008; Oba et al. 2009; Dulieu et al. 2010; Hidaka et al. 2011; Linnartz et al. 2011; Oba et al. 2012; Lamberts et al. 2013, 2014; Fedoseev et al. 2015b). At later stages, when densities increase and temperatures decrease along with the ongoing cloud collapse, CO freeze-out from the gas-phase occurs, forming a CO coating on top of the water rich layer (Tielens et al. 1991; Pontoppidan 2006). Subsequent hydrogenation processes transform CO to H₂CO and H₂CO to CH₃OH (Watanabe & Kouchi 2002; Fuchs et al. 2009), resulting in CO ice intimately mixed with methanol (Cuppen et al. 2011; Penteado et al. 2015). Radical recombination processes in different starting mixtures, triggered by energetic (i.e. UV photons or cosmic rays) or non-energetic (i.e. atom additions) were shown to provide pathways towards the formation of more complex molecules (see reviews of Linnartz et al. 2015; berg 2016).

The molecules H₂O, CO, CO₂, CH₄, NH₃ and CH₃OH make up the bulk of interstellar ice (Ehrenfreund & Charnley 2000; Öberg et al. 2011), but less abundant species have been observed as well. These include species such as OCS and OCN⁻ (Palumbo et al. 1995; van Broekhuizen et al. 2004). A number of COMs like formic acid (HCOOH), acetaldehyde (CH₃CHO) and ethanol (CH₃CH₂OH), have been tentatively detected based on spectroscopic features at 7.2 and 7.4 μm (Schutte et al. 1999; Öberg et al. 2011). Several other spectroscopic features, such as the 6.0 and 6.8 μm bands, remain only partly identified (Schutte et al. 1996; Boudin et al. 1998; Gibb & Whittet 2002; Boogert et al. 2008). Limited astronomical detection sensitivity combined with a lack of high resolution laboratory data have thus far prohibited secure solid state identifications of COMs other than methanol, but their presence in interstellar ices is generally accepted and also further supported by the recent detection of a number of COMs on comet 67P/Churyumov-Gerasimenko and in its coma (Goesmann et al. 2015; Altwegg et al. 2017).

With the upcoming launch of the *James Webb Space Telescope* (JWST) in 2018, new instruments such as MIRI (Mid InfraRed Instrument, Wright et al. 2015) and

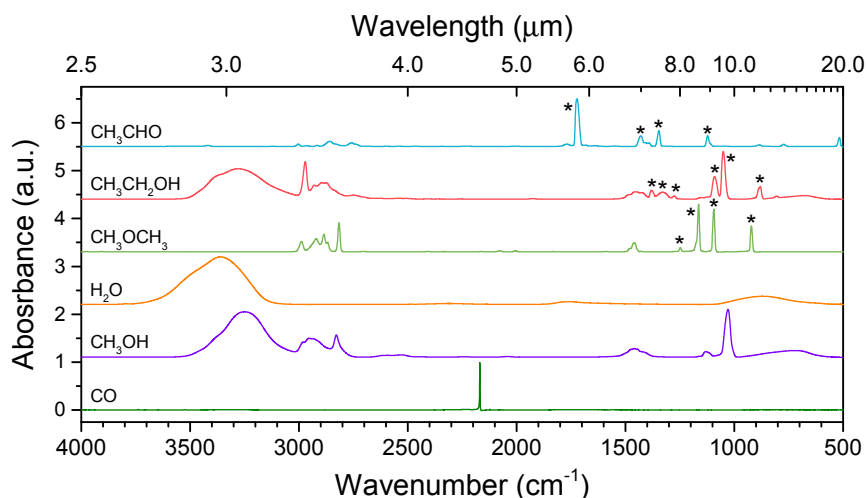
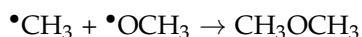


Figure 5.1: Spectra of pure acetaldehyde (blue), ethanol (red), dimethyl ether (green), water (orange) methanol (purple) and CO (dark green) normalised to one, in the range of 2.5 to 20.0 μm . The bands investigated in this work are indicated with an asterisk (*).

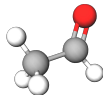
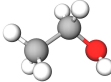
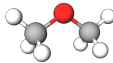
NIRSpec (Near InfraRed Spectrograph) will become available to record telluric free spectra of interstellar ices at higher spectral and spatial resolution and with higher sensitivity than before. This opens up new possibilities to search for and study the level of molecular complexity in interstellar ices. To aid in the search for larger molecules in the solid state, high resolution IR laboratory spectra are required. The ice matrix environment and its temperature have to be taken into account, since these influence the spectral appearance of vibrational bands.

In this work we present the infrared spectra of acetaldehyde, ethanol and dimethyl ether, respectively, CH_3CHO , $\text{CH}_3\text{CH}_2\text{OH}$, and CH_3OCH_3 . The choice for these three species is motivated by previous tentative identifications (Boudin et al. 1998; Schutte et al. 1999; Öberg et al. 2011), their astronomical gas-phase identification and high abundance (e.g. Turner 1991; Gibb et al. 2000a; Cazaux et al. 2003; Bisschop et al. 2007b; Taquet et al. 2015; Müller et al. 2016), and their common formation scheme upon UV irradiation of methanol ice (Öberg et al. 2009a). Formation of these molecules is seen in energetic processing experiments of methanol ice (Gerakines et al. 1996; Bennett et al. 2007; Öberg et al. 2009a; Boamah et al. 2014), and start with cleavage of the CH_3OH bonds. This results in a reservoir of radicals that can be used for their formation:



Formation of dimethyl ether and ethanol has also been studied by radical

Table 5.1: Selected bands of acetaldehyde, ethanol and dimethyl ether

Species	Formula	Mode	Peak position ^a		
			cm ⁻¹	μm	
	Acetaldehyde	CH ₃ CHO	C-C stretch	1122.3	8.909
			CH ₃ s-deform.	1346.2	7.427
			CH ₃ d-deform.	1429.4	6.995
			C=O stretch	1723.0	5.803
	Ethanol	CH ₃ CH ₂ OH	C-C stretch	879.8	11.36
			C-O stretch	1051.0	9.514
			CH ₃ rocking	1090.5	9.170
			CH ₂ torsion	1275.2	7.842
			OH deform.	1330.2	7.518
			CH ₃ s-deform.	1381.3	7.240
	Dimethyl ether	CH ₃ OCH ₃	C-O s-stretch	921.3	10.85
			C-O a-stretch	1093.9	9.141
			CH ₃ rocking	1163.8	8.592
			CH ₃ rocking	1248.2	8.011

Notes. ^aPeak position of the pure molecule at 15 K.

recombination reactions starting from CH₄:H₂O mixtures (Bergantini et al. 2017). Besides energetic radical recombination reactions, other formation pathways and links between the three molecules exist as well. For example, acetaldehyde has been proposed as a solid state precursor of ethanol. A hydrogen atom addition experiment showed that acetaldehyde can at least partially ($\geq 20\%$) be transformed into ethanol (Bisschop et al. 2007a). Acetaldehyde itself has been proposed to form as a spin-off in the well studied CO+H \rightarrow HCO \rightarrow H₂CO \rightarrow H₃CO \rightarrow CH₃OH chain (Charnley 2004). HCO may directly interact with a C-atom, to form HCCO that upon hydrogenation yields CH₃CHO (Charnley & Rodgers 2005).

This work presents a detailed study of the IR spectral characteristics of CH₃CHO, CH₃CH₂OH, and CH₃OCH₃ in pure form and mixed in the interstellar relevant ice matrices H₂O, CO, CH₃OH and CO:CH₃OH. Section 5.2 contains the experimental details and measurement protocols. The results of the measurements are presented and discussed in section 5.3. In section 5.4 the astronomical relevance of the new data is illustrated. The conclusions are summarized in Sect. 5.5. A complete overview with all data obtained in this study is available from the Appendices.

5.2. Experimental

5.2.1. Set-up

The ice spectra are recorded in a high-vacuum (HV) set-up which is described in detail by Bossa et al. (2015). A central stainless steel chamber is evacuated by a 300 l s^{-1} turbomolecular pump, backed by a double stage rotary vane pump ($8 \text{ m}^3 \text{ hr}^{-1}$). This allows a base pressure of $\sim 10^{-7}$ mbar at room temperature. The pressure is monitored by an Agilent FRG-720 full range gauge. Ices are grown on an infrared transmissive ZnSe window which is cryogenically cooled to a lowest temperature of 12 K by a closed cycle helium cryostat. The temperature of the window is monitored by a LakeShore 330 temperature controller, which regulates a feedback loop between a resistive heating wire and a silicon diode temperature sensor. An absolute temperature accuracy of ± 2 K and a relative accuracy of ± 1 K is acquired with this diode. The IR beam of a Fourier Transform InfraRed Spectrometer (FTIRS, Varian 670-IR) is aligned through the window in order to obtain IR spectra of the samples. The spectrometer covers a range of 4000 to 500 cm^{-1} ($2.5\text{--}20 \text{ }\mu\text{m}$) at spectral resolutions as high as 0.1 cm^{-1} . Pure or premixed gases are background deposited onto the sample via an inlet valve. Samples are externally prepared in a gas mixing system. The gas mixing line is turbomolecularly pumped to pressures $\leq 1 \times 10^{-4}$ mbar. Two gas independent gauges, covering different pressure ranges ensure that accurate mixing ratios are obtained. The liquids and gases used in these experiments are: acetaldehyde (Sigma-Aldrich, 99.5%), ethanol (Biosolve, 99.9%), dimethyl ether (Sigma-Aldrich, 99.9%), water (Milli-Q, Type I), carbon monoxide (Linde gas, 99.997%), and methanol (Sigma-Aldrich, 99.9%). Liquid samples are purified with freeze-pump-thaw cycles before use.

5.2.2. Measurement protocol

A 2L glass bulb is filled on the gas mixing system with a pure or mixed gas sample to a standard pressure of 20 mbar. This is a large enough gas reservoir to prevent a decreasing inlet pressure gradient during deposition. Bi-mixed gases are prepared in a 1:20 ratio and tri-mixed gases in a 1:20:20 ratio, where the smallest fraction is the COM under investigation. These dilution factors ensure that the COM mainly interacts with the surrounding matrix, resulting in matrix shifted IR vibrational bands. Ices are grown at 15 K to a thickness of $\sim 4500 \text{ ML}$ ($1 \text{ ML} = 1 \times 10^{15} \text{ molecules cm}^{-2}$) on the window. This thickness ensures that any influence of background contamination, mainly water depositing at a rate of less than 30 ML hr^{-1} , can be neglected. During deposition, IR spectra are recorded at 1 cm^{-1} resolution (0.5 cm^{-1} step size) and averaged over 61 scans (equals 2 minutes) to trace the ice growth and determine when the ice is $\sim 4500 \text{ ML}$ thick. From the integration of the IR band absorption, the column density of the species N_{species} is determined according to:

$$N_{\text{species}} = \ln(10) \frac{\int_{\text{band}} \tau d\nu}{A_{\text{band}}}, \quad (5.1)$$

where $\int_{\text{band}} \tau dv$ is the integrated absorbance of the band and A_{band} the band strength in cm molecule^{-1} . It is important to realize that strong absorbing bands may get saturated at high coverages, resulting in unreliable thickness measurements. In the experiments conducted, the CO band at 2135 cm^{-1} reaches saturation at high coverage, as do certain bands of pure acetaldehyde and dimethyl ether. For these species bands with a lower band strength can be used. An independent verification between the gas and ice mixture ratio is realized through solid state column density measurements using the IR spectra.

After deposition the sample is linearly heated at a rate of 25 K hr^{-1} , until it is fully desorbed from the window. The low temperature ramp ensures that the ice has sufficient time to undergo structural changes, particularly from the amorphous to the crystalline phase. During heating IR spectra are continuously recorded and averaged over 256 scans to trace spectral changes versus temperature.

5.2.3. Analysis protocol

Due to the very large amount of spectra that are recorded during the experiment, here only samples of representative IR spectra at temperatures where significant spectral changes occur are presented. These spectra are baseline subtracted and the peak position and band width at Full Width at Half Maximum (FWHM) are determined for selected spectral features. When the band of a COM is embedded in a spectral feature of a matrix molecule, also the matrix feature is subtracted when possible. In the case of peak splitting, the least intense peak is only taken into account when its peak position is clearly distinguishable. In a few cases splitted peaks rival in intensity and are heavily overlapping and it is not possible to fit a FWHM for the individual components. Here the FWHM of the combined peaks is determined. Peaks are selected for analysis mainly based on their intensity and potential as a molecule tracer, i.e., selecting wavelengths for which no strong overlap with known interstellar features exist. Identification of vibrational modes of the three species studied here is realized by comparison with available spectra from gas phase and solid state literature (Plyler 1952; Schneider & Bernstein 1956; Evans & Bernstein 1956; Taylor & Vidale 1956; Mikawa et al. 1971).

Optical effects like Longitudinal Optical - Transverse Optical (LO-TO) splitting and particle shape effects are not explicitly taken into account. Since spectra are recorded at normal incidence with unpolarized light, only the TO modes are recorded. However, certain combinations of polarized light and angles of incidence can result in the LO phonon mode showing up (Baratta et al. 2000; Palumbo et al. 2006). Also particle shape effects can shift transition bands with respect to recorded laboratory spectra (Baratta & Palumbo 1998). Such effects will affect only the spectra of more abundant species, like CO or CO_2 , and are not considered to be relevant for COMs.

5.3. Results and Discussion

In this section selected results of the acetaldehyde, ethanol and dimethyl ether experiments are presented. These are representative for the much larger

Table 5.2: Peak position and FWHM of the acetaldehyde CH₃ s-deformation mode at 15 K in various matrices.

Mixture	Temperature (K)	$\lambda_{\text{peak,-baseline}}$		$\lambda_{\text{peak,-matrix}}$		FWHM	
		(cm ⁻¹)	(μm)	(cm ⁻¹)	(μm)	(cm ⁻¹)	(μm)
CH ₃ CHO	15	1346.6	7.4264	–	–	13.5	0.0744*
CH ₃ CHO :H ₂ O		1349.9	7.4078	1349.9	7.4078	9.2	0.0502
CH ₃ CHO :CO		1349.4	7.4104	–	–	4.8	0.0262
CH ₃ CHO :CH ₃ OH		1347.5	7.4211	–	–	13.0	0.0714
CH ₃ CHO :CO:CH ₃ OH		1349.4	7.4105	–	–	12.6	0.0691
CH ₃ CHO	30	1346.1	7.4290	–	–	13.7	0.0754
CH ₃ CHO :H ₂ O		1349.9	7.4078	1349.9	7.4078	8.8	0.0481
CH ₃ CHO :CO		1349.9	7.4078	–	–	6.1	0.0337*
CH ₃ CHO :CH ₃ OH		1347.5	7.4211	–	–	12.5	0.0686
CH ₃ CHO :CO:CH ₃ OH		1349.0	7.4131	–	–	12.2	0.0671
CH ₃ CHO	70	1346.1	7.4290	–	–	13.2	0.0729
CH ₃ CHO :H ₂ O		1349.4	7.4105	1349.4	7.4105	7.7	0.0420
CH ₃ CHO :CO		–	–	–	–	–	–
CH ₃ CHO :CH ₃ OH		1348.0	7.4184	–	–	10.9	0.0600
CH ₃ CHO :CO:CH ₃ OH		1348.5	7.4158	–	–	10.8	0.0592

Notes. Excerpt from Table B.1 in AOP. *FWHM result of two or more blended peaks.

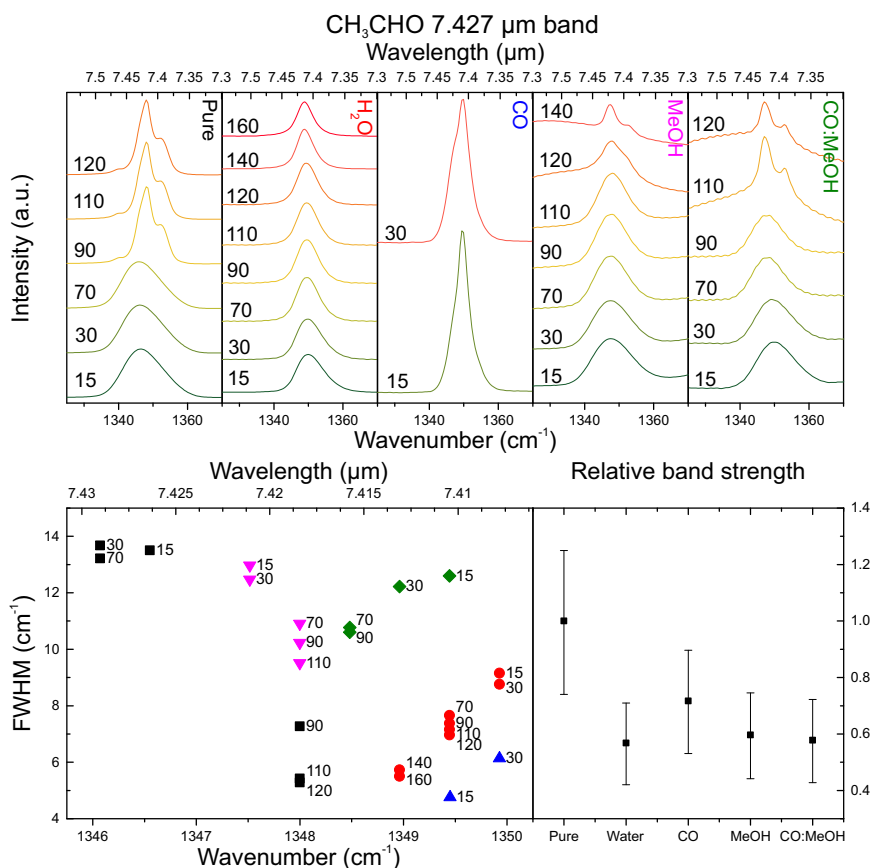


Figure 5.2: Top, from left to right the acetaldehyde 7.427 μm band pure (black) and in water (red), CO (blue), methanol (purple) and CO:CH₃OH (green) at various temperatures. Bottom left, peak position versus FWHM plot, using the same color coding. Bottom right, the relative band strength for the 7.427 μm band at 15 K in various matrices.

data set given in the Supplementary material. The extensive tables that contain information on peak positions and FWHM of the molecules investigated in this work can be found in the Appendix of the Original Publication, which is abbreviated to AOP throughout this chapter. All the baseline subtracted spectra used in this work are publicly available from the Leiden Database for Ice (<http://icedb.strw.leidenuniv.nl>). Figure 5.1 shows the IR spectra of pure acetaldehyde, ethanol and dimethyl ether ice at 15 K, with the bands that are fully analysed indicated with an asterisk (*) and spectra of pure water, CO and methanol ice. Figures of the spectra of COMs mixed in water, CO, methanol and CO:methanol at 15 K are shown in Appendix A in the original publication. In Table 5.1 these selected bands are listed together with their peak positions in pure ices at 15 K. Appendix B in the original publication presents the results of the analysis of the selected bands, listing peak positions, FWHMs and integrated absorbance ratios at various temperatures and ice matrices. A representative example of the tables listed in the Appendix is shown in Table 5.2 for the

acetaldehyde CH₃ s-deformation mode at 15, 30 and 70 K.

For easier interpretation the results have been visualised in a number of plots, see Figs. 5.2, 5.3 and 5.4 for examples. Each plot covers the data of one band. The top part shows spectroscopic changes of the band under thermal processing in pure and mixed ices. The bottom left part plots peak position versus FWHM, showing trends in the band. The bottom right part gives an indication how the band strengths change relative from each other in various matrices. Assuming that the ice thickness is roughly the same for each experiment and that the gas mixing ratio represents the ice mixing ratio, the mixed ices are corrected for their dilution factor. The remaining figures of other bands can be found in Appendix C in the original publication.

A few general observations can be made. Most peaks display peak narrowing under thermal processing, which is due the ice changing to a crystalline phase. Mixed ice in CO and CO:CH₃OH can be exceptions, due to the volatility of CO and its removal from the ice at relatively low temperatures. Above 30 K, the desorption temperature of CO, these ices are often seen to display peak broadening.

Peak splitting, especially at high temperature is another effect that is generally seen. This can be caused by two or more modes contributing to a single feature at low temperature and becoming visible as the peaks begin to narrow at higher temperatures. Alternatively, the matrix can play a role and a peak is split due to different interactions of a functional group with its surroundings. For example, an ice can segregate under thermal processing and have part of the COM still intimately mixed with the matrix molecule, while another part is forming COMs cluster. Segregation is an effect most clearly seen in the COMs:CO ice mixtures.

Integrated absorbance ratios are given for the bands under investigation in each ice mixture. These ratios can provide a tool to estimate the likelihood of observing other bands upon detection of a specific transition. They can also be used as conversion factors to determine band strengths from known band strengths. The bands are normalised on the band with highest integrated absorbance at 15 K, unless this band is suspected to be in saturation or when the data set is incomplete over the investigated temperature range.

5.3.1. Acetaldehyde

Acetaldehyde hosts four significant features in the 5.5 - 12.5 μm region (see Fig. 5.1). Some smaller features are also visible, such as the C-C stretching mode close to 11 μm , however, its intensity is very small compared to the other bands. Two characteristic vibrational modes of acetaldehyde at 6.995 and 8.909 μm , coincide with methanol CH₃ rocking and deformation modes and are likely obscured in interstellar spectra. A solid state identification of acetaldehyde based on these vibrational modes is unlikely. The C=O stretching mode is the most prominent band in this spectrum. However, its location at 5.8 μm coincides with the C=O stretching mode of many other molecules, such as formaldehyde (H₂CO), formic acid (HCOOH) or formamide (NH₂CHO), that are expected to be present in interstellar ice, making it likely that this band is blended. The fourth band is the CH₃ s-deformation mode around 7.427 μm , which is found to have no substantial overlap with abundant bulk interstellar ice components and therefore

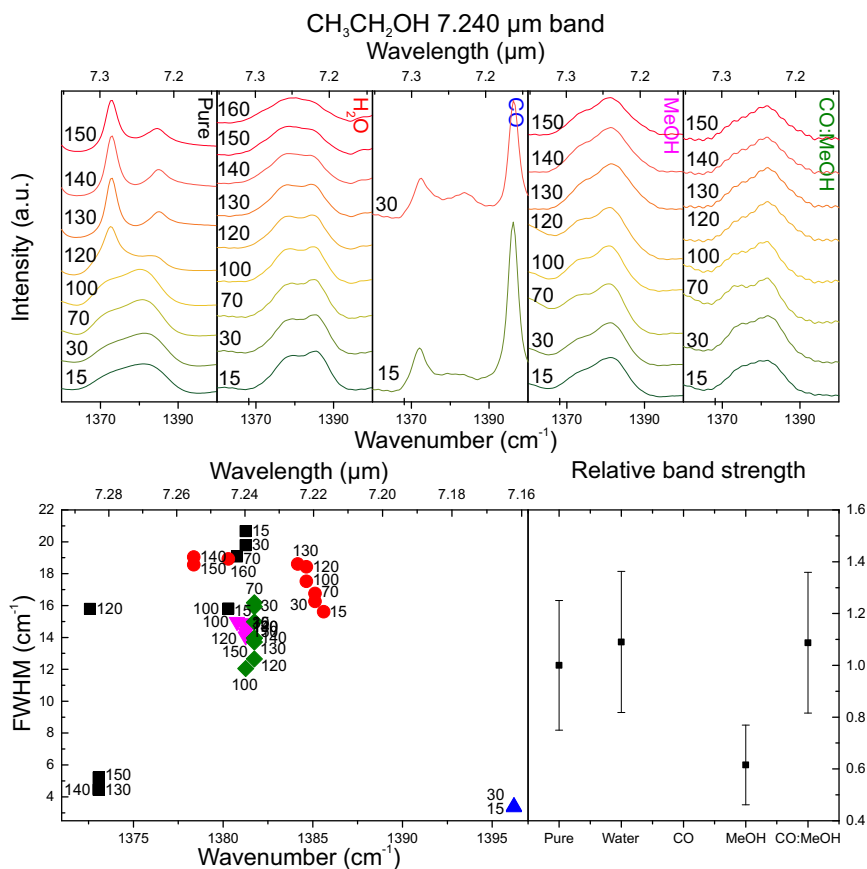


Figure 5.3: Top, from left to right the ethanol 7.842 μm band pure (black) and in water (red), CO (blue), methanol (purple) and CO:CH₃OH (green) at various temperatures. Bottom left, peak position versus FWHM plot, using the same color coding. Bottom right, the relative band strength for the 7.842 μm band at 15 K in various matrices.

is most suited for a successful solid state identification of this molecule.

Figure 5.2 shows the results of the analysed data of the CH₃ s-deformation band. Under thermal processing the band widths are generally seen to decrease, caused by crystallization in the ice. Peak positions shift as well, with clear blue shifting trends visible for the CO:CH₃OH and water mixtures. In the case of the CO:CH₃OH mixture this has likely to do with the loss of CO from the matrix, while for the water mixture the interaction between acetaldehyde and crystalline water is more likely the cause. In some cases, at high temperature CH₃CHO undergoes peak splitting, making identification through FWHM challenging. However, this can also be used as a tool to determine the ice temperature. The comparison of peak position makes it in general easy to distinguish between pure acetaldehyde, mixed in CO:CH₃OH and CH₃OH, mixed in CO and mixed in water. The 7.427 μm band shows a substantial decrease in band strength by about 40% when acetaldehyde is surrounded by matrix molecules.

The acetaldehyde C=O stretch band underlines the above findings, given it is

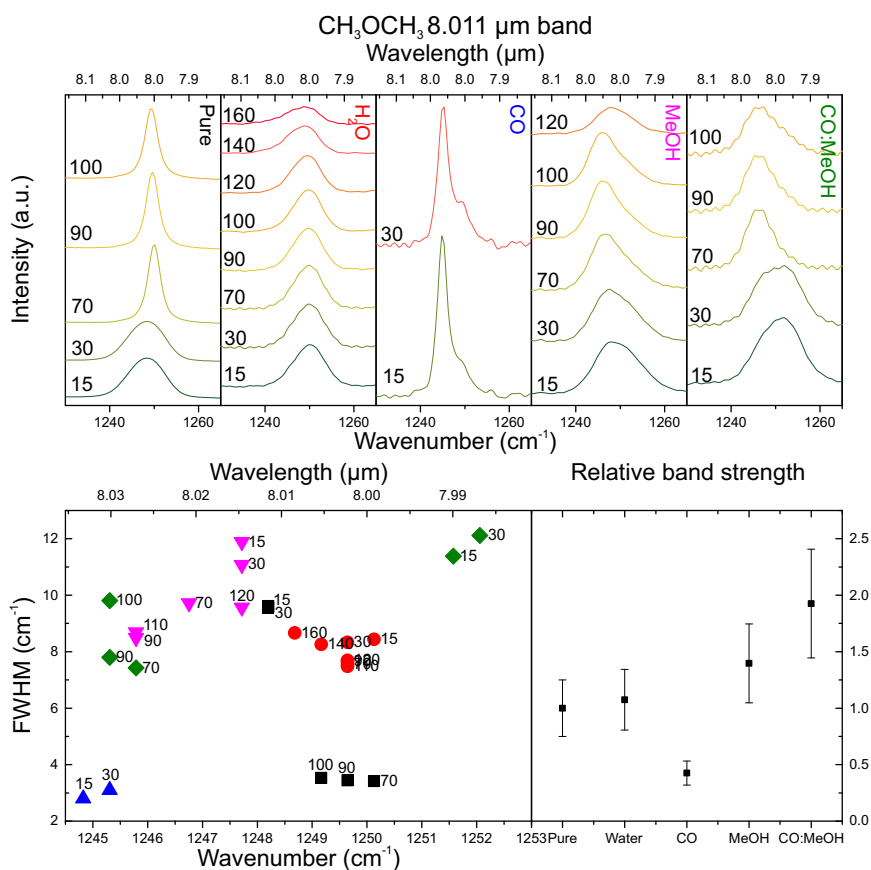


Figure 5.4: Top, from left to right the dimethyl ether 8.011 μm band pure (black) and in water (red), CO (blue), methanol (purple) and CO: CH_3OH (green) at various temperatures. Bottom left, peak position versus FWHM plot, using the same color coding. Bottom right, the relative band strength for the 8.011 μm band at 15 K in various matrices.

clearly observed (see Fig. C.3, *AOP*). Especially at low ice temperatures of 15 and 30 K clear peak shifts are visible between the CO:CH₃OH matrix at 5.84 μm , the water matrix at 5.825 μm and pure or in CH₃OH matrix at around 5.805 μm ices.

5.3.2. Ethanol

The spectrum of pure ethanol in Fig. 5.1 shows a strong C-C stretching band at 11.36 μm , C-O stretching mode at 9.514 μm and CH₃ rocking mode at 9.170 μm . A number of weaker modes are seen between 6.5 and 8.5 μm , specifically the CH₂ torsion mode at 7.842 micron, the OH deformation mode at 7.518 micron and the CH₃ symmetric deformation mode at 7.240 micron. Overlap with spectral features of bulk interstellar ice species like water and methanol is an issue for the three strongest bands, coinciding with either the water libration mode or C-O stretch and CH₃ rocking modes of methanol. Also the prominent broad silicate feature is present at ~ 9.7 μm . Although the other ethanol modes are substantially weaker, they fall within a spectral region that is generally clean of strong transitions.

The ethanol 7.240 μm band is a likely candidate for identification. Figure 5.3 shows the data of this band. Ethanol mixed in water can be distinguished from other features by a ~ 3 cm^{-1} peak shift from other mixtures. In general it is found that the ethanol:water mixture is relatively easy to distinguish, but the other mixtures display much overlap in peak position and FWHM. The CH₂ torsion, OH deformation mode and CH₃ symmetric deformation mode are hard to identify in the ethanol:CO mixture due to the appearance of many more modes. Band areas and relative band strengths of these modes are therefore not considered. The band strength is seen to vary substantially for the various bands, but does not show a clear trend.

5.3.3. Dimethyl ether

Three strong bands of dimethyl ether are found at 10.85, 9.141 and 8.592 μm for the C-O s-stretch, C-O a-stretch and CH₃ rocking mode, respectively. A much weaker CH₃ rocking mode is found at 8.011 μm . The first two overlap with known interstellar ice features of methanol, water and silicates and are therefore less suited for an identification, while the third likely falls in the wing of such features and may still be used. Despite being a weak mode, the 8.011 μm band does fall in a relatively empty region of interstellar ice spectra. This feature could therefore be most suited for an dimethyl ether identification, see Fig. 5.4.

For the 8.011 μm band clear differences are seen depending on the matrix. The spectra of pure and methanol mixture are distinguishable from those of the water and CO:CH₃OH mixtures by a ~ 2 cm^{-1} peak shift of the low temperature spectra at 15 and 30 K. In water this band displays a narrower peak compared to the other ices. The other bands also show many clear differences in peak position and FWHM between the various ice mixtures. A characteristic peak splitting structure at low temperatures is seen for the 10.85 μm band when mixed in water, methanol or CO:CH₃OH. Interestingly the relative band strength shows a substantial increase in the CH₃OH and CO:CH₃OH mixtures for the 8.011 μm band. Other modes do not show such clear differences. Also interesting to note

is the fact that the C-O a-stretch has the largest band area when mixed in water, while in the other mixtures this is always the CH₃ rocking mode at 8.592 μm .

5.4. COM ice features in W33A

Our extensive measurements of frozen COMs will be needed in the analysis of the many spectra of dense clouds, embedded protostars, and inclined protoplanetary disks that will be obtained with the upcoming *JWST* mission at high sensitivity and medium spectral resolution (R of up to 3,000). Here, we demonstrate their use by a re-analysis of a spectrum of the massive protostar W 33A obtained with the Infrared Space Observatory's Short Wavelength Spectrometer (Astronomical Observation Template 1; $R = 800$). This is one of the few sources for which a high quality mid-IR spectrum is available (Gibb et al. 2000a). In the 7 to 8 μm region three prominent features at 7.25, 7.41 and 7.67 μm are described in the literature. The 7.25 μm feature has been attributed to both CH₃CH₂OH and HCOOH (Schutte et al. 1999; Öberg et al. 2011), the 7.41 μm feature has been attributed to HCOO⁻ and CH₃CHO (Schutte et al. 1999) and the 7.67 μm band has been identified as solid methane with potentially contributions of SO₂ (Boogert et al. 1996).

In this work we make use of the water and silicate subtracted spectrum of W33A, shown in Fig. 5.5 with a straight line local continuum subtraction. The aforementioned features are visible, although the 7.41 μm feature seems to have two contributions at 7.47 and 7.40 μm and the 7.25 μm feature is found at 7.22 μm . The spectra of ethanol and acetaldehyde mixed in CO:CH₃OH and H₂O are plotted in the same figure. The peak position of the 7.40 μm feature can be reproduced well by the acetaldehyde CH₃ s-deformation mode in both mixtures. However, the band in CO:methanol mixture seems to be too broad to justly reproduce the W33A 7.40 μm feature and also covers the 7.47 μm feature next to it. The other two features at 7.22 and 7.47 μm could be the result of the CH₃ s-deformation and OH deformation modes of ethanol. Particularly the CH₃CH₂OH:H₂O mixture coincides with the peak locations of the 7.22 and 7.47 μm features in the W33A spectrum. While the identification of acetaldehyde and ethanol are plausible, detection of additional features would strengthen the assignment. We checked and found that none of the other CH₃CHO and CH₃CH₂OH bands have an anticoincidence with the W33A spectrum.

Upper limits to the ice column densities of ethanol and acetaldehyde can be given based on the integrated optical depth of their potential features. Schutte et al. (1999) give integrated τ values of 2.0 ± 0.3 and $1.6 \pm 0.5 \text{ cm}^{-1}$, respectively. Band strength values of ethanol and acetaldehyde are taken from the literature and used to calculate the column densities of the two features. The ethanol band strength of the C-O stretch mode at 9.514 μm has been determined in IR reflection experiments to be $7.3 \times 10^{-18} \text{ cm molecule}^{-1}$ (Moore & Hudson 1998). Since transmission bandstrengths for ethanol are not listed in the literature, we use this reflection value as an approximation. One has to be aware that experience learns that a mismatch by a factor of three can easily occur between transmission and reflection bandstrengths. Using the integrated absorbance ratio CH₃ s-def. / C-O str. = 0.20 at 15 K from Table B.16 (AOP), the band strength of the CH₃ stretch mode is determined to be $1.5 \times 10^{-18} \text{ cm molecule}^{-1}$. The effect of the

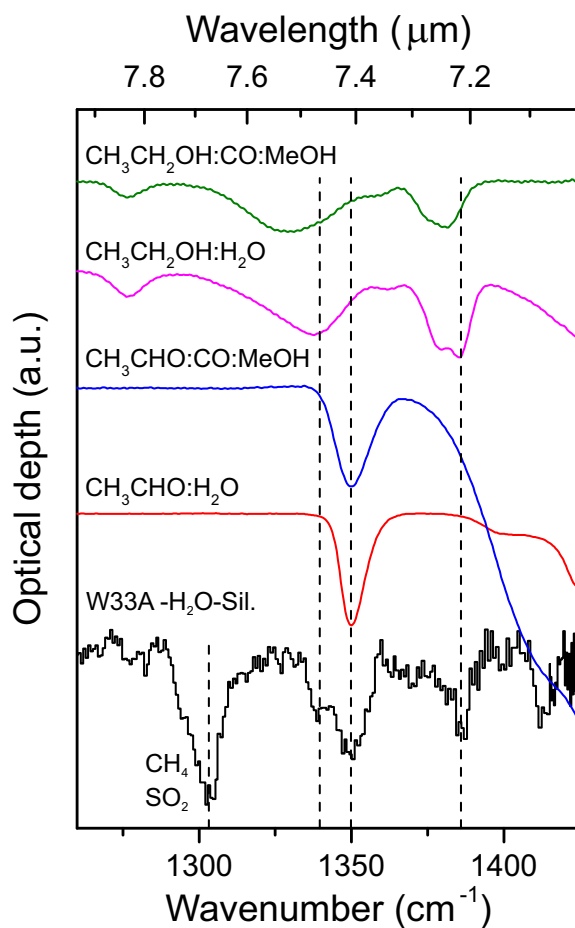


Figure 5.5: Continuum, water and silicate subtracted spectrum of W33A plotted together with ice spectra of ethanol and acetaldehyde at 15 K, mixed in :CO:CH₃OH and H₂O. Features in the W33A spectrum are indicated with dashed lines at 7.22, 7.40 and 7.47 micron. The large spectral feature at 7.67 μm is due to CH₄ and SO₂.

Table 5.3: Ice and gas-phase abundances of COMs toward W33A. Abundances given in %.

Species	Ice		Gas-phase ^c
	$/N(\text{H}_2\text{O})^a$	$/N(\text{CH}_3\text{OH})^b$	$/N(\text{CH}_3\text{OH})$
$\text{CH}_3\text{CH}_2\text{OH}$	≤ 3.4	≤ 76	2.4
CH_3CHO	≤ 2.3	≤ 52	≤ 0.2

Notes. ^aKeane et al. (2001); ^bDartois et al. (1999); ^cBisschop et al. (2007b)

matrix on the relative band strength is small for both the ethanol C-O stretch and CH_3 s-deformation modes, as can be seen from Figs. 5.3 and C.5 (AOP), and therefore assumed to be negligible. Assuming the entire $7.22 \mu\text{m}$ feature is caused by ethanol, this results in a column density of $1.3 \pm 0.2 \times 10^{18} \text{ cm}^{-2}$.

The acetaldehyde band strength is given as 1.3×10^{-17} for the C=O stretch mode (Wexler 1967). The integrated absorbance ratio of C=O str. / CH_3 s-deform. = 4.32 in pure acetaldehyde at 15 K in laboratory experiments, although the C=O stretch mode is likely saturated and the ratio may thus be higher. Using this ratio, the band strength of the CH_3 s-deformation mode is found to be $3.0 \times 10^{-18} \text{ cm molecule}^{-1}$. As can be seen in Fig. 5.2, the relative band strength of this mode decreases substantially in mixtures by about 40%. The band strength of the CH_3 s-deformation mode in mixed ices is thus $1.8 \times 10^{-18} \text{ cm molecule}^{-1}$. If the entire $7.40 \mu\text{m}$ feature is attributed to CH_3CHO , the resulting column density is $8.9 \pm 3 \times 10^{17} \text{ cm}^{-2}$.

In all likelihood the 7.22 and $7.40 \mu\text{m}$ features contain contributions of other molecules, mainly HCOOH and HCOO^- and the reported values should therefore be seen as upper limits. Using solid water and methanol column densities of 3.8×10^{19} and $1.7 \times 10^{18} \text{ cm}^{-2}$, respectively, toward W33A (Dartois et al. 1999; Keane et al. 2001), the upper limit abundance ratios of ethanol and acetaldehyde can be determined. $N(\text{COM})/N(\text{H}_2\text{O})$ are found to be $\leq 3.4\%$ and $\leq 2.3\%$, while $N(\text{COM})/N(\text{CH}_3\text{OH})$ are $\leq 76\%$ and $\leq 52\%$ for ethanol and acetaldehyde, respectively. The abundances with respect to water are in good agreement with previously reported values of $\leq 4\%$ and $\leq 3.6\%$ for ethanol and acetaldehyde, respectively (Boudin et al. 1998; Schutte et al. 1999).

The $N(\text{COM})/N(\text{CH}_3\text{OH})$ upper limit ice abundance can be compared with known gas-phase abundances toward W33A. These are given as $N(\text{CH}_3\text{CH}_2\text{OH})/N(\text{CH}_3\text{OH}) = 2.4\%$ and $N(\text{CH}_3\text{CHO})/N(\text{CH}_3\text{OH}) \leq 0.2\%$ (Bisschop et al. 2007b) and are substantially lower than the ice upper limits. Interferometric observations with the Atacama Large Millimeter/submillimeter Array are needed to spatially resolve these molecules and determine more accurate abundances. Beside being upper limits, this difference may be linked to the process that transfers solid state species into the gas phase, causing molecules to fragment, or to destruction of species in the gas-phase. An overview of the COM abundances in ice and in the gas-phase toward W33A is given in Table 5.3.

The spectroscopic data presented in this chapter, combined with the improvements in terms of sensitivity and resolution of JWST will aid in confirming these detections and distinguish potential other contributors to these features. More observations, particularly towards low-mass sources, will give additional information about the carriers of these features.

5.5. Conclusions

This chapter adds to and extends on data of three important interstellar ice candidates, acetaldehyde, ethanol and dimethyl ether. A number of selected bands are fully characterized in FWHM and peak positions and show clear changes in various matrices. Our conclusions are summarized as follows:

1. The most promising bands to identify the COMs studied here in interstellar ice spectra are the 7.427 and 5.88 μm bands of acetaldehyde, the 7.240 and 11.36 μm bands of ethanol and the 8.011 and 8.592 μm bands of dimethyl ether.
2. Matrix characteristic shifts in peak position and FWHM are seen for several bands. The acetaldehyde CH_3 s-deform. and $\text{C}=\text{O}$ stretch mode can be distinguished in H_2O , CO , CH_3OH and $\text{CO}:\text{CH}_3\text{OH}$ matrices. Ethanol shows generally less distinctive shifts and only bands in the water matrix are unique. At low temperatures matrix specific dimethyl ether band shifts can be identified, specifically for the CH_3 rocking mode at 8.011 μm .
3. Given the higher complexity of the involved spectra, unambiguous identifications need to involve different bands that reflect bandwidths and intensity ratios as found in the laboratory studies. The dependence on matrix environment and temperature provides a tool to use these transitions as a remote diagnostic instrument.
4. Analysis of the ISO W33A spectrum in the 7 μm region shows a number of features that can be assigned to the COMs studied in this work. The 7.40 μm feature matches the position of the CH_3 s-deform. mode of acetaldehyde and the 7.22 μm feature is plausibly caused by the CH_3 s-deform. mode of ethanol. It is likely that 7.22 μm band is specifically caused by ethanol mixed in water. Abundances of both molecules with respect to water ice are determined to be $\leq 2.3\%$ and $\leq 3.4\%$ for acetaldehyde and ethanol, respectively.

Acknowledgement

I thank M.E. Palumbo for useful discussions on band profile changes due to grain shape differences and S. Ioppolo for many discussions. This research was funded through a VICI grant of NWO, the Netherlands Organization for Scientific Research, Astrochemistry in Leiden is supported by the European Union A-ERC grant 291141 CHEMPLAN, by the Netherlands Research School for Astronomy (NOVA) and by a Royal Netherlands Academy of Arts and Sciences (KNAW) professor prize.



V-UV



An observational and laboratory study of CH_3NCO

N.F.W. Ligterink, A. Coutens, V. Kofman, H.S.P. Müller, R.T. Garrod, H. Calcutt, S. F. Wampfler, J. K. Jørgensen, H. Linnartz, E.F. van Dishoeck

Ligterink et al. 2017, *The ALMA-PILS survey: Detection of CH_3NCO toward the low-mass protostar IRAS 16293–2422 and laboratory constraints on its formation*, MNRAS, 469, 2219

6.1. Introduction

Complex organic molecules, defined in astrochemistry as molecules that consist of six or more atoms of which at least one is a carbon atom, are widely found in star-forming regions (Herbst & van Dishoeck 2009). A special category of complex molecules is that of the prebiotics, molecules that can be linked via their chemical structures or reactivity to life bearing molecules, such as amino-acids and sugars. Methyl isocyanate, CH₃NCO, also known as isocyanomethane, is a molecule that falls in this category, because of its structural similarity with a peptide bond (Figure 6.1). This type of bond connects amino-acids to form proteins and as such is interesting because it connects to chemistry relevant to the formation of the building blocks of life.

The majority of identified complex molecules has mainly been detected toward high-mass hot cores, such as Orion KL and Sgr B2 (e.g., Blake et al. 1987; Nummelin et al. 2000; Belloche et al. 2013, 2014; Tercero et al. 2013; Neill et al. 2014; Crockett et al. 2014b), but over the past decades detections toward low mass, sun-like, protostars such as IRAS 16293-2422 (hereafter IRAS16293) have been regularly reported as well. IRAS16293 (d = 120 pc) is considered as a protostellar template for low-mass sources and is particularly rich in organic molecules (van Dishoeck et al. 1995; Cazaux et al. 2003; Bottinelli et al. 2004; Kuan et al. 2004; Bisschop et al. 2008; Jaber et al. 2014). Jørgensen et al. (2012) demonstrated the capabilities of the Atacama Large Millimeter/submillimeter Array (ALMA) with the detection of the prebiotic molecule glycolaldehyde (see also Jørgensen et al. 2016, for a history of chemical studies of this source). More recently, other complex molecules (acetone, propanal, ethylene oxide) were identified in the framework of the PILS survey (Lykke et al. 2017). Even the deuterated isotopologues of several complex molecules were detected toward this source (Parise et al. 2003; Coutens et al. 2016; Jørgensen et al. 2016).

Methyl isocyanate Isocyanic acid Generalized peptide bond

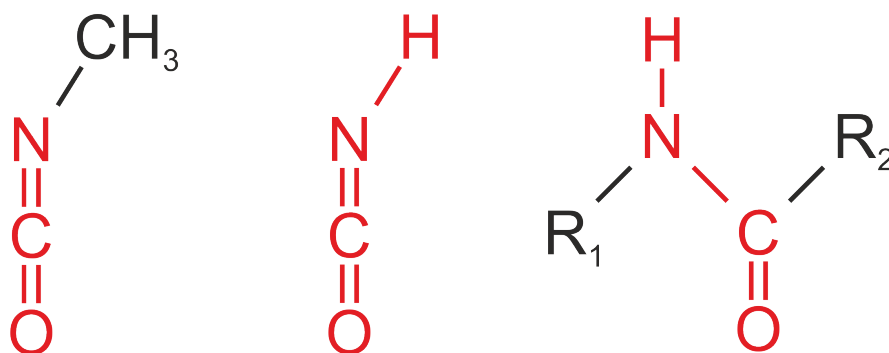


Figure 6.1: Structure of methyl isocyanate (left), isocyanic acid (middle) and the generalized structure of a peptide bond (right). In each structure the components of the peptide bond are highlighted in red. R₁ and R₂ are different molecular functional groups, which can, among other possibilities, be a methyl group as for methyl isocyanate.

Unlike other molecules such as isocyanic acid (HNCO) and formamide

(NH₂CHO)(Bisschop et al. 2007b; López-Sepulcre et al. 2015; Coutens et al. 2016), which have a similar peptide-like structure as methyl isocyanate, CH₃NCO only recently started to attract attention in the astrochemistry community. This activity was inspired by a report from Goesmann et al. (2015) that CH₃NCO may be abundantly present on the surface of comet 67P/Churyumov-Gerasimenko, as measured with the *Cometary Sampler and Composition* (COSAC) instrument of Rosetta’s Philae lander. Its measured high abundance of 1.3% with respect to H₂O and CH₃NCO/HNCO=4.3 was based on the assumption that the mass peak recorded at $m/z = 57$ is dominated by CH₃NCO, as COSAC’s low mass resolution does not allow discrimination of different species with nearly identical mass. Recent measurements with the *Rosetta Orbiter Spectrometer for Ion and Neutral Analysis* (ROSINA) at much higher mass resolution showed that the CH₃NCO coma abundance is significantly lower (K. Altwegg, private communication). Nevertheless, the possibility of linking complex molecules in star- and planet-forming regions with those present in comets triggered the search for methyl isocyanate in the interstellar medium.

Interstellar CH₃NCO was first detected toward Sgr B2(N) by Halfen et al. (2015) at low rotational temperatures of ~ 25 K with a column density ratio of $N(\text{HNCO})/N(\text{CH}_3\text{NCO}) = 35\text{--}53$ depending on the specific velocity component. Cernicharo et al. (2016) detected methyl isocyanate toward Orion KL at $N(\text{HNCO})/N(\text{CH}_3\text{NCO}) \simeq 15$ and $T_{\text{ex}} = 150$ K. Their observations toward the cold prestellar core B1-b did not yield a detection of the molecule down to an upper column density limit of $< 2 \times 10^{11} \text{ cm}^{-2}$ or $N(\text{HNCO})/N(\text{CH}_3\text{NCO}) > 42$ (based on a HNCO detection toward the same source by López-Sepulcre et al. 2015). In the same paper, publically accessible Sgr B2 observations from Belloche et al. (2013) were re-analysed with an updated spectral line list and, interestingly, yielded a detection of warm methyl isocyanate at $T_{\text{ex}} \simeq 200$ K and $N(\text{HNCO})/N(\text{CH}_3\text{NCO}) \simeq 40$. Attempts to also identify the methyl isocyanate isomer CH₃CNO were unsuccessful down to $N(\text{CH}_3\text{NCO})/N(\text{CH}_3\text{CNO}) > 100$.

The astrochemical origin of methyl isocyanate is not yet understood and this is partly due to the limited number of laboratory studies that have been performed. Henderson & Gudipati (2015) tentatively assigned a mass fragmentation peak to CH₃NCO after VUV irradiating solid-state mixtures of NH₃:CH₃OH. In other experiments by Ruzi & Anderson (2012) UV irradiation of frozen *n*-methylformamide (CH₃NHCHO) also yielded methyl isocyanate, although it was concluded to represent a minor product channel.

A number of formation routes have been hypothesized by astrochemists. Halfen et al. (2015) postulated gas-phase formation by HNCO or HOCN methylation:



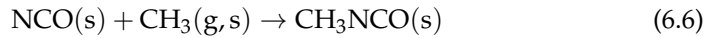
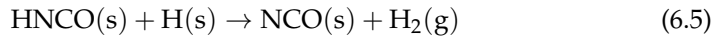
or reactions of HNCO or HOCN with protonated methane, followed by electron recombination:



Cernicharo et al. (2016) favoured solid-state formation mechanisms based on the detection of CH₃NCO toward hot cores and its non-detection in the cold dark cloud B1-b. Particularly, the methylation of HNCO has been mentioned as a possible route to form methyl isocyanate in the solid-state, i.e., on the surface of an icy dust grain:



Belloche et al. (2017) used the grain-surface radical-addition reaction $\text{CH}_3 + \text{NCO} \rightarrow \text{CH}_3\text{NCO}$ in their models, with most of the NCO formed via H-abstraction of HNCO:



These postulated routes require the reactants to be present in sufficient amounts. Gaseous HNCO is detected in high abundances in protostellar environments and has been imaged in IRAS16293, showing it to be prominent in both source A and B (Bisschop et al. 2008; Coutens et al. 2016). It likely results from sublimation of OCN⁻, known to be a major ice component in low-mass protostellar envelopes (van Broekhuizen et al. 2005). A significant abundance of CH₃ gas is a more speculative assumption since the molecule can only be observed by infrared spectroscopy and has so far only been seen in diffuse gas toward the Galactic Center (Feuchtgruber et al. 2000). Alternatively, CH₃ radicals can be produced *in situ* in ices by photodissociation of known abundant ice components like CH₄ or CH₃OH and then react with HNCO or OCN⁻. This is the solid-state route that is investigated here.

In this work we present the first detection of methyl isocyanate toward both components of the low mass protobinary IRAS16293 on scales of < 100 AU. An independent detection toward source B is also reported by Martín-Doménech et al. (2017). A set of systematic laboratory experiments is presented in order to validate the solid-state formation routes of CH₃NCO. The observational work is presented in Section 6.2 and the laboratory work in Section 6.3. In Section 6.4 the results of the observations and laboratory experiments are compared and discussed in the context of recent astrochemical models. The conclusions of this chapter are given in Section 6.5.

6.2. Observations

6.2.1. The ALMA PILS survey

We searched for methyl isocyanate in the Protostellar Interferometric Line Survey (PILS) data, an unbiased spectral survey of the low-mass protostellar binary IRAS16293 with ALMA. A full description and data reduction of the survey is presented in Jørgensen et al. (2016). Briefly, this survey covers a spectral range from 329.147 to 362.896 GHz and was obtained with both the 12m array and the Atacama Compact Array (ACA). The beam size ranges between ~0.4 and 0.7 arcsec depending on the configuration at the time of the observations.

The rms of the combined data sets is about 7–10 mJy beam⁻¹ channel⁻¹, i.e., approximately 4–5 mJy beam⁻¹ km s⁻¹. To facilitate the analysis, the combined data set used in this chapter was produced with a circular restoring beam of 0.5 arcsec at a spectral resolution of 0.2 km s⁻¹.

Two positions are analysed in this study. The first position is offset by one beam diameter (~ 0.5 arcsec) from the continuum peak of source B in the south west direction ($\alpha_{J2000}=16^{\text{h}}32^{\text{m}}22^{\text{s}}.58$, $\delta_{J2000}=-24^{\circ}28'32''.8$) (see high resolution images in Baryshev et al. 2015). Source B presents narrow lines (FWHM ~ 1 km s⁻¹). This position is found to be optimal for line identifications, as the lines are particularly bright, do not have strong absorption features toward the bright continuum of source B, and do not suffer from high continuum optical depth (Coutens et al. 2016; Lykke et al. 2017; Jørgensen et al. 2016). In this chapter, we also analyse source A, which exhibits broader lines than source B making the line identification quite challenging (Pineda et al. 2012). The linewidth varies, however, depending on the spatial separation from this source. With an average FWHM of ~ 2.5 km s⁻¹, the position $\alpha_{J2000}=16^{\text{h}}32^{\text{m}}22^{\text{s}}.90$, $\delta_{J2000}=-24^{\circ}28'36''.2$ appears to be one of the best positions to search for new species toward source A (0.3'' offset). At this position, the emission is centered at v_{LSR} of ~ 0.8 km s⁻¹, blueshifted from the source A velocity of $v_{\text{LSR}} = 3.2$ km s⁻¹ (Jørgensen et al. 2011).

Bisschop et al. (2008) found HNC and other nitrogen containing species such as CH₃CN to be more prominent toward source A than source B. Consequently, it is also interesting to check whether there exists a small scale chemical differentiation among the N-bearing species for the two sources.

6.2.2. Results

Methyl isocyanate is detected toward both components A and B of IRAS16293. The identification is based on spectroscopic data from the Cologne Database for Molecular Spectroscopy (CDMS, Müller et al. 2001, 2005), taken from Cernicharo et al. (2016) as well as from Koput (1986). CH₃NCO is an asymmetric rotor with the NCO group lying at an angle of 140° and a low-lying (~ 182 cm⁻¹) C-N-C bending mode ν_b . Moreover, the barrier to internal rotation of the CH₃ group is low, only 21 cm⁻¹. The pure rotational spectrum therefore has *A* and *E* torsional states and vibrationally excited transitions can become detectable at temperatures of a few hundred K. The labelling of the states used here refers to the quantum numbers *J* (rotational angular momentum), *K_a* and *K_c* (projection of angular momentum on the respective inertial axes) with internal rotation interactions indicated by the quantum number *m*, with *m*=0 and ± 3 for the *A* states and *m*=1, -2 and 4 for the *E* states (Halfen et al. 2015; Cernicharo et al. 2016).

Using the CASSIS software¹, we have been able to identify 43 unblended lines of CH₃NCO in the bending ground state ($\nu_b = 0$) with upper energy levels E_{up} ranging from 320 to 670 K toward source B (see Table 6.2). Figure 6.3 shows the unblended lines detected toward this component as well as the LTE modeling for two different excitation temperatures at 100 and 300 K. Both excitation temperatures allow to reproduce the observations; only predicted transitions are observed. Our data are not sensitive to any cold CH₃NCO component

¹<http://cassis.irap.omp.eu/>

Table 6.1: Comparison of molecular abundance ratios toward different sources

Source	HNCO/CH ₃ NCO	CH ₃ CN/CH ₃ NCO	CH ₃ OH/CH ₃ NCO
IRAS16293 B ^a	12	8	3333
IRAS16293 A ^a	4	9	3200
Orion KL A ^b	15	10	400
Orion KL B ^b	15	25	225
Sgr B2(N1) ^b	40	50	40
Sgr B2(N2) ^c	9	10	182
67P/C-G ^d	≥0.2	≥0.2	–

Notes. ^aThis work; ^bCernicharo et al. (2016); ^cBelloche et al. (2016, 2017); ^dGoesmann et al. (2015); Altwegg et al. (2017)

since lines with low E_{up} values are missing in the spectral range of the PILS survey. Among the complex molecules that were detected and analysed towards source B, some (acetaldehyde, ethylene oxide) exhibit a relatively low excitation temperature of ~ 125 K (Lykke et al. 2017), while others (formamide, isocyanic acid, methanol, methyl formate, glycolaldehyde, ethylene glycol) show a higher excitation temperature of ~ 300 K (Jørgensen et al. 2012; Coutens et al. 2016; Jørgensen et al. 2016). Their spatial distribution is however rather similar and it is not possible to determine to which category CH₃NCO belongs. The methyl isocyanate column density is not very sensitive to the exact value of the excitation temperature: assuming the same source size of 0.5 arcsec as used in previous PILS studies (Coutens et al. 2016; Jørgensen et al. 2016; Lykke et al. 2017), the CH₃NCO column density is found to be about $3 \times 10^{15} \text{ cm}^{-2}$ and $4 \times 10^{15} \text{ cm}^{-2}$ for $T_{\text{ex}} = 300$ and 100 K, respectively. All lines are optically thin. It is expected that for the same assumptions all column densities toward source B are accurate to better than 30%.

Toward source A, most of the lines are blended due to the larger linewidths ($\sim 2.5 \text{ km s}^{-1}$). We can, however, identify 11 unblended lines of CH₃NCO (see Figure 6.4). A column density of $\sim 6 \times 10^{15} \text{ cm}^{-2}$ and $\sim 9 \times 10^{15} \text{ cm}^{-2}$ (assuming a source size of 0.5 arcsec) is in good agreement with observations for excitation temperatures of 300 and 100 K, respectively, again with an uncertainty of about 30%.

At high excitation temperatures, rotational levels in the first excited bending state ($\nu_b=1$) may be populated as well and predictions for possible transitions are shown in Figure 6.7. For $T_{\text{ex}} = 300$ K, some faint lines can indeed be tentatively attributed to CH₃NCO $\nu_b=1$ transitions toward source B. An integrated intensity map of one of the brightest CH₃NCO lines, the $39_{0,39,0}-38_{0,38,0}$ transition at 336339.9 MHz, is presented in Figure 6.2. Similarly to other complex molecules, the emission is quite compact with a size of ~ 60 AU radius and centred near the two sources, with little difference between them (Coutens et al. 2016; Jørgensen et al. 2016; Lykke et al. 2017). For source B, the emission is somewhat offset due to the continuum becoming optically thick on source.

We also searched for spectral evidence of two isomers of methyl isocyanate - acetonitrile oxide (CH₃CNO, Winnewisser et al. 1982) and methyl cyanate (CH₃OCN, Sakaizumi et al. 1990; Kolesniková et al. 2016) - but the corresponding

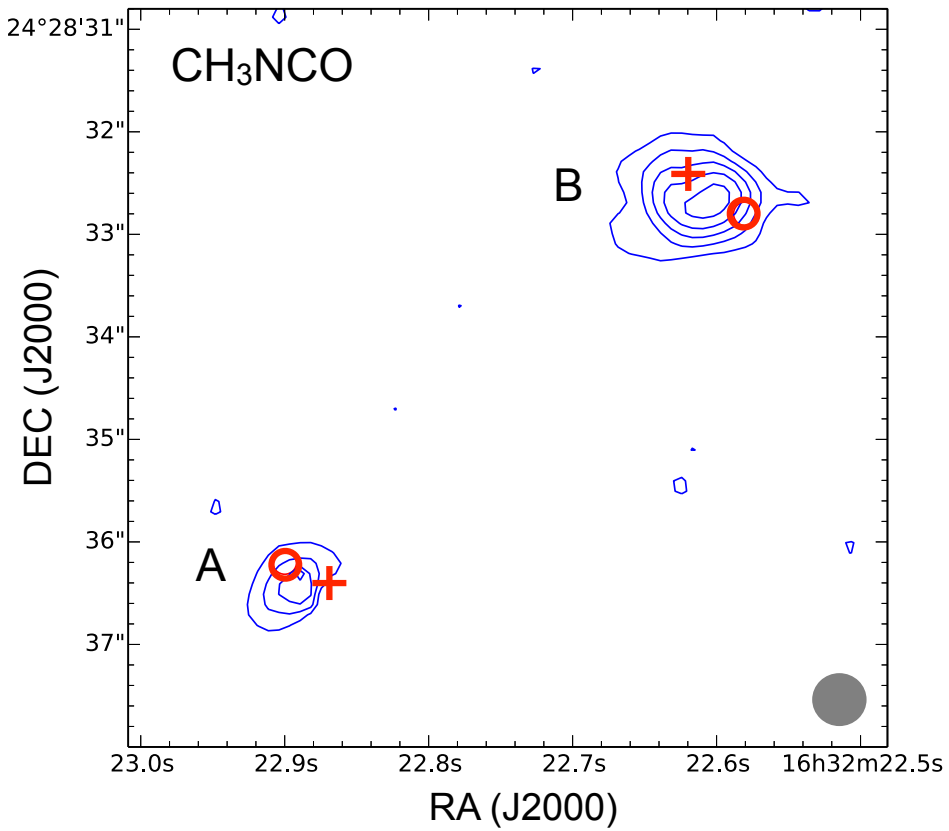


Figure 6.2: Integrated intensity map of the CH_3NCO $39_{0,39,0}-38_{0,38,0}$ transition at 336339.9 MHz and $E_{\text{up}} = 323.7$ K between 1.7 and 3.7 km s^{-1} . The positions of the continuum of source A (South East source) and source B (North West source) are indicated with red crosses, while the positions studied in this chapter are indicated with red circles. The contour levels start at 5σ with additional steps of 5σ . The circular restoring beam of 0.5 arcsec size is indicated in grey in the right hand lower corner.

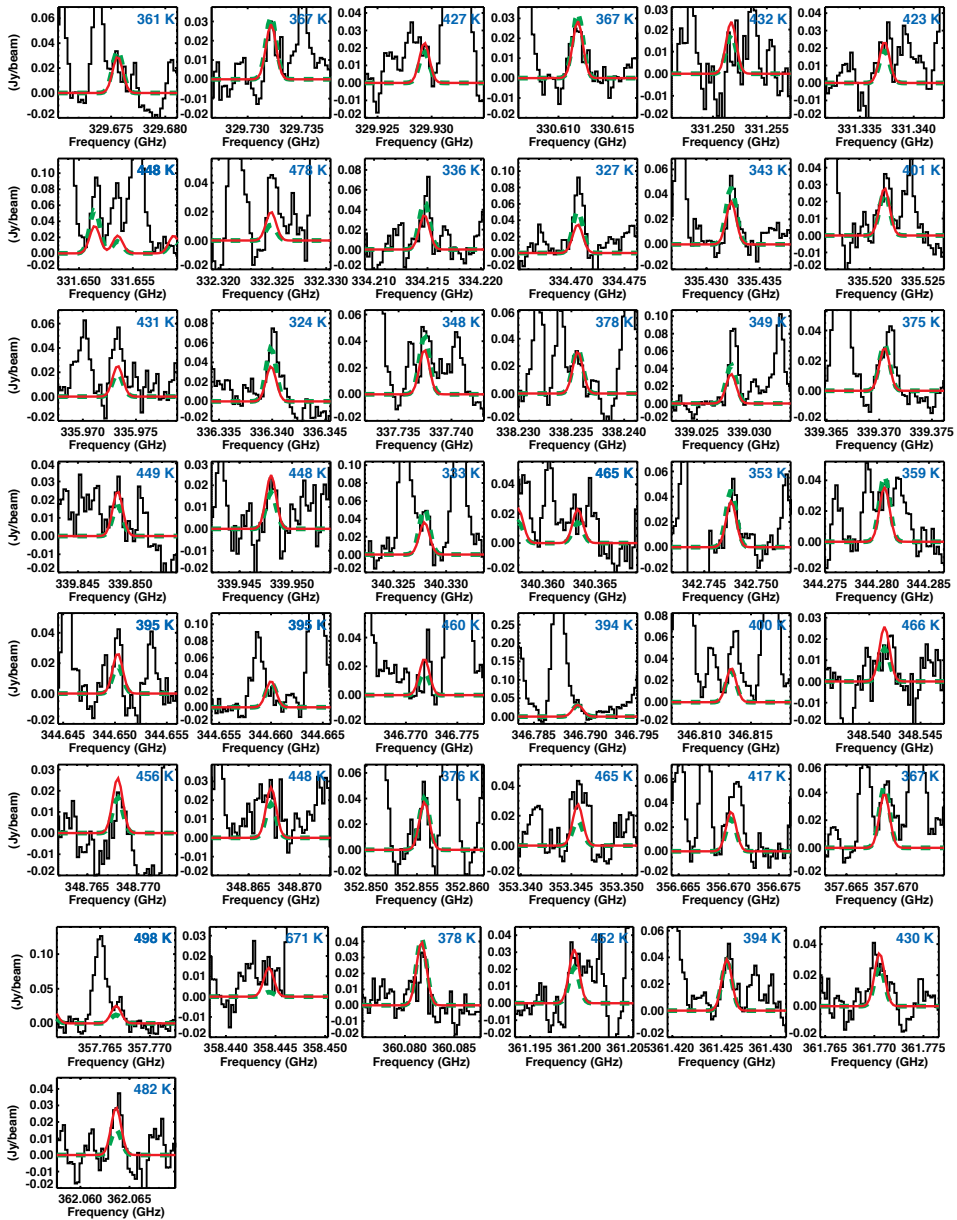


Figure 6.3: Black: detected unblended lines of CH₃NCO toward source B. Red solid: best-fit model for $T_{\text{ex}} = 300$ K. Green dashed: best-fit model for $T_{\text{ex}} = 100$ K. The E_{up} values of the lines are indicated in blue in the right upper part of each panel.

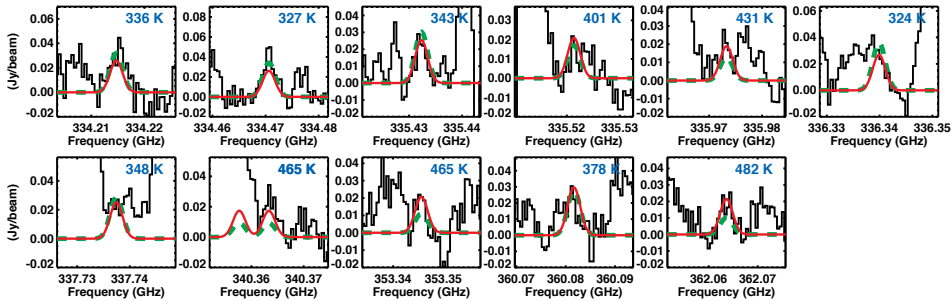


Figure 6.4: Black: detected unblended lines of CH_3NCO toward source A. Red solid: best-fit model for $T_{\text{ex}} = 300$ K. Green dashed: best-fit model for $T_{\text{ex}} = 100$ K. The E_{up} values of the lines are indicated in blue in the right upper part of each panel.

transitions were not found in the PILS data set. From this non-detection 3σ upper limits of $5 \times 10^{13} \text{ cm}^{-2}$ and $5 \times 10^{14} \text{ cm}^{-2}$ are derived, respectively (assuming an excitation temperature of 100 K). These isomers are consequently less abundant than methyl isocyanate by at least two and one orders of magnitude, in agreement with recent findings toward Orion KL (Cernicharo et al. 2016; Kolesníková et al. 2016).

In view of the important role that HNC and HOCN may play in the formation of CH_3NCO , we also searched for spectral signatures of these precursor species. The analysis of the PILS data for HNC toward source B is presented in Coutens et al. (2016). The HNC lines are optically thick, so lines of the isotopologue HN^{13}CO were analysed and the HNC column density was derived assuming a $^{12}\text{C}/^{13}\text{C}$ ratio of 68 (Milam et al. 2005). To get precise abundance ratios, we re-analysed the HN^{13}CO data using the same dataset (with the circular restoring beam of 0.5 arcsec) and obtained a HNC column density of $3.7 \times 10^{16} \text{ cm}^{-2}$, which is within the 30% uncertainty range. The resulting HNC/ CH_3NCO abundance ratio is about 12 toward source B with an uncertainty of less than a factor 2. Within the error margins, this is similar to the value derived in Orion KL (Cernicharo et al. 2016) or Sgr B2(N2) (Belloche et al. 2016, 2017). For source A, the column density of HNC is estimated to be about $3.4 \times 10^{16} \text{ cm}^{-2}$ ($T_{\text{ex}} = 100$ K). The corresponding HNC/ CH_3NCO ratio is consequently about 4 toward this component, with a somewhat larger uncertainty of a factor of 3 due to the difficulty of deriving a precise column density for HNC because of line blending. Overall, we can conclude that the two HNC/ CH_3NCO ratios are comparable toward the two components of the binary.

Whereas HNC is readily identified, this is not the case for HOCN. No HOCN lines were detected and a 3σ upper limit of $3 \times 10^{13} \text{ cm}^{-2}$ is derived toward source B. HOCN is consequently less abundant than HNC and CH_3NCO by at least 3 and 2 orders of magnitude, respectively. Therefore, it is highly unlikely that the gas-phase formation pathway involving HOCN, as proposed by Halfen et al. (2015) in Eq. 6.1 and 6.2, contributes significantly to the production of methyl isocyanate in this source.

We have also determined the abundance ratios of CH_3NCO with respect

to CH₃OH and CH₃CN for comparison with other sources in which methyl isocyanate has been detected (see Table 6.1). The column density of CH₃OH was estimated based on CH₃¹⁸OH by Jørgensen et al. (in prep.) for the one beam offset position toward source B ($\sim 1 \times 10^{19} \text{ cm}^{-2}$) using a ¹⁶O/¹⁸O ratio of 560 (Wilson & Rood 1994). With the same assumptions, we estimate a column density of CH₃OH of $\sim 2 \times 10^{19} \text{ cm}^{-2}$ in source A. CH₃CN was analysed by Calcutt et al. (in prep.) toward both source A ($\sim 8 \times 10^{16} \text{ cm}^{-2}$) and source B ($\sim 3 \times 10^{16} \text{ cm}^{-2}$). Similarly to the HNCO/CH₃NCO ratio, the abundance ratio of CH₃CN/CH₃NCO is comparable to the values found in Orion KL (Cernicharo et al. 2016) and lower than toward Sgr B2(N1), but again comparable to Sgr B2(N2) (Belloche et al. 2016, 2017). Methanol is, however, clearly more abundant than methyl isocyanate toward IRAS16293 than toward Orion KL and Sgr B2.

The HNCO/CH₃NCO and CH₃CN/CH₃NCO abundance ratios derived in IRAS16293 are much larger than the lower limits found in comet 67P (>0.2). A proper comparison awaits the new results derived with the ROSINA instrument (Altwegg et al. in prep.).

6.3. Laboratory experiments

Grain surface formation routes of complex molecules have been investigated experimentally for many years using cryogenic set-ups to mimic specific chemical processes under fully controlled laboratory conditions (see Herbst & van Dishoeck 2009; Linnartz et al. 2015, for reviews). In the present work the formation of methyl isocyanate is investigated by energetically processing solid-state CH₄:HNCO mixtures with vacuum-UV radiation. VUV irradiated methane ice is known to efficiently yield methyl radicals (Bossa et al. 2015), and these radicals are expected to further react through surface diffusion with HNCO to form CH₃NCO, as proposed by Goesmann et al. (2015) and Cernicharo et al. (2016), reaction 6.4. The Cryogenic Photoproduct Analysis Device 2 (CryoPAD2) in the Sackler Laboratory for Astrophysics is used to perform the measurements to investigate the role of methylation of HNCO in methyl isocyanate formation. A short description of this set-up, experimental procedure and reference data is given below.

Note that in these experiments CH₄ is used as the parent of CH₃ but in interstellar space methyl radicals active in the ice may also originate from CH₃OH dissociation (Öberg et al. 2009a) or from direct CH₃ accretion from the gas-phase. The main aim of this section is to investigate whether or not the proposed solid-state reaction as shown in reaction 6.4 can proceed at temperatures typical for dark cloud conditions in the ISM, i.e., independent of the exact precursor species.

6.3.1. Set-up and method

CryoPAD2 consists of a central chamber operating under ultra-high vacuum conditions ($P \simeq 10^{-10}$ mbar), to which various instruments are attached. On the top a cryostat is mounted which cools a gold-coated reflective surface down to 12 K. The temperature of this surface can be controlled through resistive heating

and varied between 12 and 300 K, with an absolute temperature accuracy better than 1 K. Pure and mixed gases are prepared separately in a gas-mixing system which is attached to a high-precision leak valve to the main chamber and which doses the gases onto the cooled surface. The deposited ice samples are irradiated with VUV radiation from a Microwave Discharge Hydrogen-flow Lamp (MDHL), which emits radiation peaking at 121 nm and a region between 140 to 160 nm, corresponding to photon energies in the range of 7.5 to 10.2 eV (Chen et al. 2014; Ligterink et al. 2015). The total lamp flux is $(1.1 \pm 0.1) \times 10^{14}$ photons s^{-1} that is determined using a calibrated NIST diode. CryoPAD2 possesses two diagnostic tools to monitor the VUV induced processes in the ice. The beam of a Fourier-Transform IR Spectrometer (FTIRS) is directed under grazing incidence onto the gold-coated surface, in order to perform Reflection Absorption IR Spectroscopy (RAIRS). The sample preparation and chemical changes under influence of VUV radiation are monitored by recording vibrational fingerprint spectra of molecules on the surface. To decrease the perturbing role of atmospheric CO_2 and H_2O , the system is purged with filtered dry air. The second instrument is a highly sensitive Quadrupole Mass Spectrometer (QMS), with an ionization element at 70 eV, which is able to trace gas-phase molecules in the chamber that are released from the ice surface upon linear heating during a Temperature Programmed Desorption (TPD) experiment. TPD is a very useful method that allows to identify desorbing species through their specific desorption temperature and mass fragmentation pattern. Unambiguous identifications become possible through the use of isotopologues and searching for the corresponding mass shifts of specific fragments. Obviously, TPD comes with the destruction of the ice.

In the experiments CH_4 (Linde Gas, 99.995% purity), $^{13}\text{CH}_4$ (Sigma-Aldrich, 99% purity) and HNCO are used. HNCO is produced from cyranic acid (Sigma-Aldrich, 98% purity), the solid trimer of HNCO, following the protocol described in van Broekhuizen et al. (2004). Impurities of the HNCO production process are removed by freeze-thaw cycles to obtain a HNCO purity of $>99\%$.

For the experiments samples of pure HNCO and methane, and mixtures of $^{13}\text{CH}_4/\text{CH}_4:\text{HNCO}$ at 5:1 ratio are prepared. This ratio is within a factor of 2 of that observed for interstellar ices (Öberg et al. 2011) but is particularly chosen to create a large abundance of CH_3 radicals to test whether reaction 6.4 proceeds or not. Homogeneously mixed ices are grown on the surface at 20 K and irradiated with a total fluence of $\sim 3.3 \times 10^{17}$ photons. During irradiation of the sample, IR spectra are continuously recorded at 1 cm^{-1} resolution. After the irradiation TPD is started, while still recording IR spectra.

The strongest vibrational features of solid methyl isocyanate are found between 2320 and 2280 cm^{-1} ($\sim 4.34 \mu\text{m}$) for the $-\text{N}=\text{C}=\text{O}$ antisymmetric stretching vibration and overtone $2\nu_7$ CH_3 rocking mode. Sullivan et al. (1994) lists these at 2320 , 2280 , 2270 , 2240 and 2228 cm^{-1} , with 2280 cm^{-1} being the strongest band. Zhou & Durig (2009) positioned all bands around 2300 cm^{-1} and Reva et al. (2010) puts the band for methyl isocyanate in a nitrogen matrix at 2334.7 , 2307.9 , 2288.9 , 2265.2 and 2259.7 cm^{-1} , finding the strongest transition at 2288.9 cm^{-1} . The region around these bands is used to monitor CH_3NCO formation in the ice. We focus on the region between $2400 - 2100 \text{ cm}^{-1}$. From previous experiments it is known that CO_2 (2340 cm^{-1}), OCN^- (2165 cm^{-1}) and CO (2135 cm^{-1}) are produced from HNCO (2265 cm^{-1}) upon irradiation

and these photo-products also have spectral features in the region characterizing methyl isocyanate (Raunier et al. 2004; van Broekhuizen et al. 2004). Other known products of HNCO irradiation are formamide, urea and formaldehyde, which do not have any interfering IR features in the region of interest. Energetic processing of methane does not yield products that show up in the region of interest. Products that are formed from methane are mainly ethane and to a lesser extent ethene and ethyn (Bennett et al. 2006; Bossa et al. 2015). These species are seen in our spectra at their appropriate frequencies. The abundant formation of ethane demonstrates that CH₃ is indeed produced in the experiments, since ethane is the direct product of methyl-radical recombination.

In order to identify methyl isocyanate in the gas-phase using TPD, the mass fragmentation pattern available from the NIST database² is used. The fragmentation pattern at 70 eV comprises unique peaks at $m/z = 57$ and 56 (hereafter also called the primary and secondary mass peak), which have a m/z 57:56 ratio of 5:2 and these will be used as main TPD mass tracers. Known products of pure HNCO and methane irradiation does not have a mass fragmentation peak at $m/z = 57$ (see also Appendix 6.6.3).

It is important to mention that methyl isocyanate is severely toxic and specialised laboratories and equipment are needed to work with this substance. This complicates the extensive use of this species and for this reason additional experiments, starting from the pure precursor, have not been performed.

6.3.2. Results – IR Spectra

Figure 6.5 presents the IR spectra recorded during the first 1×10^{17} photons irradiating the ^{12/13}CH₄:HNCO samples. All spectra are normalized to the HNCO peak. Three known spectroscopic features of CO₂, OCN⁻ and CO (blue) show up during irradiation. Also, two new features become visible around 2300 cm⁻¹ (red), which do not show up while processing samples of pure HNCO or CH₄. Also a clear red shift of about 10 cm⁻¹ of the two features is seen between the sample of ¹²CH₄ and ¹³CH₄, moving transitions at 2322 and 2303 cm⁻¹ to 2313 and 2294 cm⁻¹. These spectroscopic features are therefore the result of a product formed in the reaction between methane and isocyanic acid, and, since they are found close to known CH₃NCO features (given by Sullivan et al. (1994) and Reva et al. (2010)), are plausibly identified with methyl isocyanate. Another feature is seen in the wing of the HNCO peak around 2235 cm⁻¹, which does not clearly shift with methane isotopologues. The origin of this band is unclear.

Bandstrength values for methyl isocyanate are not available from the literature, however, a rough indication of the amount of formed methyl isocyanate versus lost HNCO can be given by making the assumption that the bandstrength of the NCO antisymmetric stretch vibration of methyl isocyanate equals that of the corresponding vibration of HNCO. To obtain the ratio, the integrated area of the 2303 cm⁻¹ feature is divided by the integrated loss area of the 2265 cm⁻¹ HNCO band for a number of spectra. A ratio of $N(\text{HNCO})/N(\text{CH}_3\text{NCO}) = 100 - 200$ is found, which is about an order of

²NIST Mass Spec Data Center, S.E. Stein, director, "Mass Spectra" in NIST Chemistry WebBook, NIST Standard Reference Database Number 69, Eds. P.J. Lindstrom and W.G. Mallard, National Institute of Standards and Technology, Gaithersburg MD, 20899, <http://webbook.nist.gov>.

magnitude higher than the ratio observed toward IRAS16293. It should be noted, that it is not *a priori* clear whether solid state laboratory and gas phase astronomical abundances can be directly compared (see e.g. Chuang et al. 2017). It is likely that ongoing gas phase reactions, for one or the other species, change the solid state to gas phase ratios. It is also possible that non-linear RAIRS effects can offset the column density (Teolis et al. 2007) or that the CH₃NCO bandstrength is significantly different. In a same manner CH₃NCO photodestruction may affect the overall abundances.

6.3.3. Results – temperature programmed desorption

The desorption temperature of methyl isocyanate has not been reported in the literature, but the TPD traces of our experiments on UV processed CH₄:HNCO ices do show the combined release of the primary and secondary masses of methyl isocyanate $m=57$ and 56 at 145 K (Figure 6.6). The verification experiment of pure HNCO did not show these masses and only $m/z = 56$ (and no 57) was seen after the irradiation of pure methane ice, releasing at 105 K (Figure 6.8 in the Appendix). At the 145 K desorption peak the primary over secondary mass ratio is around 1-1.5, lower than the value of 2.5 suggested by NIST upon 70 eV electron impact ionization. The NIST calibration values are a good indicator of the values to be expected, but are to some extent set-up specific. In such cases, the expected reactant can be deposited directly and the fragmentation pattern can be studied adapted to the set-up in use. This is unfortunately not possible here due to the aforementioned toxicity of methyl isocyanate. Moreover, contributions from other reaction products cannot be fully excluded. In Figure 6.6B a second desorption peak is found around 205 K, which is seen only as a shoulder in panel A. It is unlikely that this peak is associated with methyl isocyanate, instead it shows that the chemical network involves the formation of other species as well. In fact, since the additional product(s) have a mass fragmentation pattern which contributes to the secondary mass of methyl isocyanate, this could explain why the primary/secondary mass ratio does not exactly match with that given by NIST. Additionally, the unidentified product of pure methane irradiation could be trapped in the ice and contribute to other desorption peaks. Therefore the 145 K desorption peak is still consistent with methyl isocyanate. There is also no other candidate molecule with a primary mass of 57 in the NIST database that could plausibly explain the TPD spectra.

CryoPAD2 offers the unique feature to combine IR and TPD data, i.e., at the moment a specific ice feature starts thermally desorbing, the IR signal starts decreasing and simultaneously the mass signal is increasing. In the measurements presented here, this effect is not as clearly visible as in previous studies (e.g. Öberg et al. (2009a)), but this may be partly due to the low final S/N of the feature, making it difficult to link RAIRS and TPD signals. The present data are as accurate as possible, but obviously their interpretation would benefit from focused experiments determining the thermal desorption peak of pure CH₃NCO and the IR bandstrengths.

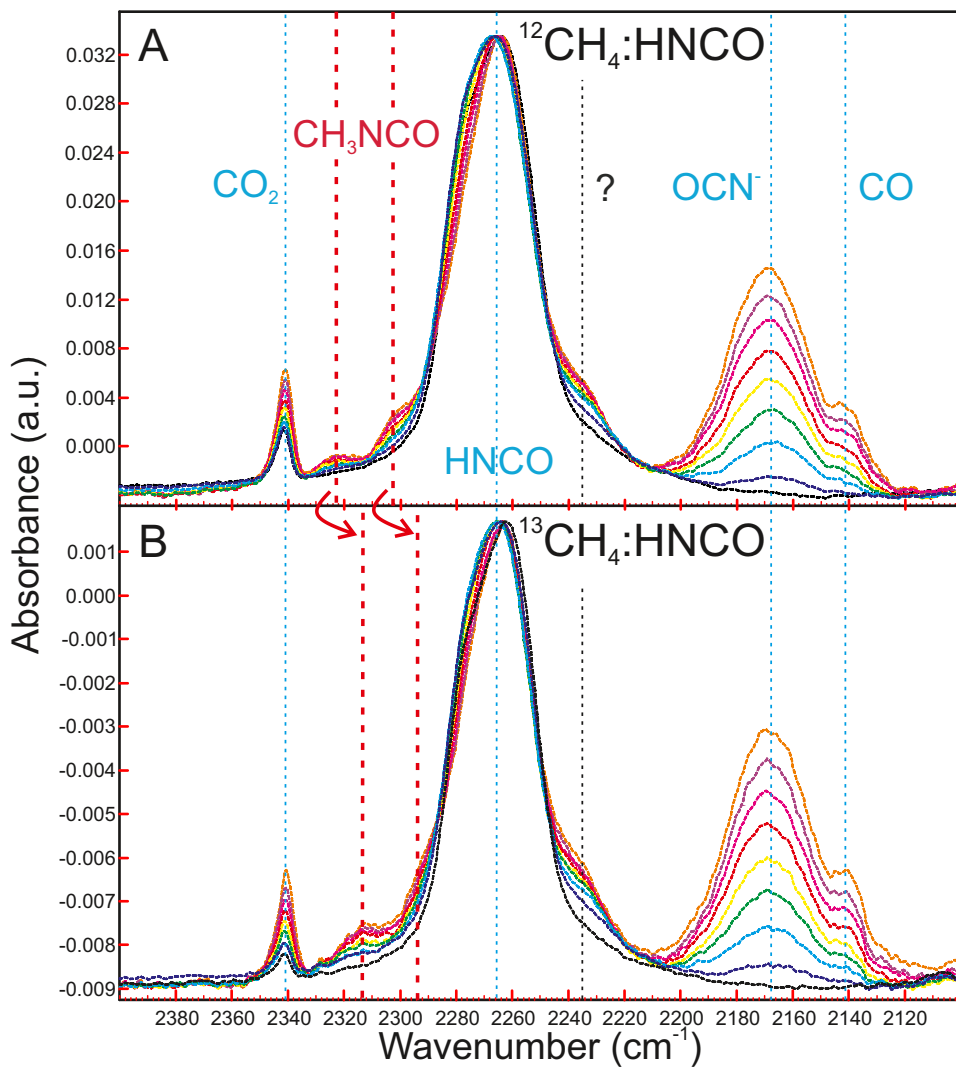


Figure 6.5: IR spectra taken over time for the $^{12}\text{CH}_4$:HNCO (A) and $^{13}\text{CH}_4$:HNCO (B) mixture. HNCO and the products CO_2 , OCN^- and CO are listed (blue). Spectroscopic features that coincide with CH_3NCO are found at the red lines and show a clear shift with the $^{13}\text{CH}_4$ isotopologue. One unidentified peak is found in the right wing of the HNCO peak, indicated by a question mark.

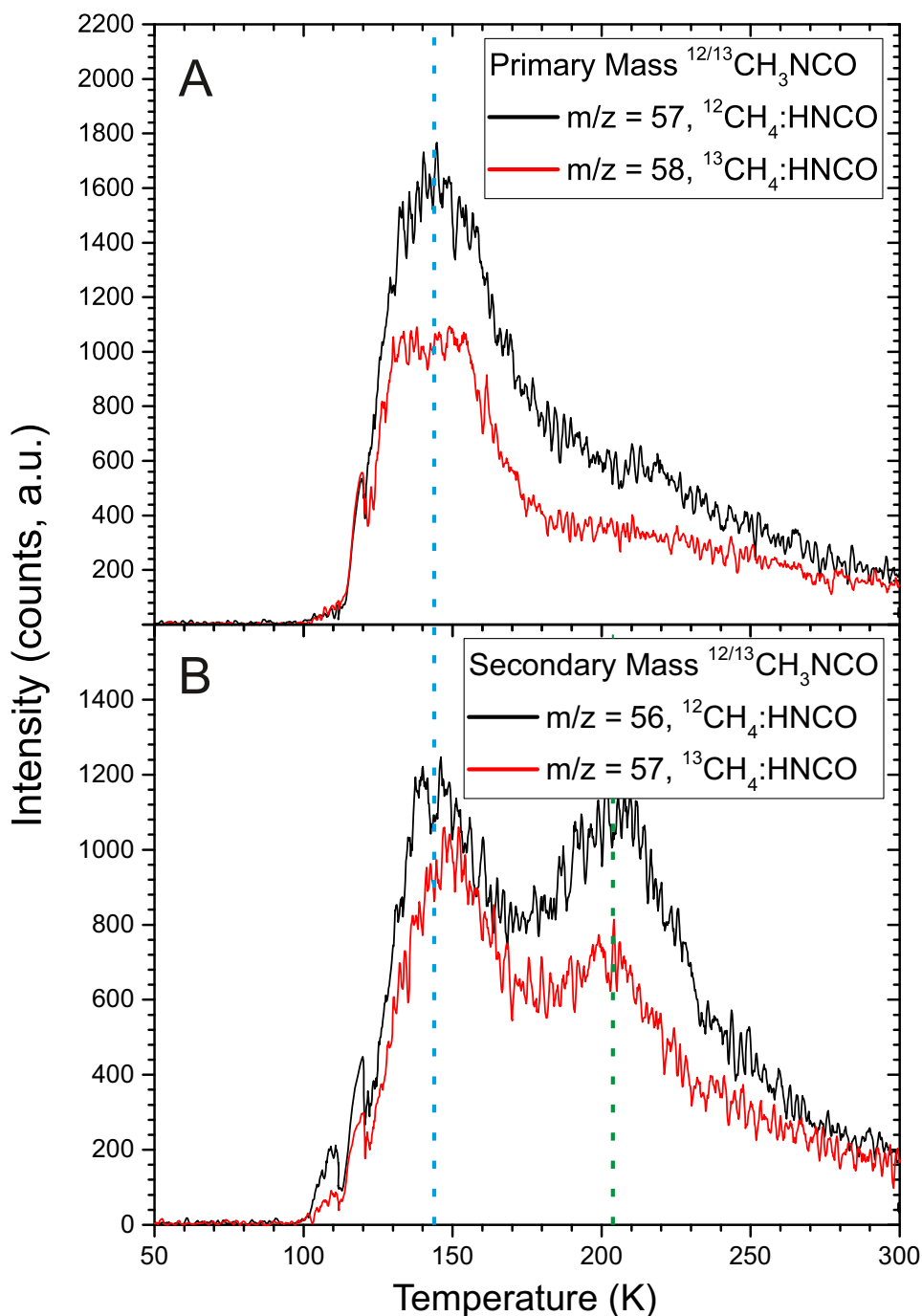


Figure 6.6: TPD trace of the primary (A) and secondary (B) masses of $^{12/13}\text{CH}_3\text{NCO}$. Both the primary and secondary mass are seen being released around 145 K (blue line). The secondary mass shows another release peak around 205 K (green), which is suspected to also contribute to first release peak, thus altering respectively the m/z 57/56 and 58/57 ratio.

6.4. Linking observations and laboratory data

Methyl isocyanate is detected in a significant abundance toward both components of IRAS16293 with an excitation temperature of at least 100 K. The two isomers, CH₃CNO and CH₃OCN, are not detected. Abundance ratios with respect to HNCO and CH₃CN are found to be similar to those found for Orion KL and comparable within a factor of a few to Sgr B2, making a common formation pathway in these three sources likely. Moreover, no chemical differentiation between source A and B is found. Gas-phase production of CH₃NCO via HOCN (reaction 6.1) can be seen as insignificant due to the low upper limit on this molecule, but a gas-phase route involving HNCO cannot be excluded.

The laboratory experiments on the formation of CH₃NCO strongly suggest that a solid-state formation scheme is possible, starting from two astronomically relevant precursor species, CH₄ and HNCO. The proposed reaction CH₃ + HNCO → CH₃NCO + H indeed seems to proceed, confirming a solid state reaction pathway, but other routes such as hydrogen stripping CH₃ + HNCO → CH₄ + NCO may take place in parallel. Reactions involving the OCN⁻ anion, which is abundantly formed in these experiments, provide alternative routes. Irradiation of a sample of OCN⁻:CH₄, where OCN⁻ is formed via the acid-base reaction of HNCO with NH₃, will be interesting to study in future work since this anion is also a well known component of interstellar ice (Boogert et al. 2015).

Belloche et al. (2017) have incorporated reactions 6.5 and 6.6 (see Section 6.1) into the large gas-grain model MAGICKAL (Garrod 2013) and simulated the cold collapse + warm-up phase of a hot core region. Although tailored to the high-mass source SgrB2(N) many of the model features are also expected to be valid for the case of IRAS16293. In this model, HNCO is formed by reaction of NH + CO, a route that has been demonstrated experimentally by Fedoseev et al. (2015b, 2016). Depending on assumptions about the barriers of the grain surface reactions involved in the formation of HNCO and CH₃NCO, abundance ratios HNCO/CH₃NCO of 3-50 following ice sublimation are readily found in the models, consistent with the IRAS16293 observations.

6.5. Conclusions

The main observational and experimental conclusions are listed below:

1. Methyl isocyanate is detected for the first time toward a low mass protostar, IRAS16293, on solar system scales (emission radius of 60 AU). Column densities of $\sim (3-4) \times 10^{15}$ and $\sim (6-9) \times 10^{15} \text{ cm}^{-2}$ are obtained toward source B and A, respectively, yielding $N(\text{HNCO})/N(\text{CH}_3\text{NCO}) = 12$ and 4, with no significant variation between the two sources.
2. The abundance ratios of CH₃NCO relative to the N-bearing species HNCO and CH₃CN are similar to those found toward Orion KL and deviate by at most an order of magnitude from Sgr B2.
3. The isomers of methyl isocyanate, CH₃CNO and CH₃OCN, are not detected. These species are less abundant than CH₃NCO by at least a factor 100 and 10, respectively.

4. HOCN is not found down to $\leq 3 \times 10^{13} \text{ cm}^{-2}$, giving $N(\text{HOCN})/N(\text{HNCO}) \geq 1000$, which makes this an insignificant gas-phase precursor to methyl isocyanate in IRAS16293.
5. Laboratory experiments strongly suggest that it is possible to form CH_3NCO on an icy surface, irradiating CH_4 and HNCO as astronomically relevant precursor species with VUV light, generating methyl radicals as reactive intermediates to form methyl isocyanate.

The detection of CH_3NCO adds to the growing list of complex molecules known to be present around solar mass protostars, showing that the ingredients for prebiotic molecules are abundant. Future deeper searches for even more complex molecules relevant for the origin of life are warranted.

Acknowledgement

Thanks go out to A. Belloche (Max-Planck-Institut für Radioastronomie) for useful input to the original paper and the referee of the publication for the constructive comments. This chapter makes use of the following ALMA data: ADS/JAO.ALMA#2013.1.00278.S. ALMA is a partnership of ESO (representing its member states), NSF (USA) and NINS (Japan), together with NRC (Canada) and NSC and ASIAA (Taiwan), in cooperation with the Republic of Chile. The Joint ALMA Observatory is operated by ESO, AUI/NRAO and NAOJ. Astrochemistry in Leiden is supported by the European Union A-ERC grant 291141 CHEMPLAN, by the Netherlands Research School for Astronomy (NOVA) and by a Royal Netherlands Academy of Arts and Sciences (KNAW) professor prize. CryoPAD2 was realized with NOVA and NWO (Netherlands Organisation for Scientific Research) grants. The work of A.C. was funded by the STFC grant ST/M001334/1. The group of J.K.J. acknowledges support from a Lundbeck Foundation Group Leader Fellowship, as well as the ERC under the European Union's Horizon 2020 research and innovation programme through ERC Consolidator Grant S4F (grant agreement No 646908). Research at the Centre for Star and Planet Formation is funded by the Danish National Research Foundation.

6.6. Appendix

6.6.1. Line list

Table 6.2 contains the full list of detected CH_3NCO , $v_t=0$ transitions toward IRAS16293. A total of 43 lines are observed.

Table 6.2: Unblended lines of CH₃NCO detected toward source B.

Species	Transition	Frequency (MHz)	E_{up} (K)	A_{ij} (s ⁻¹)	g_{up}
CH ₃ NCO, $v_b=0$	(38 0 0 2 – 37 0 0 2)	329675.6	361.3	1.71×10^{-3}	77
CH ₃ NCO, $v_b=0$	(38 1 0 2 – 37 1 0 2)	329732.1	367.3	1.71×10^{-3}	77
CH ₃ NCO, $v_b=0$	(38 -1 0 -3 – 37 -1 0 -3)	329929.3	427.1	1.67×10^{-3}	77
CH ₃ NCO, $v_b=0$	(38 -1 0 2 – 37 -1 0 2)	330611.8	367.3	1.71×10^{-3}	77
CH ₃ NCO, $v_b=0$	(38 1 0 3 – 37 1 0 3)	331251.7	431.6	1.74×10^{-3}	77
CH ₃ NCO, $v_b=0$	(38 0 0 -3 – 37 0 0 -3)	331337.3	423.4	1.70×10^{-3}	77
CH ₃ NCO, $v_b=0$	(38 2 0 3 – 37 2 0 3)	331653.6	447.5	1.72×10^{-3}	77
CH ₃ NCO, $v_b=0$	(38 3 0 -3 – 37 3 0 -3)	332324.9	477.7	1.71×10^{-3}	77
CH ₃ NCO, $v_b=0$	(39 0 0 1 – 38 0 0 1)	334214.7	336.5	1.82×10^{-3}	79
CH ₃ NCO, $v_b=0$	(39 1 39 0 – 38 1 38 0)	334470.6	327.3	1.78×10^{-3}	79
CH ₃ NCO, $v_b=0$	(39 -1 0 1 – 38 -1 0 1)	335432.3	342.5	1.83×10^{-3}	79
CH ₃ NCO, $v_b=0$	(39 2 0 2 – 38 2 0 2)	335521.3	401.3	1.83×10^{-3}	79
CH ₃ NCO, $v_b=0$	(39 3 0 2 – 38 3 0 2)	335973.3	431.1	1.82×10^{-3}	79
CH ₃ NCO, $v_b=0$	(39 0 39 0 – 38 0 38 0)	336339.9	323.7	1.82×10^{-3}	79
CH ₃ NCO, $v_b=0$	(39 2 38 0 – 38 2 37 0)	337737.4	348.4	1.83×10^{-3}	79
CH ₃ NCO, $v_b=0$	(39 0 0 2 – 38 0 0 2)	338235.6	377.6	1.85×10^{-3}	79
CH ₃ NCO, $v_b=0$	(39 2 37 0 – 38 2 36 0)	339028.2	349.0	1.85×10^{-3}	79
CH ₃ NCO, $v_b=0$	(38 3 0 1 – 37 3 0 1)	339370.5	374.5	1.75×10^{-3}	77
CH ₃ NCO, $v_b=0$	(39 1 0 -3 – 38 1 0 -3)	339848.8	448.8	1.88×10^{-3}	79
CH ₃ NCO, $v_b=0$	(39 1 0 3 – 38 1 0 3)	339948.0	448.0	1.88×10^{-3}	79
CH ₃ NCO, $v_b=0$	(39 1 38 0 – 38 1 37 0)	340327.9	333.1	1.88×10^{-3}	79
CH ₃ NCO, $v_b=0$	(39 2 0 -3 – 38 2 0 -3)	340363.3	464.6	1.87×10^{-3}	79
CH ₃ NCO, $v_b=0$	(40 0 0 1 – 39 0 0 1)	342747.6	353.1	1.97×10^{-3}	81
CH ₃ NCO, $v_b=0$	(40 1 0 1 – 39 1 0 1)	344280.7	359.2	1.98×10^{-3}	81
CH ₃ NCO, $v_b=0$	(40 3 0 2 – 39 3 0 2)	344650.3	447.7	1.97×10^{-3}	81
CH ₃ NCO, $v_b=0$	(40 3 38 0 – 39 3 37 0)	344660.0	395.0	1.97×10^{-3}	81
CH ₃ NCO, $v_b=0$	(40 -1 0 -3 – 39 -1 0 -3)	346771.8	459.6	1.95×10^{-3}	81
CH ₃ NCO, $v_b=0$	(40 0 0 2 – 39 0 0 2)	346789.2	394.2	1.99×10^{-3}	81
CH ₃ NCO, $v_b=0$	(40 1 0 2 – 39 1 0 2)	346813.1	400.2	1.99×10^{-3}	81
CH ₃ NCO, $v_b=0$	(40 1 0 -3 – 39 1 0 -3)	348541.5	465.6	2.03×10^{-3}	81
CH ₃ NCO, $v_b=0$	(40 0 0 -3 – 39 0 0 -3)	348768.0	456.2	1.99×10^{-3}	81
CH ₃ NCO, $v_b=0$	(40 -3 0 2 – 39 -3 0 2)	348867.2	447.9	1.99×10^{-3}	81
CH ₃ NCO, $v_b=0$	(41 1 0 1 – 40 1 0 1)	352855.7	376.2	2.13×10^{-3}	83
CH ₃ NCO, $v_b=0$	(41 3 0 2 – 40 3 0 2)	353345.6	464.8	2.12×10^{-3}	83
CH ₃ NCO, $v_b=0$	(41 -1 0 2 – 40 -1 0 2)	356670.2	417.3	2.15×10^{-3}	83
CH ₃ NCO, $v_b=0$	(41 1 40 0 – 40 1 39 0)	357668.8	367.0	2.18×10^{-3}	83
CH ₃ NCO, $v_b=0$	(41 2 0 -3 – 40 2 0 -3)	357766.6	498.4	2.17×10^{-3}	83
CH ₃ NCO, $v_b=0$	(41 0 0 5 – 40 0 0 5)	358444.3	671.4	2.16×10^{-3}	83
CH ₃ NCO, $v_b=0$	(42 1 42 0 – 41 1 41 0)	360081.7	378.0	2.23×10^{-3}	85
CH ₃ NCO, $v_b=0$	(42 2 0 2 – 41 2 0 2)	361199.5	452.4	2.28×10^{-3}	85
CH ₃ NCO, $v_b=0$	(42 1 0 1 – 41 1 0 1)	361425.5	393.7	2.29×10^{-3}	85
CH ₃ NCO, $v_b=0$	(42 3 40 0 – 41 3 39 0)	361770.5	429.5	2.28×10^{-3}	85
CH ₃ NCO, $v_b=0$	(42 3 0 2 – 41 3 0 2)	362063.6	482.2	2.28×10^{-3}	85

6.6.2. $\text{CH}_3\text{NCO } v_b=1$

Figure 6.7 shows the tentative identification of the first excited state of methyl isocyanate.

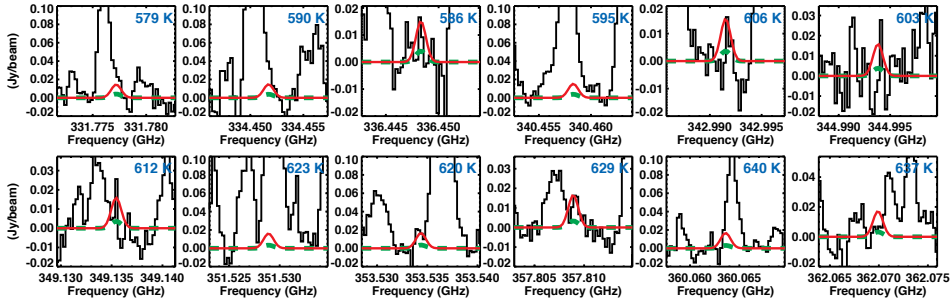


Figure 6.7: Predictions for the $\text{CH}_3\text{NCO } v_b=1$ lines toward source B (red solid: best-fit model for $T_{\text{ex}} = 300$ K, green dashed: best-fit model for $T_{\text{ex}} = 100$ K).

6.6.3. $m/z = 56, 57$ and 58 upon VUV irradiation of pure CH_4 and HNCO samples

Several publications address the energetic processing of pure HNCO and CH_4 ice and much is known about the chemistry that can be induced in these species (Raunier et al. 2004; Bennett et al. 2006; Bossa et al. 2015). Of the known chemical products, none of them contributes to the primary and secondary masses of methyl isocyanate. To verify this, pure methane and isocyanic acid have been VUV irradiated. The HNCO sample (Figure 6.8A) does not show any significant release of these masses. However, after irradiation of methane a substantial amount of $m/z = 56$, coinciding with a lesser amount of $m/z = 58$, is seen releasing at a desorption temperature of 105 K. Some $m/z = 57$ is seen to be released as well, although there is no clear peak found in this case. The resulting contribution of $m/z = 56$ can interfere with the $m/z = 57/56$ amu mass ratio of methyl isocyanate.

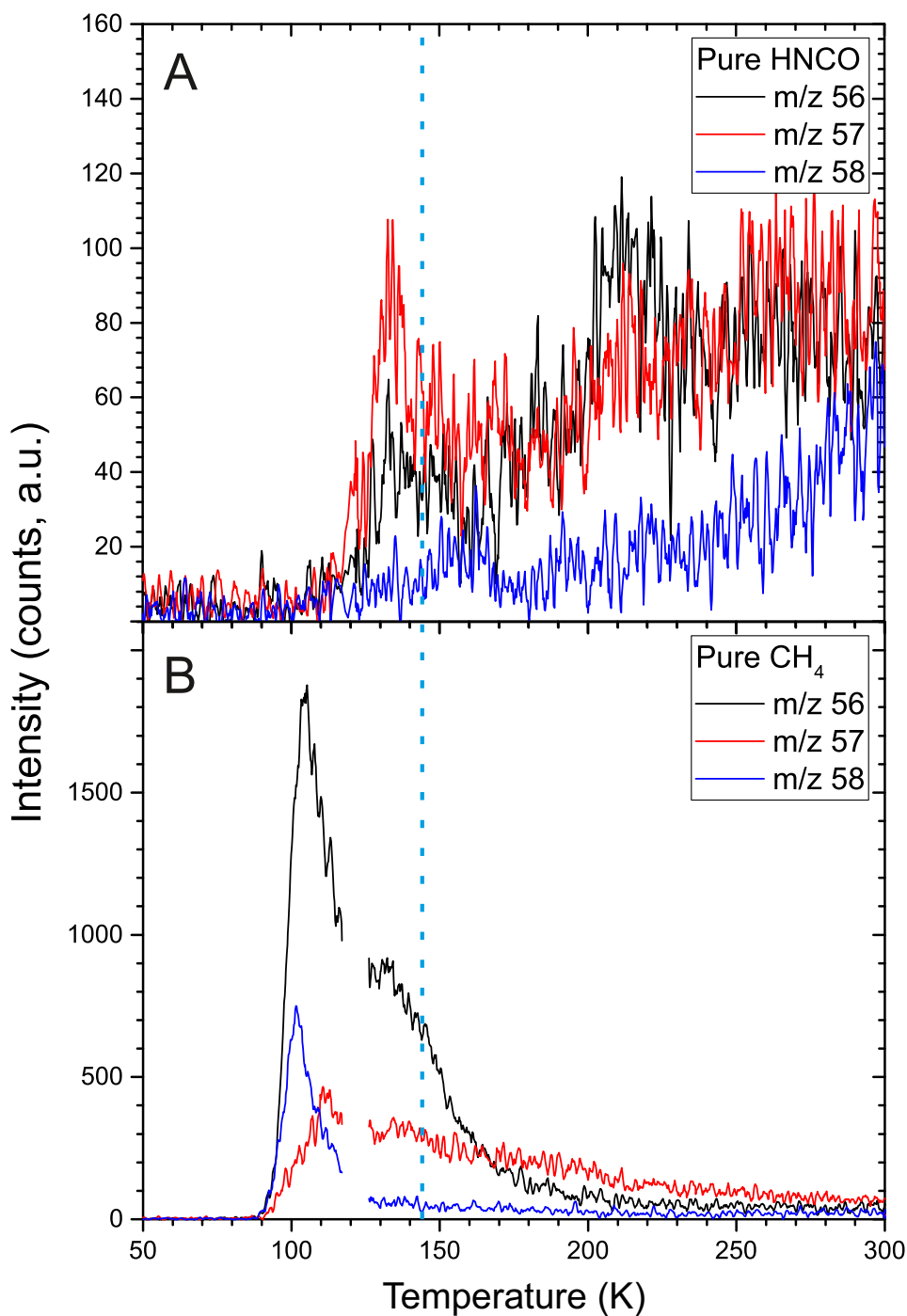
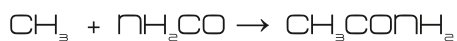


Figure 6.8: TPD trace of $m/z = 57$ (primary mass CH_3NCO), $m/z = 56$ (secondary mass CH_3NCO) and $m/z = 58$ after the irradiation of pure HNCO (A) and pure CH_4 (B). The desorption peak found in the CH_4 :HNCO mixtures is indicated by the dashed line at 145 K.



V-UV



Formation of amides in interstellar relevant ices

N.F.W. Ligterink, J. Terwisscha van Scheltinga, E.F. van Dishoeck & H. Linnartz

7.1. Introduction

Prebiotic molecules resemble functional groups of biotic molecules and are thought to be involved in the formation of life-bearing molecules, such as amino acids, nucleosides and sugars (Herbst & van Dishoeck 2009; Caselli & Ceccarelli 2012). The interstellar presence of prebiotic molecules supports the idea that the building blocks of life may have an extraterrestrial origin. A number of prebiotic molecules have been detected in the ISM, such as the simplest sugar glycolaldehyde (Hollis et al. 2004; Jørgensen et al. 2012; Jørgensen et al. 2016) and methylamine and aminoacetonitril, potential precursors of the amino acid glycine (Kaifu et al. 1974; Belloche et al. 2008). Among prebiotics, molecules with an amide or amide-like (i.e. species that resemble the structure of an amide bond, hereafter generally also called amides) structure are of particular interest because they resemble the peptide bond that binds amino acids, see Fig 7.1. In terrestrial biochemistry amino acids link to form so-called peptide chains that eventually form proteins, the engines of life.

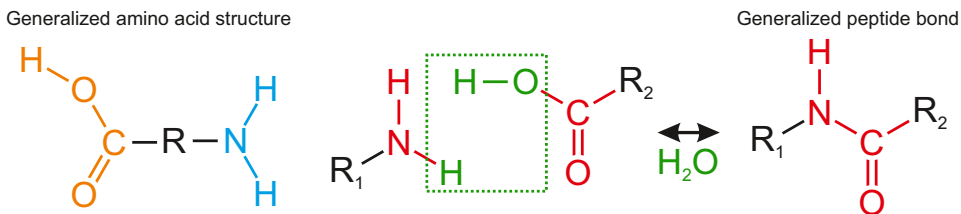


Figure 7.1: Left: General structure of an amino acid, with the acid group in orange and amine group in blue. Center: Binding between an amine and acid group while losing a water molecule. Right: Generalized peptide bonded or amide structure.

Besides being prebiotic molecules, amides are also interesting as tracers of interstellar environments due to their widespread presence throughout the ISM. Isocyanic acid (HNCO) and formamide (NH_2CHO) are the most abundant ones and have been detected in a large variety of interstellar sources (e.g., Bisschop et al. 2007b; Kahane et al. 2013; Adande et al. 2013; Corby et al. 2015; Bergner et al. 2017) and comets, including 67P/Churyumov-Gerasimenko (67P/C-G) (Bockelée-Morvan et al. 2000; Goesmann et al. 2015). Strong observational evidence exists for a formational relationship between HNCO and NH_2CHO in interstellar ice (Bisschop et al. 2007b; López-Sepulcre et al. 2015; Coutens et al. 2016). In the form of the OCN^- anion, HNCO has directly been detected in interstellar ices at abundances as high as 2% with respect to water (Lacy et al. 1984; Gibb et al. 2004; van Broekhuizen et al. 2005). Tentatively, the presence of formamide in interstellar ice has been claimed toward NGC 7538 IRS9 (Raunier et al. 2004).

The more complex molecule acetamide (CH_3CONH_2) has been detected toward Sgr B2 and Orion KL (Hollis et al. 2006; Halfen et al. 2011; Cernicharo et al. 2016; Belloche et al. 2017) and in 67P/C-G (Goesmann et al. 2015; Altwegg et al. 2017). Its formation has been linked with the presence of formamide. Methyl isocyanate (CH_3NCO) has been detected toward Sgr B2 and Orion KL

(Halfen et al. 2015; Cernicharo et al. 2016) and recently also toward the sun-like protostar IRAS 16293–2422 (Ligterink et al. 2017; Martín-Doménech et al. 2017). Its formational origin is likely found in interstellar ices and involves reactions between (H)NCO and CH_3 radicals. Hydrogenation of CH_3NCO can lead to N-methyl formamide (CH_3NHCHO), a molecule that has tentatively been identified toward Sgr B2 (Belloche et al. 2017). Finally, carbamide, also known as urea (NH_2CONH_2), has been tentatively identified toward Sgr B2 (Remijan et al. 2014).

The high interstellar abundances of HNCO and NH_2CHO have resulted in many laboratory studies with the aim to understand their formation paths (Hagen et al. 1979; Gerakines et al. 2004; Raunier et al. 2004; Jones et al. 2011; Islam et al. 2014; Muñoz Caro et al. 2014; Fedoseev et al. 2015b, 2016; Kaňuchová et al. 2016). In these studies, ice mixtures containing a source of carbon, like CH_3OH or CO, and a source of nitrogen, such as HCN, HNCO, NH_3 , N_2 or NO are hydrogenated and/or energetically processed. A number of mechanisms have been shown to produce these species, such as the $\text{NH} + \text{CO}$ reaction to produce HNCO (Fedoseev et al. 2015b), $\text{NH}_2 + \text{CHO}$ radical combination to produce NH_2CHO (Jones et al. 2011) and hot, i.e., energetic H-atom addition to HNCO can explain the formation of NH_2CHO (Raunier et al. 2004).

The larger amides urea and acetamide have been detected in various experiments (e.g., Berger 1961; Agarwal et al. 1985; Bernstein et al. 1995; Raunier et al. 2004; Henderson & Gudipati 2015; Förstel et al. 2016), but formation mechanisms have not been experimentally investigated. Some reactions have been proposed, such as the $\text{NH}_2 + \text{NH}_2\text{CO}$ radical addition to form NH_2CONH_2 (Agarwal et al. 1985). Modelling investigations have predicted the formation of CH_3CONH_2 through the $\text{CH}_3 + \text{HNCO}$ reaction followed by hydrogenation (Garrod et al. 2008) or the hydrogen abstraction of NH_2CHO followed by CH_3 addition (Belloche et al. 2017). The formation of N-methylformamide has been claimed in VUV irradiated $\text{CH}_3\text{NH}_2:\text{CO}$ ice mixtures through the reaction $\text{CH}_3\text{NH} + \text{CHO}$ (Bossa et al. 2012), while modelling investigations have shown that hydrogenation of CH_3NCO is one of the main channels of CH_3NHCHO formation (Belloche et al. 2017). Recently, the reaction $\text{CH}_3 + (\text{H})\text{NCO}$ was shown to result in the formation of CH_3NCO (Ligterink et al. 2017), a process that likely in a similar way takes places on interstellar dust grains.

In this work we aim to elucidate the chemical network that links various small amides that have been detected in the ISM and to explain their formation. This work is linked to that of Ligterink et al. (2017) and investigates reactions that can occur simultaneously with the formation of CH_3NCO . The possible hydrogen atom addition reaction $\text{CH}_3\text{NCO} + \text{H} \rightarrow \text{CH}_3\text{NHCHO}$ is one that needs further investigation. Two types of hydrogen addition can occur. With so-called hot H-atom addition the hydrogen atoms are produced in an energetic dissociation process, for example VUV induced photodissociation, and carry excess energy which allows these atoms to more easily overcome energy barriers. Hydrogenation is the term used for cold or low energy hydrogen atom addition. These atoms are usually made with hydrogen dosing beams (e.g., Fuchs et al. 2009), but can also occur when hydrogen atoms produced in energetic processes are thermalised by their surroundings. Also the radical addition reactions $\text{CH}_3 + \text{NHCHO} \rightarrow \text{CH}_3\text{NHCHO}$ and $\text{CH}_3 + \text{NH}_2\text{CO} \rightarrow \text{CH}_3\text{CONH}_2$ are possible. To

this extend mixtures of HNCO:CH₄ are VUV irradiated in order to form the CH₃ radical from methane and various intermediate radicals and products of HNCO. HNCO in the form of OCN⁻ and CH₄ are known to be present in interstellar ices with median abundances of 0.6 and 4.5 % with respect to water, respectively (Boogert et al. 2015). The resulting products from reactions between the two are identified and analysed.

Section 7.2 discusses the laboratory set-up and protocol. The results of the experiments are presented in Sec. 7.3 and discussed in Sec. 7.4. The conclusions of this work are presented in Sec. 7.5.

7.2. Experimental

7.2.1. Setup and protocol

For this study the CryoPAD2 setup is used, which has been described in Ligterink et al. (2017). In short it consists of a central chamber at ultra-high vacuum conditions ($P \leq 10^{-10}$ mbar). A cryogenically cooled gold-coated reflective surface is positioned at the center of the chamber. On this surface gases are deposited by direct deposition to form an ice layer, simulating the interstellar icy dust grain environment. The output of a Microwave Discharge Hydrogen-flow Lamp (MDHL, Ligterink et al. 2015, and references therein) is directed at the surface and used to energetically process the ice. Chemical changes within the ice are traced by Reflection Absorption IR Spectroscopy (RAIRS) and mass spectrometry in combination with Temperature Programmed Desorption (TPD).

MDHLs generally have strong emission at the Lyman- α transition at 121.6 nm and H₂ continuum emission between 140-160 nm. In this work we make use of lamp conditions optimized for Lyman- α rich or poor emission to process the ice samples, see Fig. 7.2, in order to test the influence of high energetic Lyman- α radiation on the chemistry in the ice. This can for example influence the production of CH₃ radicals from CH₄ as can be derived from the methane photo absorption cross section, which is high around the Lyman- α transition, but low for wavelengths longer than 140 nm (Cruz-Diaz et al. 2014b). The total photon flux is $(1.1 \pm 0.1) \times 10^{14}$ photons s⁻¹ for the Lyman- α rich emission, while it is $(6.1 \pm 1.0) \times 10^{13}$ photons s⁻¹ in the Lyman- α poor case.

Gases used during the experiments are CH₄ (Linde Gas, 99.995% purity), ¹³CH₄ (Sigma-Aldrich, 99% purity) and CO (Linde Gas, 99.995% purity). The regular methane gas contains the natural isotope abundances of ¹²/¹³C of ~90. However, throughout this chapter methane gas will generally be called ¹²CH₄ to stress the mass difference in those experiments making use of either ¹²C or ¹³C rich gas. Gas-phase HNCO is produced from thermal decomposition of cyranic acid (Sigma-Aldrich, 98% purity), the solid trimer of HNCO, similar to the protocol used by van Broekhuizen et al. (2004). Freeze-pump-thaw cycles are used to purify the HNCO sample and mainly remove CO₂, O₂ and N₂. Hydrogen cyanide (HCN) impurities are sometimes present in the prepared gas, but can not be removed by this technique. Samples of solid acetamide (Sigma-Aldrich, 99% purity) and liquid N-methyl formamide (Sigma-Aldrich, 99% purity) are used for verification experiments.

Gas mixtures are prepared in a gas mixing line by volume mixing with an

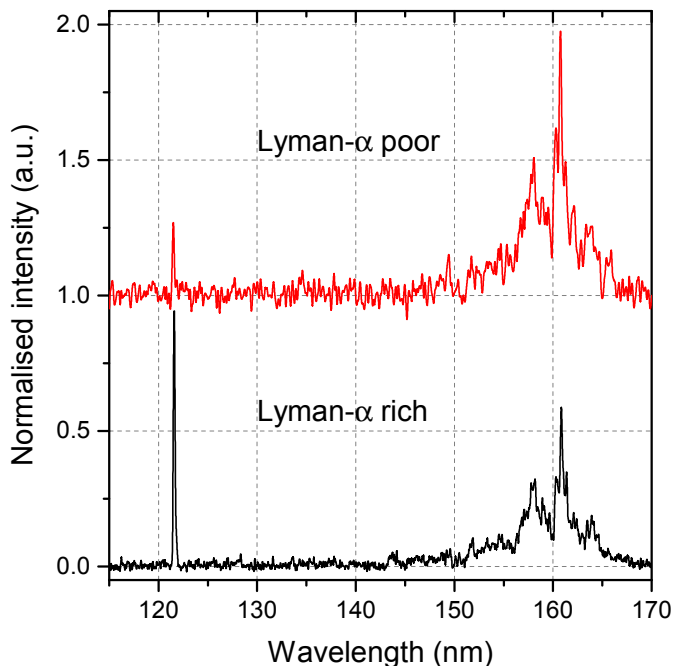


Figure 7.2: Vacuum-UV spectrum of the MDHL emission between 115 and 170 nm. The top spectrum (red) shows lamp emission poor in Lyman- α , while the bottom spectrum (black) shows lamp emission rich in Lyman- α .

gas independent gauge. The mixture is deposited on the gold-coated substrate at 20 K. Residual gases of the deposition are removed from the chamber during a short waiting period until a pressure of $\sim 1 \times 10^{-10}$ mbar is reached. Next, the samples are VUV irradiated for 20 minutes, corresponding with a total fluences of 1.3×10^{17} or 7.3×10^{16} photons for the Lyman- α rich and poor case, respectively. After irradiation the sample is heated from 20 to 300 K and the desorbing contents are analysed with a sensitive Quadrupole Mass Spectrometer (QMS) over a large range of masses. After deposition and during irradiation and TPD, IR spectra are recorded at $1\text{-}2 \text{ cm}^{-1}$ resolution using a Fourier Transform InfraRed Spectrometer (FTIRS, $500\text{-}4000 \text{ cm}^{-1}$) to trace chemical changes in the ice.

7.2.2. Data analysis

IR data

RAIR spectra of the experiments are baseline subtracted and IR features are identified by comparing with literature data. Deviations between literature values and this work can arise from differences in transmission versus reflection

Table 7.1: Peak positions and transmission bandstrengths of parent and product species

Species	band	Peak position (cm^{-1})		Band strength cm molecule^{-1}
		Literature	Experiment*	
HNCO^a	OCN str.	2260	2266	7.8×10^{-17}
CH_4^b	d-str.	1301	1302	7.3×10^{-18}
CH_4^b	d-str.	3010	3010	1.1×10^{-17}
CO^c	CO str.	2138	2142	1.1×10^{-17}
$\text{OCN}^{-,a}$	OCN str.	2160	2170	1.3×10^{-16}
CO_2^c	CO a-str.	2342	2341	7.6×10^{-17}
$\text{HCN}^{d,**}$	CN str.	2099	2108	–
$\text{CH}_3\text{NCO}^{e,**}$	NCO a-str.	2322	2322	–
CH_3CH_3^f	CH_3 d-str.	2975	2976	6.5×10^{-18}
$\text{NH}_4^{+,a}$	deform.	1485	1466	4.6×10^{-17}
$\text{NH}_2\text{CHO}^{g,h}$	CO str.	1700	~ 1687	3.3×10^{-17}
$\text{NH}_2\text{CONH}_2^h$	CO str.	1590	–	–
$\text{NH}_2\text{CONH}_2^h$	NH s-bend	1675	~ 1687	–
$\text{NH}_2\text{CONH}_2^h$	NH a-bend	1630	~ 1687	–

Notes. *Peak positions found for experiment 1 (see Table 7.2); **Indicates IR data obtained from reflection experiments. ^avan Broekhuizen et al. (2004), water poor conditions; ^bHudgins et al. (1993); Boogert et al. (1997); ^cBouilloud et al. (2015); ^dGerakines et al. (2004); ^eLigterink et al. (2017); ^fGerakines et al. (1996); ^gWexler (1967); ^hRaunier et al. (2004)

values or matrix effects. The column density (N_{species}) of an IR feature is determined from its integrated band area ($\int_{\text{band}} \tau dv$) by:

$$N_{\text{species}} = \frac{1.1}{3.4} \ln(10) \frac{\int_{\text{band}} \tau dv}{A_{\text{band}}}, \quad (7.1)$$

where A_{band} is the bandstrength of a specific band of a species and $\frac{1.1}{3.4}$ is a RAIRS scaling factor. Due to longer pathlength through the ice and dipole surface coupling, the RAIRS sensitivity differs from transmission IR spectroscopy and therefore bandstrength values are different from transmission bandstrength values. For the CryoPAD2 setup the bandstrength of the CO stretch mode of carbon monoxide at 2138 cm^{-1} is determined to be $3.4_{-0.5}^{+0.5} \times 10^{-17} \text{ cm molecule}^{-1}$ (Ligterink et al. 2017, subm.). Using the transmission bandstrength of $1.1 \times 10^{-17} \text{ cm molecule}^{-1}$ for the same CO mode (Bouilloud et al. 2015) and assuming that for identical conditions band strengths of different molecules scale in the same way, the general scaling factor between RAIRS and transmission IR spectroscopy of $\frac{1.1}{3.4}$ is found.

Table 7.1 gives an overview of band positions and bandstrength values of parent and expected product species. Most IR parameters are taken from transmission experiments available from literature, with the exception of the HCN CN stretching mode and CH_3NCO NCO asymmetric stretching mode

(Gerakines et al. 2004; Ligterink et al. 2017, respectively).

Recently methane gained interest due to inconsistencies in literature on the assignment of methane modes in amorphous or crystalline phase (Gerakines & Hudson 2015). Experiments in this work are conducted with ices at temperatures of 20 K and therefore we consider the methane to be of crystalline nature. Consequently, we choose to use a *crystalline bandstrength value* by applying the same correction as performed by Boogert et al. (1997) on data recorded by Hudgins et al. (1993) to retrieve the bandstrength for the CH₄ mode at 3010 cm⁻¹ as 1.1×10^{-17} cm molecule⁻¹. Finally, because no water is used in these experiments, the water-poor bandstrength values listed by van Broekhuizen et al. (2004) are used for HNCO and OCN⁻.

Temperature Programmed Desorption QMS data

During TPD, parent and product species desorb from the gold surface and are measured by the QMS, with an ionization source tuned to 70 eV. Each species has a characteristic desorption temperature and fragmentation pattern which can be used for identification. However, this is not always as straight forward. Species can have desorption temperatures close together or co-desorb with each other. A desorption signal at a certain m/z measured by the QMS can therefore have two or more contributions. In these experiments particularly the parent species HNCO, which desorbs around 120 K, can contaminate the TPD signal of other species. Due to its high abundance compared to reaction products, even small fragmentation channels of HNCO, such as m/z 28 and 29, can influence product fragmentation patterns. Many of the products studied in this work display similar fragmentation patterns and desorption temperatures and therefore complicate the interpretation of the TPD signal.

A number of measures are taken to circumvent some of the problems described above. First, the focus of the TPD data is on the region between 150 and 300 K, to avoid the HNCO desorption peak as much as possible. This also means that potentially co-desorbing species with HNCO are not extensively analysed. Second, isotopic labelling is used to distinguish products. Third, a specific analysis protocol is used to determine fragmentation patterns of desorbing species; The QMS output is first corrected for its work functions. For a desorption peak, all the masses that desorb at or close to the same temperature are selected. If necessary, baseline subtraction is performed to remove contributions of other desorbing species. Next, the intensity of the signal at each m/z is determined at the peak desorption temperature. These signals are normalised, mostly to the highest signal or highest m/z in the feature. The resulting fragmentation pattern is compared with literature and *in-situ* measured fragmentation patterns of molecules.

7.2.3. Fragmentation patterns and desorption temperatures

This work relies for a large part on molecule specific desorption temperatures and mass fragmentation patterns. Desorption temperatures of many small species, like CO, water or methanol, have been well studied. However, for larger species such data are often not available. This includes two the potential isomeric products CH₃NHCHO and CH₃CONH₂. Therefore, the desorption temperatures

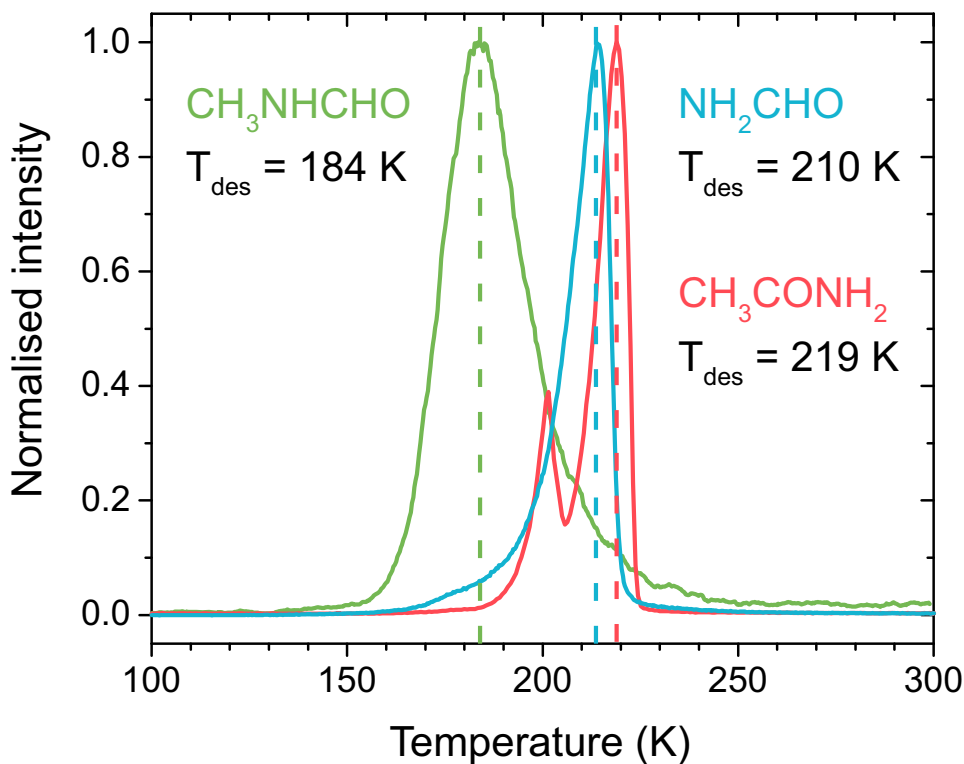


Figure 7.3: TPD traces of m/z 59 of pure N-methylformamide (green), pure formamide (blue) and pure acetamide (red).

of these two species are measured in the CryoPAD2 setup. Figure 7.3 shows the TPD traces of these two molecules at m/z 59, the main mass of both molecules. The peak desorption temperature of N-methylformamide is found at 184 K, while that of acetamide is found at 219 K. The origin of the smaller peak at ~ 200 K in the acetamide TPD trace is unknown, but could be the result of acetamide desorption due to a phase change in the ice. Another important product is formamide, for which the desorption temperature is determined to be 210 K (see Fig. 7.3).

Most fragmentation patterns of parent and possible product species are available in the NIST database¹, listed for an ionization energy of 70 eV. For N-methylformamide and acetamide the NIST fragmentation patterns are compared with *in situ* measured fragmentation patterns, see Fig. 7.4. The general structure of both patterns is similar for each molecule. N-Methylformamide has its main fragmentation channels around m/z 30 and 29 (the CH_3NH fragment), while those of acetamide are found at m/z 44, 43 and 42 (the NH_2CO fragment). However, deviations in pattern intensities are visible, most noticeable in the m/z

¹NIST Mass Spec Data Center, S.E. Stein, director, "Mass Spectra" in NIST Chemistry WebBook, NIST Standard Reference Database Number 69, Eds. P.J. Lindstrom and W.G. Mallard, National Institute of Standards and Technology, Gaithersburg MD, 20899, <http://webbook.nist.gov>.

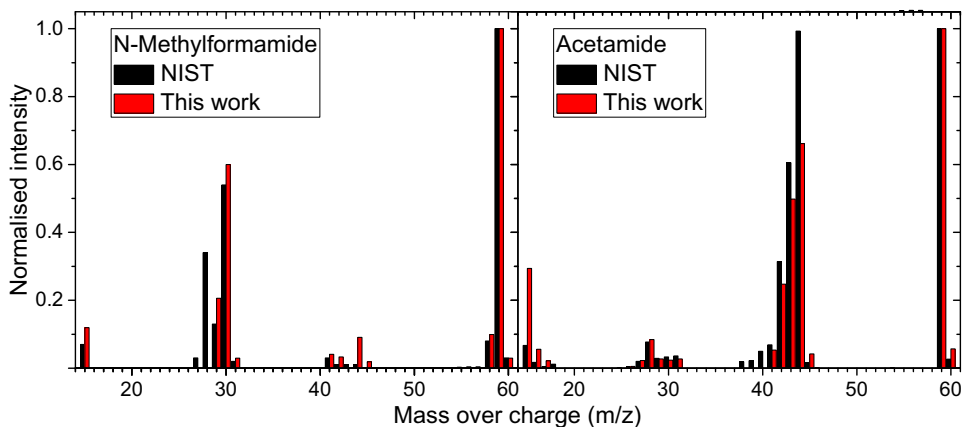


Figure 7.4: Fragmentation pattern comparison between NIST data and values measured in this work for N-methylformamide (top) and Acetamide (bottom).

44 channel of acetamide. Throughout this work the fragmentation patterns of N-methylformamide and acetamide presented here will be used. Fragmentation patterns of other species rely on NIST and literature data.

7.3. Results

7.3.1. Identification of the main products

The identification of products in the VUV processed $\text{CH}_4:\text{HNCO}$ mixed ices is mainly based on three experiments. These are a 1:1 $\text{HNCO}:\text{C}^{12}\text{CH}_4$ mixed ice, a pure HNCO ice and a 1:1 $\text{HNCO}:\text{C}^{13}\text{CH}_4$ mixture. Table 7.2 lists these as (1-3) together with other experiments performed in this work. In the following subsections the IR spectroscopic data of experiment 1 and mass spectrometric data of experiment 1 to 3 are analysed.

IR analysis of VUV processed ice

Figure 7.5 shows the IR spectrum between 1200 and 3100 cm^{-1} of the $\text{HNCO}:\text{CH}_4$ mixture (experiment 1) before and after VUV irradiation with a fluence of 1.3×10^{17} photons. Before irradiation, besides the HNCO band at 2266 cm^{-1} and the CH_4 bands at 1302 and 3010 cm^{-1} , trace amounts of HCN and CO_2 contamination are visible at 2108 and 2341 cm^{-1} , respectively. After processing, spectroscopic features appear that can be assigned to CH_3CH_3 , $\text{OCN}^-\text{NH}_4^+$ and CO . These are known products of VUV processing of pure methane and isocyanic acid ice. The presence of these products indicates that the CH_3 radical is formed and that HNCO fragments into CO and NH (or N and H separate). The NH radical reacts with H atoms or strips them from other molecules to form NH_3 , which engages in an acid-base reaction with HNCO to form $\text{OCN}^-\text{NH}_4^+$.

A feature in the wing of the HNCO peak at 2322 cm^{-1} indicates the formation of CH_3NCO , as was discussed in a previous study by Ligterink et al. (2017). At

Table 7.2: Overview of performed experiments, giving deposited material at the start of the experiment and irradiation source.

Exp.	$N(\text{HNCO})$	$N(\text{CH}_4)$ ML	$N(\text{CO})$	Lyman- α High/Low
1	14.3	17.0	–	H
2	17.4	–	–	H
3	15.1	15.7 ^a	–	H
4	29.9	5.5	–	H
5	11.4	24.6	–	L
6	2.9	8.5	95.6	L
7	4.8	13.9	164.2	L

Notes. ^aExperiment using $^{13}\text{CH}_4$, bandstrength value of 1.1×10^{-17} is assumed to apply to the $^{13}\text{CH}_4$ degenerate stretching mode as well.

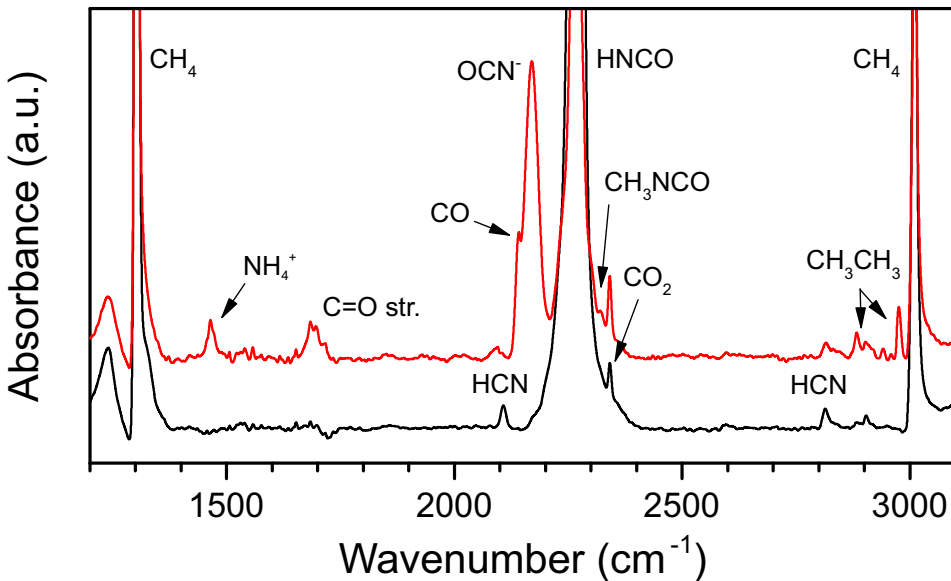


Figure 7.5: IR spectrum between 1200 and 3100 cm^{-1} before (black) and after (red) irradiation of the $\text{HNCO}:\text{}^{12}\text{CH}_4$ ice mixture of experiment 1.

$\sim 1687\text{ cm}^{-1}$ another feature is seen. In VUV processing of pure HNCO ice, it was identified as contributions of the H_2CO and NH_2CHO C=O stretch modes and NH bending modes of NH_2CONH_2 (Raunier et al. 2004). These species likely contribute to this feature, but can not be clearly distinguished. More complex amides, such as N-methylformamide and acetamide can contribute to this feature as well. Since other spectroscopic features characteristic of complex amides are not clearly identified in the IR spectrum, mass spectrometry must be used to identify these species. An overview of the identified peak positions in experiment 1 is given in Table 7.1.

Primary amide formation seen in TPD

Figure 7.6 shows the TPD traces between 150 and 300 K of the main masses of the simplest, or primary, amides that can be formed from $\text{HNCO}:\text{CH}_4$ ice mixtures. These masses are m/z 45 for NH_2CHO , m/z 59 for either CH_3CONH_2 or CH_3NHCHO and m/z 60 for NH_2CONH_2 . The secondary mass channel of HNCO, m/z 42, is included as well to trace HNCO. The panels show from top to bottom the results of the $^{12}\text{CH}_4:\text{HNCO}$, HNCO and $^{13}\text{CH}_4:\text{HNCO}$ experiments (experiment 1, 2 and 3, respectively).

In each of the panels a prominent trailing slope of m/z 42, with a desorption feature between 205 and 210 K is seen. The trailing slope is due to residual gas of the main HNCO desorption peak at 120 K. The desorption feature is caused by the thermal decomposition of the $\text{OCN}^-\text{NH}_4^+$ (or potentially other cations) salt complex and subsequent desorption of HNCO.

Three desorption peaks of m/z 45, 59 and 60 are visible at ~ 207 , ~ 215 and ~ 267 K, respectively. m/z 45 and 60 show up in all panels, including the irradiated pure HNCO ice, and are therefore photoproducts directly resulting from HNCO. Furthermore the desorption peak of m/z 45 at 207 K is close to the pure formamide desorption temperature of 210 K. This feature we identify therefore as formamide. Urea is a known product of HNCO processing (Raunier et al. 2004) and the position of the TPD trace is consistent with TPD traces of urea obtained by Förstel et al. (2016). Thus, the m/z 60 TPD trace is identified as urea.

The m/z 59 feature is caused by a reaction between CH_4 and HNCO, as can be inferred from its non-presence in the pure HNCO experiment and 1 amu mass shift to m/z 60 in the $\text{HNCO}:\text{CH}_4$ experiment. Therefore this product is either CH_3NHCHO or CH_3CONH_2 . Other isomers like acetaldoxime (CH_3CHNOH) and nitrosoethane ($\text{CH}_3\text{CH}_2\text{NO}$) are deemed unlikely to be responsible for the m/z 59 feature, due to the many fragmentation and reaction steps that need to be invoked to form these products. The desorption peak of m/z 59 at 215 K is close to the desorption temperature of pure acetamide at 219 K. Desorption temperatures measured from pure ices are known to shift in mixed ices due to differences in binding energies of co-desorption effects. One could make the same case for N-methylformamide and claim that it is trapped in the remaining ice, mainly $\text{OCN}^-\text{NH}_4^+$ and NH_2CHO . This seems very unlikely however, due to the relatively volatile nature of CH_3NHCHO . One would expect it to desorb before or with the signal of NH_2CHO and $\text{OCN}^-\text{NH}_4^+$, which is not the case for the m/z 59 desorption feature in these TPD traces. Therefore, the m/z 59 feature is very likely the result of acetamide formation in the ice in $\text{CH}_4:\text{HNCO}$ mixtures.

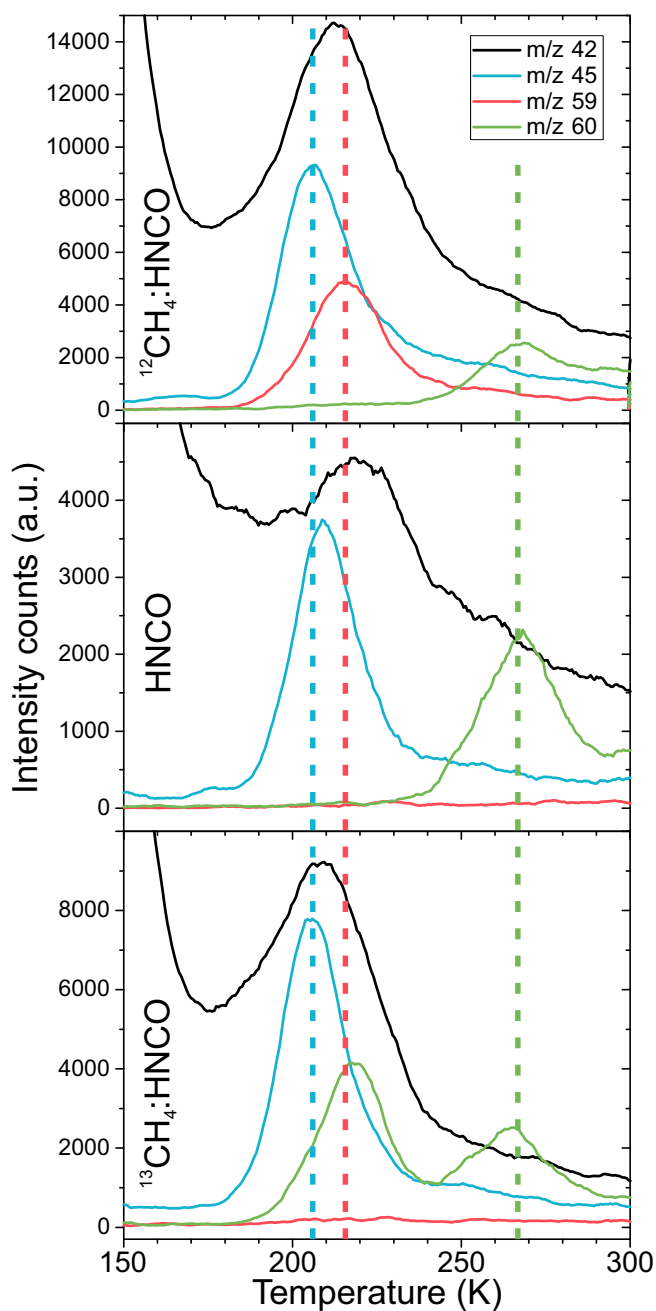


Figure 7.6: TPD traces of m/z 42 (black, HNCO), 45 (blue, NH_2CHO), 59 (red, CH_3CONH_2) and 60 (green, NH_2CONH_2) between 150 and 300 K of VUV processed HNCO: $^{12}\text{CH}_4$ (experiment 1, top), pure HNCO (experiment 2, middle) and HNCO: $^{13}\text{CH}_4$ (experiment 3, bottom) ice. Dashed lines indicate the desorption peaks of products.

Table 7.3: Mass fragmentation patterns of NH_3 , HNCO , NH_2CHO and CH_3CONH_2 at selected masses.

m/z	NH_3	HNCO^a	NH_2CHO	$\text{CH}_3\text{CONH}_2^b$
15	0.08	0.07	0.01	0.29
16	0.80	–	0.12	0.06
17	1.00	–	0.33	0.02
27	–	0.02	0.08	0.02
28	–	0.07	0.06	0.08
29	–	0.14	0.34	0.03
30	–	0.02	–	0.02
31	–	–	–	0.03
42	–	0.22	0.02	0.25
43	–	1.00	0.11	0.50
44	–	0.02	0.25	0.66
45	–	–	1.00	0.04
59	–	–	–	1.00

Notes. ^aFragmentation pattern from Bogan & Hand (1997), ^bFragmentation pattern measured in this work.

Methylamine seen in TPD

The analysis of the mass fragmentation patterns of NH_2CHO , $\text{OCN}^-\text{NH}_4^+$ and CH_3CONH_2 is challenging due to their similar fragmentation patterns and proximity in desorption temperature (200–220 K). This point is emphasised in Table 7.3, which shows the fragmentation patterns of these molecules normalised to their main fragment for the most prominent masses. For example, the acetamide fragmentation pattern at m/z 44, 43 and 42 is difficult to match due to contributions of NH_2CHO and HNCO fragmentation channels. On the other hand it is also clear that these four species hardly contribute to fragment masses of m/z 30 and 31 (highlighted in red). The presence of these two masses as significant desorption features at ~ 213 K is therefore peculiar (see top panel Fig. 7.7). In the experiment making use of $^{13}\text{CH}_4$ the same pattern is seen to shift to m/z 31 and 32 (see bottom panel Fig. 7.7).

This signal can not be explained as being a fragmentation channel of N-methylformamide. For one, the respective m/z 30/59 and m/z 31/60 ratios are ~ 2.5 in both isotope experiments, which is much larger than the m/z 30/59 ratio of 0.6 of the pure N-methylformamide fragmentation pattern. Also, m/z 31 (or m/z 32 in the ^{13}C experiment) is not a prominent feature in the N-methylformamide fragmentation pattern (see Fig. 7.4). Another product must be responsible for these mass features and, within the constraints given by the experiment, this is likely methylamine (CH_3NH_2). A comparison between the m/z 31/30 (or 32/31) fragmentation channel (inset Fig. 7.7) shows that the experimental ratios match quite well with the given NIST value. The small deviations may be explained by minor contributions of fragmentation channels of HNCO and NH_2CHO to m/z 30 as can be distinguished with the $^{13}\text{CH}_4:\text{HNCO}$

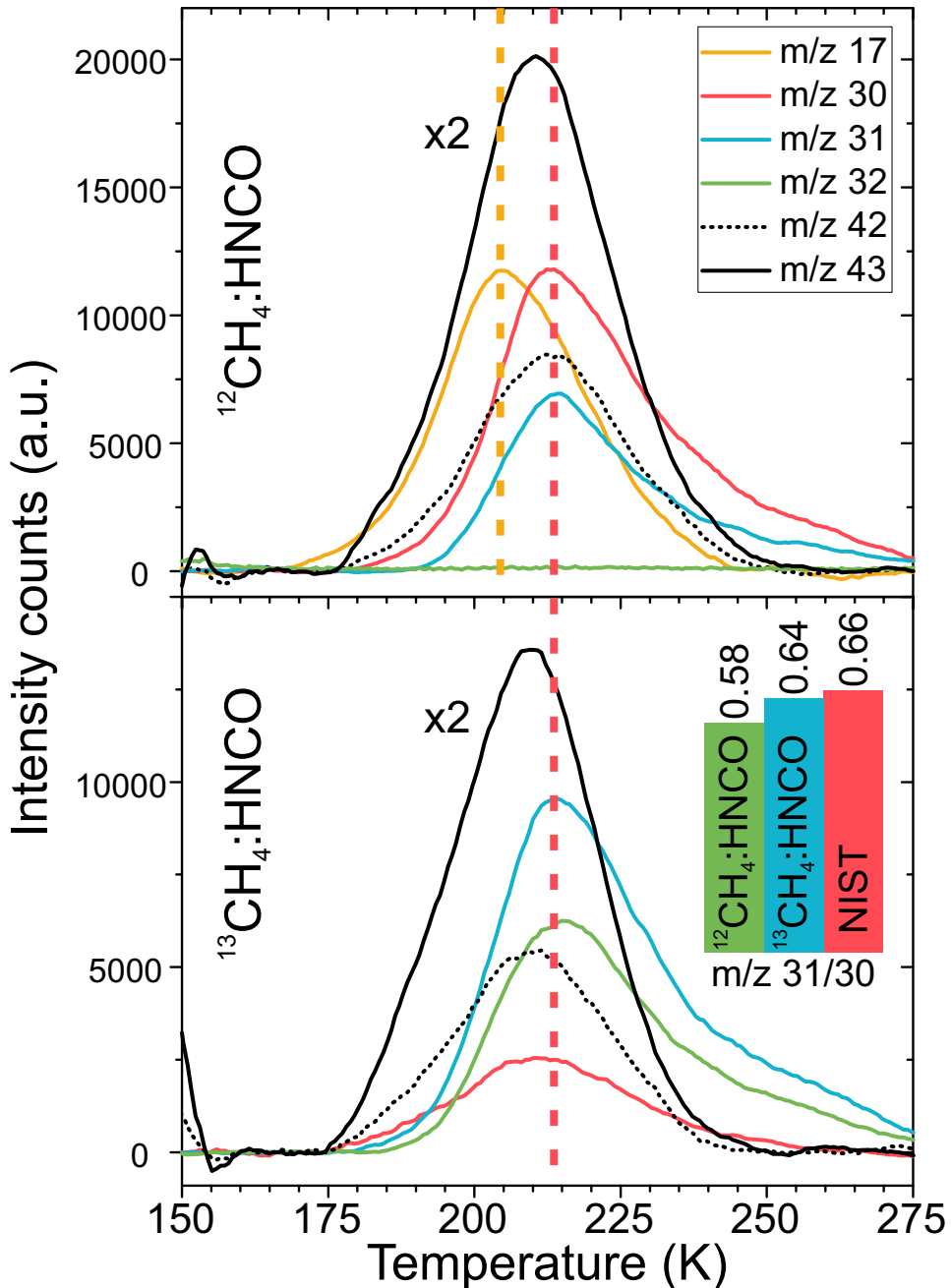


Figure 7.7: TPD trace of m/z 17 (yellow), 30 (red), 31 (blue), 32 (green), 42 (black dashed) and 43 (black, scaled by factor 1/2) of $\text{HNCO}:\text{}^{12}\text{CH}_4$ (experiment 1, top) and $\text{HNCO}:\text{}^{13}\text{CH}_4$ (experiment 3, bottom) ice. The dashed yellow line indicates the peak desorption temperature of m/z 17 and the red dashed line indicates the peak desorption temperature of m/z 30, 31 and 32. The inset gives the m/z 31/30 ratio for the two experiments and as given in the NIST database.

experiment. Comparisons of the m/z 29/30 and 28/30 ratios would help to further strengthen the identification of methylamine, however both HNCO and NH_2CHO have prominent fragmentation channels at these masses and therefore it is not possible to determine reliable ratios for these masses.

The peak desorption of m/z 30 and 31 occurs at 213 K, which is substantially higher than the desorption temperature of pure methylamine at 114 K (Theule et al. 2011). This is due to the formation of the $\text{OCN}^- \text{CH}_3\text{NH}_3^+$ salt complex. Just like ammonia, methylamine is a strong base and therefore readily engages in acid-base reactions with HNCO. Both $\text{OCN}^- \text{NH}_4^+$ and $\text{OCN}^- \text{CH}_3\text{NH}_3^+$ complexes are seen to decompose at different temperatures, as can be seen by the release of m/z 17 (ammonia) at 205 K and m/z 30 and 31 at 213 K, see Fig. 7.7. The desorption of HNCO around 215 K is therefore due to the decomposition of both salt complexes.

Secondary amides and larger species seen in TPD

The production of more complex species is also seen in these processed ices at a low level. Three features at m/z 73, 74 and 88 are detected in the TPD traces of $\text{CH}_4\text{:HNCO}$ ice, see Fig. 7.8 (note the low signal count compared to Figs. 7.6 and 7.7). The first feature of m/z 73 at 218 K does not show up in the processed pure HNCO sample. In the mixture with $^{13}\text{CH}_4$ the feature shows up at m/z 75, indicating that two $^{13}\text{C}_x$ groups are part of this product. The m/z 74 feature at 258 K also does not show up in the pure HNCO processed ice and shifts by one mass to m/z 75 in the $^{13}\text{CH}_4$ mixture. Therefore this product incorporates only one $^{13}\text{C}_x$ group. m/z 88 is seen in all three the panels around 250 K. Since it is observed in the pure HNCO ice and no isotope shifts are seen, it must be a product of HNCO products or intermediates. Note that the low intensity signals limits the efficiency with which new products can be identified. For example, the middle panel of Fig. 7.8 seems to show a double peak which is not seen in the other two panels. This can hint to another product, but may also just be noise in the signal. Similarly, the bottom panel of Fig. 7.8 does a small feature at m/z 73, which can be a product that was not covered in the mass range of the top panel (experiment 1). For the moment, three relatively clear features of different products are seen, but potentially more complex products are present in these processed ices.

The secure identification of the three features is difficult because desorption temperatures are not available for candidate species and matching fragmentation patterns is hindered due to overlap with fragmentation channels of other species, mainly NH_2CHO , CH_3CONH_2 and NH_2CONH_2 . Nevertheless, some candidates can be suggested, especially when one assumes that these higher mass species are derived from or related to the first generation of amides. For the m/z 73 signal propionamide ($\text{CH}_3\text{CH}_2\text{CONH}_2$), N-methylacetamide ($\text{CH}_3\text{NHCOCH}_3$) and dimethylformamide ($(\text{CH}_3)_2\text{NCHO}$) could be responsible. The latter two seem unlikely because they involve a $\text{CH}_3\text{-N}$ bond, while the simplest of such species, N-methylformamide or CH_3NHCHO , was not detected as a product in these mixtures. The two most likely options for m/z 74 are methylurea ($\text{CH}_3\text{NHCONH}_2$) and 2-amino acetamide ($\text{NH}_2\text{CH}_2\text{CONH}_2$). Finally, for $m/z = 88$ two options are oxamide ($\text{NH}_2\text{-(CO)-(CO)-NH}_2$) or 1,2-hydrazinedicarboxaldehyde (CHO-NH-NH-CHO).

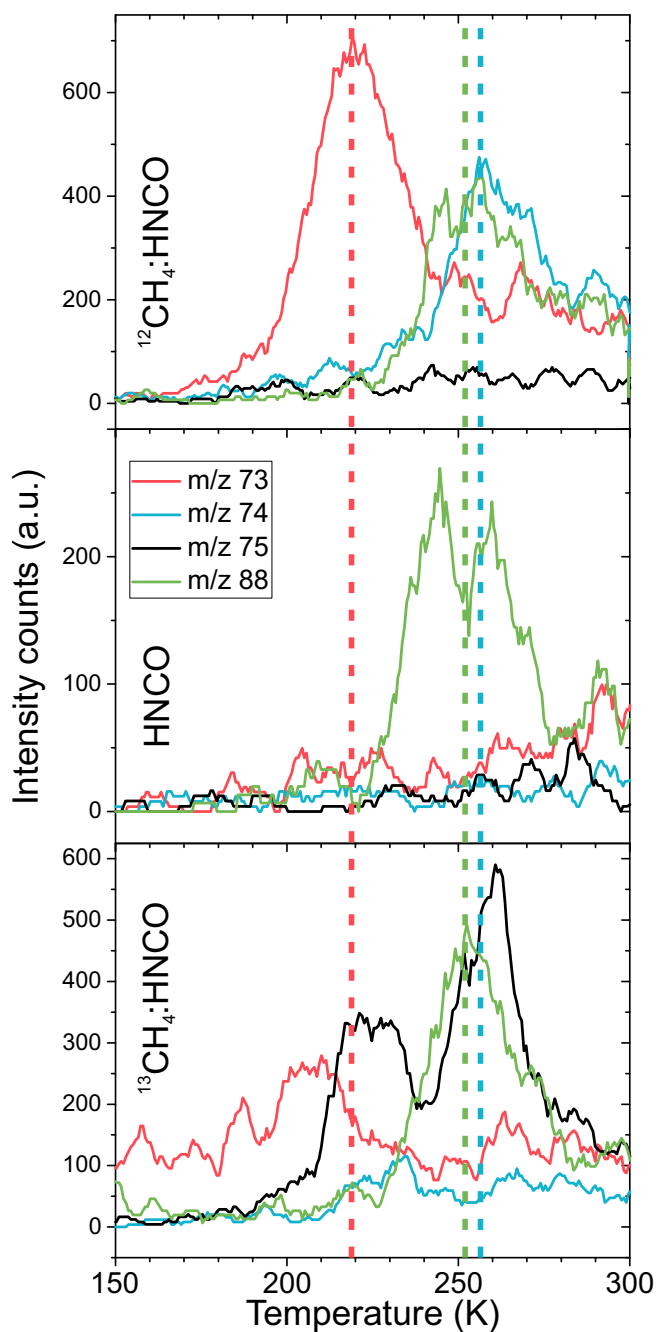


Figure 7.8: TPD of m/z 73 (red), 74 (blue), 75 (black) and 88 (green) between 150 and 300 K of VUV processed $\text{HNCO}:\text{}^{12}\text{CH}_4$ (top), HNCO (middle) and $\text{HNCO}:\text{}^{13}\text{CH}_4$ (bottom). Dashed lines indicate the desorption peaks of various products.

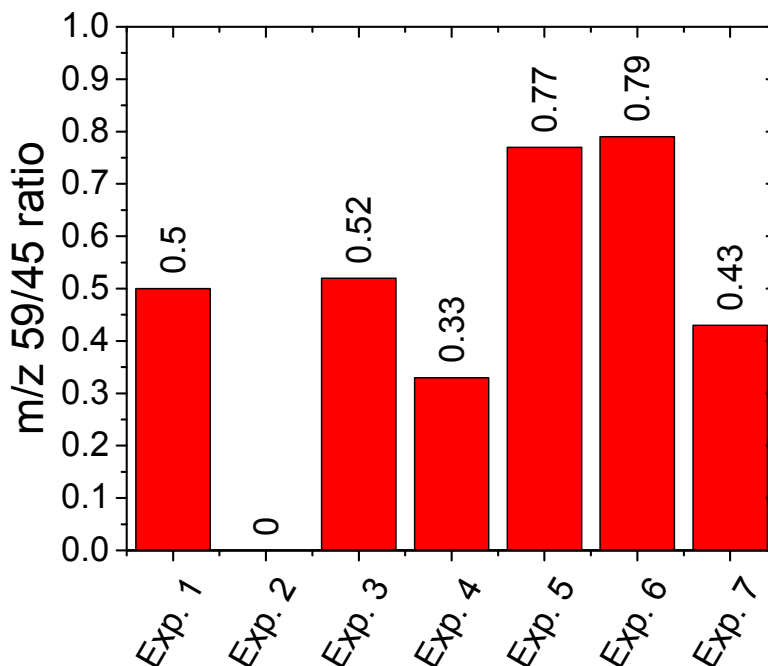


Figure 7.9: m/z 59 (acetamide) / 45 (formamide) ratio of the experiments performed in this work.

7.3.2. Comparison between experimental conditions

Besides the experiments presented above, additional experiments have been performed with different HNCO and methane abundances, lower Lyman- α intensities and dilution in a CO matrix to see how these parameters influence the production of acetamide. TPD data of formamide (m/z 45) and acetamide (m/z 59) are compared by determining the integrated area of each feature and deriving the m/z 59/45 ratio (see Fig. 7.9). Both NH_2CHO and CH_3CONH_2 are present in all experiments (except in pure HNCO, experiment 2), although absolute abundances do vary. A mass ratio of about 0.5 is found for experiment 1 and 3.

A first observation is that the m/z 59/45 ratio does not show any major shifts in ratio between the experiments and the deviation with respect to experiment 1 is at most $\pm 50\%$. This is despite processing by high fluence Lyman- α rich (Exp. 1-4) and low fluence Lyman- α poor (Exp. 5-7) radiation and high dilution in a CO matrix (6-7). This indicates that the processes that produce NH_2CHO and CH_3CONH_2 can occur in a variety of interstellar ices under different physical conditions.

Experiments 4 and 5 hint at a relationship with the CH_4 abundance. A low abundance (Exp. 4) results in less CH_3CONH_2 being produced, while a high abundance (Exp. 5) results in more produced CH_3CONH_2 . The same effect is

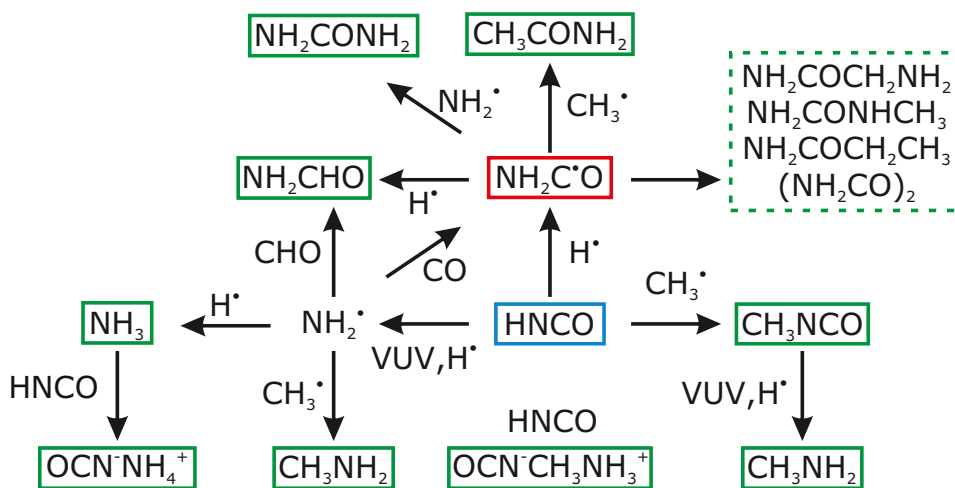


Figure 7.10: Possible reaction pathways to various amides and other products, contained by the findings of this work. Blue boxed is the parent species HNCO, green boxed are molecules detected in this work, green dashed boxes are suggested molecules that form. The important NH_2CO radical is shown in a red box, but not directly observed in the experiments.

not seen in experiments 6 and 7, which both have an equal HNCO to CH_4 ratio in the ice, albeit at different abundances. The CO matrix may be the cause of the observed difference in mass ratios.

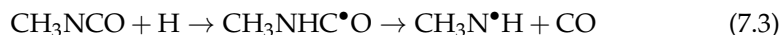
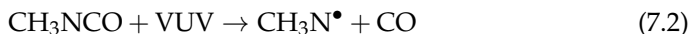
In experiment 6 and 7 CH_4 and HNCO are relatively isolated in the CO matrix, with CH_4 to CO and HNCO to CO ratios of $\sim 1:10$ and $1:30$, respectively. Any molecular fragments produced from the VUV irradiation are expected to thermalised before reacting. This can hinder reactions of molecules, but still similar m/z 59/45 ratios with respect to the other experiments are found. This could hint to the production and storage of radicals in the ice. Upon heating the ice sample for the TPD, the radicals become mobile and produce the products that eventually are measured. This also makes it likely that NH_2CHO and CH_3CONH_2 have a common parent radical.

7.4. Discussion

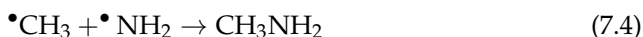
7.4.1. Key reactions and reaction network

The results presented in Sec. 7.3 show that several complex, amide-bearing, molecules can be formed from VUV irradiated HNCO: CH_4 ices. Previous work by Ligterink et al. (2017) showed that CH_3NCO is formed in CH_4 :HNCO mixed ices. In this work IR and QMS data show its presence as well. However, the related molecule CH_3NHCHO , suggested to form in hydrogen addition reactions, is not detected. This suggests that hydrogen addition reactions to CH_3NCO are not possible due to a high reaction barrier. Since hydrogen atoms in the CO matrix experiment are likely thermalised, it seems that both hot H-atom

addition and hydrogenation do not proceed. Alternatively, intermediates like $\text{CH}_3\text{NHC}\bullet\text{O}$ or $\text{CH}_3\text{N}\bullet\text{CHO}$ are not stable and efficiently destroyed, potentially under the influence of the VUV irradiation. CH_3NCO may be a source of the observed CH_3NH_2 via the reactions:



Hydrogenation and VUV irradiation experiments of pure CH_3NCO samples would help investigate these mechanisms and confirm or rule out the possibility to form N-methylformamide from methyl isocyanate. Besides forming CH_3NH_2 from CH_3NCO , other reaction pathways are possible as well. The VUV processing of the ice leads to various NH_x radicals and neutrals, as well as the NH_4^+ cation formed from HNCO. Reactions with CH_4 , CH_3 and potentially smaller radicals derived from methane can occur and result in methylamine. Although in this work direct evidence for a specific formation mechanism of CH_3NH_2 is lacking, the main formation route described by Förstel et al. (2017) is plausible in this work as well:

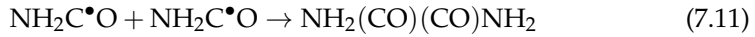
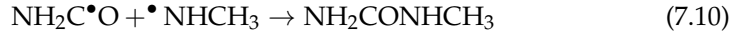
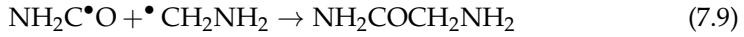
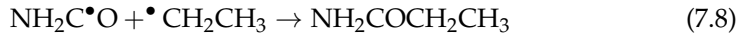


Two main scenarios can explain the formation of amides and their relation to each other. The first is hydrogen addition to HNCO which leads to the formation of the $\text{NH}_2\text{C}\bullet\text{O}$ or carbamyl radical and is followed by radical recombination reactions. Hydrogen addition leading to the $\text{N}\bullet\text{CHO}$ radical can be excluded due to the non-detection of CH_3NHCHO . All main products found in this work can be formed from $\text{NH}_2\text{C}\bullet\text{O}$ in radical-radical addition reactions:



The second option starts with the dissociation of HNCO in NH and CO, followed by hydrogen addition reactions to form NH_2 and CHO. Formamide can be formed from the $\text{NH}_2 + \text{CHO}$ reaction (Jones et al. 2011). However, the formation of CH_3CONH_2 and NH_2CONH_2 likely proceeds via the NH_2CO radical again formed from $\text{NH}_2 + \text{CO}$ (see also Förstel et al. 2016, for this reaction). The experiments performed in a CO matrix likely have thermalised, cold or low energy hydrogen atoms in them. Since Noble et al. (2015) showed that (cold H-atom) hydrogenation of HNCO does not proceed, it strengthens the case that a radical recombination mechanism is responsible for the observed reaction products. However, with this mechanism one would intuitively also expect the formation of CH_3NHCHO . VUV irradiation experiments of $\text{NH}_3:\text{CO}:\text{CH}_4$ mixed ices should be conducted to further investigate this radical-radical recombination network.

If the $\text{NH}_2\text{C}\cdot\text{O}$ radical indeed is a dominant radical in these ice mixtures, as above results suggest, desorption features found at m/z 73, 74 and 88 can be explained with it as well:



As above examples show, the $\text{NH}_2\text{C}\cdot\text{O}$ radical can be an important intermediate for interstellar chemistry and the formation of complex amide-bearing molecules, as also indicated by Agarwal et al. (1985). In interstellar ices, its formation does not necessarily have to originate from HNCO or OCN^- , but can also be the result of $\text{NH}_2 + \text{CO}$ addition or hydrogen abstraction of NH_2CHO .

The reactions described in this section result in the reaction network in Fig. 7.10. Starting from HNCO (blue box), the NH_2CO radical (red box) can either directly or indirectly be formed. Subsequent reactions with H , CH_3 and NH_2 result in the formation of the primary amides (green boxes). Larger amides can be formed in similar reactions (dashed green box). Finally, the dissociation reactions are responsible for the formation of NH_3 and CH_3NH_2 and followed by acid-base reactions to form salts with HNCO .

7.4.2. Comparison with interstellar abundance ratios

It is possible to compare the experimental m/z 59/45 ratio of acetamide/formamide with interstellar abundances. If corrections are applied for the fragmentation pattern and the molecule specific electron impact absorption cross sections are taken into account, the experimental mass ratio can be converted into an abundance ratio (AR):

$$AR = \frac{C_{\text{formamide}}}{C_{\text{acetamide}}} \times \frac{F_{45,\text{formamide}}}{F_{59,\text{acetamide}}} \times \frac{I_{\text{acetamide}}}{I_{\text{formamide}}}, \quad (7.12)$$

where C_{species} is the total electron impact absorption cross section of the selected species at 70 eV ionization energy and F_{species} and I_{species} are the fragmentation ratio and the signal intensity, respectively, of a species at a certain mass. $I_{\text{acetamide}}/I_{\text{formamide}}$ is given by the m/z 59/45 ratio, and for the abundance comparison we take the ratio of 0.5 found in experiment 1. Fragmentation patterns give $F_{59,\text{acetamide}} = 0.29$ and $F_{45,\text{formamide}} = 0.41$. To our knowledge, total electron impact absorption cross sections have not experimentally been determined for these species. Theoretical predictions are available, however. The absorption cross section for formamide is given as 5.595^2 (Gupta et al. 2014). A value for acetamide is not given, but for N-methylformamide it is calculated to be 10.063^2 . We adopt this value with a generous error bar of $\pm 5^2$ for this comparison. From the given values an abundance ratio between acetamide and formamide of $0.4^{+0.39}_{-0.14}$ is derived.

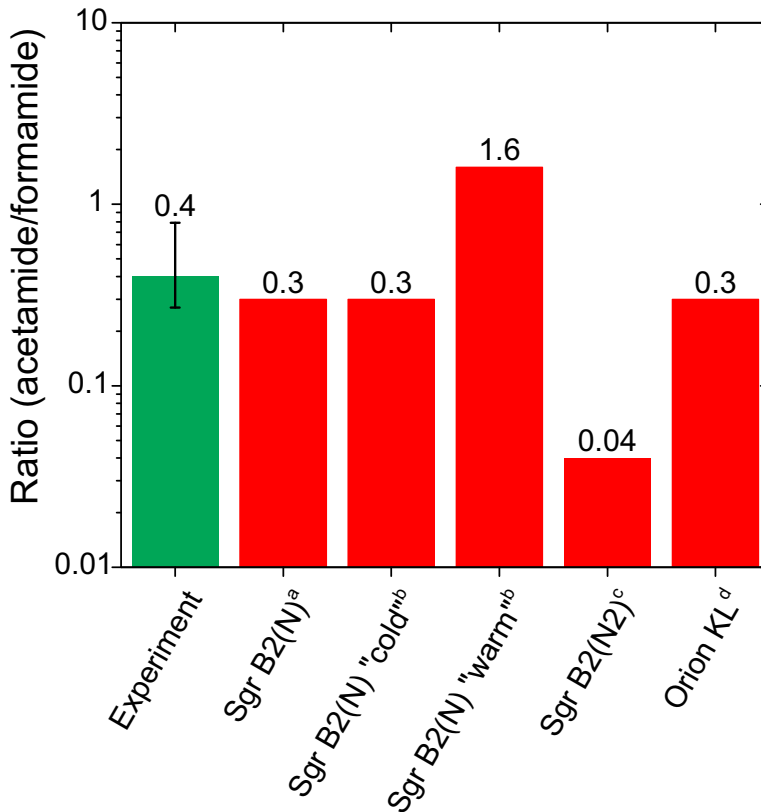


Figure 7.11: Acetamide over formamide abundance ratio as found in experiment 1 of this work compared with ratios derived in observational studies. ^aHollis et al. (2006); ^bHalfen et al. (2011); ^cBelloche et al. (2017); ^dCernicharo et al. (2016).

The experimental abundance ratio is compared with observationally determined ratios towards Sgr B2 and Orion KL in Fig. 7.11. In general, the experimental abundance ratio agrees well with observational abundance ratios. A clear outlier is the ratio of 0.04 derived by Belloche et al. (2017), in which interferometric data of ALMA are used to sample Sgr B2(N2). It contrast with the single dish observations toward Sgr B2(N) (Hollis et al. 2006; Halfen et al. 2011) but also with ALMA observations towards Orion KL (Cernicharo et al. 2016). The single dish observations sample larger spatial scales and cover emission from both Sgr B2(N1) and Sgr B2(N2), while Orion KL is not as extreme an environment as Sgr B2. These differences could explain the different abundance ratios found in these sources.

Overall the similarity between experimental and observational abundance ratios suggests that formamide and acetamide are related and both are formed in ice processes from a common parent molecule such as NH_2CO . More observations on the formamide and acetamide abundances towards other sources, particularly low-mass protostars, will aid in affirming this claim.

7.5. Conclusions

The main conclusions of this work are summarized as follows:

- The solid-state formation of acetamide (CH_3CONH_2) upon VUV irradiation is shown in $\text{CH}_4:\text{HNCO}$ mixed ices, simultaneous with formamide (NH_2CHO) and urea (NH_2CONH_2), suggesting a common formational origin.
- Methyl isocyanate (CH_3NCO) is likely present in the ices studied, but formation of the related molecule N-methylformamide (CH_3NHCHO) is not seen, indicating that hydrogen addition to CH_3NCO is not possible or leads to the destruction of CH_3NCO .
- Formation of more complex molecules is seen, which could be species such as propanamide and methylcarbamide. These molecules can be targets to further investigate interstellar amide chemistry.
- Experimental evidence suggests that the NH_2CO radical is an important intermediate to the formation of acetamide and may also be an intermediate in the formation of formamide, urea and more complex species. In interstellar ice, the NH_2CO radical may also be formed from $\text{NH}_2 + \text{CO}$ reactions or hydrogen abstraction of NH_2CHO .
- Comparison between the experimental and interstellar acetamide/formamide abundance ratios suggests that interstellar acetamide and formamide have a common formational origin that can be found in interstellar ice.



V-UV



Search for methylamine in high mass hot cores

N.F.W. Ligterink, E.D. Tenenbaum & E.F. van Dishoeck

8.1. Introduction

Complex organic molecules are thought to be formed primarily on dust grains in dense cores, see reviews by Herbst & van Dishoeck (2009) and Caselli & Ceccarelli (2012). Before the onset of star formation, the atomic and molecular reservoir is contained in large dark clouds. Due to the high densities ($\geq 10^4 \text{ cm}^{-3}$) and low temperatures (10 K) reached in these environments, gas-phase species will freeze out on sub-micron sized grains forming ice mantles on timescales shorter than the lifetime of the cloud. It is here that atoms and molecules can potentially react with each other to form the zeroth order species like ammonia, methane, water and methanol. UV radiation interacts with these ice mantles by dissociating molecules to produce radicals and by photodesorbing species back to the gas phase. If these radicals are sufficiently mobile, they can find each other on the grain and react to form even more complex first generation (organic) species (Garrod & Herbst 2006). However, it is not entirely clear if UV radiation is essential to form these complex molecules or whether they can also be formed just by thermal processing and atom bombardment of solid CO with C, N and O atoms (Tielens & Charnley 1997).

In this context methylamine, CH_3NH_2 , is a particularly interesting molecule, since its formation is hypothesised by Garrod et al. (2008) to be completely dependent on radicals produced by UV photons, and is one of the few molecules that can definitely not be produced in the routes starting from solid CO:



These radicals can form in the ice mantles in the dark cloud or in the protostellar phase through cosmic-ray induced photons and/or UV photons from the protostar. After gravitational collapse of the cloud and formation of a protostar, the dust around it will start to warm up. The increased temperature will cause the radicals to become mobile on the grains and react with each other, forming methylamine. Further heating will evaporate the formed methylamine from the grain and raise its gas-phase abundance.

Another interesting amine-containing molecule is formamide, NH_2CHO . This is so far the most abundantly observed amine-containing molecule (e.g., Bisschop et al. 2007b; Halfen et al. 2011), making it an interesting molecule to compare with other amines like methylamine. In contrast with CH_3NH_2 , this molecule can possibly be produced by reactions of H and N with solid CO. The comparison of the abundances of these two species could potentially give more information about the relative importance of UV-induced versus thermal grain surface reactions.

Hot cores are particularly well-suited to study methylamine. These high mass star-forming regions reach high temperatures between 100 to 300 K and are known for their rich complex organic chemistry (Walmsley 1992; van Dishoeck & Blake 1998; Tielens & Charnley 1997; Ehrenfreund & Charnley 2000; Caselli &

Ceccarelli 2012). The ice covered grains move inwards to the protostar and will heat up. When sufficient temperatures are reached, molecules will start to desorb depending on their respective binding energies. Less abundant molecules mixed with water ice will desorb together with water around 100 K.

Previous detections of methylamine have all been made toward the galactic center. Kaifu et al. (1974) first detected CH_3NH_2 in Sagittarius B2 and Orion A. Later that same year Fourikis et al. (1974) reported the detection of methylamine in the same sources, but with a different telescope. Much more sensitive surveys by Turner (1991), Nummelin et al. (2000), Halfen et al. (2013), Belloche et al. (2013) and Neill et al. (2014) also all detected methylamine lines toward SgrB2, with typical inferred abundance ratios with respect to NH_2CHO between 0.5 to 3. No detections of methylamine have been reported in sensitive surveys with modern detectors toward Orion, however (Blake et al. 1987; Turner 1991; Sutton et al. 1995; Schilke et al. 1997; Crockett et al. 2014b).

To study the importance of UV processing of ice-covered dust grains, we present the results of searches for methylamine in a number of hot cores (see Table 8.1). These results are combined and compared with data from Bisschop et al. (2007b) and Isokoski et al. (2013), which were taken toward the same hot cores with the same telescope and analysis method and include detections of NH_2CHO and other nitrogen-containing species. In Section 8.2 the observational details are given, followed by the analysis method in Section 8.3. Section 8.4 summarizes all the results of our analysis and these are discussed in Section 8.5. Finally conclusions are drawn in Section 8.6.

8.2. Observations

Observations were performed with the James Clerk Maxwell Telescope (JCMT) ¹ on the sources listed in Table 8.1 between July 2010 and August 2011. The sources were selected based on their particularly rich chemistry, being isolated, having narrow line widths to prevent line confusion and on their relatively nearby distance (Bisschop et al. 2007b; Fontani et al. 2007; Rathborne et al. 2008; Isokoski et al. 2013).

Nummelin et al. (1998) detected methylamine emission lines between 218 to 263 GHz toward Sgr B2N. Therefore the RxA3 front-end double side band receiver, functioning between 210 to 276 GHz, was chosen to observe the hot cores. The 250 and 1000 MHz wide back-end ACSIS configurations were used. A number of methylamine transitions covering a range of excitation energies were selected in this frequency range based on high Einstein A coefficients and lack of line confusion (Table 8.2). However, not all transitions were observed for all sources. The 235735 MHz transition was only recorded for W3(H_2O) and the 260293 MHz transition only toward W3(H_2O) and NGC 7538 IRS1.

Because double side band spectra were obtained, our spectra contain transitions from two different frequency regimes superposed. To disentangle lines from the two side bands, each source was observed twice with an 8 MHz

¹The James Clerk Maxwell Telescope is operated by the Joint Astronomy Centre on behalf of the Science and Technology Facilities Council of the United Kingdom, the National Research Council of Canada, and (until 31 March 2013) the Netherlands Organisation for Scientific Research.

Table 8.1: Source list and source parameters

Source	RA J2000	Dec J2000	θ_S^a AU	θ_B^a AU	L^a L_\odot	d^a (kpc)	V_{LSR} (km s ⁻¹)	ΔV (km s ⁻¹)	$\delta\nu$ (km s ⁻¹)	RMS (mK)
AFGL 2591	20:29:24.60	+40:11:18.9	1800	21000	2.0E+05	3.3	-5.5	4.0	1.28	10
G24.78	18:36:12.60	-07:12:11.0	13000	162000	7.9E+05	7.7	111.0	6.3	1.28	9
G31.41+0.31	18:47:34.33	-01:12:46.5	7840	166000	2.6E+05	7.9	98.7	7.3	1.28	7
G75.78	20:21:44.10	+37:26:40.0	5600	86100	1.9E+05	4.1	-0.04	5.6	1.28	9
IRAS 18089-1732	18:11:51.40	-17:31:28.5	2750	49000	3.2E+04	2.3	33.8	4.5	1.28	9
IRAS 20126+4104	20:14:26.40	+41:13:32.5	1753	34400	1.3E+04	1.6	-3.8	6.0	1.28	10
NGC 7538 IRS1	23:13:45.40	+61:28:12.0	4900	58800	1.3E+05	2.8	-57.4	4.0	1.28	10
W3(H ₂ O)	02:27:04.60	+61:52:26.0	2400	42000	2.0E+04	2.0	-46.4	5.0	1.28	11
W 33A	18:14:38.90	-17:52:04.0	4500	84000	1.0E+05	4.0	37.5	4.9	1.28	11

Notes. ^aData for AFGL 2591 taken from (Rygl et al. 2012). Other data taken from Bisschop et al. (2007b) and Isokoski et al. (2013).

Table 8.2: Methylamine transitions observed in this study^a

Transition	Freq (MHz)	E_{up} (K)	A (s^{-1})	g_{up}
$4_2 \rightarrow 4_1^b$	229310.298	36.9	1.32E-05	108
$7_2 \rightarrow 7_1^b$	229452.603	75.5	5.88E-06	60
$8_2 \rightarrow 8_1^c$	235735.037	92.8	6.13E-05	204
$6_2 \rightarrow 6_1^b$	236408.788	60.8	5.94E-05	52
$2_2 \rightarrow 2_1^b$	237143.530	22.0	3.82E-05	60
$10_2 \rightarrow 10_1^d$	260293.536	132.7	2.26E-05	52

Notes. ^a Data from JPL database for molecular spectroscopy. ^b Transition observed in all sources. ^c Only observed in W3(H₂O). ^d Only observed in W3(H₂O) and NGC 7538 IRS1.

shift in the local oscillator setting between the two observations. This allows each transition to be uniquely assigned to either of the two side bands.

In the 230 GHz band, the JCMT has a beam size (θ_B) of 20-21''. Spectra were scaled from the antenna temperature scale, T_A^* , to main beam temperature, T_{MB} , by using the main beam efficiency of 0.69 at 230 GHz. Integration times were such that T_{RMS} is generally better than 10 mK for data binned to 1.3 km s⁻¹ velocity bins. Noise levels were improved by adding the shifted spectra together in a narrow frequency region around the CH₃NH₂ lines, effectively doubling the integration time.

8.3. Data analysis

To analyse the data, exactly the same method as described by Bisschop et al. (2007b) and Isokoski et al. (2013) was used. It will be shortly reiterated here. The hot core spectra corrected for source velocity were analysed with the "Weeds" extension (Maret et al. 2011) of the Continuum and Line Analysis Single-dish Software (CLASS²) coupled with the Jet Propulsion Laboratory (JPL³) database for molecular spectroscopy (Pickett et al. 1998). Focus was on identifying the transitions of methylamine listed in Table 8.2, but other lines in the spectra were measured as well (see Table 8.5 Appendix). After each positive identification the integrated main-beam temperature, $\int T_{\text{MB}} dV$, was determined by gaussian fitting of the line. From the integrated main-beam intensity the column density N_{up} and thus the *beam-averaged* total column density N_{T} could be determined, assuming Local Thermodynamic Equilibrium (LTE) at a single excitation temperature T_{rot} :

$$\frac{3k \int T_{\text{MB}} dV}{8\pi^3 \nu \mu^2 S} = \frac{N_{\text{up}}}{g_{\text{up}}} = \frac{N_{\text{T}}}{Q(T_{\text{rot}})} e^{-E_{\text{up}}/T_{\text{rot}}} \quad (8.4)$$

where g_{up} is the level degeneracy, k the Boltzmann constant, ν the transition

²<http://www.iram.fr/IRAMFR/GILDAS>

³<http://spec.jpl.nasa.gov>

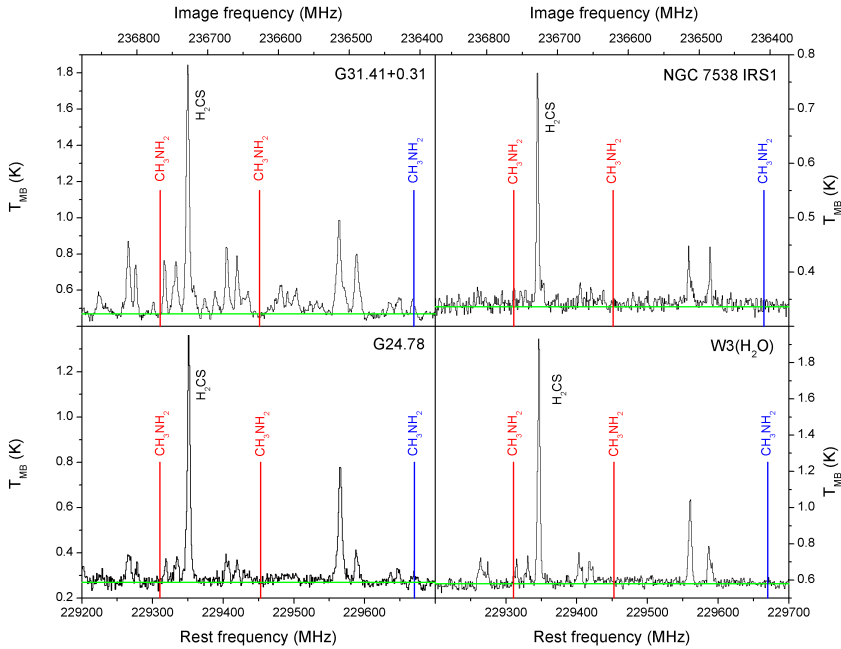


Figure 8.1: JCMT spectra of the massive hot cores G31.41+0.31, G24.75, NGC 7538 IRS1 and W3(H₂O). The 229310 and 229452 MHz transitions in the lower sideband are indicated in red and that at 236408 MHz in the upper sideband in blue. In green is the baseline, obtained by fitting line free portions of the spectrum. In all spectra the H₂CS $7_1 \rightarrow 6_1$ transition at 236726 MHz is fitted to determine the typical linewidth in the sources, as listed in Table 8.1.

frequency, μ the dipole moment and S the line strength. $Q(T_{\text{rot}})$ is the rotational partition function and E_{up} is the upper state energy in Kelvin.

In case of a non-detection, 3σ upper limits were determined from the Root Mean Square (RMS) of the base line of the spectra in combination with the velocity resolution $\delta\nu$ and line width ΔV :

$$\alpha\epsilon = 1.2 \sqrt{\delta\nu\Delta V} \cdot \text{RMS} \quad (8.5)$$

ΔV is estimated from other transitions (see Table 8.1) in the spectra, for example from the nearby H₂CS $7_1 \rightarrow 6_1$ transition, and assumed to be the same for all transitions in the spectral range. A telescope flux calibration error of 20% is taken into account in the 1.2 factor. The 3σ value is then used in the same way as the main-beam intensity of detected lines to obtain the upper limit on the total column density through Eq. 8.4.

Since no rotational temperature can be determined for a non-detection, this has to be estimated. In the models of Garrod et al. (2008) the peak abundance temperatures for methylamine range from 117 to 124 K depending on the model used. Öberg (2009) determined that methylamine forms in CH₄/NH₃ UV irradiation experiments and sublimates at 120 K. There is a small difference between laboratory and hot core desorption temperatures, because

of the pressure difference between the two. Also, if CH_3NH_2 is embedded in water ice the desorption temperature will probably be limited to roughly 100 K, when water desorbs in space. Therefore T_{rot} is assumed to be 120 K when methylamine lines could not be identified, but the effects of lower and higher rotation temperatures are explored as well.

Correction for beam dilution is done in the same way as Bisschop et al. (2007b):

$$\eta_{BF} = \frac{\theta_S^2}{\theta_S^2 + \theta_B^2} \quad (8.6)$$

resulting in the *source*-averaged column density:

$$N_S = \frac{N_T}{\eta_{BF}} \quad (8.7)$$

The beam diameter θ_B is set at 21". For the source diameter, θ_S , values have been taken from Bisschop et al. (2007b) and Isokoski et al. (2013) and constitute the area where the temperature is 100 K or higher and hot gas-phase molecules are present. Both beam and source diameters are listed in AU in Table 8.1. Using the CASSIS line analysis software⁴ it was verified that the source-averaged column densities are still small enough that the observed lines are optically thin.

8.4. Results

8.4.1. CH_3NH_2 limits

Figure 8.1 presents examples of spectra obtained for our sources, whereas Figure 8.4 in the Appendix shows the $2_2 - 2_1$ line in all sources. In general, no transitions of CH_3NH_2 are detected. Only one possible methylamine transition is identified in G31.41+0.31 coincident with the $6_2 \rightarrow 6_1$ line at 236408 MHz, with an integrated intensity of 0.44 K kms⁻¹. Following the procedure summarized in Section 8.3, a column density of 3.4×10^{17} cm⁻² is inferred from this line assuming $T_{\text{rot}} = 120$ K. However, modelling of the spectrum shows that the other targeted CH_3NH_2 lines, $4_2 \rightarrow 4_1$ and $2_2 \rightarrow 2_1$, should have comparable or even higher intensities if this identification is correct (Figure 8.3). The $8_2 \rightarrow 8_1$ line should be readily detected but was not observed toward G31.41+0.31. This makes it unlikely that the detected feature belongs to methylamine, since we would expect to see at least two other CH_3NH_2 transitions in our spectrum.

In Figure 8.2 upper limit column densities of the six investigated transitions of methylamine are plotted versus rotational temperature taking a typical $3\sigma = 0.100$ K kms⁻¹. At 120 K the $8_2 \rightarrow 8_1$, 235735 MHz transition gives the lowest limits on the column densities, see Figure 8.2. However, since this particular transition was only included in the observations for one source, the second most sensitive transition at 120 K, $2_2 \rightarrow 2_1$, will be used (see Figure 8.4 in the Appendix for a blow-up of this particular spectral region in all investigated sources). All

⁴CASSIS has been developed by IRAP-UPS/CNRS (<http://cassis.irap.omp.eu>).

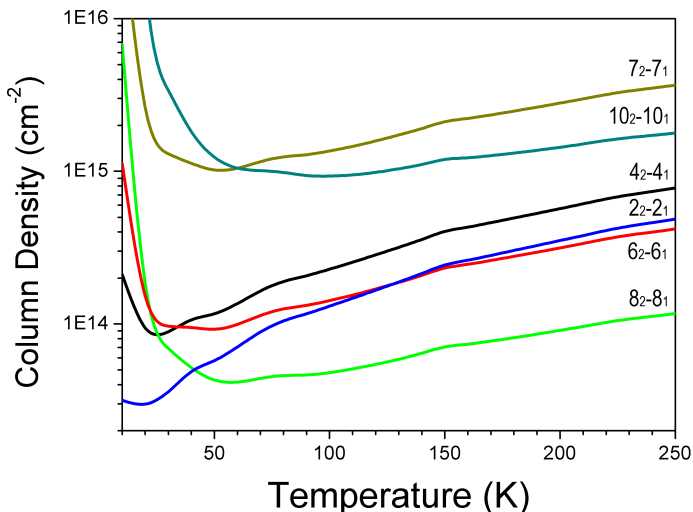


Figure 8.2: Column densities for the six methylamine transitions plotted versus temperature. This plot is made for a 3σ limit of 0.1 K km s^{-1} , as found for W3(H₂O). This figure demonstrates that the $8_2 - 8_1$ transition (green) gives the most sensitive limits on column density for the relevant range of excitation temperatures in hot cores, when observed. The other five transitions ($4_2 \rightarrow 4_1$, black; $7_2 \rightarrow 7_1$, gold; $10_2 \rightarrow 10_1$, cyan; $2_2 \rightarrow 2_1$, blue and $6_2 \rightarrow 6_1$, red) clearly imply higher column densities. Only below 40 K does the $2_2 \rightarrow 2_1$ line give lower column density limits.

following molecular ratios are based on CH₃NH₂ column densities obtained from this line, assuming $T_{\text{rot}} = 120 \text{ K}$. The corresponding upper limits are presented in Table 8.3

8.4.2. Abundance ratio comparison

Combined with NH₂CHO and CH₃OH column densities from Bisschop et al. (2007b) and Isokoski et al. (2013) derived in the same way, abundance ratios for methylamine and formamide with respect to each other and to methanol are calculated. These ratios are listed in Table 8.3. Methanol is chosen as a reference since it is the most readily observed complex organic molecule. Its disadvantage is that some of the transitions have high optical depth and that a cold component may be present (Isokoski et al. 2013), but this is circumvented by only taking the warm methanol column density derived from optically thin lines. Abundances relative to methanol rather than H₂ are preferred since the H₂ column depends on extrapolation of dust models to smaller scales than actually observed (Bisschop et al. 2007b). Another point that needs to be taken into account is that the models of Garrod et al. (2008) do show a slight overproduction of CH₃OH, which could influence the comparison between the ratios. Overall, the abundance ratios are estimated to be accurate to a factor of a few.

It should be noted that methylamine and formamide have significantly different dipole moments (1.31 and 3.73 Debye respectively) and could therefore

be excited in different ways. Formamide has a larger critical density than methylamine, so the situation could arise where the critical density is not reached for formamide or even both molecules. The corresponding excitation temperatures will then be lower. In particular, the situation in which the critical density is not reached for formamide but is for methylamine, could affect the inferred ratios. As can be seen from Figure 8.2, if T_{rot} drops from 120 to 50 K, the column density drops by a factor of a few, depending on transition. If T_{rot} were 120 K for methylamine but 50 K for formamide, the observed column density of formamide would be lower than that listed here and thus result in a higher $\text{CH}_3\text{NH}_2/\text{NH}_2\text{CHO}$ ratio. We note, however, that there is no observational evidence that T_{rot} is systematically lower than 100 K for formamide (Bisschop et al. 2007b).

Table 8.3 includes the observational results toward Sgr B2, the only source where methylamine is firmly detected, from Turner (1991), Belloche et al. (2013) and Neill et al. (2014). These results, obtained over the course of more than two decades, agree well with each other within the estimated uncertainties due to slightly different adopted source sizes. Nummelin et al. (2000) also detect methylamine in their Sgr B2 survey but find a surprisingly small beam filling factor and consequently very large column density compared with most other complex organic molecules. If their beam filling factor for CH_3NH_2 is taken to be the same as for NH_2CHO , the Nummelin et al. (2000) ratios are more in line with those derived by Turner (1991), Belloche et al. (2013) and Neill et al. (2014). The non-detections of methylamine toward the chemically rich and well studied Orion hot core imply abundance limits that are at least a factor of 5 lower than for SgrB2 (Neill et al. 2014; Crockett et al. 2014b).

Table 8.3 also contains the model results from Garrod et al. (2008), who present three hot core models which differ from each other by their warm-up timescale from 10 to 200 K. The timescales for F(ast), M(edium) and S(low) are 5×10^4 , 2×10^5 and 1×10^6 years, respectively, and start after the cold collapse phase. In the slow models more time is spent in the warm-up phase where radicals are mobile. Values used in this comparison are taken from the so-called reduced ice composition, where cold phase methane and methanol abundances were modified to match observations of these ices toward W33A, NGC 7538 IRS9 and Sgr A*, see Gibb et al. (2000b). Another comparison can be made with the gas-phase abundances in protoplanetary disk models of Walsh et al. (2014) which have similar or higher densities and temperatures as in protostellar cores. Their ratios range from 7.2×10^{-1} to 6.5×10^{-2} for $\text{CH}_3\text{NH}_2/\text{CH}_3\text{OH}$, 4.2×10^{-1} to 1.5 for $\text{CH}_3\text{NH}_2/\text{NH}_2\text{CHO}$ and 1.7 to 8.8×10^{-2} for the $\text{NH}_2\text{CHO}/\text{CH}_3\text{OH}$. These ratios are close to the predicted values of Garrod et al. (2008) listed in Table 8.3, which may be partly due to using the same surface-chemistry network.

From Table 8.3 several trends become apparent for our results. The $\text{CH}_3\text{NH}_2/\text{NH}_2\text{CHO}$ limits lie about an order of magnitude above model values whereas the $\text{CH}_3\text{NH}_2/\text{CH}_3\text{OH}$ limit approximately matches with theoretical predictions. Because the observed values are actually 3σ upper limits, this suggests that models overproduce CH_3NH_2 . For the sources with the most stringent limits, such as G31.41+0.31 and the $8_2 - 8_1$ line in W3(H₂O), the $\text{CH}_3\text{NH}_2/\text{CH}_3\text{OH}$ limits are comparable or even lower than the abundance ratios for Sgr B2. The third ratio, $\text{NH}_2\text{CHO}/\text{CH}_3\text{OH}$, is also found to be lower than the

models by up to one order of magnitude.

Close inspection of the Bisschop et al. (2007b) data shows that the NH_2CHO column densities may have larger uncertainties than quoted in their figures and tables. We have therefore re-analysed all NH_2CHO data from that paper taking larger uncertainties into account. In general, this leads to lower NH_2CHO column densities. Even using the upper limits from this re-analysis as well as those from Isokoski et al. (2013) (which were obtained with generous error bars), the $\text{NH}_2\text{CHO}_{\text{upper}}/\text{CH}_3\text{OH}$ ratios are significantly lower than the models. This suggests that both the methylamine and formamide abundances are too high in the models.

The Sgr B2 detections tend to have lower $\text{CH}_3\text{NH}_2/\text{NH}_2\text{CHO}$ and $\text{CH}_3\text{NH}_2/\text{CH}_3\text{OH}$ ratios than our upper limits and are also somewhat below the models, but generally do not differ more than a factor of a few. The SgrB2 $\text{NH}_2\text{CHO}/\text{CH}_3\text{OH}$ ratios are also closer to the models results, at least for the faster models. However, the Orion Compact Ridge $\text{NH}_2\text{CHO}/\text{CH}_3\text{OH}$ value from Crockett et al. (2014b) is comparable to that found for our sources and clearly lower than the models. Further observations are needed to determine to what extent Sgr B2 is a special case.

To further elucidate the differences between theory and our and the Sgr B2 observations, an additional analysis was made of the $\text{CH}_3\text{NH}_2/\text{CH}_3\text{CN}$ ratio. These results are listed in Table 8.4. Acetonitrile is produced in the gas-phase, but more abundantly on grains: an important route to its formation is via $\text{CH}_3^\bullet + \text{CN}^\bullet \rightarrow \text{CH}_3\text{CN}$, according to Garrod et al. (2008). This would mean that both molecules compete for the methyl radical on the surface, thus relating the two molecules.

Our observed ratios involving CH_3CN are clearly at odds with the theoretical predictions. The observed $\text{CH}_3\text{NH}_2/\text{CH}_3\text{CN}$ ratios are in most cases an order of magnitude lower than theory and approach the observed ratios for Sgr B2. However, the observed $\text{CH}_3\text{CN}/\text{CH}_3\text{OH}$ ratios are 1-2 orders of magnitude higher than theoretical predictions. Both these cases point to CH_3CN being underproduced in the models.

Finally, abundance ratios, with some notable exceptions, do not vary more than an order of magnitude between different sources, as also found by Bisschop et al. (2007b) for other species.

8.5. Discussion

Despite a significant number of successfully identified molecules (see Table 8.5 in the Appendix for examples of W3(H₂O) and G31.41+0.31), only upper limits were found for methylamine in the various hot cores, limiting the conclusions that can be drawn. Nevertheless, trends are seen in our abundance ratios. The results suggest that theoretically predicted abundances for both methylamine and formamide are too high. In contrast, acetonitrile is found to be underproduced in the models. In the following, each of these species is discussed individually.

Table 8.3: Upper limit column densities and abundance ratios for methylamine.

Source	$N_{S, \text{CH}_3\text{NH}_2}$ cm^{-2}	$\text{CH}_3\text{NH}_2/\text{NH}_2\text{CHO}$	$\text{CH}_3\text{NH}_2/\text{CH}_3\text{OH}$	$\text{NH}_2\text{CHO}/\text{CH}_3\text{OH}$	$\text{NH}_2\text{CHO}_{\text{upper}}/\text{CH}_3\text{OH}$
Model F		1.1	3.4E-02	3.1E-02	3.1E-02
Model M		1.7	1.0E-01	7.3E-02	7.3E-02
Model S		1.3	1.3E-01	1.0E-01	1.0E-01
AFGL 2591	$\leq 1.9\text{E}+16$	-	-	$\leq 3.9\text{E}-01$	-
G24.78	$\leq 2.4\text{E}+16$	$\leq 3.3\text{E}+01$	$\leq 8.5\text{E}-02$	2.6E-03	9.0E-04
G31.41+0.31	$\leq 5.8\text{E}+16$	$\leq 2.8\text{E}+01$	$\leq 4.9\text{E}-02$	1.8E-03	3.8E-03
G75.78	$\leq 3.5\text{E}+16$	$\leq 1.7\text{E}+02$	$\leq 3.1\text{E}-01$	1.8E-03	2.6E-02
IRAS 18089-1732	$\leq 4.2\text{E}+16$	$\leq 5.0\text{E}+01$	$\leq 1.9\text{E}-01$	3.8E-03	7.9E-03
IRAS 20126+4104	$\leq 6.4\text{E}+16$	-	≤ 2.2	-	-
NGC 7538 IRS1	$\leq 2.0\text{E}+16$	$\leq 3.5\text{E}+01$	$\leq 1.8\text{E}-01$	4.8E-03	2.1E-04
W3(H ₂ O)	$\leq 5.0\text{E}+16$	$\leq 3.9\text{E}+01$	$\leq 5.0\text{E}-02$	1.3E-03	6.4E-04
W3(H ₂ O)*	$\leq 1.7\text{E}+16$	$\leq 1.3\text{E}+01$	$\leq 1.7\text{E}-02$	1.3E-03	6.4E-04
W 33A	$\leq 5.7\text{E}+16$	$\leq 2.7\text{E}+01$	$\leq 2.9\text{E}-01$	1.1E-02	4.6E-03
Sgr B2 ^a	1.2E+14	5.7E-01	1.7E-02	1.3E-02	
Sgr B2(M) ^b	4.5E+16	3.2	1.7E-02	5.2E-03	
Sgr B2(N) ^b	6.0E+17	4.3E-01	3.3E-02	7.8E-02	
Sgr B2(N) ^c	5.0E+17	2.1	1.0E-01	4.8E-02	
Orion Compact Ridge ^d	-	-	-	1.6E-03	

Notes. Column densities for the assumed source size and upper limit abundance ratios for methylamine, derived from the $2_2 - 2_1$ line assuming $T_{\text{rot}} = 120$ K. The values for NH_2CHO and CH_3OH were taken from Bisschop et al. (2007b) and Isokoski et al. (2013). The upper limits of NH_2CHO were determined by our own re-analysis of the Bisschop et al. (2007b) data and taken from the appendix of Isokoski et al. (2013). * Column density calculated for the $8_2 - 8_1$ line. **References.** ^a Turner (1991), beam sizes between $65''$ and $107''$, assuming no beam dilution; ^b Belloche et al. (2013), beam sizes between $\sim 25''$ and $\sim 30''$, assuming a $3''$ source size for (N) and $5''$ source size for (M); ^c Neill et al. (2014), beam sizes between $\sim 10''$ and $\sim 40''$, assuming source size of $2.5''$; and ^d Crockett et al. (2014b) beam sizes between $44''$ and $11''$ and assuming a $10''$ size of the Compact Ridge.

Table 8.4: Upper limit column densities and abundance ratios for methylamine.

Source	CH ₃ NH ₂ /CH ₃ CN	CH ₃ CN/CH ₃ OH
Model F	5.5E+01	6.3E-04
Model M	3.8E+01	2.6E-03
Model S	1.5E+01	8.6E-03
AFGL 2591	≤5.3	≤7.5E-02
G24.78	≤5.1E-01	2.1E-01
G31.41+0.31	≤3.6	5.9E-02*
G75.78	≤1.9E+01	1.6E-02
IRAS 18089-1732	≤8.9	1.1E-02*
IRAS 20126+4104	≤4.3E+01	5.2E-02
NGC 7538 IRS1	≤2.5	6.8E-02
W3(H ₂ O)	≤7.2	7.0E-03
W 33A	≤2.1	1.4E-01
Sgr B2 ^a	1.2	1.5E-02
Sgr B2(N) ^b	3.0E-01	1.1E-01
Sgr B2(M) ^b	2.5E-01	6.7E-02
Sgr B2(N) ^c	5.9E+01	1.7E-02
Orion Compact Ridge ^d	-	1.1E-02

Notes. Abundance ratios for methylamine. The values for CH₃OH and CH₃CN were taken from Bisschop et al. (2007b) and Isokoski et al. (2013). *Ratio derived from optically thin ¹³C isotope. ^a Turner (1991), ^b Belloche et al. (2013), ^c Neill et al. (2014) and ^d Crockett et al. (2014b).

8.5.1. CH₃NH₂

Garrod et al. (2008) suggest that methylamine is primarily formed by grain-surface chemistry using UV to create the CH₃ and NH₂ radicals from photodissociation of primarily CH₄ and NH₃. Perhaps the amount of UV processing is overestimated in these models. An alternative route is hydrogen atom addition to solid HCN, proposed by Theule et al. (2011) and found to lead to both CH₂NH (methanimine) and CH₃NH₂. Walsh et al. (2014) find in their models that methylamine is indeed efficiently formed on grains at 10 K by atom addition reactions to solid CH₂NH. Burgdorf et al. (2010) have detected HCN ice on Triton, but so far no detection of solid HCN has been made in the ISM. Methanimine is actually readily observed in the gas-phase (Turner 1991; Nummelin et al. 1998; Belloche et al. 2013) so the presence of both species makes the H-atom addition scheme probable. However, Halfen et al. (2013) detect CH₂NH in Sgr B2(N) at a rotational temperature of 44 K, which is distinctly colder than the 159 K observed for CH₃NH₂, suggesting that the two molecules may not co-exist. An alternative route would therefore be to form these molecules by two different gas-phase reaction pathways (CH[•](g) + NH₃(g) → CH₂NH + H and CH₃[•](g) + NH₃(g) → CH₃NH₂ + H), with CH being present primarily in the colder outer envelope and CH₃ in the warmer center. Further modeling is needed to determine whether these gas-phase reactions can reproduce the

observed abundances quantitatively.

8.5.2. NH_2CHO

Formamide also appears to be overproduced in the hot core model. Since Garrod et al. (2008) use both gas-phase, radical and atom addition reactions to form formamide, it is difficult to pin down where the discrepancies could come from. It is known that NH_2CHO is formed in $\text{CO}:\text{NH}_3$ mixtures after UV and electron irradiation (Grim et al. 1989; Demyk et al. 1998; Jones et al. 2011) and it has also been proposed that it can form from H- and N-atom addition to solid CO (Tielens & Charnley 1997). Gas-phase formation from CO and NH_3 is viable as well (Hubbard et al. 1975), although these experiments were conducted under high-pressure conditions, not the low pressures applicable in the ISM. Further quantification of both gas-phase and solid phase routes through laboratory experiments is needed. Recent laboratory experiments by Fedoseev et al. (2015b) do not find NH_2CHO production in H- and N-atom bombardment studies of solid CO, consistent with a large barrier for H- addition to HNCO found in ab initio calculations (Nguyen et al. 1996), so perhaps the efficiency of this route has been overestimated in the models. An alternative solution would be that the high-mass sources studied here have not gone through a long (pre-stellar) phase in which the dust temperature was low enough for CO to be frozen out and turned into other molecules.

8.5.3. CH_3CN

The clear mismatches between theory and observations for the ratios involving CH_3CN point toward an underproduction of acetonitrile by more than an order of magnitude in the models. As with formamide, gas-phase, radical and atom addition reactions contribute to the formation of CH_3CN in the models, making it difficult to determine the cause. The main formation route in the models by radical addition of solid CH_3^\bullet and solid CN^\bullet has never experimentally been investigated. It would therefore be useful to determine if this is a viable solid state formation route and if it potentially has a higher efficiency than assumed.

Alternatively it is possible that photodestruction of solid acetonitrile is not as efficient as assumed in the models. Gratier et al. (2013) find high gas-phase CH_3CN abundances in the Horsehead PDR, indicative of a high photodesorption rate and slow destruction of CH_3CN in the ice. Bernstein et al. (2004) indeed find slower photolysis of solid CH_3CN compared with other organic molecules. If such a slower photodissociation rate would also hold for gas-phase CH_3CN , it would be an attractive explanation why the CH_3CN rotational temperatures are generally higher than those of other complex molecules (e.g., Bisschop et al. (2007b) and many other hot core studies), since the molecule could then approach the protostar closer before being destroyed. However, the gas phase photoabsorption cross sections of CH_3CN are well determined and if the bulk of these absorptions lead to dissociation this would result in a photodissociation rate of gaseous CH_3CN at least as fast as that of CH_3OH (van Dishoeck et al. 2006).

Another important parameter for all molecules studied here is the mobility of radicals and neutral molecules on the surface assumed in the gas-grain models. For many species no experimental data are available on diffusion barriers, only theoretically-inspired guesses. Observational evidence suggests that at least parts of the ice mantles are segregated in CO-rich and CO-poor layers (Tielens et al. 1991; Pontoppidan et al. 2008). Therefore, more knowledge of the structure of ice mantles and the mobility of radicals and neutral molecules as a function of surface temperature and in various chemical environments is necessary to determine if addition reactions are likely to happen and at which rates.

8.5.4. Prospects for ALMA

In the near future, much deeper searches for CH_3NH_2 can be carried out by ALMA (Appendix 8.7.2). Figure 8.5 shows that the strongest transitions within Band 6 are mainly located between 240 and 275 GHz and in Band 7 around 310, 340 and 355 GHz. In Table 8.6 the strongest transitions in ALMA's Band 6 and 7 are listed. It becomes apparent that lines covered by Band 7 are more intense, but at the cost of a lower line density.

Estimates done for the W 33A source with the CASSIS line analysis software and the ALMA Sensitivity Calculator show that ALMA should be able to reach the 3σ detection limits for the CH_3NH_2 lines around 236 GHz in less than 1 hour of integration time, assuming the column density for methylamine of $1.2 \times 10^{14} \text{ cm}^{-2}$ as found by Turner (1991) in a large beam and two orders of magnitude lower than those inferred here for a small source size. This estimate assumes a spectral resolution of 0.64 km s^{-1} as used in our JCMT data, the number of ALMA antennas set to 34 (as in Cycle 2) and a synthesized beam of $1.1''$, appropriate for the W33A hot core (100 K radius).

8.6. Conclusions

We have analysed nine hot core regions in search of methylamine. The molecule has not been convincingly detected, so upper limit abundances are determined for all the sources. From these limits, ratios of methylamine to other molecules (NH_2CHO , CH_3OH , CH_3CN) have been determined and compared with theory and Sagittarius B2 surveys. Our conclusions are as follows:

1. Trends in our results indicate that both methylamine and formamide are overproduced in the models of Garrod et al. (2008). Acetonitrile is underproduced with respect to these models. This is especially true for the slow models.
2. Abundance ratios do not differ more than an order of magnitude between various sources suggesting that the (nitrogen) chemistry is very similar between hot cores, as has been found previously for other species.
3. More (laboratory) studies are needed to clarify the formation pathway of methylamine and to determine differences and similarities with formamide, methanimine and, to a lesser extent, acetonitrile formation.

4. The upper limits determined for CH_3NH_2 here can guide future more sensitive observations, especially with ALMA. Based on the ratios found in the Sgr B2 observations it is very likely that ALMA will reach the detection limit for methylamine in the sources studied here. Particularly strong transitions and spectral regions to target with ALMA are given.

Acknowledgement

Thanks go out to C. Walsh, I. San Jose García, M. Drozdovskaya, N. van der Marel, M. Kama, M. Persson, J. Mottram, G. Fedoseev, M.H.D. van der Wiel and H. Linnartz for their support and input on this project. Thoughtful comments by the referee are much appreciated.

Astrochemistry in Leiden is supported by the Netherlands Research School for Astronomy (NOVA), by a Royal Netherlands Academy of Arts and Sciences (KNAW) professor prize, and by the European Union A-ERC grant 291141 CHEMPLAN.

8.7. Appendix

8.7.1. Transitions of methylamine and other molecules

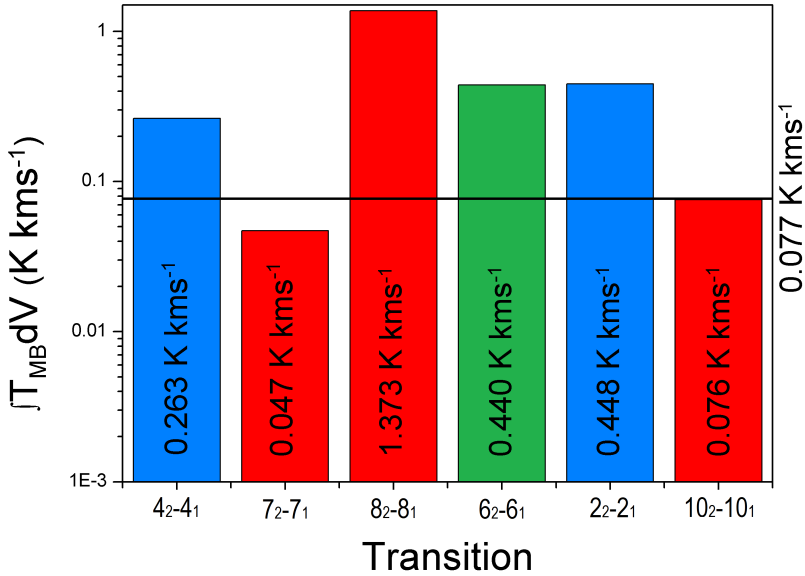


Figure 8.3: Bargraph plot of the integrated main-beam intensities for the six investigated methylamine transitions. $\int T_{MB} dV$ values were calculated for a total column density of $3.4 \times 10^{17} \text{ cm}^{-2}$ as inferred toward G31.41+0.31 from the $6_2 \rightarrow 6_1$ transition, assuming a rotational temperature of 120 K. The horizontal line shows the 0.077 K kms^{-1} 3σ value for G31.41+0.31. It is unlikely that the detection of the 236408 feature (green) in this hot core is methylamine, since the main-beam intensities of other CH_3NH_2 transitions are above the 3σ value. Particularly the $4_2 \rightarrow 4_1$ and $2_2 \rightarrow 2_1$ transition (blue) should be visible in our spectra. The remaining transitions (red) are either below detection limit or not observed toward this source.

Table 8.5: All identified transitions for the sources G31.41+0.31 and W3(H₂O), with integrated peak area listed.

Species	Freq (MHz)	E_{up} (K)	A (s ⁻¹)	Transition	G31.41+0.31 (K kms ⁻¹)	W3(H ₂ O) (K kms ⁻¹)
CH ₃ OCHO	228628.876	118.8	1.66E-04	18 ₅₁₃₂ → 17 ₅₁₂₂	-	0.39
CH ₃ OCHO	228651.404	118.8	1.66E-04	18 ₅₁₃₀ → 17 ₅₁₂₀	-	0.53
CH ₃ COCH ₃	228668.358	85.4	1.69E-04	14 ₉₆₁ → 13 ₈₅₂	-	0.24
CH ₃ OCHO	229388.947	217.0	1.62E-05	23 ₉₁₅₀ → 23 ₈₁₆₀	0.79	-
CH ₃ OCHO	229405.021	110.7	1.75E-04	18 ₃₁₅₂ → 17 ₃₁₄₂	2.18	0.78
CH ₃ OCHO	229420.342	110.7	1.75E-04	18 ₃₁₅₀ → 23 ₃₁₄₀	1.86	0.71
CH ₃ OCHO	229504.724	134.3	1.18E-05	20 ₃₁₇₀ → 19 ₄₁₆₀	1.52	-
CH ₃ OH	229589.056	374.4	2.08E-05	15 ₄₀ → 16 ₃₀	2.58	1.06
CH ₃ OH	229758.756	89.1	4.19E-05	8 ₁₀ → 7 ₀₀	7.17	-
CH ₃ OCHO	236355.948	128.0	1.93E-04	20 ₃₁₈₁ → 19 ₃₁₇₁	2.38	-
CH ₃ OCHO	236365.574	128.0	1.93E-04	20 ₃₁₈₀ → 19 ₃₁₇₀	1.93	-
CH ₃ NH ₂	236408.788	60.8	5.94E-05	6 ₂₁ → 6 ₁₀	0.44	-
HCCCN	236512.777	153.2	1.05E-03	26 → 25	4.67	2.27
H ₂ CS	236726.770	58.6	1.91E-04	7 ₁₇ → 6 ₁₆	7.54	5.75
CH ₃ OCHO	236743.697	129.6	1.86E-04	19 ₅₁₅₁ → 18 ₅₁₄₁	2.21	? ^a
CH ₃ OCHO	236759.687	129.6	1.86E-04	19 ₅₁₅₀ → 18 ₅₁₄₀	1.40	0.53
CH ₃ OCHO	236800.589	136.7	1.80E-04	19 ₆₁₄₁ → 18 ₆₁₃₁	1.21	?
CH ₃ OCHO	236810.314	136.7	1.81E-04	19 ₆₁₄₀ → 18 ₆₁₃₀	2.50	1.20
CH ₃ OH	236936.089	260.2	2.79E-05	14 ₁₀ → 13 ₂₀	2.74	1.91
CH ₃ OCHO	236975.844	320.3	2.01E-04	22 ₁₂₂₄ → 21 ₁₂₁₄	0.86	0.33
CH ₃ OCHO	236976.390	320.3	2.01E-04	22 ₀₂₂₅ → 21 ₀₂₁₀	0.86	0.33
CH ₃ OCHO	236975.844	320.3	2.01E-04	22 ₁₂₂₄ → 21 ₁₂₁₄	1.19	0.52
CH ₃ OCHO	236976.390	320.3	2.01E-04	22 ₀₂₂₅ → 21 ₀₂₁₅	1.19	0.52
CH ₃ OCH ₃	237046.092	31.3	2.33E-05	7 ₂₅₃ → 6 ₁₆₃	2.90	0.80
CH ₃ OCH ₃	237046.106	31.3	2.33E-05	7 ₂₅₂ → 6 ₁₆₂	2.90	0.80
CH ₃ OCH ₃	237048.797	31.3	2.32E-05	7 ₂₅₁ → 6 ₁₆₁	2.90	0.80
CH ₃ OCH ₃	237051.495	31.3	2.33E-05	7 ₂₅₀ → 6 ₁₆₀	2.90	0.80
SO ₂	237068.870	94.0	1.14E-04	12 ₃₉ → 12 ₂₁₀	1.07	1.96
OC ³⁴ S	237273.635	119.6	3.88E-05	20 → 19	1.24	0.58
CH ₃ OCHO	237297.482	128.0	1.95E-04	20 ₂₁₈₂ → 19 ₂₁₇₂	?	2.45
CH ₃ OCHO	237309.540	131.6	1.98E-04	21 ₂₂₀₁ → 20 ₂₁₉₁	?	2.45
CH ₃ OCHO	237315.082	131.6	1.98E-04	21 ₂₂₀₀ → 20 ₂₁₉₀	?	2.45
CH ₃ OCHO	237344.870	131.6	1.98E-04	21 ₁₂₀₂ → 20 ₁₁₉₂	3.48	1.19
CH ₃ OCHO	237350.386	131.6	1.98E-04	21 ₁₂₀₀ → 20 ₁₁₉₀	3.48	1.19
OCS	243218.040	122.6	4.18E-05	20 → 19	-	2.95
CH ₃ OCH ₃	259982.561	226.6	7.27E-05	20 ₅₁₆₂ → 20 ₄₁₇₂	-	1.54
CH ₃ OCH ₃	259982.596	226.6	7.27E-05	20 ₅₁₆₃ → 20 ₄₁₇₃	-	1.54
CH ₃ OCH ₃	259984.480	226.6	7.27E-05	20 ₅₁₆₁ → 20 ₄₁₇₁	-	1.54
CH ₃ OCH ₃	259982.561	226.6	7.27E-05	20 ₅₁₆₀ → 20 ₄₁₇₀	-	1.54
NH ₂ CHO	260189.848	92.4	1.25E-03	12 ₂₁₀ → 11 ₂₉	-	1.46
H ¹³ CO+	260255.339	25.0	1.33E-03	3 → 2	-	11.76
CH ₃ OCH ₃	260327.165	208.3	7.21E-05	19 ₅₁₅₂ → 19 ₄₁₆₂	-	1.27
CH ₃ OCH ₃	260327.238	208.3	7.21E-05	19 ₅₁₅₃ → 19 ₄₁₆₃	-	1.27
CH ₃ OCH ₃	260329.312	208.3	7.21E-05	19 ₅₁₅₁ → 19 ₄₁₆₁	-	1.27
CH ₃ OCH ₃	260331.422	208.3	7.21E-05	19 ₅₁₅₀ → 19 ₄₁₆₀	-	1.27
SiO	260518.020	43.8	7.21E-05	6 → 5	-	9.24

Notes. ^a Indicates an identified transition where it was not possible to determine the peak area.

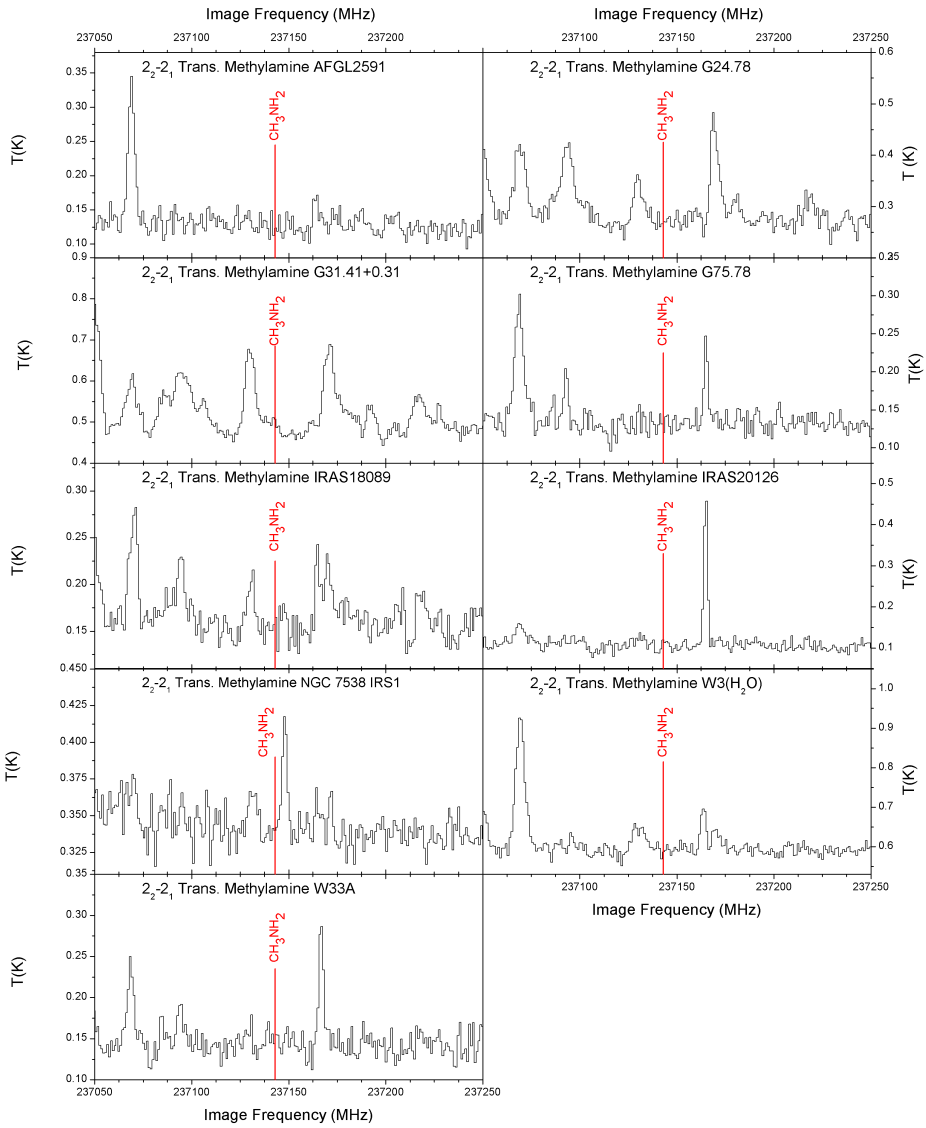


Figure 8.4: Blow-up of the spectral region around the $2_2 \rightarrow 2_1$ transition at 237143 MHz of all analysed hot cores. Despite being a particularly strong transition, it was not observed in any of the spectra.

8.7.2. ALMA

In the following figure the simulated spectrum of methylamine is shown for a column density of $1.0 \times 10^{15} \text{ cm}^{-2}$ at an excitation temperature of 120 K. Simulations were done with CASSIS using the JPL spectroscopic database. The frequency ranges were taken to cover ALMA Bands 6 and 7. The resolution was set at 0.1 MHz for this spectrum.

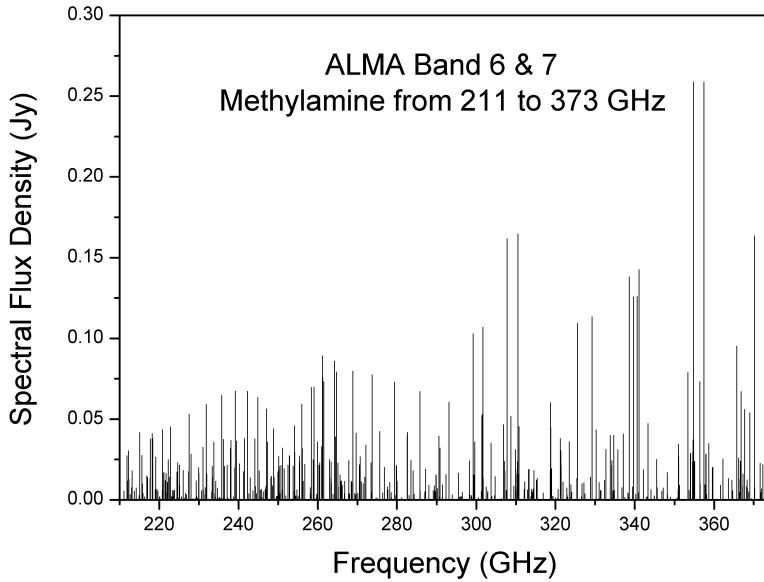


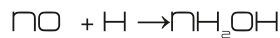
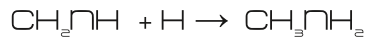
Figure 8.5: 211 to 373 GHz spectrum of methylamine, covering ALMA bands 6 and 7. A column density of 10^{15} cm^{-2} , T_{rot} and beam size of $1''$ are used.

Table 8.6: Methylamine transition target candidates for ALMA Band 6 and 7

Transition	Freq (MHz)	E_{up} (K)	A (s^{-1})
$7_{2\ 6} \rightarrow 7_{1\ 6}$	227498.06	75.4	4.80E-05
$5_{2\ 6} \rightarrow 5_{1\ 6}$	232003.95	47.7	4.73E-05
$8_{2\ 3} \rightarrow 8_{1\ 2}$	235735.04	92.8	6.13E-05
$7_{2\ 2} \rightarrow 7_{1\ 3}$	239209.63	75.8	6.29E-05
$6_{2\ 3} \rightarrow 6_{1\ 2}$	242262.02	60.9	6.39E-05
$5_{2\ 2} \rightarrow 5_{1\ 3}$	244886.90	48.1	6.42E-05
$8_{0\ 5} \rightarrow 7_{1\ 5}$	259042.46	77.0	5.73E-05
$6_{2\ 2} \rightarrow 6_{1\ 3}$	261252.89	60.9	7.14E-05
$8_{0\ 2} \rightarrow 7_{1\ 3}$	261563.15	76.8	5.98E-05
$4_{1\ 5} \rightarrow 3_{0\ 5}$	264172.21	25.9	8.74E-05
$8_{2\ 2} \rightarrow 8_{1\ 3}$	268898.14	92.8	7.44E-05
$9_{0\ 5} \rightarrow 8_{1\ 5}$	299189.80	96.1	8.78E-05
$9_{0\ 3} \rightarrow 8_{1\ 2}$	301654091	95.9	9.11E-05
$5_{-1\ 3} \rightarrow 4_{0\ 2}$	307791.75	36.3	1.44E-04
$14_{2\ 2} \rightarrow 14_{-1\ 3}$	310750.84	240.0	8.33E-05
$10_{0\ 5} \rightarrow 9_{1\ 5}$	338628.32	117.3	1.25E-04
$10_{0\ 2} \rightarrow 9_{-1\ 3}$	341059.48	117.1	1.30E-04
$6_{1\ 2} \rightarrow 5_{0\ 3}$	354843.73	49.2	2.16E-04
$6_{1\ 5} \rightarrow 5_{0\ 5}$	357440.12	49.5	2.16E-04
$3_{2\ 4} \rightarrow 2_{1\ 4}$	370166.34	28.4	2.11E-04



V-UV



9

Small -NH₂ and NO molecules towards IRAS 16293–2422B

N.F.W. Ligterink, H. Calcutt, A. Coutens, T.L. Bourke, M.N. Drozdovskaya, L.E. Kristensen, H.S.P. Müller, S.F. Wampfler, M.H.D. van der Wiel, E.F. van Dishoeck & J.K. Jørgensen

Ligterink et al. 2017, *The ALMA-PILS survey: Stringent limits on small amines and nitrogen-oxides towards IRAS 16293–2422B*, *subm. to A&A*

9.1. Introduction

The small molecules methylamine (CH₃NH₂) and hydroxylamine (NH₂OH) with an amine (-NH₂) functional group have both been suggested as precursors to the formation of amino acids (Blagojevic et al. 2003; Snow et al. 2007; Holtom et al. 2005; Bossa et al. 2009; Barrientos et al. 2012; Garrod 2013). Reactions involving these molecules might explain the presence of the simplest amino acid glycine in comets (Elsila et al. 2009; Altwegg et al. 2016). Despite their importance, both CH₃NH₂ and NH₂OH have turned out to be quite elusive molecules in the interstellar medium. CH₃NH₂ has exclusively been detected towards Sgr B2 and tentatively towards Orion KL (e.g., Kaifu et al. 1974; Pagani et al. 2017). Upper limit abundances of CH₃NH₂ towards other high-mass sources are generally found to be consistent to values determined towards Sgr B2 (Ligterink et al. 2015). In the Solar System CH₃NH₂ has been detected in comets 81P/Wild 2 and 67P/Churyumov-Gerasimenko (Elsila et al. 2009; Goesmann et al. 2015; Altwegg et al. 2017). NH₂OH has not been detected thus far, down to upper limit abundances of $\sim 10^{-11}$ with respect to H₂ (Pulliam et al. 2012; McGuire et al. 2015).

The lack of detection of these two molecules not only constrains amino acid formation, but also contrasts with model predictions. Garrod et al. (2008) predicted efficient CH₃NH₂ formation from the radical addition reaction CH₃ + NH₂, whereas NH₂OH is formed from NH + OH addition followed by hydrogenation and NH₂ + OH reactions on ice surfaces. Abundances of CH₃NH₂ and NH₂OH are predicted to be of the order of 10^{-6} – 10^{-7} , depending on the model. It is generally found that these models overproduce both molecules (Pulliam et al. 2012; Ligterink et al. 2015). Other formation or destruction mechanisms may need to be considered. Several laboratory experiments have investigated the formation of NH₂OH and CH₃NH₂. Zheng & Kaiser (2010) show the formation of NH₂OH from electron irradiated H₂O:NH₃ ice mixtures, while He et al. (2015) produce the molecule by oxidation of NH₃ ice. Alternatively, NH₂OH is seen to efficiently form from the solid-state hydrogenation of nitric oxide (NO, Congiu et al. 2012; Fedoseev et al. 2012). In this scenario, NO is accreted from the gas-phase onto dust grains during cloud collapse (Visser et al. 2011). Nitrous oxide (N₂O) is found as a by-product of NO hydrogenation reactions. NO has been observed in a variety of sources (e.g., Liszt & Turner 1978; Yıldız et al. 2013). It is thought to mainly form via the N + OH → NO + H neutral-neutral reaction in the gas-phase. Observations suggest that N₂O is related to NO (Ziurys et al. 1994; Halfen et al. 2001).

CH₃NH₂ formation has been demonstrated in electron irradiated CH₄:NH₃ ice mixtures (Kim & Kaiser 2011; Förstel et al. 2017), with the main formation pathways suggested to proceed through CH₃ + NH₂ radical reactions. Theule et al. (2011) investigated hydrogenation of solid hydrogen cyanide (HCN) and methanimine (CH₂NH), both of which lead to CH₃NH₂ formation. CH₂NH is hypothesized to have a larger reaction probability than HCN and reaction pathways to CH₃NH₂ may be completely different for reactions starting from either HCN or CH₂NH. In contrast with CH₃NH₂, its potential precursor CH₂NH has been observed in numerous sources (Dickens et al. 1997; Nummelin et al. 2000; Belloche et al. 2013; Suzuki et al. 2016). Halfen et al. (2013) investigated

the relationship between this molecule and CH_3NH_2 in Sgr B2 and concluded that the two species have different formation routes, due to found differences in rotational temperature and distribution. Interestingly, CH_2NH has also been implied as a precursor to amino acid formation (e.g., Woon 2002; Danger et al. 2011).

Searches for CH_3NH_2 and NH_2OH have so far mainly focused on high-mass sources. Detections or upper limits of these two molecules and their potential precursors towards a low-mass source would therefore expand our understanding of amine-containing molecules and their formation in the ISM. The low-mass solar-type protostellar binary IRAS 16293–2422 (hereafter IRAS 16293) is an ideal source for such a study. Its physics and chemistry are well studied and it is abundant in complex organic molecules (Jørgensen et al. 2016). Abundance ratios will therefore constrain the chemistry of $-\text{NH}_2$ molecules as has been done for other nitrogen-bearing species (Coutens et al. 2016; Ligterink et al. 2017). In this letter we present the first detection of CH_2NH towards a low-mass source, as well as detections of NO and N_2O . The abundances of NH_2OH and CH_3NH_2 are constrained by upper limits from non-detections.

9.2. Observations and data analysis

The observations were taken as part of the Protostellar Interferometric Line Survey (PILS), an unbiased spectral survey using the Atacama Large Millimeter Array (ALMA, Jørgensen et al. 2016). The survey covers a spectral range of 329.147 to 362.896 GHz in Band 7, obtained with the 12 m array and the Atacama Compact Array (ACA). The combined data set analysed in this letter was produced with a circular restoring beam of $0''.5$. The largest filtered scale is $13''$. A spectral resolution of 0.2 km s^{-1} and an RMS of about 7–10 mJy $\text{beam}^{-1} \text{ channel}^{-1}$, i.e., approximately 4–5 mJy $\text{beam}^{-1} \text{ km s}^{-1}$ is obtained. The dataset has a calibration uncertainty of 5–10%.

The spectral analysis presented below is performed towards source B in IRAS 16293 at a position offset by one beam diameter ($0''.5$) from the continuum peak position in the south west direction ($\alpha_{J2000}=16^{\text{h}}32^{\text{m}}22^{\text{s}}.58$, $\delta_{J2000}=-24^{\circ}28'32.8''$). This position is used for most other PILS molecular identifications and abundance analyses. Lines are particularly narrow towards this position, only 1 km s^{-1} , limiting line confusion.

The spectra are analysed with the CASSIS software¹ and linelists from the Jet Propulsion Laboratory (JPL²) catalog for molecular spectroscopy (Pickett et al. 1998) and Cologne Database for Molecular Spectroscopy (CDMS, Müller et al. 2001, 2005). The detected transitions are fitted with synthetic spectra to derive column densities, excitation temperatures, linewidths and peak velocities assuming Local Thermodynamic Equilibrium (LTE) and a source size of $0''.5$ based on emission maps of the source.

Due to the strong continuum component towards IRAS 16293B, the continuum is included in the spectral model as a background temperature. The continuum is dominated by the high column density dust in the disk while the

¹<http://cassis.irap.omp.eu/>

²<http://spec.jpl.nasa.gov>

Table 9.1: Column densities for the species investigated in this work.

Molecule	Formula	N_{tot}^{\dagger} (cm ⁻²) (cm ⁻²)	T_{ex} (K) (K)	FWHM (km s ⁻¹) (km s ⁻¹)	V_{peak} (km s ⁻¹) (km s ⁻¹)
Nitric oxide	NO	2.0 (0.5) × 10 ¹⁶	100 ⁺⁵⁰ ₋₆₀	1.0	2.5
Nitrous oxide	N ₂ O	5.0 (1.0) × 10 ¹⁶	100 ⁺¹⁵⁰ ₋₂₀	1.0	2.5
Hydroxylamine	NH ₂ OH	≤ 3.7 × 10 ¹⁴	100	1.0	2.7
Methanimine	CH ₂ NH	8.0 (2.0) × 10 ¹⁴	100 ⁺²⁰ ₋₃₀	1.0	2.7
Methylamine	CH ₃ NH ₂	≤ 5.3 × 10 ¹⁴	100	1.0	2.7

Notes. All models assume LTE, an excitation temperature of 100 K, a FWHM of 1 km s⁻¹ and a source size of 0'.5. †Upper limits are 3σ.

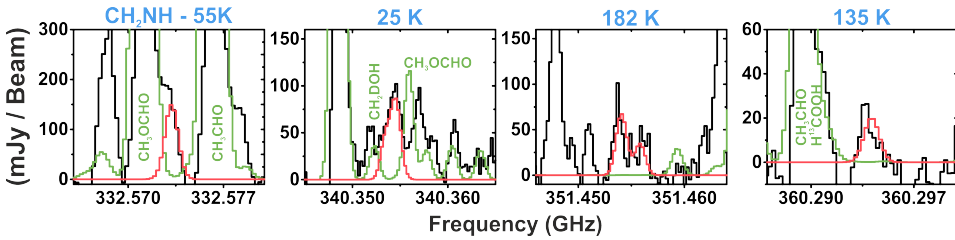


Figure 9.1: All detected transitions of CH₂NH in the PILS spectrum (black), with the best fit at $T_{\text{ex}} = 100$ K (red) and template of other detected species in PILS overplotted (green). The upper state energy of each transition is indicated in blue.

lines arise from the infalling gas in the envelope, and therefore the dust and gas are not fully coupled at the offset position analysed in this work. The correction factor is 1.15 at 100 K.

For the non-detected species the formalism in Ligterink et al. (2015) is used to derive upper limit column densities based on the 3σ upper limit line intensities of the strongest transitions in line-free ranges of the PILS data. The 1σ limit is given by $1.1 \times \Delta V \times \text{RMS}$, where ΔV is the linewidth in source B (1 km s⁻¹) and 1.1 is a factor to account for a 10% calibration uncertainty. Corrections for beam dilution and background dust temperature are applied as well.

9.3. Results

Spectral lines of CH₂NH, NO and N₂O are identified towards source B, while those of CH₃NH₂ and NH₂OH are not. An overview of the detected transitions is presented in Table 9.4 in Appendix A. Figures 9.1, 9.2 and 9.3 show the detected transitions of CH₂NH, NO and N₂O, respectively, towards source B, with synthetic spectra overplotted. A synthetic spectrum of other species identified in the framework of PILS is also plotted to show which lines are blended.

CH₂NH is detected for the first time towards a low-mass protostellar source. A total of 18 hyperfine lines in four different spectral features are detected. The first feature shows up at 332.575 GHz and is blended with a neighbouring CH₃OCHO line. At 340.354 GHz five hyperfine lines form a distinct feature

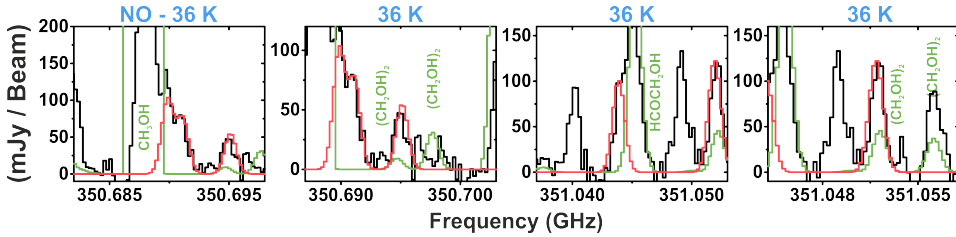


Figure 9.2: All detected transitions of NO in the PILS spectrum (black), with the best fit at $T_{\text{ex}} = 100$ K (red) and template of other detected species in PILS overplotted (green). The upper state energy of each transition is indicated in blue.

that is unblended with any other molecule. Around 351.455 GHz a distinct double peak feature is found. Finally, at 360.294 GHz the last feature is seen, that seems to be blended with another, unidentified feature. ALMA observations in bands 4, 6 and 9 towards IRAS 16293 were used to search for additional lines, but spectral features of CH_2NH fall outside the spectral windows of these observations. Publicly available data of the single dish TIMASSS survey towards IRAS 16293 were analysed for CH_2NH spectral features, but no lines were found.

Upper state energies (E_{up}) of the detected features range from 26 to 183 K, making it possible to constrain the excitation temperature. With a grid of models the emission of this species can be fitted with excitation temperatures ranging between 70–120 K and column densities of $6.0 \times 10^{14} - 10.0 \times 10^{14} \text{ cm}^{-2}$. Outside this temperature range synthetic spectra can not reproduce the observed spectrum, as can be seen in Fig. 9.5 in Appendix 9.5.2 for fits at $T_{\text{ex}} = 50$ and 150 K. In the best fits, no anti-coincidences are found between the synthetic and observed spectrum. At $T_{\text{ex}} = 100$ K the best fit column density is found to be $8.0 \times 10^{14} \text{ cm}^{-2}$.

Five NO transitions, each with an upper state energy of 36 K, are detected. A number of NO lines at $E_{\text{up}} = 209$ K are in range of the data, but are not observed in the spectrum. The excitation temperature can therefore be constrained to be lower than 150 K, due to anti-coincidences of the $E_{\text{up}} = 209$ K lines in the synthetic spectrum at 150 K and higher, as can be seen in Fig. 9.6 in Appendix 9.5.2. At an excitation temperature of 100 K a best fit column density of $2.0 \times 10^{16} \text{ cm}^{-2}$ is found, but it can vary between $1.5 \times 10^{16} - 2.5 \times 10^{16} \text{ cm}^{-2}$ for $T_{\text{ex}} 40 - 150$ K. The emission is best fitted with a velocity of $V_{\text{peak}} = 2.5 \text{ km s}^{-1}$, slightly offset from the $V_{\text{LSR}} = 2.7 \text{ km s}^{-1}$ of source B. A similar offset is seen in some other species in the PILS dataset (see Jørgensen et al. in preparation for more details), however this offset only corresponds to 1 velocity channel in the data. We therefore can't interpret this difference at this time.

Three N_2O transitions fall in the frequency range of the PILS data, one $v=0$ line, $E_{\text{up}} = 127$ K and two $v_2=1$ lines, $E_{\text{up}} = 973$ K. In the observed spectrum a feature is found that fits the $v=0$ line at 351.667 GHz. Since no other known species were found to fit this spectral feature, a tentative detection of N_2O can be claimed. We have also searched additional datasets to try and find further lines to support this detection. We have searched band 4, 6 and 9 ALMA datasets towards IRAS 16293, as well as data from the single dish TIMASSS survey. We

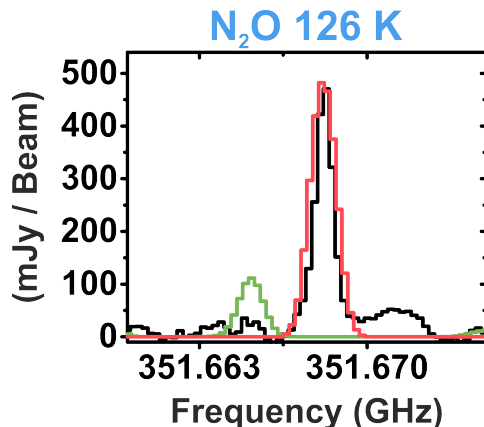


Figure 9.3: The tentatively identified transition of N₂O in the PILS spectrum (black), with the best fit at $T_{\text{ex}} = 100$ K (red) and template of other detected species in PILS overplotted (green). The upper state energy of each transition is indicated in blue.

are however unable to detect more lines as those that fall in the frequency range of the data are too weak to be identified. Similar to NO, $V_{\text{peak}} = 2.5$ km s⁻¹ for this line. Lines of the ¹⁵N and ¹⁸O isotopologues of N₂O were searched for, but not detected to levels above the standard ¹⁵N/¹⁴N and ¹⁸O/¹⁶O ISM ratios. Based on the non-detection of the $v_2=1$ lines, the excitation temperature can be determined to be lower than 250 K. At $T_{\text{ex}} = 100$ K a column density of 5.0×10^{16} cm⁻² for N₂O is derived, with an uncertainty of $\pm 1.0 \times 10^{16}$ cm⁻² over the entire possible temperature range.

Figure 9.4 shows the emission maps of the 332.572 GHz line of CH₂NH, the 351.052 GHz line of NO, and the 351.668 GHz line of N₂O towards source B. Emission is generally found to be compact and compares well with emission maps of other molecules towards source B, such as NH₂CHO (Coutens et al. 2016). Emission of N₂O is more extended than that of NO.

Transitions of both CH₃NH₂ and NH₂OH are not detected and therefore upper limit column densities are determined. For CH₃NH₂, the $6_1 \rightarrow 5_0$ transition at 357.440 GHz best constrains the upper limit column density. For a 3σ upper limit line intensity of 23 mJy km s⁻¹ the upper limit column densities versus the rotational temperatures are plotted in Fig. 9.7 in Appendix C. At $T_{\text{ex}} = 100$ K the upper limit column density is $\leq 5.3 \times 10^{14}$ cm⁻².

NH₂OH has three strong transitions at 352.522, 352.730 and 352.485 GHz for the $7_0 \rightarrow 6_0$, $7_1 \rightarrow 6_1$, $7_2 \rightarrow 6_2$ transitions, respectively. Slightly different RMS noise conditions apply around each of these transitions, resulting in a 3σ of 27, 21 and 27 mJy km s⁻¹, respectively. The upper limit column density versus rotational temperature plot is shown in Fig. 9.8. The transition at 352.522 GHz constrains the column density the most and the upper limit column density of NH₂OH is found to be $\leq 3.7 \times 10^{14}$ cm⁻² at $T_{\text{ex}} = 100$ K.

Table 9.1 lists the column densities at $T_{\text{ex}} = 100$ K for the five molecules under investigation in this work. The range of excitation temperatures that can fit the emission has been included in this Table and the resulting uncertainty in the

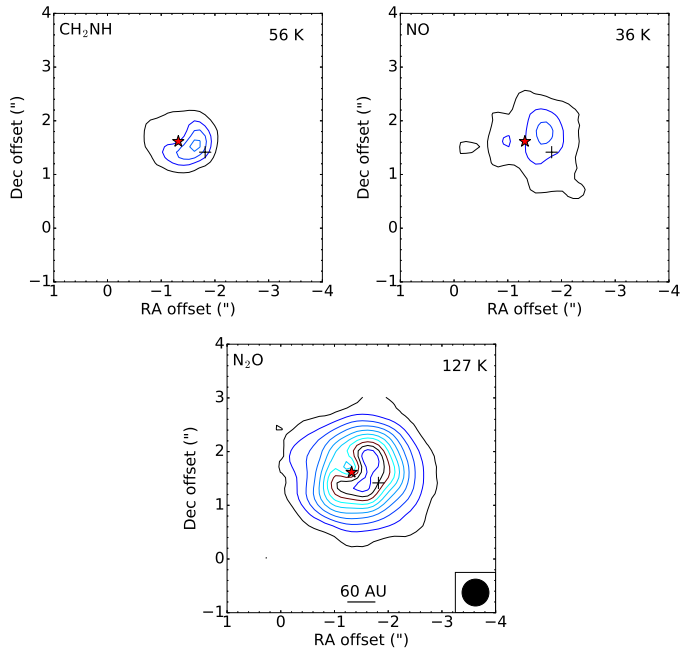


Figure 9.4: Integrated emission maps of the 332.572 GHz line of CH_2NH , the 351.052 GHz line of NO , and the 351.668 GHz line of N_2O . The emission is integrated between 2.2 and 3.2 km s^{-1} . The axes show the position offset from phase centre of the observations. Contour levels start at 20σ and increase in steps of 30σ . The red star marks the peak continuum position and the black cross marks the 1 beam offset position where the spectra are analysed.

column density is given in brackets. For both CH_3NH_2 and NH_2OH the typical uncertainty in column density for a reasonable range of excitation temperatures is a factor of ~ 2 .

Table 9.2: Comparison of methylamine abundance ratios.

Source	$\text{CH}_3\text{NH}_2/\text{CH}_2\text{NH}$	$\text{CH}_3\text{NH}_2/\text{NH}_2\text{CHO}$	$\text{CH}_3\text{NH}_2/\text{CH}_3\text{OH}$
IRAS 16293–2422B	≤ 0.79	≤ 0.053	$\leq 5.3 \times 10^{-5}$
Sgr B2 ^a	~ 1	0.57	0.017
Sgr B2(M) ^b	31	3.2	0.017
Sgr B2(N) ^b	0.75	0.43	0.033
Sgr B2(N) ^c	5.5	–	–
Sgr B2(N) ^d	7.1	2.1	0.1
Hot core model ^e	–	1.1–1.7	0.034–0.13

Notes. ^aTurner (1991); ^bBelloche et al. (2013); ^cHalfen et al. (2013); ^dNeill et al. (2014); ^eGarrod et al. (2008), models F, M and S.

Table 9.3: Comparison of CH₂NH abundance ratios.

Source	CH ₂ NH/NH ₂ CHO	CH ₂ NH/CH ₃ OH	CH ₂ NH/H ₂
IRAS 16293-2422B	0.08	8.0×10^{-5}	$< 6.7 \times 10^{-11}$
Sgr B2 ^a	~0.57	~0.017	–
Sgr B2(M) ^b	0.10	5.5×10^{-4}	–
Sgr B2(N) ^b	0.57	0.044	–
Sgr B2(N) ^c	–	–	3.0×10^{-10}
Sgr B2(N) ^d	0.30	0.014	8.8×10^{-9}
Orion KL ^e	–	1.9×10^{-3}	4.2×10^{-9}

Notes. ^aTurner (1991); ^bBelloche et al. (2013); ^cHalfen et al. (2013); ^dNeill et al. (2014); ^eCrockett et al. (2014b)

9.4. Astronomical implications

To put the results into context the abundance ratios with formamide, methyl cyanide, methanol and molecular hydrogen are compared with other sources. The column densities of these species towards the 1 beam offset position in source B are: NH₂CHO = 1×10^{16} , CH₃OH = 1×10^{19} and H₂ $> 1.2 \times 10^{25}$ cm⁻² (Coutens et al. 2016; Jørgensen et al. 2016). The H₂ lower limit column density is determined towards the continuum peak position of source B, but within the uncertainties of the observations is not expected to differ much for the one beam offset position being analysed in this chapter. Many papers with which our ratios are compared to make use of single dish data, whereas in this work we use interferometric data. It is important to stress that differences in abundance ratios do not necessarily reflect chemical differences, but could arise from the fact that single dish observations generally probe larger spatial scales and are more affected by beam dilution (see Jørgensen et al. 2016).

The NH₂OH upper limit abundance of $N(\text{NH}_2\text{OH})/N(\text{H}_2) \leq 3.1 \times 10^{-11}$ found in this work is comparable to upper limit abundances found for high-mass sources by Pulliam et al. (2012), but significantly lower than the ice abundances of 7×10^{-9} $N(\text{H}+\text{H}_2)$ found with a dark cloud model in Fedoseev et al. (2012). However, this model does not take destruction and reaction pathways into account and could overpredict the NH₂OH abundance. The non-detection of NH₂OH in the gas-phase could be explained by efficient destruction of the molecule. Laboratory experiments show that thermal processing of NH₂OH:H₂O mixtures result in the conversion of NH₂OH into HNO, NH₃ and O₂ before the onset of desorption (Jonusas & Krim 2016). Also, UV processing of ice mixtures containing NH₂OH results in the efficient destruction of this molecule (Fedoseev et al. 2016). The low gas-phase abundance of NH₂OH limits its involvement in gas-phase production routes of amino acids.

The NO abundance in IRAS 16293B ($N(\text{NO})/N(\text{H}_2) \leq 1.7 \times 10^{-9}$) is low compared to observational and modelling studies of dark clouds, where NO abundances of 10^{-8} – 10^{-6} are found (e.g., McGonagle et al. 1990; Visser et al. 2011). Modelling shows that NO is readily lost in the ice by conversion to other species, mainly NH₂OH (Yıldız et al. 2013), and in the gas-phase by photodissociation reactions in the hot core (Visser et al. 2011) and thus could explain the depletion of NO in IRAS 16293B. The high N₂O abundance may indicate destruction of NO as well. It is found in laboratory ice experiments

as a side product of NO hydrogenation and UV irradiation (Congiu et al. 2012; Fedoseev et al. 2012, 2016) and suggested to form via the reaction $\text{NO} + \text{NH}$ in warm gas (Halfen et al. 2001). The $N(\text{N}_2\text{O})/N(\text{NO}) = 2.5$ ratio may hint to a scenario where NO is depleted in the ice and gas surrounding IRAS 16293B, while N_2O is one of the products of NO.

Table 9.2 lists the abundance ratios of CH_3NH_2 in IRAS 16293B, Sgr B2 and hot core models of Garrod et al. (2008). Abundances differ by at least one to two orders of magnitude between IRAS 16293B and Sgr B2 and models. CH_2NH is also much less abundant in IRAS 16293B than Sgr B2 (Table 9.3). This can indicate that the formation of both species is less efficient in IRAS 16293B, perhaps due to different physical conditions of the sources. CH_3NH_2 was mass spectrometrically detected on the comet 67P/C-G (Goesmann et al. 2015). However, recent measurements with the ROSINA-DFMS instrument determined it to be present at lower abundance than initially thought (Altwegg et al. 2017). Since IRAS 16293B is assumed to resemble an early formation stage of our solar system, the low abundance of CH_3NH_2 and non-detection in IRAS 16293B suggest that CH_3NH_2 is not efficiently formed in these environments. The low abundance of CH_3NH_2 limits the relevance of amino acid formation routes involving this species. Conversely, the detection of CH_2NH makes amino acid formation routes involving this molecule a more relevant possibility.

Acknowledgement

This letter makes use of the following ALMA data: ADS/JAO.ALMA#2013.1.00278.S. ALMA is a partnership of ESO (representing its member states), NSF (USA) and NINS (Japan), together with NRC (Canada) and NSC and ASIAA (Taiwan), in cooperation with the Republic of Chile. The Joint ALMA Observatory is operated by ESO, AUI/NRAO and NAOJ. Astrochemistry in Leiden is supported by the European Union A-ERC grant 291141 CHEMPLAN, by the Netherlands Research School for Astronomy (NOVA) and by a Royal Netherlands Academy of Arts and Sciences (KNAW) professor prize. The group of J.K.J. acknowledges support from a Lundbeck Foundation Group Leader Fellowship, as well as the ERC under the European Union's Horizon 2020 research and innovation programme through ERC Consolidator Grant S4F (grant agreement No 646908). Research at the Centre for Star and Planet Formation is funded by the Danish National Research Foundation. A.C. postdoctoral grant is funded by the ERC Starting Grant 3DICE (grant agreement 336474).

9.5. Appendix

9.5.1. Spectroscopic data

Table 9.4 lists the transitions of NO, N_2O and CH_2NH detected towards IRAS 16293B (Pickett et al. 1979; Ting et al. 2014; Kirchhoff et al. 1973).

Table 9.4: Detected lines of NO, N₂O and CH₂NH.

Molecules	Transitions	Frequency (MHz)	E_{up} (K)	A_{ij} (s ⁻¹)	g_{up}	Blended	Database
NO	4 -1 7/2 9/2 -3 1 5/2 7/2	350 689.49	36	5.42×10^{-6}	10	Y	JPL
NO	4 -1 7/2 7/2 -3 1 5/2 5/2	350 690.76	36	4.97×10^{-6}	8	N	JPL
NO	4 -1 7/2 5/2 -3 1 5/2 3/2	350 694.77	36	4.81×10^{-6}	6	N	JPL
NO	4 1 7/2 9/2 -3 -1 5/2 7/2	351 043.52	36	5.43×10^{-6}	10	Y	JPL
NO	4 1 7/2 7/2 -3 -1 5/2 5/2	351 051.46	36	4.99×10^{-6}	8	Y	JPL
NO	4 1 7/2 5/2 -3 -1 5/2 3/2	351 051.70	36	4.83×10^{-6}	6	Y	JPL
N ₂ O	14 -13	351 667.81	127	6.32×10^{-6}	29	N	JPL
CH ₂ NH	5 1 4 5 -4 1 3 4	332 573.04	56	3.15×10^{-4}	11	Y	JPL
CH ₂ NH	5 1 4 6 -4 1 3 5	332 573.07	56	3.28×10^{-4}	13	Y	JPL
CH ₂ NH	5 1 4 4 -4 1 3 3	332 573.11	56	3.12×10^{-4}	9	Y	JPL
CH ₂ NH	3 1 3 3 -2 0 2 3	340 353.05	26	3.44×10^{-5}	7	N	JPL
CH ₂ NH	3 1 3 3 -2 0 2 2	340 353.37	26	2.75×10^{-4}	7	N	JPL
CH ₂ NH	3 1 3 4 -2 0 2 3	340 354.31	26	3.09×10^{-4}	9	N	JPL
CH ₂ NH	3 1 3 2 -2 0 2 1	340 354.58	26	2.60×10^{-4}	5	N	JPL
CH ₂ NH	3 1 3 2 -2 0 2 2	340 355.08	26	4.81×10^{-5}	5	N	JPL
CH ₂ NH	10 1 9 9 -10 0 10 9	351 453.85	183	3.61×10^{-4}	19	Y	JPL
CH ₂ NH	10 1 9 11 -10 0 10 11	351 454.02	183	3.62×10^{-4}	23	Y	JPL
CH ₂ NH	10 1 9 10 -10 0 10 9	351 454.43	183	3.30×10^{-6}	21	Y	JPL
CH ₂ NH	10 1 9 10 -10 0 10 11	351 454.55	183	3.30×10^{-6}	21	Y	JPL
CH ₂ NH	10 1 9 11 -10 0 10 11	351 454.02	183	3.62×10^{-4}	23	Y	JPL
CH ₂ NH	10 1 9 11 -10 0 10 10	351 455.17	183	3.02×10^{-6}	23	Y	JPL
CH ₂ NH	10 1 9 10 -10 0 10 10	351 455.70	183	3.58×10^{-4}	21	Y	JPL
CH ₂ NH	6 3 4 6 -7 2 5 7	360 293.85	135	6.91×10^{-5}	13	Y	JPL
CH ₂ NH	6 3 4 7 -7 2 5 8	360 294.05	135	6.93×10^{-5}	15	Y	JPL
CH ₂ NH	6 3 4 5 -7 2 5 6	360 294.08	135	7.05×10^{-5}	11	Y	JPL

Notes. Quantum numbers are given as $N' K' J' F' - N'' K'' J'' F''$ for NO, $J' - J''$ for N₂O and $J' K'_a' K'_c' F' - J'' K''_a'' K''_c'' F''$ for CH₂NH.

9.5.2. Additional fit spectra of CH₂NH and NO

Figure 9.5 shows CH₂NH synthetic spectra at T_{ex} 50 and 150 K. Best fit column densities of 7×10^{14} and 8×10^{14} , respectively, are found. However, clear discrepancies in the fits exist, which are especially visible for the transitions at 340.354 and 351.454 GHz.

Figure 9.6 shows the NO synthetic spectrum at T_{ex} 150 K and $N_{\text{tot}} = 2.3 \times 10^{16}$. The transitions at $E_{\text{up}} = 36$ K are well fitted, however, clear anti-coincidences start to arise at the transitions of $E_{\text{up}} = 209$ K, as can be seen for the transitions at 360.935 and 360.941 GHz. Excitation temperatures for NO are therefore constrained to $T_{\text{ex}} < 150$ K.

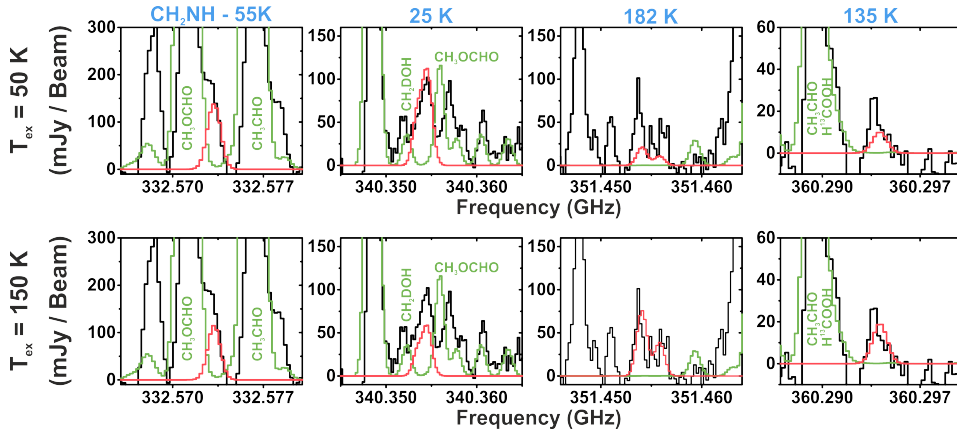


Figure 9.5: Fit models (red) of CH_2NH at $T_{\text{ex}} = 50$ K (top) and $T_{\text{ex}} = 150$ K (bottom) overlapped on the PILS data (black) and other detected species in PILS given in green. Upper state energies of the transitions are indicated in blue.

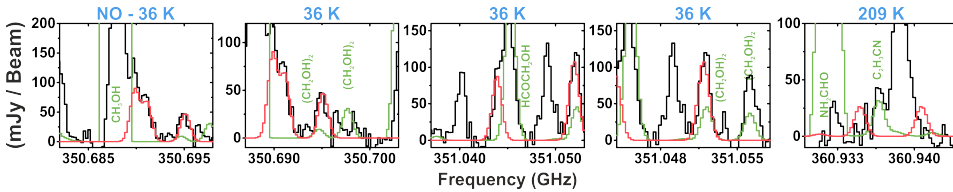


Figure 9.6: Fit models (red) of NO at $T_{\text{ex}} = 150$ K (bottom) overlapped on the PILS data (black) and other detected species in PILS given in green. Upper state energies of the transitions are indicated in blue.

9.5.3. Upper limit column densities of NH_2OH and CH_3NH_2

Upper limit column densities of NH_2OH and CH_3NH_2 have been determined for excitation temperatures between 10 and 300 K (Morino et al. 2000; Ilyushin et al. 2005). These are plotted in Figure 9.8 and 9.7. The upper limit column densities of NH_2OH are determined on the three transitions: $7_0 \rightarrow 6_0$, $7_1 \rightarrow 6_1$, $7_2 \rightarrow 6_2$ transitions at 352 522, 352 730 and 352 485 MHz, respectively. These transitions are modelled with a 3σ line intensity of 27, 21 and 27 mJy km s $^{-1}$, respectively. The upper limit column densities of CH_3NH_2 are determined on the $6_5 \rightarrow 5_0$ transition at 357 440 MHz for a 3σ line intensity of 23 mJy km s $^{-1}$.

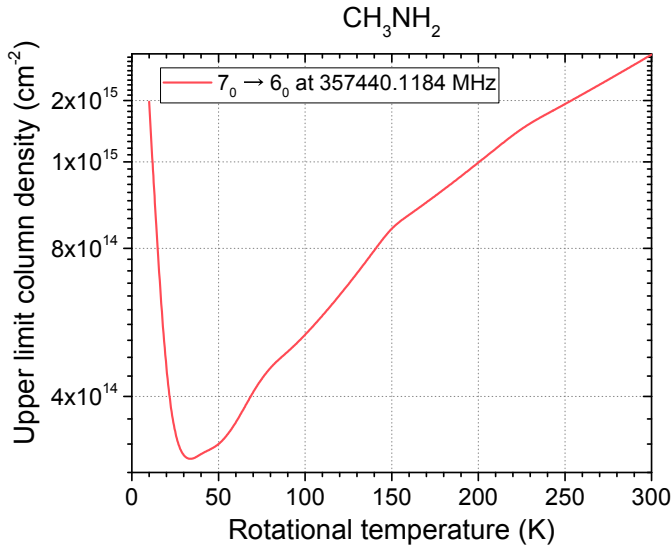


Figure 9.7: Upper limit column density for the strongest CH₃NH₂ transition. A 3σ value of 23 mJy km s^{-1} is used.

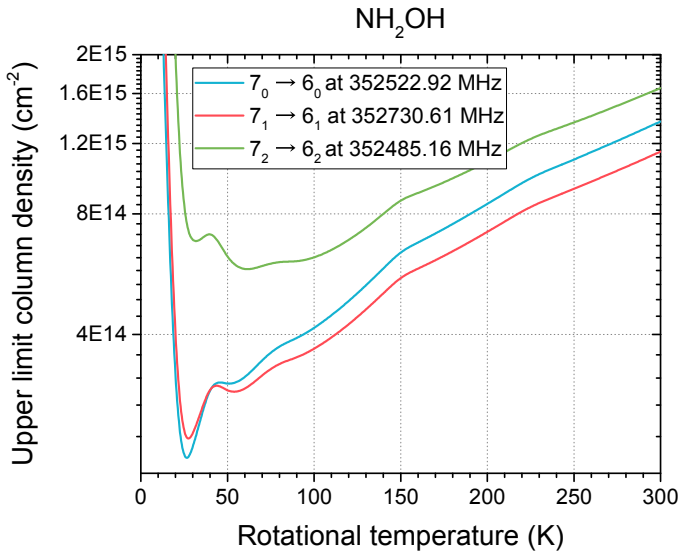
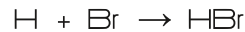


Figure 9.8: Upper limit column densities for the three strongest NH₂OH transitions. 3σ values of 27, 21 and 27 mJy km s^{-1} are used for the respective lines.



V-UV



10

Interstellar bromine depletion matches cometary ices from *Rosetta*

N.F.W. Ligterink & M. Kama

Ligterink & Kama 2017, *Interstellar bromine depletion matches cometary ices from Rosetta*, subm. to A&A

10.1. Introduction

Observations of halogen-bearing species in molecular gas can probe the gas-to-ice depletion of volatiles during star and planet formation and constrain the H_2 column density (Gerin et al. 2016). Previous studies have characterized the abundance of fluorine (F) and chlorine (Cl) in protostellar gas. We analyse archival data from the *Herschel* Space Observatory to constrain the gas-phase abundance budget of bromine (Br).

The solar abundances of F and Cl are $(3.63 \pm 0.11) \times 10^{-8}$ and $(3.16 \pm 0.95) \times 10^{-7}$, respectively (Asplund et al. 2009). The gas-phase HCl abundance in dense protostellar cores is $[HCl/H_2] \sim 10^{-10}$, with Cl depleted by a factor 100–1000 (Blake et al. 1985; Schilke et al. 1995; Zmuidzinas et al. 1995; Salez et al. 1996; Neufeld & Green 1994; Peng et al. 2010; Kama et al. 2015). Models indicate that the missing Cl is in HCl ice (Kama et al. 2015). A high Cl fraction in HCl ice was confirmed *in-situ* for comet 67P/Churyumov-Gerasimenko (hereafter 67P/C-G) with *Rosetta*, which recently measured $HCl/H_2O \approx 1.2 \cdot 10^{-4}$ (Dhooghe et al. 2017), close to *Herschel* upper limits at comets Hartley 2 and Garradd (Bockelée-Morvan et al. 2014).

In contrast to F and Cl, the solar and interstellar Br abundance is unknown, but in meteorites it is equivalent to $Br/H = (3.47 \pm 0.02) \times 10^{-10}$ (Lodders et al. 2009). The two stable isotopes of bromine are ^{79}Br and ^{81}Br , with a terrestrial abundance ratio of $[^{79}Br]/[^{81}Br] = 1.03$ (Böhlke et al. 2005). For comet 67P/C-G, the *Rosetta* spacecraft detected HBr and measured an elemental ratio of $Br/O = (1 - 7) \times 10^{-6}$ in the inner coma, consistent with nearly all bromine being locked in ice, analogously to chlorine.

Accounting for the range of variation seen in 67P/C-G and the uncertainties in terrestrial data, the cometary Br/Cl value of ≈ 0.02 (Dhooghe et al. 2017) is consistent with the bulk Earth estimate of $Br/Cl \approx 0.04$ (Allègre et al. 2001).

If Br has a similar depletion level as Cl in protostellar gas, it may be detectable as HBr at a sensitivity of $\delta T \lesssim 0.01 \times T(HCl)$, where T is the intensity in kelvin. The lowest rotational transitions of HBr are at around 500, 1000, and 1500 GHz. These frequencies are not observable from the ground, but were covered by the *Herschel*/HIFI spectrometer. We also consider the potentially abundant molecular ion HBr^+ . During regular science observations, HIFI serendipitously covered transitions of HBr and HBr^+ towards the bright protostellar regions Orion KL, Sagittarius B2 North – hereafter Sgr B2(N), and NGC6334I. We use these data to constrain the gas-phase abundance of Br-carriers.

In Section 10.2, we summarize the spectroscopy and the archival *Herschel* data, which are analysed and discussed in Section 10.3. In Section 10.5, we review the interstellar chemistry of Br. Our conclusions are presented in Section 10.6.

10.2. Data

10.2.1. Spectroscopy of HBr and HBr^+

Measurements on rotational lines of HBr were performed by Van Dijk & Dymanus (1969) for the hyperfine components of the first rotational transition and later extended by Di Lonardo et al. (1991) up to $J_u = 9$. The first three

Table 10.1: Source parameters in HIFI band 1a

Source	θ_S "	RMS (mK)	V_{LSR} (km s ⁻¹)	ΔV (km s ⁻¹)	3σ Flux (mK km s ⁻¹)	Continuum K
Orion KL ^a Plat.	30	23.0	7 – 11	≥ 20	364	1.6
Orion KL HC	10	23.0	4 – 6	7	216	1.6
Orion KL CR	10	23.0	7 – 9	6	200	1.6
Sgr B2(N) ^b HC	~ 5	29.3	50 – 100	9	311	2.5
Sgr B2(N) env.	–	29.3	50 – 100	20	464	2.5
NGC6334I ^c HC	~ 5	7.8	-20 – 7	4	55	1.0
NGC6334I env.	20*	7.8	-20 – 7	8	78	1.0

Notes. Plat. – Plateau, HC – Hot Core, CR – Compact Ridge, env. – envelope. ^aCrockett et al. (2014b); ^bNeill et al. (2014); ^cZernickel et al. (2012); *based on the derived HCl source size.

rotational transitions of both H⁷⁹Br and H⁸¹Br are found at frequencies just above 500, 1000, and 1500 GHz, respectively (Table 10.4 in the Appendix). The three lowest rotational transitions of HBr⁺ are found at 1188.2, 1662.7 and 2136.8 GHz and also display hyperfine splitting (Saykally & Evenson 1979; Lubic et al. 1989). However, insufficient spectroscopic data of HBr⁺ are available to determine column densities. The lowest HBr and HBr⁺ transition frequencies fall in spectral regions with heavy atmospheric absorption and are best observed from space.

10.2.2. Archival *Herschel* observations and selected sources

The *Herschel* Space Observatory mission (Pilbratt et al. 2010), active from 2009 to 2013, was the most sensitive observatory to date in the terahertz frequency range. We investigate archival high spectral resolution and broad wavelength coverage data from its heterodyne instrument, HIFI (de Graauw et al. 2010).

The HEXOS guaranteed-time key program (PI E.A. Bergin, Bergin et al. 2010) obtained full spectral scans of Orion KL and Sgr B2 (Crockett et al. 2014b,a; Neill et al. 2014), covering three rotational transitions of HBr in HIFI bands 1a, 4a and 6a and HBr⁺ transitions in band 5a and 6b. The CHESSE key program (PI C. Ceccarelli, Ceccarelli et al. 2010) observed NGC6334I in the same HIFI bands (Zernickel et al. 2012). These three sources are bright and well-studied, and have yielded strong detections of the halogens HF and HCl ($\int T_{mb} dv = 701.9$ K km s⁻¹ for Orion KL, $\int T_{mb} dv = 40$ K km s⁻¹ for NGC6334I). Line intensities one to two orders of magnitude lower than the HCl peak brightness should be detectable. The observational details of these three sources are listed in Table 10.1.

10.2.3. Analysis method

All sources are inspected for features corresponding to transitions of H^{79/81}Br and HBr⁺ using the Weeds addition (Maret et al. 2011) of the Continuum and Line Analysis Single-dish Software (CLASS¹). For line identification, we use the JPL²

¹<http://www.iram.fr/IRAMFR/GILDAS>

²<http://spec.jpl.nasa.gov>

(Pickett et al. 1998) and CDMS³ (Müller et al. 2001, 2005) spectroscopy databases. Source velocities matching previous detections of halogen bearing molecules are considered most relevant, but we explore a large V_{LSR} range to check for emission or absorption components matching the hyperfine pattern. For emission features, the total column density N_{T} of the peak can be calculated by assuming local thermodynamic equilibrium (LTE):

$$\frac{3k_{\text{B}} \int T_{\text{MB}} dV}{8\pi^3 \nu \mu^2 S} = \frac{N_{\text{up}}}{g_{\text{up}}} = \frac{N_{\text{T}}}{Q(T_{\text{rot}})} e^{-E_{\text{up}}/T_{\text{rot}}}, \quad (10.1)$$

where $\int T_{\text{MB}} dV$ is the integrated main-beam intensity, ν the transition frequency, μ^2 the dipole moment, S the strength, g_{up} the upper state degeneracy, $Q(T_{\text{rot}})$ the rotational partition function, E_{up} the upper state energy and T_{rot} the rotational temperature. Upper limits are given at 3σ confidence and calculated by $\sigma = 1.1 \sqrt{\delta\nu \Delta V} \cdot \text{RMS}$, where $\delta\nu$ is the velocity resolution, ΔV the line width (estimated based on other transitions in the spectrum) and RMS the root mean square noise in Kelvin. A factor of 1.1 accounts for the flux calibration uncertainty of 10% (Roelfsema et al. 2012).

In the source sample, the hydrogen halides HF and HCl are also found in absorption. We calculate the column density corresponding to absorption features by:

$$\tau = -\ln \left(\frac{T_{\text{MB}}}{T_{\text{cont}}} \right) \quad (10.2)$$

and

$$N_{\text{T}} = \frac{8\pi^{3/2} \cdot \Delta V}{2 \sqrt{\ln 2} \cdot \lambda^3} \frac{g_{\text{l}}}{g_{\text{u}}} \cdot \tau, \quad (10.3)$$

where τ is the optical depth, T_{MB} the brightness temperature of the feature and T_{cont} the continuum level. λ is the wavelength of the transitions and g_{l} and g_{u} are its lower and upper state degeneracies. For non-detections, a 3σ upper limit column density is determined by using $T_{\text{MB}} = T_{\text{cont}} \cdot 3 \cdot \text{RMS}$ and assuming ΔV equals the average line width for other species in the source.

If the source does not fill the entire HIFI beam (at 500 GHz, $\theta_{\text{B}}=44''$), we correct the column densities for beam dilution by applying the factor $\eta_{\text{BF}} = \theta_{\text{S}}^2 / (\theta_{\text{S}}^2 + \theta_{\text{B}}^2)$, where θ_{S} is the source size and θ_{B} the beam size. Source sizes are taken from literature, see Table 10.1. The *source-averaged* column density is calculated from $N_{\text{S}} = N_{\text{T}} / \eta_{\text{BF}}$.

To make use of the best noise levels, we determined the upper limit column densities for the HBr $J = 1_x \rightarrow 0_2$ transitions at 500 GHz in HIFI band 1a. In HBr, we consider the sum of H⁷⁹Br and H⁸¹Br. We assume that the cosmic and local isotope ratios are equal (in the solar system $[^{79}\text{Br}]/[^{81}\text{Br}]=1.03$). Aside from the molecular mass, several spectroscopic parameters for transitions of both isotopes, such as A_{ij} and E_{up} , are identical. The $1_3 \rightarrow 0_2$ line constrains the column density the most and is therefore used to give the most stringent upper limits.

³<http://www.astro.uni-koeln.de/cdms>

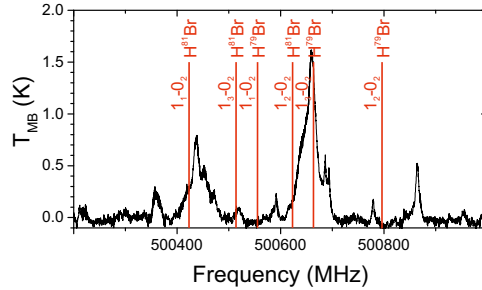


Figure 10.1: Positions of the $J = 1_x \rightarrow 0_2$ transitions of H^{79}Br and H^{81}Br at 500 GHz towards Orion KL for $V_{\text{LSR}} = 9 \text{ km s}^{-1}$.

10.3. Search for HBr and HBr⁺ in the *Herschel* spectra

Analysis of the HIFI spectra of Orion KL, Sgr B2(N) and NGC6334I yielded no detections of HBr or HBr⁺ features in emission or absorption. Figure 10.1 shows the positions of the HBr transitions at 500 GHz in the Orion KL spectrum at $V_{\text{LSR}} = 9 \text{ km s}^{-1}$. The data were analysed over a large range of source velocities, mainly focussing on velocities of known components. For Sgr B2(N) and NGC6334I the same figures can be found in Appendix 10.7.2.

10.4. Protostellar *vs* cometary abundance

The upper limit abundance ratios of HBr toward the protostellar sources can be compared with measurements taken by the *Rosetta* mission of the coma gas of comet 67P/C-G (Dhooghe et al. 2017). We look at column density ratios of HBr (Table 10.5) with respect to that of H_2 , H_2O , CH_3OH , HF, and HCl (Table 10.6). The $N(\text{H}^{79+81}\text{Br})/N(\text{X})$ column density ratios based either on emission or absorption upper limits for Orion KL, Sgr B2(N), and NGC6334I are listed in Table 10.2.

The upper limits in emission are based on an excitation temperature of 100 K, which is chosen to be within a factor of a few of all the detected molecules we compare with. For an assessment of the impact of T_{ex} , Fig. 10.6 shows the temperature dependence of the 3σ upper limit for the first three hyperfine transitions of $\text{H}^{79/81}\text{Br}$, including beam dilution correction for the Orion KL Hot Core. For Sgr B2(N) and NGC6334I a distinction is made between the hot core and envelope components. If a source contains multiple kinematic components of a species, we adopt the dominant one.

For 67P/C-G, Dhooghe et al. (2017) give the Br/O ratio and the CH_3OH abundance. The cometary halogens are equal to the halides (HX), but the O abundance is the sum of H_2O , CO, CO_2 and O_2 . For the comet, we can therefore take $\text{Br} \equiv \text{HBr}$, and we further assume $\text{O} \approx \text{H}_2\text{O}$. A ratio of $\text{CH}_3\text{OH}/\text{H}_2\text{O} = 3.1\text{--}5.5 \times 10^{-3}$ has been measured by Le Roy et al. (2015).

A comparison of HBr with H_2O and CH_3OH is shown in Fig. 10.2, and the full set of abundance ratios of HBr with other molecules is given in Table 10.2. The HBr/ CH_3OH ratio in all our targets is constrained to be below that in comet

Table 10.2: Abundance ratios of $\text{H}^{79+81}\text{Br}$ ($\equiv\text{B}$) upper limit column density with H_2 , CH_3OH , H_2O , HF , and $\text{H}^{35+37}\text{Cl}$ ($\equiv\text{HCl}$) for Orion KL, Sgr B2(N) and NGC6334I, compared with abundance ratios derived for 67P/C-G

Source	B/ H_2	B/ H_2O	B/ CH_3OH	B/ HF	B/ HCl
Orion KL Plat. ^a	$\leq 8.9 \times 10^{-11}$	$\leq 1.9 \times 10^{-5}$	–	$\leq 1.2 \times 10^{1*}$	$\leq 1.3 \times 10^{-2}$
Orion KL HC ^a	$\leq 3.1 \times 10^{-10}$	$\leq 4.8 \times 10^{-7}$	$\leq 1.4 \times 10^{-4}$	–	–
Orion KL CR ^a	$\leq 2.3 \times 10^{-10}$	$\leq 4.9 \times 10^{-5}$	$\leq 1.9 \times 10^{-4}$	–	–
Sgr B2(N) HC ^b	$\leq 6.5 \times 10^{-11}$	$\leq 1.0 \times 10^{-2}$	$\leq 1.0 \times 10^{-4}$	–	–
Sgr B2(N) env. ^b	–	–	$\leq 1 \times 10^{-3}$	$\leq 1.1 \times 10^{-1*}$	$\leq 6.9 \times 10^{-2*}$
NGC6334I HC ^c	$\leq 8.4 \times 10^{-11}$	$\leq 4.4 \times 10^{-5}$	$\leq 6.6 \times 10^{-6}$	–	$\leq 4.8 \times 10^{-1}$
NGC6334I env. ^c	–	–	–	$\leq 2.0 \times 10^{-1*}$	$\leq 9.3 \times 10^{-1*}$
67P/C-G ^a	–	$4.5^{+3.5}_{-3.5} \times 10^{-6}$ ^b	$1.4^{+1.2}_{-0.7} \times 10^{-3}$	$1.7^{+5.1}_{-1.3} \times 10^{-2}$	$4.8^{+13.8}_{-3.7} \times 10^{-2}$

Notes. Plat. – Plateau, HC – Hot Core, CR – Compact Ridge, env. – envelope. ^aDhooghe et al. (2017); ^bBr/O elemental ratio, O has contributions of water, but also CO, CO₂ and O₂; *indicates values based on an upper limit in absorption, other values are based on the emission upper limits.

67P/C-G. This is not necessarily due to a particularly high methanol abundance in our targets, but rather could signify a low fraction of Br atoms locked up in gas-phase HBr molecules. The only source where we can constrain the HBr/ H_2O ratio to be below that in 67P/C-G is the Orion KL Hot Core. This may, again, be explained with a low fraction of Br atoms in gas-phase HBr. If all elemental bromine were in gaseous HBr, we would have expected to have made a detection in the Orion KL Hot Core. A comparison with the cometary measurements suggests, then, that the HBr molecules are formed in icy grain mantles, rather than in the gas phase, or sublimate from the grain surface at a temperature higher than water.

The HBr/ HCl abundance ratio in the Orion KL Plateau is constrained to be a factor ≥ 4 below that in 67P/C-G. This further solidifies the interpretation of an ice-phase formation of HBr, rather than a high abundance of H_2O and CH_3OH , to explain the low upper limits on protostellar HBr/X ratios described above. We return to this interpretation from a chemical network perspective in the next section.

10.5. Interstellar chemistry of Br

The inter- and protostellar chemistry of bromine is poorly characterized, compared to that of fluorine and chlorine (e.g. Jura 1974; Blake et al. 1986; Schilke et al. 1995; Neufeld & Wolfire 2009). In Table 10.3, we present a network compiled from published measurements and calculations, with missing data filled in with values from the Cl and F networks.

The neutral-neutral chemistry, reactions (1) through (3), is relatively well studied. The $\text{Br} + \text{H}_2$ reaction leading to $\text{HBr} + \text{H}$, with an 8812 K activation energy, has been investigated by e.g. Eyring (1931); Plooster & Garvin (1956) and Fettis et al. (1960). The $\text{HBr} + \text{H}$ abstraction and exchange reactions have been studied by Plooster & Garvin (1956), and by White & Thompson (1974)

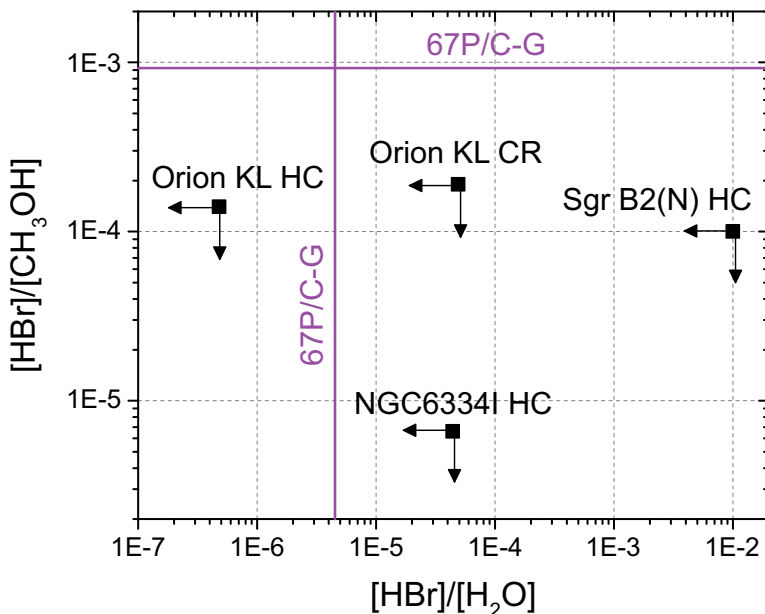


Figure 10.2: The (H)Br/CH₃OH and (H)Br/(H₂O) ratios plotted for 67P/C-G (purple lines, Dhooghe et al. 2017) and the upper limits on these ratios for the protostar sample (this work).

whose channel-by-channel rates are consistent with the total rate from Endo & Glass (1976). Based on Table 10.3, excluding other reactions, the competition between the Br+H₂ formation route and destruction via the HBr+H abstraction reaction strongly favours atomic Br. Thus gas-phase neutral-neutral chemistry is not expected to contribute to HBr formation unless temperatures of ~ 1000 K – possible in hot cores, outflow shocks, and inner regions of protoplanetary disks – are involved.

Due to its low first ionization potential (11.8 eV), Br is easily ionized and HBr can form in ion-neutral chemistry via the set of reactions (4)–(8) in Table 10.3. By analogy with F and Cl, reactions (4) through (8) should be fast, of order $10^{-10} - 10^{-7} \text{ cm}^3 \text{ s}^{-1}$ (Neufeld & Wolfire 2009). However, as pointed out by Mayhew & Smith (1990), the Br⁺+H₂ reaction is endothermic. We adopt a H₂ and HBr⁺ dissociation energy (E_D) difference of ≈ 6200 K, estimated from the proton affinity (PA) and ionization potential (IP) of Br via $E_a = \text{PA}(\text{Br}) + \text{IP}(\text{Br}) - \text{IP}(\text{H}_2) - E_D(\text{H}_2)$, suggested by D. Neufeld (private communication). The branching ratio of the dissociative recombination reactions (7) and (8) is unknown, but the dissociation energy of HBr ($D_0 \approx 3.78$ eV) is lower than that of H₂ (4.48 eV), while those of HCl and HF are similar and higher (4.43 and 5.87 eV, Darwent 1970). The branching ratio into the HBr+H channel may thus be lower than the 10% of the equivalent Cl reaction, which would lower the fraction of Br stored in HBr. For the photoionization and -dissociation rates, we adopt order-of-magnitude numbers from the corresponding Cl and F reactions in Neufeld & Wolfire (2009).

The formation of HBr via H+Br collision requires a three-body interaction and thus is most efficient on grain surfaces (e.g. Ree et al. 2004).

Table 10.3: Chemical reaction network for bromine.

#	R_1	R_2	P_1	P_2	$k(T)$ [cm^3s^{-1}]	Reference
(1)	Br	H ₂	HBr	H	$8.3 \times 10^{-11} \times \exp(-8812 K/T)$	Fettis et al. (1960)
(2)	HBr	H	Br	H ₂	$8.9 \times 10^{-11} \times \exp(-684 K/T)$	White & Thompson (1974)
(3)	HBr	H'	H'Br	H	$4.0 \times 10^{-10} \times \exp(-1140 K/T)$	White & Thompson (1974)
(4)	Br ⁺	H ₂	HBr ⁺	H	$10^{-9} \times \exp(-6200 K/T)$	Mayhew & Smith (1990) ^{a,c} Neufeld & Wolfire (2009) ^{a,c}
(5)	HBr ⁺	e ⁻	Br	H	$2 \times 10^{-7} \times (T/300 K)^{-0.5}$	Neufeld & Wolfire (2009) ^a
(6)	HBr ⁺	H ₂	H ₂ Br ⁺	H	$(13.2 \pm 1.6) \times 10^{-10}$	Belikov & Smith (2008)
(7)	H ₂ Br ⁺	e ⁻	HBr	H	$\leq 10^{-8} \times (T/300 K)^{-0.85}$	Neufeld & Wolfire (2009) ^{a,b}
(8)	H ₂ Br ⁺	e ⁻	Br	2H	$\sim 10^{-7} \times (T/300 K)^{-0.85}$	Neufeld & Wolfire (2009) ^a
(9)	HBr	$h\nu$	Br	H	$1.7 \cdot 10^{-7} \times \chi_{UV}$	Neufeld & Wolfire (2009) ^a
(10)	HBr	$h\nu$	HBr ⁺	e ⁻	$10^{-10} \times \chi_{UV}$	Neufeld & Wolfire (2009) ^a

Notes. R_i and P_i denote the reactants and products. ^a – assumed order-of-magnitude similar to corresponding Cl, F reactions from Neufeld & Wolfire (2009); ^b – upper limit based on H₂Cl⁺ + e⁻ branching ratio (see text); ^c – see Section 10.5.

10.5.1. Chemical modelling results

We appended the reactions from Table 10.3 to the OSU2009 network and ran time-dependent simulations to 1.5 Myr with the *Astrochem* gas-phase chemistry code (Maret & Bergin 2015). The physical conditions were set to $A_V = 20$ mag (assuming a standard interstellar radiation field), $n_{\text{gas}} = 10^7 \text{ cm}^{-3}$, and $T_{\text{kin}} = 50$ K. The initial halogen abundances were either entirely atomic ions (Cl⁺ and Br⁺) or entirely diatomic hydrides (HCl and HBr), but this had only a minor impact on the end-state abundances. We show the modelling results in Figure 10.3 for three cases: 1) all elemental Br and Cl in the gas-phase; 2) only Cl in the gas-phase and 3) both Br and Cl depleted from the gas by two orders of magnitude, mimicking depletion.

For the adopted physical conditions, the chemical network predictions place the gas-phase HBr abundance two orders of magnitude below the observed upper limit for the Orion KL Hot Core. All literature studies of the gas-phase Cl abundance in protostellar sources find gas-phase Cl depletions of at least a factor 100 to 1000 (Dalgarno et al. 1974; Blake et al. 1986; Schilke et al. 1995; Peng et al. 2010; Kama et al. 2015). However, the ice fraction in the Orion KL Hot Core is likely very small, so we expect model 1 to provide a reasonable prediction of the gas-phase (H)Cl and (H)Br abundance in this source.

In the NGC 6334I Hot Core, HBr may be just below the upper limit from *Herschel* if elemental Br is not depleted from the gas, while Cl is known to be depleted by a factor 1000. This seems unlikely.

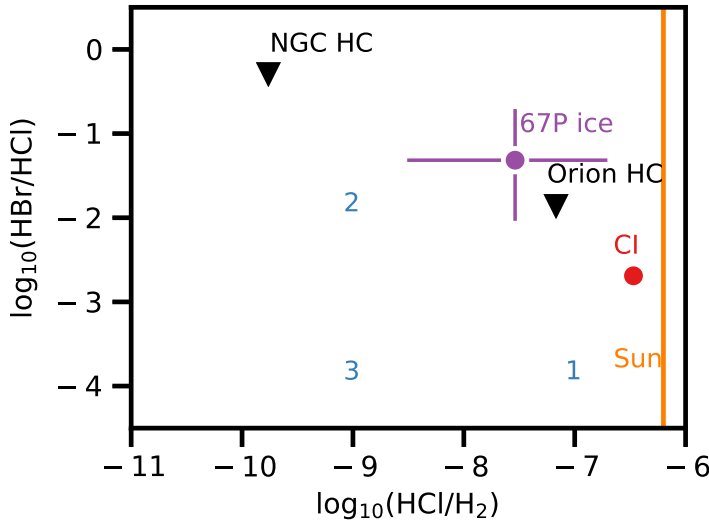


Figure 10.3: The ratio of HBr to HCl abundance in our protostellar sample and chemical models, and in comet 67P/C-G (Dhooghe et al. 2017). The elemental Cl/H₂ and Br/Cl ratios for meteorites and the sun are marked with *. Model 1 has all elemental Cl and Br in the gas; in 2 only Cl and in 3 both Cl and Br are depleted from the gas by a factor of 100. See Table 10.3 for the chemical network used in the models.

10.6. Conclusions

We present the first search for bromine-bearing molecules in the interstellar medium, employing archival *Herschel*/HIFI data. No detections of HBr or HBr⁺ are made, and we report upper limits of HBr for Orion KL, Sgr B2 (N) and NGC 6334I. Most of these upper limits lie above the values expected from a simple scaling down of HCl emission using the Cl/Br elemental ratio and are thus not very strong.

In the Orion KL Hot Core, the HBr/H₂O gas-phase abundance ratio is constrained to be an order of magnitude lower than the measured ratio in comet 67P/C-G. This result, along with the low HBr/CH₃OH ratio in all our sources and the low HBr/HCl in the Orion KL Plateau, is consistent with our chemical network modelling for Br, which suggests a high atomic fraction in the gas, and HBr formation in icy grain mantles or sublimation from the grain surface at a temperature higher than that of water.

Acknowledgement

Thanks go out to Nathan Crockett for providing the data on Orion KL and Sgr B2, and Peter Schilke for the data on NGC6334I. We also thank Frederik Dhooghe for discussing his results in before publication, David Neufeld for assistance with the chemical network, and Magnus Persson for computational

help.

MK is supported by an Intra-European Marie Skłodowska-Curie Fellowship. Astrochemistry in Leiden is supported by the Netherlands Research School for Astronomy (NOVA), by a Royal Netherlands Academy of Arts and Sciences (KNAW) professor prize, and by the European Union A-ERC grant 291141 CHEMPLAN.

10.7. Appendix

10.7.1. Linelist of HBr transitions in range of HIFI

The HIFI instrument on the *Herschel* Space Observatory covered the three lowest rotational transition groups of HBr, which are summarised in Table 10.4. $J = 1_x \rightarrow 0_2$ fell in band 1a, $J = 2_x \rightarrow 1_y$ in band 4a and $J = 3_x \rightarrow 2_y$ in band 6a.

Table 10.4: $\text{H}^{79/81}\text{Br}$ transitions between 500 and 1501 GHz

ν H^{79}Br MHz	ν H^{81}Br MHz	A s^{-1}	E_{upper} K	J',F'	J'',F''
500540.1280	500407.2010	3.34E-4	24.0	1 ₁	0 ₂
500647.7450	500497.3850	3.34E-4	24.0	1 ₃	0 ₂
500780.0980	500607.7750	3.34E-4	24.0	1 ₂	0 ₂
1000859.5610	1000589.5640	5.33E-4	72.1	2 ₁	1 ₂
1000993.2470	1000701.3110	1.71E-3	72.1	2 ₂	1 ₂
1001089.1700	1000781.6850	2.24E-3	72.1	2 ₃	1 ₂
1001089.1700	1000781.6850	3.20E-3	72.1	2 ₄	1 ₃
1001099.6240	1000790.3740	2.67E-3	72.1	2 ₁	1 ₁
1001125.5610	1000811.7800	1.60E-4	72.1	2 ₂	1 ₃
1001221.3420	1000891.7620	9.61E-4	72.1	2 ₃	1 ₃
1001233.1690	1000901.9040	1.33E-3	72.1	2 ₂	1 ₁
1500828.0700	1500397.4070	2.31E-4	144.1	3 ₂	2 ₃
1500923.7510	1500477.5790	3.24E-3	144.1	3 ₂	2 ₂
1500961.8100	1500509.4550	2.82E-3	144.1	3 ₃	2 ₃
1501025.2220	1500562.4860	9.91E-3	144.1	3 ₄	2 ₃
1501025.2220	1500562.4860	1.16E-2	144.1	3 ₅	2 ₄
1501057.6120	1500589.4380	8.10E-3	144.1	3 ₂	2 ₁
1501057.6120	1500589.4380	8.64E-3	144.1	3 ₃	2 ₂
1501094.0810	1500619.5480	1.10E-4	144.1	3 ₃	2 ₄
1501157.1420	1500672.5180	1.65E-3	144.1	3 ₄	2 ₄

10.7.2. Sgr B2(N) and NGC6334I at 500 GHz

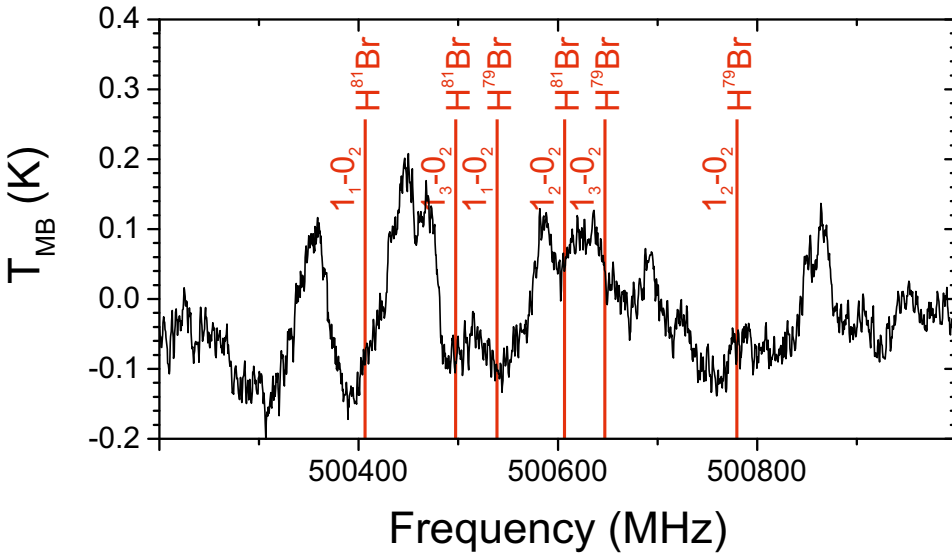


Figure 10.4: Positions of $\text{H}^{79/81}\text{Br}$ transitions for $J = 1_x \rightarrow 0_2$ around 500 GHz in HIFI band 1a towards Sgr B2(N) for $V_{\text{LSR}} = 64 \text{ km s}^{-1}$.

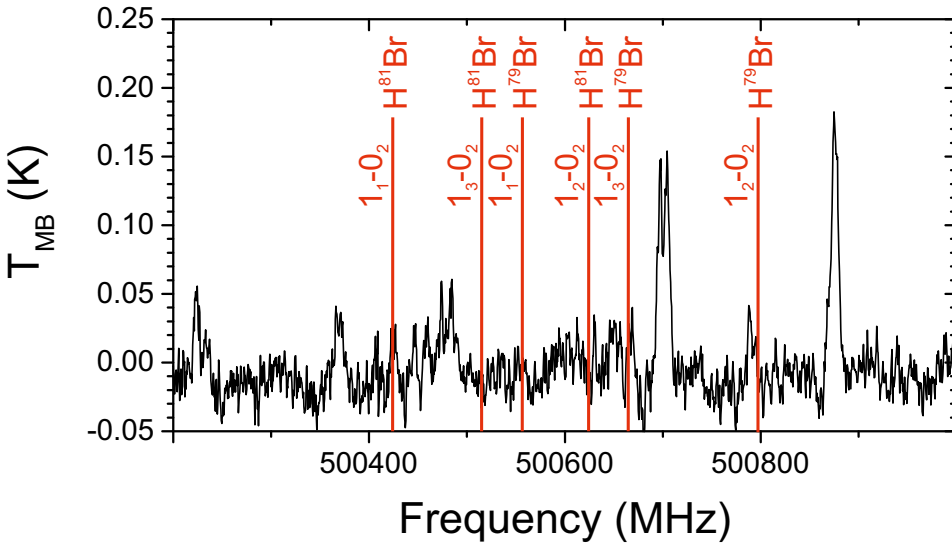


Figure 10.5: Positions of $\text{H}^{79/81}\text{Br}$ transitions for $J = 1_x \rightarrow 0_2$ around 500 GHz in HIFI band 1a towards NGC6334I for $V_{\text{LSR}} = -10 \text{ km s}^{-1}$.

10.7.3. Upper limit column densities of $\text{H}^{79+81}\text{Br}$ and column densities of reference molecules

Table 10.5 lists the upper limit column densities of $\text{H}^{79+81}\text{Br}$ for the full HIFI band 1a beam ($= 44''$) in emission and absorption, calculated according to Equations 10.1 and 10.3. Upper limits have been derived for an excitation temperature of 100 K. The following columns in this table list the beam dilution correction factor and subsequently the beam dilution corrected upper limit column densities.

Table 10.6 lists the column densities of the reference molecules H_2 , H_2O , CH_3OH , HF , $\text{H}^{35+37}\text{Cl}$ taken from Crockett et al. (2014b), Neill et al. (2014) and Zernickel et al. (2012).

Table 10.5: $\text{H}^{79+81}\text{Br}$ column densities and beam dilution correction

Source	$N_{\text{T}}(\text{H}^{79+81}\text{Br})$ (cm^{-2})		η_{BF}	N_{S}	
	Emission*	Absorption		Emission*	Absorption
Orion KL Plat.	$\leq 7.9 \times 10^{12}$	$\leq 1.1 \times 10^{14}$	3.2×10^{-1}	$\leq 2.5 \times 10^{13}$	$\leq 3.4 \times 10^{14}$
Orion KL HC	$\leq 4.7 \times 10^{12}$	$\leq 3.8 \times 10^{13}$	4.9×10^{-2}	$\leq 9.6 \times 10^{13}$	$\leq 7.8 \times 10^{14}$
Orion KL CR	$\leq 4.3 \times 10^{12}$	$\leq 3.3 \times 10^{13}$	4.9×10^{-2}	$\leq 8.8 \times 10^{13}$	$\leq 6.7 \times 10^{14}$
Sgr B2(N) HC	$\leq 6.7 \times 10^{12}$	$\leq 4.0 \times 10^{13}$	1.3×10^{-2}	$\leq 5.2 \times 10^{14}$	$\leq 3.1 \times 10^{15}$
Sgr B2(N) env.	$\leq 1.0 \times 10^{13}$	$\leq 8.9 \times 10^{13}$	-	-	-
NGC6334I HC	$\leq 1.2 \times 10^{12}$	$\leq 1.2 \times 10^{13}$	1.3×10^{-2}	$\leq 9.2 \times 10^{13}$	$\leq 9.2 \times 10^{14}$
NGC6334I env.	$\leq 1.7 \times 10^{12}$	$\leq 2.4 \times 10^{13}$	$1.7 \times 10^{-1**}$	$\leq 1.0 \times 10^{13}$	$\leq 1.4 \times 10^{14}$

Notes. *Emission at $T_{\text{ex}} = 100$ K; **Beam dilution factor based on HCl source size.

Table 10.6: Column densities of the reference molecules H_2 , H_2O , CH_3OH , HF , $\text{H}^{35+37}\text{Cl}$

Source	H_2	H_2O	CH_3OH (cm^{-2})	HF	$\text{H}^{35+37}\text{Cl}$
Orion KL Plat. ^a	2.8×10^{23}	1.3×10^{18}	-	$2.9 \times 10^{13*}$	1.9×10^{15}
Orion KL HC ^a	3.1×10^{23}	2×10^{20}	6.8×10^{17}	-	-
Orion KL CR ^a	3.9×10^{23}	1.8×10^{18}	4.7×10^{17}	-	-
Sgr B2(N) HC ^b	8×10^{24}	$5-10 \times 10^{16}$	5×10^{18}	-	-
Sgr B2(N) env. ^b	-	-	1×10^{16}	$8.2 \times 10^{14*}$	$1.3 \times 10^{15*}$
NGC6334I HC ^c	1.1×10^{24}	2.1×10^{18}	1.4×10^{19}	-	1.9×10^{14}
NGC6334I env. ^c	-	-	-	$1.2 \times 10^{14*}$	$1.5 \times 10^{14*}$

Notes. ^aCrockett et al. (2014b), ^bNeill et al. (2014) ^cZernickel et al. (2012) and references therein; *absorption component

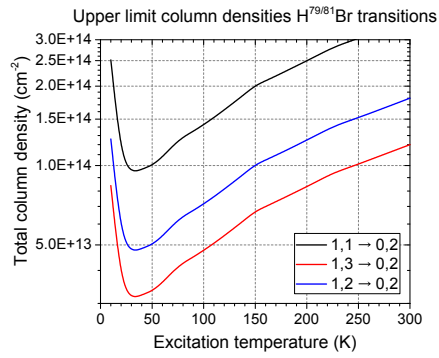


Figure 10.6: Upper limit column densities for the H^{79/81}Br (e.g. ⁷⁹Br and ⁸¹Br are used interchangeably here) $J = 1_x \rightarrow 0_2$ transitions plotted versus rotational temperature based on the 3σ values (216 mK km s^{-1}) found for the Orion KL Hot Core and beam-dilution corrected ($\eta = 0.049$)

Bibliography

- Acharyya, K., Fuchs, G. W., Fraser, H. J., van Dishoeck, E. F., & Linnartz, H. 2007, *A&A*, 466, 1005
- Adande, G. R., Woolf, N. J., & Ziurys, L. M. 2013, *Astrobiology*, 13, 439
- Agarwal, V. K., Schutte, W., Greenberg, J. M., et al. 1985, *Origins of Life*, 16, 21
- Allamandola, L. J., Sandford, S. A., & Valero, G. J. 1988, *Icarus*, 76, 225
- Allègre, C., Manhès, G., & Lewin, É. 2001, *Earth and Planetary Science Letters*, 185, 49
- Allodi, M. A., Baragiola, R. A., Baratta, G. A., et al. 2013, *SSR*, 180, 101
- Altwegg, K., Balsiger, H., Bar-Nun, A., et al. 2016, *Science Advances*, 2, e1600285
- Altwegg, K., Balsiger, H., Berthelier, J. J., et al. 2017, *MNRAS*, 469, S130
- Anderl, S., Maret, S., Cabrit, S., et al. 2016, *A&A*, 591, A3
- Andersson, S., Kroes, G.-J., & van Dishoeck, E. F. 2005, *Chemical Physics Letters*, 408, 415
- Andersson, S. & van Dishoeck, E. F. 2008, *A&A*, 491, 907
- Andrews, S. M., Wilner, D. J., Zhu, Z., et al. 2016, *ApJL*, 820, L40
- Arasa, C., Koning, J., Kroes, G.-J., Walsh, C., & van Dishoeck, E. F. 2015, *A&A*, 575, A121
- Asplund, M., Grevesse, N., Sauval, A. J., & Scott, P. 2009, *ARA&A*, 47, 481
- Bacmann, A. & Faure, A. 2016, *A&A*, 587, A130
- Ball, J. A., Gottlieb, C. A., Lilley, A. E., & Radford, H. E. 1970, *ApJ*, 162, L203
- Bar-Nun, A., Herman, G., Laufer, D., & Rappaport, M. L. 1985, *Icarus*, 63, 317
- Baratta, G. A., Leto, G., & Palumbo, M. E. 2002, *A&A*, 384, 343
- Baratta, G. A. & Palumbo, M. E. 1998, *Journal of the Optical Society of America A*, 15, 3076
- Baratta, G. A., Palumbo, M. E., & Strazzulla, G. 2000, *A&A*, 357, 1045
- Barrientos, C., Redondo, P., Largo, L., Rayón, V. M., & Largo, A. 2012, *The Astrophysical Journal*, 748, 99
- Baryshev, A. M., Hesper, R., Mena, F. P., et al. 2015, *A&A*, 577, A129
- Belikov, A. E. & Smith, M. A. 2008, *Russian Journal of Physical Chemistry A*, 82, 789
- Belloche, A., Garrod, R. T., Müller, H. S. P., & Menten, K. M. 2014, *Science*, 345, 1584
- Belloche, A., Menten, K. M., Comito, C., et al. 2008, *A&A*, 482, 179
- Belloche, A., Meshcheryakov, A. A., Garrod, R. T., et al. 2017, *A&A*, 601, A49
- Belloche, A., Müller, H. S. P., Garrod, R. T., & Menten, K. M. 2016, *A&A*, 587, A91
- Belloche, A., Müller, H. S. P., Menten, K. M., Schilke, P., & Comito, C. 2013, *A&A*, 559, A47
- Benilan, Y., Gazeau, M.-C., Es-Sebbar, E.-T., et al. 2011, in *EPSC-DPS Joint Meeting 2011*, 1317
- Bennett, C. J., Chen, S.-H., Sun, B.-J., Chang, A. H. H., & Kaiser, R. I. 2007, *ApJ*, 660, 1588
- Bennett, C. J., Jamieson, C. S., Osamura, Y., & Kaiser, R. I. 2006, *ApJ*, 653, 792
- berg, K. I. 2016, *Chemical Reviews*, 116, 9631

- Bergantini, A., Maksyutenko, P., & Kaiser, R. I. 2017, *ApJ*, 841, 96
- Berger, R. 1961, *Proceedings of the National Academy of Science*, 47, 1434
- Bergin, E. A., Aikawa, Y., Blake, G. A., & van Dishoeck, E. F. 2007, *Protostars and Planets V*, B. Reipurth, D. Jewitt, and K. Keil (eds.), University of Arizona Press, 751
- Bergin, E. A., Phillips, T. G., Comito, C., et al. 2010, *A&A*, 521, L20
- Bergner, J. B., Öberg, K. I., Garrod, R. T., & Graninger, D. M. 2017, *ApJ*, 841, 120
- Bernstein, M. P., Ashbourn, S. F. M., Sandford, S. A., & Allamandola, L. J. 2004, *ApJ*, 601, 365
- Bernstein, M. P., Sandford, S. A., Allamandola, L. J., Chang, S., & Scharberg, M. A. 1995, *ApJ*, 454, 327
- Bertin, M., Fayolle, E. C., Romanzin, C., et al. 2013, *ApJ*, 779, 120
- Bertin, M., Romanzin, C., Doronin, M., et al. 2016, *ApJL*, 817, L12
- Bisschop, S. E., Fuchs, G. W., van Dishoeck, E. F., & Linnartz, H. 2007a, *A&A*, 474, 1061
- Bisschop, S. E., Jørgensen, J. K., Bourke, T. L., Bottinelli, S., & van Dishoeck, E. F. 2008, *A&A*, 488, 959
- Bisschop, S. E., Jørgensen, J. K., van Dishoeck, E. F., & de Wachter, E. B. M. 2007b, *A&A*, 465, 913
- Blagojevic, V., Petrie, S., & Bohme, D. K. 2003, *MNRAS*, 339, L7
- Blake, G. A., Anicich, V. G., & Huntress, Jr., W. T. 1986, *ApJ*, 300, 415
- Blake, G. A., Keene, J., & Phillips, T. G. 1985, *ApJ*, 295, 501
- Blake, G. A., Sutton, E. C., Masson, C. R., & Phillips, T. G. 1987, *ApJ*, 315, 621
- Boamah, M. D., Sullivan, K. K., Shulenberger, K. E., et al. 2014, *Faraday Discussions*, 168, 249
- Bockelée-Morvan, D., Biver, N., Crovisier, J., et al. 2014, *A&A*, 562, A5
- Bockelée-Morvan, D., Colom, P., Crovisier, J., Despois, D., & Paubert, G. 1991, *Nature*, 350, 318
- Bockelée-Morvan, D., Lis, D. C., Wink, J. E., et al. 2000, *A&A*, 353, 1101
- Bogan, D. J. & Hand, C. W. 1997, *The Journal of Physical Chemistry*, 75, 1532
- Böhlke, J. K., de Laeter, J. R., De Bièvre, P., et al. 2005, *Journal of Physical and Chemical Reference Data*, 34, 57
- Boogert, A. C. A., Gerakines, P. A., & Whittet, D. C. B. 2015, *ARA&A*, 53, 541
- Boogert, A. C. A., Pontoppidan, K. M., Knez, C., et al. 2008, *ApJ*, 678, 985
- Boogert, A. C. A., Schutte, W. A., Helmich, F. P., Tielens, A. G. G. M., & Wooden, D. H. 1997, *A&A*, 317, 929
- Boogert, A. C. A., Schutte, W. A., Tielens, A. G. G. M., et al. 1996, *A&A*, 315, L377
- Bossa, J.-B., Borget, F., Duvernay, F., et al. 2012, 65, 129
- Bossa, J.-B., Duvernay, F., Theulé, P., et al. 2009, *Astronomy and Astrophysics*, 506, 601
- Bossa, J.-B., Maté, B., Fransen, C., et al. 2015, *ApJ*, 814, 47
- Bossa, J. B., Theule, P., Duvernay, F., & Chiavassa, T. 2009, *ApJ*, 707, 1524
- Bottinelli, S., Boogert, A. C. A., Bouwman, J., et al. 2010, *ApJ*, 718, 1100
- Bottinelli, S., Ceccarelli, C., Neri, R., et al. 2004, *ApJL*, 617, L69
- Boudin, N., Schutte, W. A., & Greenberg, J. M. 1998, *A&A*, 331, 749
- Bouilloud, M., Fray, N., Bénilan, Y., et al. 2015, *MNRAS*, 451, 2145
- Brown, W. A. & Bolina, A. S. 2007, *MNRAS*, 374, 1006
- Brucato, J. R., Baratta, G. A., & Strazzulla, G. 2006, *A&A*, 455, 395

- Bruderer, S., van der Marel, N., van Dishoeck, E. F., & van Kempen, T. A. 2014, *A&A*, 562, A26
- Bruderer, S., van Dishoeck, E. F., Doty, S. D., & Herczeg, G. J. 2012, *A&A*, 541, A91
- Burgdorf, M., Cruikshank, D. P., Dalle Ore, C. M., et al. 2010, *ApJ*, 718, L53
- Burke, D. J. & Brown, W. A. 2015, *MNRAS*, 448, 1807
- Calmonte, U., Altwegg, K., Balsiger, H., et al. 2016, *MNRAS*, 462, S253
- Capaccioni, F., Coradini, A., Filacchione, G., et al. 2015, *Science*, 347, 628
- Caselli, P. & Ceccarelli, C. 2012, *A&A Rev.*, 20, 56
- Cazaux, S., Tielens, A. G. G. M., Ceccarelli, C., et al. 2003, *ApJ*, 593, L51
- Ceccarelli, C., Bacmann, A., Boogert, A., et al. 2010, *A&A*, 521, L22
- Cernicharo, J., Kisiel, Z., Tercero, B., et al. 2016, *A&A*, 587, L4
- Charnley, S. B. 2004, *Advances in Space Research*, 33, 23
- Charnley, S. B. & Rodgers, S. D. 2005, in *IAU Symposium*, Vol. 231, *Astrochemistry: Recent Successes and Current Challenges*, ed. D. C. Lis, G. A. Blake, & E. Herbst, 237–246
- Chen, Y.-J., Chuang, K.-J., Muñoz Caro, G. M., et al. 2014, *ApJ*, 781, 15
- Chuang, K.-J., Fedoseev, G., Ioppolo, S., van Dishoeck, E. F., & Linnartz, H. 2016, *MNRAS*, 455, 1702
- Cleeves, L. I., Bergin, E. A., Qi, C., Adams, F. C., & Öberg, K. I. 2015, *ApJ*, 799, 204
- Collings, M. P., Anderson, M. A., Chen, R., et al. 2004, *MNRAS*, 354, 1133
- Congiu, E., Fedoseev, G., Ioppolo, S., et al. 2012, *The Astrophysical Journal*, 750, L12
- Cook, A. M., Mattioda, A. L., Quinn, R. C., et al. 2014, *ApJs*, 210, 15
- Corby, J. F., Jones, P. A., Cunningham, M. R., et al. 2015, *MNRAS*, 452, 3969
- Cottin, H., Moore, M. H., & Bénilan, Y. 2003, *ApJ*, 590, 874
- Coutens, A., Jørgensen, J. K., van der Wiel, M. H. D., et al. 2016, *A&A*, 590, L6
- Crockett, N. R., Bergin, E. A., Neill, J. L., et al. 2014a, *ApJ*, 781, 114
- Crockett, N. R., Bergin, E. A., Neill, J. L., et al. 2014b, *ApJ*, 787, 112
- Cruz-Diaz, G. A. 2014, PhD thesis, Centro de Astrobiología, Universidad Autónoma de Madrid
- Cruz-Diaz, G. A., Martín-Doménech, R., Muñoz Caro, G. M., & Chen, Y.-J. 2016, *A&A*, 592, A68
- Cruz-Diaz, G. A., Muñoz Caro, G. M., Chen, Y.-J., & Yih, T.-S. 2014a, *A&A*, 562, A119
- Cruz-Diaz, G. A., Muñoz Caro, G. M., Chen, Y.-J., & Yih, T.-S. 2014b, *A&A*, 562, A120
- Cuadrado, S., Goicoechea, J. R., Cernicharo, J., et al. 2017, *A&A*, 603, A124
- Cuppen, H. M., Ioppolo, S., Romanzin, C., & Linnartz, H. 2010, *Physical Chemistry Chemical Physics*, 12, 12077
- Cuppen, H. M., Penteado, E. M., Isokoski, K., van der Marel, N., & Linnartz, H. 2011, *MNRAS*, 417, 2809
- Cuppen, H. M., Walsh, C., Lamberts, T., et al. 2017, *SSR*
- Dalgarno, A., de Jong, T., Oppenheimer, M., & Black, J. H. 1974, *ApJ*, 192, L37
- Danger, G., Borget, F., Chomat, M., et al. 2011, *A&A*, 535, A47
- Dartois, E., Schutte, W., Geballe, T. R., et al. 1999, *A&A*, 342, L32
- Darwent, B. d. 1970, *NIST Spec. Publ.*, 1

- Davis, D. & Braun, W. 1968, *Appl. Opt.*, 7, 2071
- de Graauw, T., Helmich, F. P., Phillips, T. G., et al. 2010, *A&A*, 518, L6
- Demyk, K., Dartois, E., D'Hendecourt, L., et al. 1998, *A&A*, 339, 553
- D'Hendecourt, L. B., Allamandola, L. J., Grim, R. J. A., & Greenberg, J. M. 1986, *A&A*, 158, 119
- Dhooghe, F., Altwegg, K., Berthelier, J.-J., et al. 2016, in *EGU General Assembly Conference Abstracts*, Vol. 18, *EGU General Assembly Conference Abstracts*, 9864
- Dhooghe, F., De Keyser, J., Altwegg, K., et al. 2017, *MNRAS*, 472, 1336
- Di Lonardo, G., Fusina, L., De Natale, P., Inguscio, M., & Prevedelli, M. 1991, *Journal of Molecular Spectroscopy*, 148, 86
- Dickens, J. E., Irvine, W. M., DeVries, C. H., & Ohishi, M. 1997, *ApJ*, 479, 307
- Drozdovskaya, M. N., Walsh, C., van Dishoeck, E. F., et al. 2016, *MNRAS*, 462, 977
- Drozdovskaya, M. N., Walsh, C., Visser, R., Harsono, D., & van Dishoeck, E. F. 2014, *MNRAS*, 445, 913
- Dulieu, F., Amiaud, L., Congiu, E., et al. 2010, *A&A*, 512, A30
- Dupuy, R., Bertin, M., Féraud, G., et al. 2017, *A&A*, 603, A61
- Ehrenfreund, P. & Charnley, S. B. 2000, *ARA&A*, 38, 427
- Eistrup, C., Walsh, C., & van Dishoeck, E. F. 2016, *A&A*, 595, A83
- Eistrup, C., Walsh, C., & van Dishoeck, E. F. 2017, *ArXiv e-prints*
- Elsila, J. E., Glavin, D. P., & Dworkin, J. P. 2009, *Meteoritics and Planetary Science*, 44, 1323
- Endo, H. & Glass, G. 1976, *The Journal of Physical Chemistry*, 80, 1519
- Es-Sebbar, E.-t., Bénilan, Y., Fray, N., et al. 2015, *ApJs*, 218, 19
- Evans, J. & Bernstein, H. 1956, *Canadian Journal of Chemistry*, 34
- Eyring, H. 1931, *Journal of the American Chemical Society*, 53, 2537
- Favre, C., Bergin, E. A., Cleeves, L. I., et al. 2015, *ApJ*, 802, L23
- Fayolle, E. C., Bertin, M., Romanzin, C., et al. 2011, *ApJL*, 739, L36
- Fayolle, E. C., Bertin, M., Romanzin, C., et al. 2013, *A&A*, 556, A122
- Fedoseev, G., Chuang, K.-J., van Dishoeck, E. F., Ioppolo, S., & Linnartz, H. 2016, *MNRAS*, 460, 4297
- Fedoseev, G., Cuppen, H. M., Ioppolo, S., Lamberts, T., & Linnartz, H. 2015a, *MNRAS*, 448, 1288
- Fedoseev, G., Ioppolo, S., Lamberts, T., et al. 2012, *J. Chem. Phys.*, 137, 054714
- Fedoseev, G., Ioppolo, S., Zhao, D., Lamberts, T., & Linnartz, H. 2015b, *MNRAS*, 446, 439
- Fettis, G., Knox, J., & Trotman-Dickenson, A. 1960, *Canadian Journal of Chemistry*, 38, 1643
- Feuchtgruber, H., Helmich, F. P., van Dishoeck, E. F., & Wright, C. M. 2000, *ApJL*, 535, L111
- Fillion, J.-H., Fayolle, E. C., Michaut, X., et al. 2014, *Faraday Discussions*, 168, 533
- Foest, R., Kindel, E., Lange, H., et al. 2007, *Contributions to Plasma Physics*, 47, 119
- Fontani, F., Pascucci, I., Caselli, P., et al. 2007, *A&A*, 470, 639
- Förstel, M., Bergantini, A., Maksyutenko, P., Góbi, S., & Kaiser, R. I. 2017, *ApJ*, 845, 83
- Förstel, M., Maksyutenko, P., Jones, B. M., et al. 2016, *ApJ*, 820, 117

- Fourikis, N., Takagi, K., & Morimoto, M. 1974, *ApJ*, 191, L139
- Friberg, P., Hjalmarsen, A., Madden, S. C., & Irvine, W. M. 1988, *A&A*, 195, 281
- Fuchs, G. W., Acharyya, K., Bisschop, S. E., et al. 2006, *Faraday Discussions*, 133, 331
- Fuchs, G. W., Cuppen, H. M., Ioppolo, S., et al. 2009, *Astronomy & Astrophysics*, 505, 629
- Fulvio, D., Brieva, A. C., Cuyllé, S. H., et al. 2014, *Applied Physics Letters*, 105, 014105
- Garrod, R., Park, I. H., Caselli, P., & Herbst, E. 2006, *Faraday Discussions*, 133, 51
- Garrod, R. T. 2013, *ApJ*, 778, 158
- Garrod, R. T. & Herbst, E. 2006, *A&A*, 457, 927
- Garrod, R. T., Wakelam, V., & Herbst, E. 2007, *A&A*, 467, 1103
- Garrod, R. T., Weaver, S. L. W., & Herbst, E. 2008, *ApJ*, 682, 283
- Geppert, W. D., Hellberg, F., Österdahl, F., et al. 2005, in *IAU Symposium*, Vol. 231, *Astrochemistry: Recent Successes and Current Challenges*, ed. D. C. Lis, G. A. Blake, & E. Herbst, 117–124
- Gerakines, P. A. & Hudson, R. L. 2015, *ApJ*, 805, L20
- Gerakines, P. A., Moore, M. H., & Hudson, R. L. 2004, *Icarus*, 170, 202
- Gerakines, P. A., Schutte, W. A., & Ehrenfreund, P. 1996, *A&A*, 312, 289
- Gerin, M., Neufeld, D. A., & Goicoechea, J. R. 2016, *ARA&A*, 54, 181
- Gibb, E., Nummelin, A., Irvine, W. M., Whittet, D. C. B., & Bergman, P. 2000a, *ApJ*, 545, 309
- Gibb, E. L. & Whittet, D. C. B. 2002, *ApJ*, 566, L113
- Gibb, E. L., Whittet, D. C. B., Boogert, A. C. A., & Tielens, A. G. G. M. 2004, *ApJ*, 151, 35
- Gibb, E. L., Whittet, D. C. B., Schutte, W. A., et al. 2000b, *ApJ*, 536, 347
- Gillett, F. C. & Forrest, W. J. 1973, *ApJ*, 179, 483
- Goesmann, F., Rosenbauer, H., Bredehoft, J. H., et al. 2015, *Science*, 349
- Gratier, P., Pety, J., Guzmán, V., et al. 2013, *A&A*, 557, A101
- Grim, R., Schutte, W., Schmitt, B., & Greenberg, M. 1989, in *IAU Symposium*, Vol. 135, *Interstellar Dust*, ed. L. J. Allamandola & A. G. G. M. Tielens, 245
- Grim, R. J. A., Baas, F., Greenberg, J. M., Geballe, T. R., & Schutte, W. 1991, *A&A*, 243, 473
- Grim, R. J. A. & Greenberg, J. M. 1987, *ApJL*, 321, L91
- Groth, W. 1937, *Z. Phys. Chem.*, 37, 307
- Gupta, D., Nagma, R., & Antony, B. 2014, *Molecular Physics*, 112, 1201
- Guzmán, V. V., Goicoechea, J. R., Pety, J., et al. 2013, *A&A*, 560, A73
- Guzmán, V. V., Pety, J., Gratier, P., et al. 2014, *Faraday Discussions*, 168, 103
- Hagen, W., Allamandola, L. J., & Greenberg, J. M. 1979, *Ap&SS*, 65, 215
- Halfen, D. T., Apponi, A. J., & Ziurys, L. M. 2001, *ApJ*, 561, 244
- Halfen, D. T., Ilyushin, V., & Ziurys, L. M. 2011, *ApJ*, 743, 60
- Halfen, D. T., Ilyushin, V. V., & Ziurys, L. M. 2013, *ApJ*, 767, 66
- Halfen, D. T., Ilyushin, V. V., & Ziurys, L. M. 2015, *ApJL*, 812, L5
- He, J., Vidali, G., Lemaire, J.-L., & Garrod, R. T. 2015, *The Astrophysical Journal*, 799, 49
- Heays, A. N., Bosman, A. D., & van Dishoeck, E. F. 2017, *A&A*, 602, A105
- Henderson, B. L. & Gudipati, M. S. 2015, *ApJ*, 800, 66
- Herbst, E. & van Dishoeck, E. F. 2009, *ARA&A*, 47, 427

- Hidaka, H., Watanabe, M., Kouchi, A., & Watanabe, N. 2011, *Physical Chemistry Chemical Physics (Incorporating Faraday Transactions)*, 13, 15798
- Hiraoka, K., Yamashita, A., Yachi, Y., et al. 1995, *ApJ*, 443, 363
- Hogerheijde, M. R., Bergin, E. A., Brinch, C., et al. 2011, *Science*, 334, 338
- Hölländer, A. & Wertheimer, M. 1994, *Journal of Vacuum Science & Technology A*, 12
- Hollis, J. M., Jewell, P. R., Lovas, F. J., & Remijan, A. 2004, *ApJ*, 613, L45
- Hollis, J. M., Lovas, F. J., Remijan, A. J., et al. 2006, *ApJ*, 643, L25
- Holtom, P. D., Bennett, C. J., Osamura, Y., Mason, N. J., & Kaiser, R. I. 2005, *The Astrophysical Journal*, 626, 940
- Hubbard, J., Voecks, G., Hobby, G., et al. 1975, *J. mol. Evol.*, 5, 223
- Hudgins, D. M., Sandford, S. A., Allamandola, L. J., & Tielens, A. G. G. M. 1993, *ApJs*, 86, 713
- Hudson, J. E., Hamilton, M. L., Vallance, C., & Harland, P. W. 2003, *Phys. Chem. Chem. Phys.*, 5, 3162
- Hudson, J. E., Vallance, C., & Harland, P. W. 2004, *Journal of Physics B: Atomic, Molecular and Optical Physics*, 37, 445
- Hudson, R. L. & Moore, M. H. 1999, *Icarus*, 140, 451
- Ilyushin, V. V., Alekseev, E. A., Dyubko, S. F., Motiyenko, R. A., & Hougen, J. T. 2005, *Journal of Molecular Spectroscopy*, 229, 170
- Ioppolo, S., Cuppen, H. M., Romanzin, C., van Dishoeck, E. F., & Linnartz, H. 2008, *ApJ*, 686, 1474
- Ioppolo, S., Fedoseev, G., Lamberts, T., Romanzin, C., & Linnartz, H. 2013, *Review of Scientific Instruments*, 84, 073112
- Ioppolo, S., Fedoseev, G., Minissale, M., et al. 2014, *Physical Chemistry Chemical Physics (Incorporating Faraday Transactions)*, 16, 8270
- Ioppolo, S., van Boheemen, Y., Cuppen, H. M., van Dishoeck, E. F., & Linnartz, H. 2011, *MNRAS*, 413, 2281
- Islam, F., Baratta, G. A., & Palumbo, M. E. 2014, *A&A*, 561, A73
- Isokoski, K., Bottinelli, S., & van Dishoeck, E. F. 2013, *A&A*, 554, A100
- Ivlev, A. V., Röcker, T. B., Vasyunin, A., & Caselli, P. 2015, *ApJ*, 805, 59
- Jaber, A. A., Ceccarelli, C., Kahane, C., & Caux, E. 2014, *ApJ*, 791, 29
- Jiménez-Escobar, A., Giuliano, B. M., Muñoz Caro, G. M., Cernicharo, J., & Marcelino, N. 2014, *ApJ*, 788, 19
- Jones, B. M., Bennett, C. J., & Kaiser, R. I. 2011, *ApJ*, 734, 78
- Jonusas, M. & Krim, L. 2016, *MNRAS*, 459, 1977
- Jørgensen, J. K. 2004, *A&A*, 424, 589
- Jørgensen, J. K., Bourke, T. L., Nguyen Luong, Q., & Takakuwa, S. 2011, *A&A*, 534, A100
- Jørgensen, J. K., Favre, C., Bisschop, S. E., et al. 2012, *ApJL*, 757, L4
- Jørgensen, J. K., Müller, H. S. P., & et al. in preparation
- Jørgensen, J. K., van der Wiel, M. H. D., Coutens, A., et al. 2016, *A&A*, 595, A117
- Jura, M. 1974, *Astrophysical Journal*, 190, L33
- Kahane, C., Ceccarelli, C., Faure, A., & Caux, E. 2013, *ApJL*, 763, L38
- Kaifu, N., Morimoto, M., Nagane, K., et al. 1974, *ApJL*, 191, L135
- Kama, M., Bruderer, S., van Dishoeck, E. F., et al. 2016, *A&A*, 592, A83
- Kama, M., Caux, E., López-Sepulcre, A., et al. 2015, *A&A*, 574, A107
- Kaňuchová, Z., Urso, R. G., Baratta, G. A., et al. 2016, *A&A*, 585, A155

- Keane, J. V., Tielens, A. G. G. M., Boogert, A. C. A., Schutte, W. A., & Whittet, D. C. B. 2001, *A&A*, 376, 254
- Kessler, M. F., Steinz, J. A., Anderegg, M. E., et al. 1996, *A&A*, 315, L27
- Kim, Y. S. & Kaiser, R. I. 2011, *The Astrophysical Journal*, 729, 68
- Kim, Y. S. & Kaiser, R. I. 2011, *ApJ*, 729, 68
- Kirchhoff, W. H., Johnson, D. R., & Lovas, F. J. 1973, *Journal of Physical and Chemical Reference Data*, 2, 1
- Kolesníková, L., Alonso, J. L., Bermúdez, C., et al. 2016, *A&A*, 591, A75
- Koput, J. 1986, *Journal of Molecular Spectroscopy*, 115, 131
- Kuan, Y.-J., Huang, H.-C., Charnley, S. B., et al. 2004, *ApJL*, 616, L27
- Lacy, J. H., Baas, F., Allamandola, L. J., et al. 1984, *ApJ*, 276, 533
- Lamberts, T., Cuppen, H. M., Fedoseev, G., et al. 2014, *A&A*, 570, A57
- Lamberts, T., Cuppen, H. M., Ioppolo, S., & Linnartz, H. 2013, *Physical Chemistry Chemical Physics (Incorporating Faraday Transactions)*, 15, 8287
- Lange, H., Foest, R., Schafer, J., & Weltmann, K.-D. 2009, *Plasma Science, IEEE Transactions on*, 37, 859
- Le Roy, L., Altwegg, K., Balsiger, H., et al. 2015, *A&A*, 583, A1
- Leto, G. & Baratta, G. A. 2003, *A&A*, 397, 7
- Ligterink, N. F. W., Coutens, A., Kofman, V., et al. 2017, *MNRAS*, 469, 2219
- Ligterink, N. F. W., Paardekooper, D. M., Chuang, K.-J., et al. 2015, *A&A*, 584, A56
- Ligterink, N. F. W., Tenenbaum, E. D., & van Dishoeck, E. F. 2015, *Astronomy & Astrophysics*, 576, A35
- Ligterink, N. F. W., Walsh, C., Bhuin, R. G., et al. 2017, *subm.*, *A&A*
- Linnartz, H., Bossa, J.-B., Bouwman, J., et al. 2011, in *IAU Symposium*, Vol. 280, *The Molecular Universe*, ed. J. Cernicharo & R. Bachiller, 390–404
- Linnartz, H., Ioppolo, S., & Fedoseev, G. 2015, *ArXiv e-prints*
- Liszt, H. S. & Turner, B. E. 1978, *ApJ*, 224, L73
- Lodders, K., Palme, H., & Gail, H.-P. 2009, *Landolt Börnstein Group VI Astronomy and Astrophysics Numerical Data and Functional Relationships in Science and Technology Volume 4B*
- Loeffler, M. J., Baratta, G. A., Palumbo, M. E., Strazzulla, G., & Baragiola, R. A. 2005, *A&A*, 435, 587
- Loomis, R. A., Zaleski, D. P., Steber, A. L., et al. 2013, *ApJL*, 765, L9
- López-Sepulcre, A., Jaber, A. A., Mendoza, E., et al. 2015, *MNRAS*, 449, 2438
- Lubic, K. G., Ray, D., Hovde, D. C., Veseth, L., & Saykally, R. J. 1989, *Journal of Molecular Spectroscopy*, 134, 21
- Lykke, J. M., Coutens, A., Jørgensen, J. K., et al. 2017, *A&A*, 597, A53
- Marcelino, N., Brünken, S., Cernicharo, J., et al. 2010, *A&A*, 516, A105
- Maret, S. & Bergin, E. A. 2015, *Astrochem: Abundances of chemical species in the interstellar medium*, *Astrophysics Source Code Library*
- Maret, S., Hily-Blant, P., Pety, J., Bardeau, S., & Reynier, E. 2011, *A&A*, 526, A47
- Martín-Doménech, R., Muñoz Caro, G. M., Bueno, J., & Goesmann, F. 2014, *A&A*, 564, A8
- Martín-Doménech, R., Muñoz Caro, G. M., & Cruz-Díaz, G. A. 2016, *A&A*, 589, A107
- Martín-Doménech, R., Rivilla, V. M., Jiménez-Serra, I., et al. 2017, *MNRAS*, 469, 2230

- Mathews, G. S., Klaassen, P. D., Juhász, A., et al. 2013, *A&A*, 557, A132
- Mathis, J. S., Mezger, P. G., & Panagia, N. 1983, *A&A*, 128, 212
- Mayhew, C. A. & Smith, D. 1990, *International Journal of Mass Spectrometry and Ion Processes*, 100, 737
- McElroy, D., Walsh, C., Markwick, A. J., et al. 2013, *A&A*, 550, A36
- McGonagle, D., Irvine, W. M., Minh, Y. C., & Ziurys, L. M. 1990, *ApJ*, 359, 121
- McGuire, B. A., Carroll, P. B., Dollhopf, N. M., et al. 2015, *The Astrophysical Journal*, 812, 76
- McGuire, B. A., Carroll, P. B., Loomis, R. A., et al. 2016, *Science*, 352, 1449
- Mikawa, Y., Brasch, J., & Jakobsen, R. 1971, *Spectrochimica Acta Part A: Molecular Spectroscopy*, 27, 529
- Milam, S. N., Savage, C., Brewster, M. A., & Ziurys, L. M. 2005, *The Astronomical Journal*, 1126
- Minissale, M., Moudens, A., Baouche, S., Chaabouni, H., & Dulieu, F. 2016, *MNRAS*, 458, 2953
- Miyauchi, N., Hidaka, H., Chigai, T., et al. 2008, *Chemical Physics Letters*, 456, 27
- Moore, M. H. & Hudson, R. L. 1998, *Icarus*, 135, 518
- Morino, I., Yamada, K., Klein, H., et al. 2000, *Journal of Molecular Structure*, 517, 367
- Muñoz Caro, G. M., Chen, Y.-J., Aparicio, S., et al. 2016, *A&A*, 589, A19
- Muñoz Caro, G. M., Dartois, E., Boduch, P., et al. 2014, *A&A*, 566, A93
- Muñoz Caro, G. M., Jiménez-Escobar, A., Martín-Gago, J. Á., et al. 2010, *A&A*, 522, A108
- Muñoz Caro, G. M., Meierhenrich, U. J., Schutte, W. A., et al. 2002, *Nature*, 416, 403
- Müller, H. S. P., Belloche, A., Xu, L.-H., et al. 2016, *A&A*, 587, A92
- Müller, H. S. P., Schlöder, F., Stutzki, J., & Winnewisser, G. 2005, *Journal of Molecular Structure*, 742, 215
- Müller, H. S. P., Thorwirth, S., Roth, D. A., & Winnewisser, G. 2001, *A&A*, 370, L49
- Neill, J. L., Bergin, E. A., Lis, D. C., et al. 2014, *ApJ*, 789, 8
- Neufeld, D. A. & Green, S. 1994, *Astrophysical Journal*, 432, 158
- Neufeld, D. A. & Wolfire, M. G. 2009, *ApJ*, 706, 1594
- Neufeld, D. A., Zmuidzinas, J., Schilke, P., & Phillips, T. G. 1997, *ApJl*, 488, L141
- Nguyen, M. T., Sengupta, D., Vereecken, L., Peeters, J., & Vanquickenborne, L. G. 1996, *Journal of Physical Chemistry*, 100, 1615
- Nishimura, H. & Tawara, H. 1994, *Journal of Physics B: Atomic, Molecular and Optical Physics*, 27, 2063
- Noble, J. A., Theule, P., Congiu, E., et al. 2015, *A&A*, 576, A91
- Nummelin, A., Bergman, P., Hjalmarsen, A., et al. 1998, *ApJS*, 117, 427
- Nummelin, A., Bergman, P., Hjalmarsen, ., et al. 2000, *ApJS*, 128, 213
- Oba, Y., Miyauchi, N., Hidaka, H., et al. 2009, *ApJ*, 701, 464
- Oba, Y., Watanabe, N., Hama, T., et al. 2012, *ApJ*, 749, 67
- Öberg, K. I. 2009, PhD thesis, Leiden Observatory, Leiden University, P.O. Box 9513, 2300 RA Leiden, The Netherlands
- Öberg, K. I., Boogert, A. C. A., Pontoppidan, K. M., et al. 2011, *ApJ*, 740, 109
- Öberg, K. I., Fuchs, G. W., Awad, Z., et al. 2007, *ApJl*, 662, L23

- Öberg, K. I., Furuya, K., Loomis, R., et al. 2015, *ApJ*, 810, 112
- Öberg, K. I., Garrod, R. T., van Dishoeck, E. F., & Linnartz, H. 2009a, *A&A*, 504, 891
- Öberg, K. I., Guzmán, V. V., Merchantz, C. J., et al. 2017, *ApJ*, 839, 43
- Öberg, K. I., Linnartz, H., Visser, R., & van Dishoeck, E. F. 2009b, *ApJ*, 693, 1209
- Öberg, K. I., van Broekhuizen, F., Fraser, H. J., et al. 2005, *ApJ*, 621, L33
- Öberg, K. I., van Dishoeck, E. F., & Linnartz, H. 2009c, *A&A*, 496, 281
- Paardekooper, D. M., Bossa, J.-B., Isokoski, K., & Linnartz, H. 2014, *Review of Scientific Instruments*, 85, 104501
- Paardekooper, D. M., Bossa, J.-B., & Linnartz, H. 2016, *A&A*, 592, A67
- Pagani, L., Favre, C., Goldsmith, P. F., et al. 2017, *A&A*, 604, A32
- Palumbo, M. E., Baratta, G. A., Collings, M. P., & McCoustra, M. R. S. 2006, *Physical Chemistry Chemical Physics (Incorporating Faraday Transactions)*, 8, 279
- Palumbo, M. E., Tielens, A. G. G. M., & Tokunaga, A. T. 1995, *ApJ*, 449, 674
- Parise, B., Simon, T., Caux, E., et al. 2003, *A&A*, 410, 897
- Peng, R., Yoshida, H., Chamberlin, R. A., et al. 2010, *The Astrophysical Journal*, 723, 218
- Penteado, E. M., Boogert, A. C. A., Pontoppidan, K. M., et al. 2015, *MNRAS*, 454, 531
- Pérez, L. M., Isella, A., Carpenter, J. M., & Chandler, C. J. 2014, *ApJL*, 783, L13
- Pickett, H. M., Cohen, E. A., Waters, J. W., & Phillips, T. G. 1979, 34th International Symposium on Molecular Spectroscopy, Columbus, OH, USA.
- Pickett, H. M., Poynter, R. L., Cohen, E. A., et al. 1998, *J. Quant. Spec. Radiat. Transf.*, 60, 883
- Pilbratt, G. L., Riedinger, J. R., Passvogel, T., et al. 2010, *A&A*, 518, L1
- Pineda, J. E., Maury, A. J., Fuller, G. A., et al. 2012, *A&A*, 544, L7
- Plooster, M. N. & Garvin, D. 1956, *Journal of the American Chemical Society*, 78, 6003
- Plyler, E. 1952, *Journal of Research of the National Bureau of Standards*, 48
- Pontoppidan, K. M. 2006, *A&A*, 453, L47
- Pontoppidan, K. M., Boogert, A. C. A., Fraser, H. J., et al. 2008, *ApJ*, 678, 1005
- Pontoppidan, K. M., Fraser, H. J., Dartois, E., et al. 2003, *A&A*, 408, 981
- Prasad, S. S. & Tarafdar, S. P. 1983, *ApJ*, 267, 603
- Pulliam, R. L., McGuire, B. A., & Remijan, A. J. 2012, *The Astrophysical Journal*, 751, 1
- Qi, C., Öberg, K. I., Andrews, S. M., et al. 2015, *ApJ*, 813, 128
- Qi, C., Öberg, K. I., Wilner, D. J., et al. 2013, *Science*, 341, 630
- Quan, D., Herbst, E., Osamura, Y., & Roueff, E. 2010, *ApJ*, 725, 2101
- Rathborne, J. M., Jackson, J. M., Zhang, Q., & Simon, R. 2008, *ApJ*, 689, 1141
- Raunier, S., Chiavassa, T., Duvernay, F., et al. 2004, *A&A*, 416, 165
- Reboussin, L., Wakelam, V., Guilloteau, S., Hersant, F., & Dutrey, A. 2015, *A&A*, 579, A82
- Ree, J., Yoon, S., Park, K., & Kim, Y. 2004, *Bulletin of the Korean Chemical Society*, 25, 1217
- Remijan, A. J., Snyder, L. E., McGuire, B. A., et al. 2014, *ApJ*, 783, 77
- Reva, I., Lapinski, L., & Fausto, R. 2010, *J. Mol. Struct.*, 976, 333
- Roelfsema, P. R., Helmich, F. P., Teyssier, D., et al. 2012, *A&A*, 537, A17

- Rubin, R. H., Swenson, Jr., G. W., Benson, R. C., Tigelaar, H. L., & Flygare, W. H. 1971, *ApJl*, 169, L39
- Ruzi, M. & Anderson, D. 2012, *J. Chem. Phys.*, 137, 194313
- Rygl, K. L. J., Brunthaler, A., Sanna, A., et al. 2012, *A&A*, 539, A79
- Sakaizumi, T., Mure, H., Ohashi, O., & Yamaguchi, I. 1990, *Journal of Molecular Spectroscopy*, 140, 62
- Salez, M., Frerking, M. A., & Langer, W. D. 1996, *ApJ*, 467, 708
- Salinas, V. N., Hogerheijde, M. R., Bergin, E. A., et al. 2016, *A&A*, 591, A122
- Sandford, S. A., Allamandola, L. J., Tielens, A. G. G. M., & Valero, G. J. 1988, *ApJ*, 329, 498
- Saykally, R. J. & Evenson, K. M. 1979, *Physical Review Letters*, 43, 515
- Schilke, P., Groesbeck, T. D., Blake, G. A., Phillips, & T. G. 1997, *ApJS*, 108, 301
- Schilke, P., Phillips, T. G., & Wang, N. 1995, *Astrophysical Journal*, 441, 334
- Schneider, W. & Bernstein, H. 1956, *Transactions of the Faraday Society*
- Schutte, W. A., Boogert, A. C. A., Tielens, A. G. G. M., et al. 1999, *A&A*, 343, 966
- Schutte, W. A., Tielens, A. G. G. M., Whittet, D. C. B., et al. 1996, *A&A*, 315, L333
- Schwarz, K. R., Bergin, E. A., Cleaves, L. I., et al. 2016, *ApJ*, 823, 91
- Shen, C. J., Greenberg, J. M., Schutte, W. A., & van Dishoeck, E. F. 2004, *A&A*, 415, 203
- Snow, J. L., Orlova, G., Blagojevic, V., & Bohme, D. K. 2007, *J. Am. Chem. Soc.*, 129, 99109917
- Snyder, L. E., Buhl, D., Schwartz, P. R., et al. 1974, *ApJ*, 191, L79
- Solomon, P. M., Jefferts, K. B., Penzias, A. A., & Wilson, R. W. 1971, *ApJl*, 168, L107
- Sullivan, J., Heusel, H., Zunic, W., & Durig, J. 1994, *Spectrochimica Acta*, 50
- Sutton, E. C., Peng, R., Danchi, W. C., et al. 1995, *ApJS*, 97, 455
- Suzuki, T., Ohishi, M., Hirota, T., et al. 2016, *ApJ*, 825, 79
- Taquet, V., López-Sepulcre, A., Ceccarelli, C., et al. 2015, *ApJ*, 804, 81
- Taylor, R. & Vidale, G. 1956, *The Journal of Chemical Physics*
- Teolis, B. D., Loeffler, M. J., Raut, U., Famá, M., & Baragiola, R. A. 2007, *Icarus*, 190, 274
- Tercero, B., Kleiner, I., Cernicharo, J., et al. 2013, *ApJl*, 770, L13
- Theule, P., Borget, F., Mispelaer, F., et al. 2011, *A&A*, 534, A64
- Tielens, A. G. G. M. 2013, *Reviews of Modern Physics*, 85, 1021
- Tielens, A. G. G. M. & Charnley, S. B. 1997, *Origins of Life and Evolution of the Biosphere*, 27, 23
- Tielens, A. G. G. M., Tokunaga, A. T., Geballe, T. R., & Baas, F. 1991, *ApJ*, 381, 181
- Ting, W.-J., Chang, C.-H., Chen, S.-E., et al. 2014, *Journal of the Optical Society of America B Optical Physics*, 31, 1954
- Turner, B. E. 1991, *ApJS*, 76, 617
- van Broekhuizen, F. A., Keane, J. V., & Schutte, W. A. 2004, *A&A*, 415, 425
- van Broekhuizen, F. A., Pontoppidan, K. M., Fraser, H. J., & van Dishoeck, E. F. 2005, *A&A*, 441, 249
- van der Marel, N., van Dishoeck, E. F., Bruderer, S., et al. 2016, *A&A*, 585, A58
- van der Marel, N., van Dishoeck, E. F., Bruderer, S., et al. 2013, *Science*, 340, 1199
- Van Dijk, F. A. & Dymanus, A. 1969, *Chemical Physics Letters*, 4, 170
- van Dishoeck, E. F. & Blake, G. A. 1998, *ARA&A*, 36, 317

- van Dishoeck, E. F., Blake, G. A., Jansen, D. J., & Groesbeck, T. D. 1995, *ApJ*, 447, 760
- van Dishoeck, E. F., Jonkheid, B., & van Hemert, M. C. 2006, *Faraday Discussions*, 133, 231
- van Hemert, M. C., Takahashi, J., & van Dishoeck, E. F. 2015, *J. Phys. Chem. A*, 119, 6354
- van 't Hoff, M. L. R., Persson, M., Harsono, D., et al. 2017, *subm.*, *A&A*
- Visser, R., Doty, S. D., & van Dishoeck, E. F. 2011, *A&A*, 534, A132
- Wakelam, V., Herbst, E., Loison, J.-C., et al. 2012, *ApJ*, 199, 21
- Walmsley, C. M. 1992, in *Chemistry and Spectroscopy of Interstellar Molecules*, ed. D. K. Bohme, 267
- Walsh, C., Loomis, R. A., Öberg, K. I., et al. 2016, *ApJL*, 823, L10
- Walsh, C., Millar, T. J., Nomura, H., et al. 2014, *A&A*, 563, A33
- Walsh, C., Nomura, H., & van Dishoeck, E. 2015, *A&A*, 582, A88
- Warneck, P. 1962, *Appl. Opt.*, 1, 721
- Watanabe, N. & Kouchi, A. 2002, *ApJ*, 571, L173
- Watanabe, N., Mouri, O., Nagaoka, A., et al. 2007, *ApJ*, 668, 1001
- Werner, M. W., Roellig, T. L., Low, F. J., et al. 2004, *ApJS*, 154, 1
- Westley, M. S., Baragiola, R. A., Johnson, R. E., & Baratta, G. A. 1995, *Nature*, 373, 405
- Wexler, A. 1967, *Applied Spectroscopy Reviews*, 1, 29
- White, J. M. & Thompson, D. L. 1974, *The Journal of Chemical Physics*, 61, 719
- Wilson, T. L. & Rood, R. 1994, *ARA&A*, 32, 191
- Winnewisser, M., Pearson, E. F., Galica, J., & Winnewisser, B. P. 1982, *Journal of Molecular Spectroscopy*, 91, 255
- Woon, D. E. 2002, *ApJ*, 571, L177
- Wright, G. S., Wright, D., Goodson, G. B., et al. 2015, *PASP*, 127, 595
- Yıldız, U. A., Acharyya, K., Goldsmith, P. F., et al. 2013, *A&A*, 558, A58
- Yu, M., Willacy, K., Dodson-Robinson, S. E., Turner, N. J., & Evans, II, N. J. 2016, *ApJ*, 822, 53
- Zernickel, A., Schilke, P., Schmiedeke, A., et al. 2012, *A&A*, 546, A87
- Zhang, K., Bergin, E. A., Blake, G. A., Cleeves, L. I., & Schwarz, K. R. 2017, *Nature Astronomy*, 1, 0130
- Zheng, W. & Kaiser, R. I. 2010, 127, 5251
- Zhou, S. & Durig, J. 2009, *JMS*, 924
- Ziurys, L. M., Apponi, A. J., Hollis, J. M., & Snyder, L. E. 1994, *ApJ*, 436, L181
- Zmuidzinas, J., Blake, G. A., Carlstrom, J., Keene, J., & Miller, D. 1995, *ApJL*, 447, L125
- Zuckerman, B., Turner, B. E., Johnson, D. R., et al. 1975, *ApJ*, 196, L99

Nederlandse samenvatting

Achtergrond

Sterren en planeten worden continue gevormd in de ruimte. Ze ontstaan uit lichtjaren grote wolken van gas en stof die onder hun eigen zwaartekracht in elkaar kunnen storten. Het gas in deze wolken bestaat voornamelijk uit waterstof (H en H₂), maar bevat ook een fractie atomaire koolstof (C), stikstof (N) en zuurstof (O). De samenstelling van het stof is vergelijkbaar met dat van zand op aarde en bestaat vooral uit silicaten en grotere koolstofstructuren. De omstandigheden zijn extreem in dit soort wolken; lage dichtheden, intense straling en ongunstige temperaturen bemoeilijken de vorming van moleculen. Zeker complexe moleculen, bestaande uit zes of meer atomen, zijn moeilijk te vormen; kunnen kleinere moleculen nog via gasfase reacties ontstaan, voor grotere moleculen wordt dat steeds lastiger. Reacties op interstellair ijs bieden uitkomst.

Onder invloed van haar eigen zwaartekracht, zal een interstellaire wolk zich samentrekken waarbij de gas en stof dichtheden toenemen (afb. 1.1). Als deze dichtheid hoog genoeg wordt, kan de wolk zich tegen externe stralings- en warmte-bronnen afschermen. Dit heeft tot gevolg dat de temperatuur in de wolk daalt, tot wel 10 Kelvin (-263 °C). Grote hoeveelheden gas vriezen nu vast op de koude oppervlakten van stofdeeltjes en vormen zo ijsmantels. In deze moleculaire reservoirs kunnen efficiënt chemische reacties plaats vinden. Reacties met de meest voorkomende atomen, H, O, N en C, resulteren in grote hoeveelheden simpele moleculen zoals water (H₂O), koolstofdioxide (CO₂), methaan (CH₄), ammoniak (NH₃) en methanol (CH₃OH). In gelijksoortige additiereacties tussen molecuulfragmenten worden vervolgens grotere moleculen gemaakt. De reacties die leiden tot grotere moleculen kunnen worden bevorderd door energie aan het ijs toe te voegen, bijvoorbeeld in de vorm van uv-straling uit het interne stralingsveld van de wolk. Laboratoriummetingen laten zien dat het mogelijk is complexe moleculen te vormen in ijs, waardoor de ijsmantels die op interstellaire stofdeeltjes vormen dus een vast onderdeel zijn van de interstellaire chemische fabriek (afb. 1.2).

In de kern van de ineenstortende wolk zal na verloop van tijd de dichtheid hoog genoeg zijn voor het ontstaan van een jonge ster. Gas en stof uit de wolk blijft neervallen op deze zogenaamde *protoster*. De energie die hierbij vrijkomt wordt uitgestraald als warmte; er vindt nog geen kernfusie plaats. Een deel van de ijzige stofdeeltjes zal direct met de straling en warmte van de jonge ster in aanraking komen. Dit heeft tot gevolg dat grote hoeveelheden ijs verdampen en het gas rond de *protoster* verrijkt wordt met complexe moleculen (afb. 1.3).

Een ander deel van de materie uit de wolk volgt een specifieke weg naar de *protoster* door een zogenaamde *protoplanetaire schijf*. Deze schijf heeft een vergelijkbare straal als ons zonnestelsel en vertoont zekere overeenkomsten met de wolk waaruit de ster geboren is: het aanwezige stof en gas hebben relatief hoge dichtheden en de binnengebieden van de schijf worden afgeschermd van

straling en warmte van de ster (afb. 1.4). Ijsmantels en de chemische complexiteit die zij bevatten kunnen intact van de wolk naar de schijf getransporteerd worden en chemische reacties kunnen hier zelfs verder gaan. Stofdeeltjes kunnen aan elkaar plakken, zeker wanneer ze zijn omgeven met een ijslaag. Dit proces leidt tot de vorming van stofkorrels en klein gruis dat steeds verder kan clusteren tot er rotsblokken en op den duur kometen en jonge planeten ontstaan (afb. 1.5). De complexe chemie die plaats vindt op de stofdeeltjes in de wolk is medebepalend voor de chemische samenstelling van kometen, planeten en planetaire atmosferen. Op deze wijze spelen reacties op interstellair stofdeeltjes uiteindelijk ook een rol bij het ontstaan van leven.

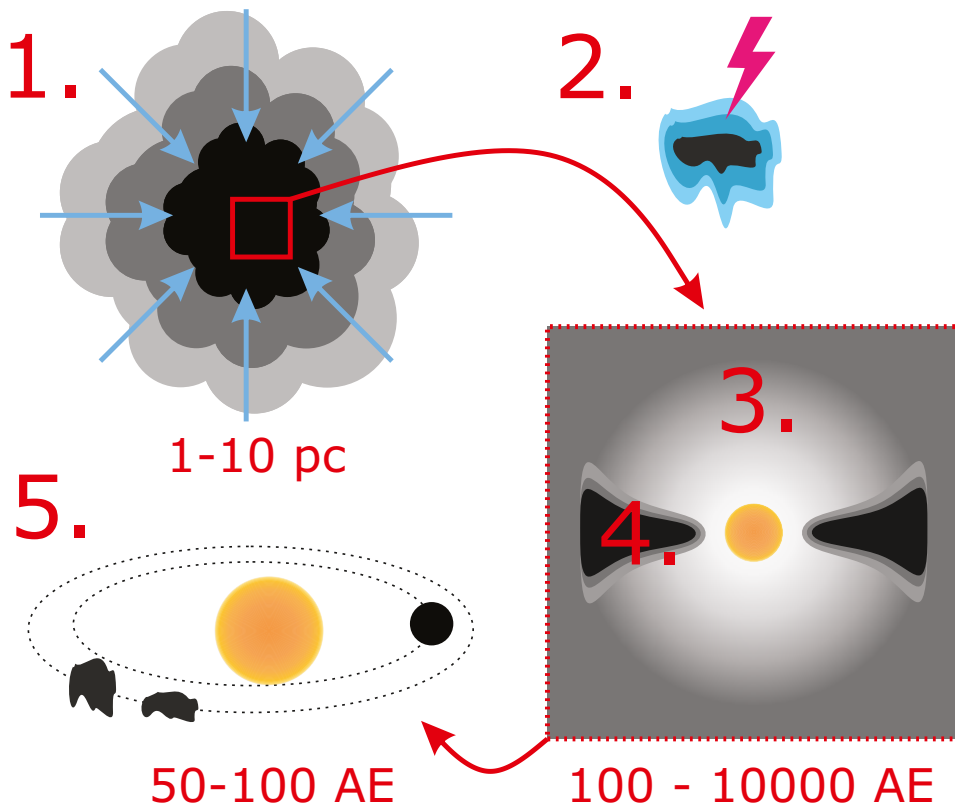
Astrochemie

Astrochemici bestuderen de chemische en fysische processen die zich gedurende ster- en planeetvorming voordoen. Dit vakgebied steunt op drie belangrijke zuilen; astronomische waarnemingen, laboratorium experimenten en astrochemische modellen.

Met telescopen worden moleculen in de ruimte bestudeerd. Deze telescopen dekken een scala aan verschillende golflengtes af, van het diepe UV tot het verre infrarood en microgolfg gebied. Hiermee is het mogelijk om het proces van ster- en planeetvorming nauwkeurig te bestuderen door naar verschillende astronomische objecten te kijken, die zich in verschillende evolutiestadia bevinden. Het is mogelijk om complexe moleculen in de gasfase te zien en kleinere moleculen in het ijs waar te nemen. Moleculen worden overal gezien, in de grootste stervormende wolken en in *protoplanetaire schijven* waarin nieuwe planeten ontstaan. Deze waarnemingen leren ons niet alleen welke soorten moleculen er aanwezig zijn, maar leveren ook informatie over relevante fysische parameters, zoals bijvoorbeeld temperatuur en dichtheid.

Door in een experiment de moleculaire spectra te meten van vastgevroren moleculen, kunnen die moleculen aan de hand van deze “vingerafdruk” ook worden geïdentificeerd in de ruimte. Daarvoor worden de astronomische waarnemingen vergeleken met die verricht in het laboratorium. Behalve de spectroscopische eigenschappen van ijs in de ruimte, kunnen ook de moleculair dynamische (lees: chemische) eigenschappen van ijs in een laboratorium worden onderzocht. Interstellair ijsmantels worden voor precies ingestelde condities gesimuleerd om zo de reacties te bekijken die complexe moleculen vormen of de processen te bestuderen die moleculen vanuit het ijs naar de gasfase brengen.

Computermodellen knopen al deze informatie aan elkaar door reacties te simuleren onder interstellair condities en voor astronomisch lange tijdschalen. Op deze manier is het mogelijk de laboratoriumdata te verbinden met astronomische waarnemingen, waarmee het traject dat moleculen afleggen, vanaf hun vorming in een grote interstellair wolk tot aan planeten rond een jonge ster, in kaart wordt gebracht.



Afbeelding 1. Illustratie van de vorming van een planetenstelsel. Onder invloed van de zwaartekracht stort een interstellair wolk ineen (1). In de koude regionen vriezen gasmoleculen vast op stofdeeltjes, en in deze ijsmantels kunnen chemische processen plaatsvinden (2). Nadat een protoster gevormd is blijft materie neervallen op de jonge ster. Door de warmte die hierbij vrijkomt verdampen ijsmantels en komen complexe moleculen in de gasfase (3). De invallende materie vormt een *protoplanetaire schijf* rond de protoster (4), waaruit uiteindelijk kometen en planeten ontstaan (5). 1 AE is de Astronomische Eenheid, de gemiddelde afstand tussen de aarde en de zon, gedefinieerd als 149 597 870,7 km. 1 pc is een parsec, gelijk aan: 3,26 lichtjaar of 206 264,8 AE.

Het astrochemisch gereedschap

Om deze studies mogelijk te maken zijn verschillende soorten “gereedschap” nodig. Deze paragraaf geeft een kort overzicht van de instrumenten die zijn gebruikt in dit proefschrift.

Het laboratoriumwerk is veelal uitgevoerd op de CryoPAD2 opstelling (Hoofdstuk 2), een machine die als onderdeel van dit promotieonderzoek is ontworpen en gerealiseerd. In deze opstelling wordt de leegte van het interstellair medium gesimuleerd in een vacuümkamer. Het oppervlak van interstellaire stofdeeltjes wordt nagebootst in de kamer op een met goud bedekte metalen ondergrond, die wordt gekoeld met een cryostaat tot een temperatuur van rond de 10 Kelvin. Gas wordt gecontroleerd in de kamer geleid en bevriest op dit koude oppervlak waarbij een laagje ijs ontstaat dat lijkt op interstellair ijs. Processen die in de ruimte plaatsvinden, bijvoorbeeld bestraling met licht van het interstellair stralingsveld, worden nagebootst door het ijs met uv-licht te bestralen (Hoofdstuk 3). Dat proces kan bij verschillende temperaturen worden onderzocht door het ijs heel precies te verwarmen. De uitwerkingen op de samenstelling van het ijs worden vervolgens bestudeerd met infraroodspectroscopie en massa spectrometrie.

Astronomische waarnemingen in dit proefschrift zijn uitgevoerd met verschillende telescopen. De *James Clerk Maxwell Telescope* (JCMT) en de *Atacama Large Millimeter/submillimeter Array* (ALMA) “zoeken” naar moleculen op frequenties in het microgolf regime. Op deze golflengtes bevinden zich de unieke rotationele overgangen van vele moleculen en deze telescopen zijn dus uitermate geschikt om te zoeken naar de “vingerafdrukken” van moleculen om zo de interstellaire chemie in kaart te brengen. Vooral de “astrochemie machine” ALMA is speciaal op dit gebied: vanwege haar hoge gevoeligheid en hoekoplossend vermogen kunnen moleculen die voorkomen in lage concentraties met ongekende scherpte op de schaal van ons zonnestelsel rond sterren bestudeerd worden.

De conclusies van dit proefschrift

In dit proefschrift worden een aantal vragen die astrochemici bezig houden behandeld. Met laboratoriumwerk en telescoopwaarnemingen is vooral de vorming van biologisch relevante moleculen onderzocht. In het volgende overzicht worden de belangrijkste conclusies van ieder hoofdstuk kort samengevat.

Hoofdstuk 4 onderzoekt het *co – desorptie* mechanisme om het transport van methanol naar de gasfase op lage temperaturen te verklaren. Door verwarming verdampt methanol rond de 100 Kelvin in het interstellair medium, maar uit waarnemingen is gebleken dat methanol aanwezig is in gebieden waar de temperatuur hier ver beneden ligt. In het *co – desorptie* mechanisme wordt gebruik gemaakt van een tweede molecuul dat op een lagere temperatuur verdampt en gedurende het verdampen methanol “meesleept” naar de gasfase. Specifiek wordt gekeken naar de interstellaire ijs componenten CO and CH₄,

die beide rond de 20 Kelvin verdampen. In experimenten was het niet mogelijk om aan te tonen dat deze twee moleculen methanol kunnen laten *co – desorberen*. Het was wel mogelijk een bovenwaarde voor dit proces te bepalen en wanneer deze limiet wordt gebruikt in chemische modellen blijkt het alsnog mogelijk om aanzienlijke hoeveelheden methanol in het gas te krijgen. *Co – desorptie* van methanol kan dus een efficiënt mechanisme zijn, maar gevoeligere experimentele technieken zijn nodig om de bovenwaarde die nu is bepaald verder te reduceren.

In Hoofdstuk 5 wordt de vibrationele spectroscopie van drie belangrijke complex organische moleculen, acetaldehyde (CH_3CHO), ethanol ($\text{CH}_3\text{CH}_2\text{OH}$) en dimethylether (CH_3OCH_3), in ijs beschreven. Deze data zijn nodig om waarnemingen van interstellair ijs met de *James Webb Space Telescope* te analyseren. Tot nu toe heeft de nadruk van interstellaire ijswaarnemingen vooral op kleinere moleculen gelegen. Met de data in dit hoofdstuk kan bepaald worden of deze complexe organische moleculen zich in de ijsmantels op stofdeeltjes bevinden en in welke hoeveelheden. Ook zal het mogelijk zijn te onderzoeken met welke andere moleculen ze zijn gemengd. Dit levert waardevolle informatie over mogelijke reactieschemas.

Het giftige, maar ook biologisch belangrijke molecuul methylisocyanat (CH_3NCO) is het onderwerp van Hoofdstuk 6. Aan de hand van ALMA data wordt de eerste gasfasedetectie gepresenteerd van CH_3NCO rond een *protoster*, genaamd IRAS 16293–2422, die grote gelijkenis vertoont met onze eigen zon. Deze waarneming maakt het aannemelijk dat dit molecuul ook aanwezig was toen ons eigen zonnestelsel gevormd werd. In het laboratorium is aangetoond dat CH_3NCO gevormd kan worden via reacties tussen de simpele en interstellair relevante ijscomponenten methaan (CH_4) en isocyaanzuur (HNCO).

Hoofdstuk 7 is gerelateerd aan Hoofdstuk 6 en richt zich op zogenaamde amide-dragende moleculen die ontstaan uit dezelfde ingrediënten als waaruit CH_3NCO gevormd wordt. Amides zijn biologisch relevant, omdat dit type verbinding hetzelfde is waarmee aminozuren aan elkaar verbonden worden om eiwitten te vormen. Verscheidene amides zijn interstellair waargenomen, wat betekent dat de bouwblokken om eiwitten te maken een buitenaardse oorsprong kunnen hebben. Over het vormingsmechanisme en de onderlinge relatie van deze amides is echter nog weinig bekend. Met dit laboratorium werk is een netwerk van amides in kaart gebracht, waarin formamide (NH_2CHO) en acetamide (CH_3CONH_2), beiden waargenomen in de interstellaire ruimte, een belangrijk onderdeel zijn. Een analyse van de laboratorium data van deze twee moleculen en vergelijking met interstellaire waarnemingen toont aan dat beide moleculen familie van elkaar zijn en een gemeenschappelijke chemische oorsprong hebben in interstellair ijs.

In Hoofdstuk 8 wordt met JCMT waarnemingen gezocht naar het molecuul methylamine (CH_3NH_2) rond zware *protosterren*. Dit molecuul is betrokken bij het vormingsmechanisme van aminozuren en chemische modellen voorspellen grote interstellaire hoeveelheden. Voorheen is het molecuul alleen waargenomen rond de chemisch hoog actieve *protoster* Sagittarius B2. In onze waarnemingen wordt het molecuul niet gevonden, wat vraagt tekenen plaatst bij de efficiëntie van methylaminevorming.

Hoofdstuk 9 bouwt voort op het vorige hoofdstuk en onderzoekt met ALMA waarnemingen de aanwezigheid van methylamine rond de jonge zon-

achtige *protoster* IRAS 16293–2422, alsook van de moleculen methanimine (CH_2NH) en hydroxylamine (NH_2OH). Net als methylamine zijn de laatste twee moleculen betrokken in reactiemechanismen die leiden tot aminozuren. Uit de waarnemingen blijkt dat methylamine en hydroxylamine niet, of in niet meetbare hoeveelheden, aanwezig zijn rond deze ster. Dit maakt de vorming van aminozuren via deze moleculen minder waarschijnlijk. De aanwezigheid van methanimine wordt wel voor het eerst aangetoond rond dit type *protoster*, waardoor reacties met dit molecuul die leiden tot aminozuren mogelijk relevanter zijn dan tot nu toe aangenomen.

Hoofdstuk 10 koppelt interstellair gasfase waarnemingen van het molecuul waterstof bromide (HBr) met metingen in het ijs op kometen in ons zonnestelsel. Dit werk toont aan dat HBr grotendeels blijft opgesloten in de interstellair ijsmantels en uiteindelijk terecht komt in de ijslaag die zich op kometen bevindt. De aanwezigheid van het molecuul in de gasfase is laag.

Dit proefschrift draagt bij aan het in kaart brengen van de interstellair chemie. Voorheen onbekende vormingsreacties van moleculen zijn nu bekend en de aanwezigheid van biologisch relevante moleculen is aangetoond rond een jonge zon-achtige ster op de schaal van de baan van de planeet Neptunus. We hebben een beter idee welke processen plaatsvinden in stervormingsgebieden. Zo zijn we een stap dichterbij het verklaren hoe bepaalde moleculen in ons eigen zonnestelsel zijn ontstaan en mogelijk op aarde terecht gekomen, waar ze als belangrijke bouwstenen hebben bijgedragen aan de vorming van leven zoals wij dat kennen.

Publications

Published papers

- *Protostellar and cometary detections of organohalogenes*
Fayolle, E.C.; Öberg, Karin I.; Jørgensen, J.K.; Altwegg, K.; Calcutt, H.; Müller, H.S.P.; Rubin, M.; van der Wiel, M.H.D.; Bjerkeli, P.; Bourke, T.L.; Coutens, A.; van Dishoeck, E.F.; Drozdovskaya, M.N.; Garrod, R.T.; **Ligterink, N.F.W.**; Persson, M.V.; Wampfler, S.F.; Rosina Team
- *The ALMA-PILS survey: detection of CH₃NCO towards the low-mass protostar IRAS 16293–2422 and laboratory constraints on its formation*
Ligterink, N.F.W.; Coutens, A.; Kofman, V.; Müller, H.S.P.; Garrod, R.T.; Calcutt, H.; Wampfler, S.F.; Jørgensen, J.K.; Linnartz, H.; van Dishoeck, E.F.; 2017, Monthly Notices of the Royal Astronomical Society, Volume 469, Issue 2
- *The (w)hole survey: An unbiased sample study of transition disk candidates based on Spitzer catalogs*
van der Marel, N.; Verhaar, B. W.; van Terwisga, S.; Mern, B.; Herczeg, G.; **Ligterink, N. F. W.**; van Dishoeck, E. F.; 2016, Astronomy & Astrophysics, Volume 592
- *The ALMA-PILS survey: First detections of deuterated formamide and deuterated isocyanic acid in the interstellar medium*
Coutens, A.; Jørgensen, J. K.; van der Wiel, M. H. D.; Müller, H. S. P.; Lykke, J. M.; Bjerkeli, P.; Bourke, T. L.; Calcutt, H.; Drozdovskaya, M. N.; Favre, C.; Fayolle, E. C.; Garrod, R. T.; Jacobsen, S. K.; **Ligterink, N. F. W.**; Öberg, K. I.; Persson, M. V.; van Dishoeck, E. F.; Wampfler, S. F.; 2016, Astronomy & Astrophysics, Volume 590
- *UV Photodesorption of Methanol in Pure and CO-rich Ices: Desorption Rates of the Intact Molecule and of the Photofragments*
Bertin, M.; Romanzin, C.; Doronin, M.; Philippe, L.; Jeseck, P.; **Ligterink, N.F.W.**; Linnartz, H.; Michaut, X.; Fillion, J.; 2016, The Astrophysical Journal Letters, Volume 817, Issue 2
- *Controlling the emission profile of an H₂ discharge lamp to simulate interstellar radiation fields*
Ligterink, N. F. W.; Paardekooper, D. M.; Chuang, K.-J.; Both, M. L.; Cruz-Diaz, G. A.; van Helden, J. H.; Linnartz, H.; 2015, Astronomy & Astrophysics, Volume 584
- *Laboratory Photo-chemistry of PAHs: Ionization versus Fragmentation*
Zhen, J.; Castellanos, P.; Paardekooper, D.M.; **Ligterink, N.F.W.**; Linnartz, H.; Nahon, L.; Joblin, C.; Tielens, A.G.G.M.; 2015, The Astrophysical Journal Letters, Volume 804, Issue 1

- *Search for methylamine in high mass hot cores*
Ligterink, N. F. W.; Tenenbaum, E. D.; van Dishoeck, E. F.; 2015, *Astronomy & Astrophysics*, Volume 576

Submitted papers

- *Interstellar bromine depletion matches cometary ices from Rosetta*
Ligterink, N.F.W. & Kama, M.; 2017, submitted for publication in *Astronomy & Astrophysics*
- *The ALMA-PILS survey: Stringent limits on small amines and nitrogen-oxides towards IRAS 16293–2422B*
Ligterink, N.F.W.; Calcutt, H.; Coutens, A.; Bourke, T.L.; Drozdovskaya, M.N.; Kristensen, L.E.; Müller, H.S.P.; Wampfler, S.F.; van der Wiel, M.H.D.; van Dishoeck, E.F.; Jørgensen, J.K.; 2017, submitted for publication in *Astronomy & Astrophysics*
- *Infrared spectra of complex organic molecules in astronomically relevant ice matrices I: Acetaldehyde, ethanol and dimethyl ether*
Terwisscha van Scheltinga, J.; **Ligterink, N.F.W.**; Boogert, A.C.A.; van Dishoeck, E.F.; Linnartz, H.; 2017, submitted for publication in *Astronomy & Astrophysics*
- *Methanol ice co-desorption as a mechanism to explain cold methanol in the gas-phase*
Ligterink, N. F. W.; Walsh, C.; Bhui, R.G.; Vissapragada, S.; Terwisscha van Scheltinga, J.; Linnartz, H.; 2017, submitted for publication in *Astronomy & Astrophysics*

Curriculum Vitae

Most of my early life I spent in and around Vinkeveen, a small village just south of Amsterdam. From 2001 to 2007 I attended secondary school at the Alkwin Kollege in Uithoorn. Here I followed the exact sciences track “Natuur & Techniek” at Gymnasium level. I was mostly interested in chemistry and after graduating decided to study chemistry at the Vrije Universiteit Amsterdam. During my bachelor I got more interested in the fundamental molecular interactions and in the field of physics and in the final year I did a research project in the physical chemistry group of Prof. Maurice Janssen. This led me to continue with the master specialization Physical Chemistry and do a master research project in femtosecond (10^{-15} seconds) chemistry under supervision of Dr. Stefan Lehmann, again in the group of Prof. Maurice Janssen. Near the end of my time as a master student I did a second research project in attosecond (10^{-18} seconds) physics at the Max Born Institute in Berlin. This work was supervised by Dr. Jesse Klei and Dr. Christian Neidel in the group of Prof. Marc Vrakking. During my times as a bachelor and master student I did not take courses in astronomy and it was thus by chance that I got into contact with Harold Linnartz at the Leiden Observatory and was introduced to the world of astronomy. After working for a few months in the Sackler Laboratory for Astrophysics as a technician, I was offered, and accepted, a PhD position under supervision of Ewine van Dishoeck and Harold Linnartz on the laboratory and observational investigation of nitrogen-bearing complex organic molecules as formed in the inter- and circumstellar medium.

My project started with the construction of an upgraded version of the CryoPAD set-up (creatively named CryoPAD2), an ultra high vacuum experiment in which photochemistry and physics of thin ice layers are studied. Also, I was given the chance to participate in an observational project and go on an observing run at the William Herschel Telescope at the island of La Palma. These last two experiences were a real eye opener and greatly raised my interest in observational astrochemistry and astronomy as a whole. Afterwards, laboratory work and observational analysis occurred mostly simultaneously, often complementary to each other, and resulted in the varied thesis that you are reading now.

The work in this thesis has been presented at various conferences in The Netherlands, United States, Spain, Switzerland, France, Denmark and Chile, awarded highlighted publication of year 2015 in Astronomy & Astrophysics (Chapter 3) and been the subject of an ESO press release (Chapter 6). Next to my research, I supervised two bachelor and a master student in laboratory projects, performed teaching duties for the course “Inleiding astrofysica” and organised the Astrochem Seminar.

Afterword

My experience as a PhD student can largely be characterized by the words “new” and “diverse”. I came from the field of chemistry and had to adapt to this new world of astronomy, of which in the beginning I only understood the laboratory techniques. A steep learning curve followed in which basic astronomy, star formation theory and telescope techniques were covered. My affection for astronomy grew and eventually resulted in a number of observational chapters in this thesis. This transformation from chemist to astronomer did teach me that there are almost no limits to what you can do as long as you keep listening, reading and learning.

When it comes to learning, astronomy is a fantastic environment. It is a diverse field which also touches upon chemistry, physics, biology and mathematics as well as many technical aspects. There is always a challenge to be found and something new to do and learn. This shows in this thesis which covers a wide variety of subjects ranging from solid-state physics and chemistry to interferometric observations of interstellar gas-phase molecules. I have also been fortunate enough to work at and see some very different scientific facilities, such as the William Herschel Telescope at La Palma, the SOLEIL synchrotron in Paris and the Very Large Telescope in the Atacama desert in Chile. I can not imagine many other fields of study where one gets to go to such a variety of high-end instruments.

The PhD experience has been a great enrichment of my life and it goes without saying that many people have contributed to this. The first two of those people are Ewine and Harold, who not just hired me, but more importantly gave me the freedom to explore the astrochemical possibilities in the laboratory and observations in my own way. In some cases this is the long way around to get scientific results, but for me an experience that helped me to better understand the many aspects of astrochemistry and science.

A large group of colleagues, collaborators and friends helped me with various projects. At the start of my PhD Edith showed me the ropes of laboratory astrochemistry on the original CryoPAD set-up (and, yes, gave me the nickname snowflake). Subsequently, Martijn has been essential in the construction of the upgraded CryoPAD2 set-up, but also in adventures in- and outside the lab (like on French highways). Aart has always been keeping a watchful eye on the organisation of the lab and if enough jokes are being told. Also, of course, the fine mechanical and electronics departments, glass workshop and computer group as well as administrative support, because without them my work and (laboratory) astrochemistry would be a lot more difficult.

Throughout the years I have worked together with many great, fun and knowledgeable collaborators. Especially Daniel P., Mihkel, Audrey, Catherine and Hannah contributed to a significant portion of the scientific work that you see in this thesis.

The input of group members have been just as important in establishing this thesis. There were many discussions on the ins and outs of laboratory experiments with Junfeng, Thanja, Gleb, Dongfeng and Jordy, introductions and

advanced courses in observational astronomy by Daniel H., Vianny, Nienke and Magnus, post-doc guidance by Gustavo and Radha, office buddy support from Kirsten, Vincent and Ko-Ju (best of luck to these three in finishing their own theses!) and a variety of discussions and fun times with Anton, J.B., Xavier, Pablo, Danna, Michal, Gwen, Andreas, Steven, Arthur, Maria, Irene, Joe, Lukasz, Merel, Paolo, Stefano, Sierk, Christian, Anna, Alvaro and Nadia.

The Protostellar Interferometric Line Survey (PILS) team has played a major part in transforming me into an observational astronomer. Jes, Matthijs, Holger, Susanne, Lars, Steffen and the rest of the team have been of great help and I very much enjoyed the team meetings we have had.

As a “teacher” I have guided Miriam, Marin and Jeroen TvS. (also my successor on CryoPAD2, best of luck in your future endeavours!) in their internships. Student supervision was often just as much a learning experience for me, but I am very happy with the successes and results of ‘my’ students.

The past few years would have been quite different without the observatory members who make for such a good atmosphere and in this way contributed to this thesis. With Eva, Heather, Jeroen F., Nico, Ricardo, Henriette, Ann-Sofie, Emanuelle, Mher and many, many others there never had to be a dull moment inside, but also outside, the workplace.

Last but not least are all the people that are not in astronomy or science, but made for the every now and then much needed distraction of science. Martial arts are a big part of my life and training and competing with the kickboxers of Team Atlas, the fighters of Gym Hoofddorp (where I received my blue belt in Brazilian jiu-jitsu) and the many martial artists and trainers of other gyms, has been a welcome pastime. Family and friends from Vinkeveen, Leiden and throughout The Netherlands have always been a welcome sight and were the greatest support throughout these years.

I thank you all for helping me in completing this thesis.

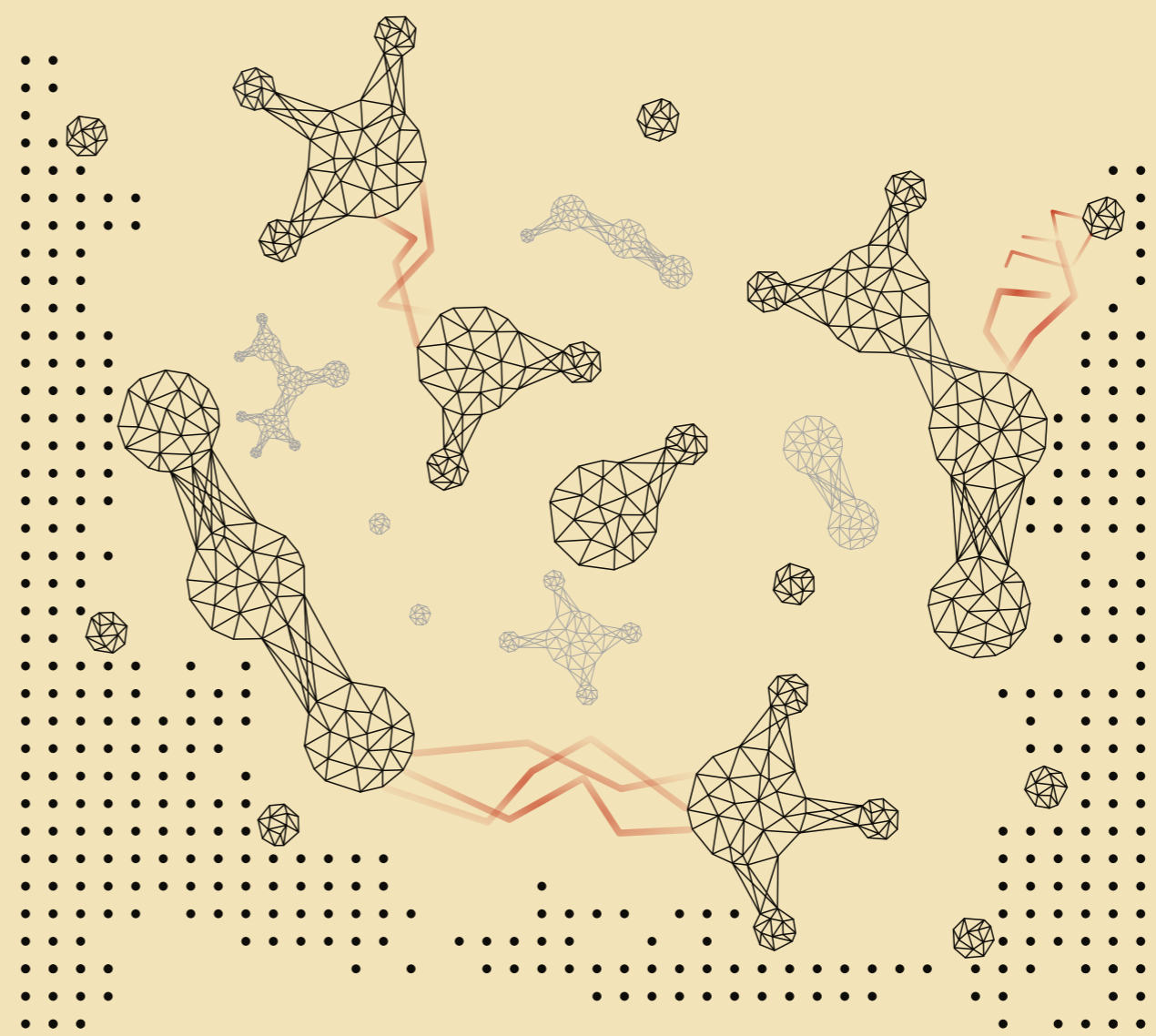


THE ASTROCHEMICAL FACTORY

NFW Ligterink

THE ASTROCHEMICAL FACTORY

a solid base for interstellar reactions

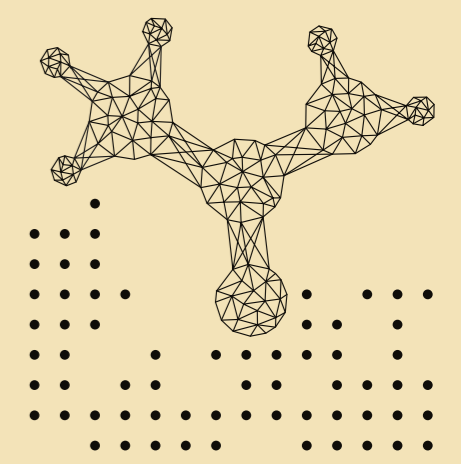


Niels Frank Willem Ligterink

Invitation

PhD defense
NFW Ligterink

THE ASTROCHEMICAL FACTORY



Monday
18 December 2017
at 11:15

Academiegebouw
Universiteit Leiden
Rapenburg 73